Thin Glass Coatings for the Corrosion Protection of Metals

Lampert, Felix

Publication date:
2017

Document Version
Publisher's PDF, also known as Version of record

DTU Mechanical Engineering
Department of Mechanical Engineering

Thin Glass Coatings for the Corrosion Protection of Metals

A dissertation by

Felix Lampert

Supervisors:

Per Møller

Jan Boye Rasmussen

September 2017

Thin Glass Coatings for the Corrosion Protection of Metals

A dissertation by

Felix Lampert

E-mail: felamp@mek.dtu.dk
Technical University of Denmark
Department of Mechanical Engineering
Produktionstorvet
Bygning 425, rum 111
DK-2800 Kgs. Lyngby

Main Supervisor:

Per Møller

E-Mail: pm@epc-info.dk
Technical University of Denmark
Department of Mechanical Engineering
Nils Koppels Allé
Bygning 404, rum 220
DK-2800 Kgs. Lyngby

Co-Supervisor:

Jan Boye Rasmussen

E-Mail: jbr@elplatek.dk
Elplatek A/S
Bybjergvej 7
DK-3060 Espergærde

Published by: Department of Mechanical Engineering, Section for Materials and Surface Engineering, Produktionstorvet, Building 425, DK-2800 Kgs. Lyngby

Preface

This dissertation is submitted in partial fulfilment of the requirements for obtaining the degree of Ph.D. at the Technical University of Denmark (DTU). The project was funded by Innovation Fund Denmark through the project Q-HEX, grant number 50-2014-1 and carried out at the Technical University of Denmark (DTU), Department of Mechanical Engineering, Section of Materials and Surface Engineering (MTU) during the period from October 1st 2014 until September 30th 2017. The project was supervised by Prof. Per Møller, Technical University of Denmark, Department of Mechanical Engineering and Jan Boye Rasmussen, Elplatek A/S.

Felix Lampert
Kongens Lyngby, Denmark, September 29th, 2017

Abstract

This dissertation presents the research work aimed at developing functional sub-micrometer thick SiO_x barrier coatings for the corrosion protection of stainless steel substrates in chloride containing media, which may enable the use of stainless steels as plate material for marine heat exchangers, and thus lower the component cost with respect to incumbent materials such as titanium alloys. The technology is of particular interest for the application on heat exchanger plates and components, since the thin coating films are expected to serve as efficient ionic barrier coatings, which prevent issues with localized corrosion and do not impact the heat transfer or the component performance.

The herein presented approach focuses primarily on the formation of SiO_x-like thin films from Hydrogen Silsesquioxane (HSQ) –based "spin-on-glass" (SOG) precursor. The technology is well known for the deposition of dielectric films in microelectronic applications and has been recently introduced as industrial surface finish for molding tools due to its ability to form stable surface films with excellent levelling. Within conventional SOG processing, a liquid precursor is deposited on the substrate and subsequently cured to form a continuous polymeric surface film. It is the aim of this work to transfer the existing technology to stainless steel substrates and establish an understanding of the effect of the curing conditions, the performance and failure mechanisms of SOG coatings on stainless steel substrates in corrosion sensitive applications. Since the deposition of SiO_x thin films is a well-established technology, the SOG technology was directly benchmarked to PVD-based SiO_2 coatings. The coating adhesion was assessed by cross cut testing and increasing load scratch testing and the efficiency of the sub-micrometer thick coatings was assessed by potentiodynamic anodic polarization measurements, EIS and neutral salt spray testing. Further, localized coating failures were investigated by the SVET and spot testing and the coating microstructure was investigated by (FIB-) SEM and a variety of analytical TEM methods. The coating chemistry was studied by FT-IR and XPS and the coating properties were characterized by water contact angle measurements, nanoindentation and AFM.

Overall, the results indicated that SOG deposition may yield well adherent coatings with excellent coverage and substrate levelling. The process yielded highly resistive coatings; however, all coatings allowed penetration of electrolyte to the substrate and no ideal barrier behavior was observed. Further, the results stress the particular importance of the interaction between the coating and the substrate for the coating performance: Oxidative curing led to pronounced interface oxidation, and thus to de-alloying of the substrate surface. As a consequence, the pitting resistance of the coated systems was found decreased or void formation between the coating and the substrate was observed. While interface oxidation can be suppressed by curing in non-oxidizing atmosphere, void formation due to coating delamination may induce critical coating defects, leading to the stabilization of growing pits. In consequence, it was shown that use of a bright surface finish minimizes the risk of coating failure. Moreover, it was shown that the degree of

coating polymerization is crucial for the chemical stability of the coatings and that coating imperfections lead to significant coating dissolution in near-neutral aqueous media.

Resumé

Denne afhandling præsenterer forskning rettet mod at udvikle en sub-mikrometer SiO_x barrierebelægning, der skal beskytte mod korrosion af rustfrie stålemner i kloridholdige miljøer, som kan gøre brugen af rustfrit stål egnet som plademateriale for marinevarmevekslere og derved mindske omkostningen til etablerede materialer som titaniumlegeringer. Teknologien er særlig interessant for applikationer som varmevekslerplader og komponenter, da den tynde belægning forventes at virke som en effektiv ionbarrier, så problemer med lokal korrosion undgås, samt at ledningsevnen af varme gennem komponenten bevares.

Den heri præsenterede fremgang fokuserer primært på udformningen af SiO_x –lignende belægninger fra Hydrogen Silsesquioxane (HSQ)-baseret ”spin-on-glass”(SOG)-teknologi. Teknologien er velkendt til deponering af dielektrisk film i mikroelektroniske applikationer, og er for nyligt blevet introduceret som industriel overflade finish i polymerstøbningsværktøj på grund af egenskaben til at danne en stabil belægning med enestående nivellering. I konventionelle SOG-processer bliver en væske deponeret på substratet og efterfølgende hærdet for at forme en kontinuerlig polymerbelægning. Det er målsætningen med afhandlingen at overføre den nuværende teknologi til rustfrie stålsubstrater og etablere en forståelse af påvirkningen på hærdningsbetingelserne og mekanismen, samt ydeevnen og nedbrydningsmekanismen af SOG-belægninger på rustfrie stålsubstrater i korrosive miljøer. SOG-teknologien vil blive rangeret overfor PVD-baseret SiO_2-belægninger, da deponeringen af SiO_x-belægninger er en etableret teknologi. Belægningens vedhæftning blev vurderet med gittersnitprøvningen og scratch test med stigende belastning og effektiviteten af den sub-mikrometer tykke belægning blev vurderet ved potentiodynamiske anodiske polaritionsmålinger, EIS og neutrale salttågeprøver. Ydermere blev lokale svigt i belægningen undersøgt med SVET samt spot test, og belægningens mikrostruktur blev undersøgt med (FIB)-SEM og en række TEM metoder. Belægningens kemiske sammensætningen blev studeret med FT-IR samt XPS, og belægningens egenskaber blev karakteriseret ved vands kontaktvinkel, nanohårdhedsmålinger og AFM.

De overordnede resultater indikerer, at SOG-deponering vil resultere i en belægning med god vedhæftning, dækkeevne og nivellering. Processen resulterer i en meget modstandsdygtig belægning; men alle belægninger tillader en penetrering af elektrolytten til substratet og ingen ideal barrier blev observeret. Ydermere understreger resultaterne vigtigheden af vekselvirkningen mellem belægningen og substratet for belægningens ydeevne: Den oxiderende hærdning fører til markant oxidering i interfacet, og resulterer i en udtømning af legeringselementer i substratets overflade. Som en konsekvens heraf blev grubetæringsmodstanden af det coatede system forværret og et tomrum dannet imellem belægningen og substratet blev observeret. Mens grænsefladeoxidering kan undgås ved at hærde i en ikke-oxiderende atmosfære, vil tomrumsformationen på grund af belægningens delaminering medføre kritiske defekter i belægningen, der stabiliserer

voksende gruber. Som følge heraf blev det vist, at ved brugen af blanke overflader blev risikoen for nedbrydning af belægningen minimeret. Yderligere blev det vist, at graden af belægningens polymerisering er afgørende for den kemiske stabilitet af belægningen samt, at belægningens fejl resulterer i en signifikant belægningsopløsning i tæt på *p*H-neutrale vandige medier.

Acknowledgements

Foremost, I express my appreciation and sincere gratitude to Prof. Dr. Per Møller, for the continuous support of study and research and for his inspiring ideas and enormous knowledge in the field. As my supervisor, he guided me through the project, the related research and dissemination process and gave valuable scientific advice and actively encouraged me to follow my own ideas. I could not have imagined a better advisor and mentor for my Ph.D. studies.

I am grateful for the research-funding from Innovation Fund Denmark, under the grant number 50-2014-1, and I wish to thank my project team for the close collaboration and support throughout the course of the project. In this context, I acknowledge the work of Dr. Alexander Bruun Christiansen and Dr. Annemette Hindhede Jensen (SiOx Aps.) and their commitment as well as determination as project leader, primary industrial partner and co-authors. Further, I am grateful to Jan Boye Rasmussen and Susanne Köhler (Elplatek A/S), Mats Nilsson, Dr. Axel Knutsson, Dr. Olga Santos and Jens Rassmus (Alfa Laval AB) for their assistance and the fruitful industrial collaboration.

Beside my project team, I am very grateful for the intense support from my co-authors as well as my many academic advisors, who have greatly supported this project with their deep scientific and technical knowledge. I wish to thank Dr. Yaiza Gonzales Garcia (TU Delft) and Dr. J.M.C. Mol for welcoming me during my external stay and enabling me to work in their group. Further, I am thankful to Dr. Rameez Ud Din (DTU), who significantly contributed to the project through long technical discussions and an outstanding commitment in the dissemination process and Dr. Kristian Vinter Dahl (DTU) for his contribution in thermodynamical modelling. I am thankful for the support from DTU-CEN and I express my special appreciation to Dr. Shima Kadkhodazadeh and Dr. Takeshi Kasama for their intense effort and scientific input in the field of ultramicroscopy. Further, I wish to thank Prof. Dr. S. Ray Taylor (University of Houston) for his teaching and mentoring in the field of Electrochemical Impedance Spectroscopy. In addition, I acknowledge the work done by René Bang Madsen (Polyteknik A/S), who greatly supported the project with his knowledge in Physical Vapor Deposition.

I am thankful for the support from my colleges at the section of Materials and Surface Engineering, who have not only supported me with their inconceivable scientific as well as technical knowledge, but also created a throughout positive and enjoyable working environment. In particular, I wish to acknowledge the help from Flemming Grumsen in advanced materials characterization, Dr. Chitta Ranjan Das for fruitful discussions about the physical metallurgy of steels and Marianne Burggraaf Buendia, Peter Schwencke Westermann as well as Steffen Munch for their daily assistance and laboratory support. I further want to thank Valeriia Reveko for being a black belt in electrochemistry and my office colleges, Chiara Tibollo, Emilie Valente, Frank Nießen, Jacob Nielsen, Mikkel Jensen, Nicolai Juul and Saber Haratian for lots of high fives and helping me to forget my work from time to time. In addition to the support from my colleges, I acknowledge the experimental work done via the student projects that I supervised. In this context I wish to

acknowledge the work done by Casper Ormstrup and Sebastian Nis Bay Villadsen, Gautham Sajan Ramachandran and Zhifeng Hao and Cecilie Vase Funch.

Lastly, I am thankful for the great support that I received from my family as well as my friends for their support throughout my life and academic career.

List of published articles and dissemination at conferences

Peer-reviewed articles (included in this thesis)

1. F. Lampert, A.H. Jensen, R.U. Din, P. Møller, Hydrogen Silsesquioxane based silica glass coatings for the corrosion protection of austenitic stainless steel, Surface & Coatings Technology 307, 879-885, 2016
2. F. Lampert, S. Kadkhodazadeh, A.H. Jensen, R.U. Din, P. Møller, Interfacial Interaction of Oxidatively Cured Hydrogen Silsesquioxane Spin-On-Glass Enamel with Stainless Steel Substrate, Journal of The Electrochemical Society 164(6), C231-239, 2017
3. F. Lampert, A.B. Christiansen, R.U. Din, Y. Gonzalez-Garcia, P. Møller, Corrosion resistance of AISI 316L coated with and air-cured hydrogen silsesquioxane based spin-on-glass enamel in chloride environment, Corrosion Science (In Press 24.08.2017)

Technical white paper (included in an excerpt)

1. F. Lampert, A.H. Jensen, P. Møller, Low Temperature Curing of Hydrogen Silsesquioxane Surface Coatings for Corrosion Protection of Aluminum, NASF Surface Technology White Papers 80(4), 1-8, 2016

Conference contributions

1. Oral presentation, NASF Sur/Fin 2015, Rosemont, USA, June 9th 2015
2. Oral presentation, Annual meeting of the Danish Electrochemical Society, Copenhagen, Denmark, October 2nd 2015
3. Oral presentation, NASF Sur/Fin 2016, Las Vegas, USA, June 7th 2016
4. Oral presentation, Annual meeting of the Danish Electrochemical Society, Nyborg, Denmark, October 13th 2016
5. Oral presentation, NASF Sur/Fin 2017, Atlanta, USA, June 23rd 2017

List of abbreviations and symbols

Chemical element symbols, chemical formulas, SI-units, product/company names and metric prefixes are not included in his list.

°	Degree (unit)
2B	Surface finish (standardized)
2R	Surface finish (standardized) – equivalent to bright annealed
A	Area
α	Constant phase element parameter
Å	Ångstøm (unit)
A_c	Projected contact area (in context of nanoindentation)
AFM	Atomic force microscope/microscopy
AISI	American Iron and Steel Institute
APCVD	Atmospheric pressure chemical vapor deposition
approx.	approximately
arb.	Arbitrary
as.	Asymmetric
ASTM	American Society for Testing Materials
at.%	Atomic percent (unit)
ATR	Attenuated total reflection
BA	Bright annealed
bar	Bar (unit)
c	Constant
C	Coulomb (unit)
C	Capacitance
°C	Degree Celsius (unit)
cal	Calorie (unit)
cc	Cubic centimeter (unit)
CCD	Charged coupled device
CCT	Critical crevice corrosion temperature
CP	Cyclic polarization
CPE	Constant phase element
CPT	Critical pitting temperature
CTE	Coefficient of thermal expansion
CVD	Chemical vapor deposition
γ_{LV}	Liquid-vapor surface tension (in context of dip-coating)
d	coating thickness (in context of impedance)
dep.	Deposition
DK	Denmark
DTU	Technical University of Denmark
G	Gibbs energy
GIF	Gatan image filter
Gy	Gray (unit)
E	Potential
EDS	Energy dispersive X-ray spectroscopy
EEL(S)	Electron energy loss (spectroscopy)
EFTEM	Energy filtered transmission electron microscopy
EIS	Electrochemical impedance spectroscopy
ELNES	Energy loss near edge structure
EN	European standard
eq.	Equation
ETD	Everhart-Thornley secondary electron detector

eV	Electron Volt (unit)
exp.	Experimental
ε_0	Dielectric permittivity of vacuum
ε_r	Dielectric constant
η	Liquid viscosity (in context of dip-coating)
F	Farad (unit)
FEG	Field emission gun
FFT	Fast Fourier transformed
FIB	Focused ion beam
FT-IR	Fourier transformed infrared spectroscopy
h	hour (unit)
h_0	Final thickness (in context of dip-coating)
h_f	Depth of the impression after unloading (in context of nanoindentation)
h_{max}	Indenter displacement at peak load (in context of nanoindentation)
HADF	High angle dark field
HV	Vickers hardness
HSQ	Hydrogen silsesquioxane
I	Electrical current
IR	Infrared
IR	Ohmic drop
ISO	International Organization for Standardization
J	Joule (unit)
k	Dielectric constant
l	Liter
Lc_1	Critical load (in context of scratch testing)
LO	Longitudinal optical
LOM	Light optical microscope/microscopy
LPCVD	Low pressure chemical vapor deposition
LPD	Liquid phase deposition
M	Molarity (unit)
min	Minute (unit)
n	Degree of polymerization
N	Normality (unit) (in context of concentrations)
N	Newton (unit) (in context of force)
no.	Number
OCP	Open circuit potential
ox.	Oxide
p	Potential
Pa	Pascal (unit)
PECVD	Plasma enhanced chemical vapor deposition
P_{max}	Maximum indentation load (in context of nanoindentation)
pp.	Partial pressure
ppm	Parts per million (unit)
PRE_N	Pitting resistance equivalent number
PVD	Physical vapor deposition
Q_0	Constant Phase Element parameter
R	Resistance
R_a	Arithmetic average value of filtered roughness
RF	Radio frequency
RTP	Rapid thermal processing
δg	Gravitational force (in context of dip-coating)
S	Unloading slope (in context of nanoindentation)
SCC	Stress corrosion cracking
SCE	Saturated calomel electrode

SD	Standard deviation
SE	Sweden
SEM	Scanning electron microscope/microscopy
SHE	Standard hydrogen electrode
SOG	Spin-on-glass
split.	Splitting
SUS	Steel use stainless (Japanese industrial standard for stainless steels)
SVET	Scanning vibrating electrode technique
STEM	Scanning transmission electron microscopy
stretch.	Stretching
sym.	Symmetric
TEM	Transmission electron microscope/microscopy
TLD	Through-lens detector
TMOS	Tetramethylortosilicate
TEOS	Tetraethylortosilicate
TO	Transverse optical
τ	Time constant
U_0	Withdrawal rate (in context of dip-coating)
UV	Ultraviolet
V	Volt (unit)
vol.%	Volumetric percent (unit)
W	Watt (unit)
WE	Working electrode
wt.%	Weight percent (unit)
x	Empirical factor for calculation of the pitting resistance equivalent number
XP(S)	X-ray photoelectron (spectroscopy)
XRD	X-ray diffraction
Z	Modulus (in context of impedance)
Ω	Ohm (unit)
ω_{max}	maximum radial frequency

Contents

1 Introduction

Gasketed plate heat exchangers are widely used in dairy, food processing, and chemical industries and find application in power plants and cooling systems, since the design enables an efficient heat transfer combined with an easy assembly/disassembly for cleaning or maintenance operations [1]. A gasketed plate heat exchanger allows the continuous circulation of two fully separated liquids, *i.e.* the circulation of a hot liquid on the one side and a cold liquid on the other side without intermixing of the liquids. In a common design, the plates are forged into a chevron pattern, stacked and separated by gaskets, as indicated in Figure 1.1. During assembly, the stack is compressed in a heat exchanger framework, which seals the gaskets and creates contact points between the plates.

The component design is used in generic heating/cooling applications in marine environment, which demands for extremely corrosion resistant materials to cope with the highly corrosive properties of heated seawater. To guarantee sufficient material stability, gasketed plate heat exchangers operating with seawater are typically fitted with Ti-alloy plates, which are highly resistant towards corrosion in the electrolyte. The high price for the plate material together with its scarcity, however, gives a strong incentive to explore further plate materials such as stainless steels to reduce the material cost under high volume production. While stainless steels guarantee excellent corrosion protection in a multitude of environments, the material is susceptible to Cl^--induced corrosion and may show severe degradation due to localized corrosion in saline environment [2].

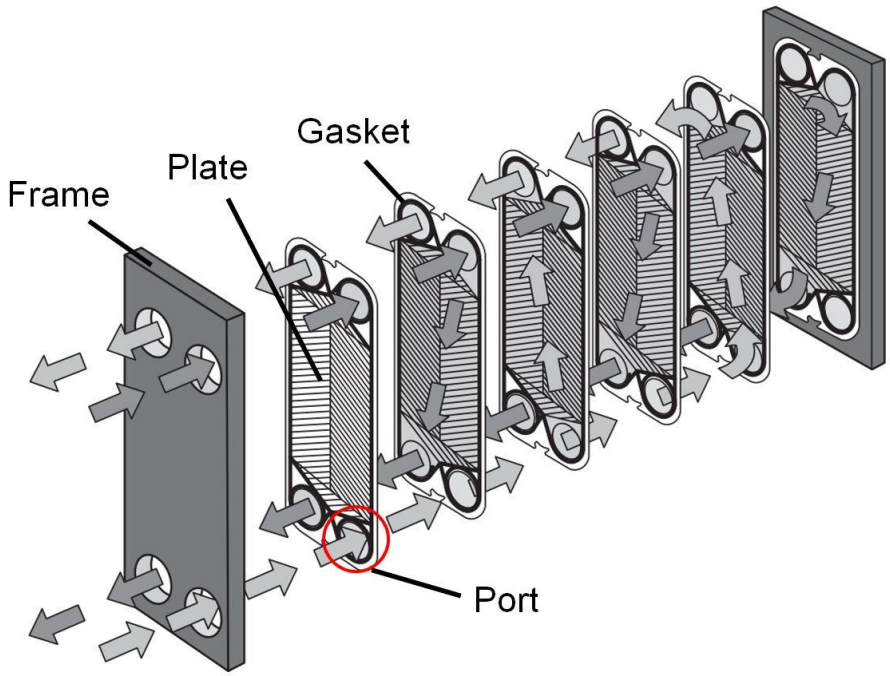

Figure 1.1: *Flow principle and basic components of a gasketed plate heat exchanger [1].*

As exemplified on an AISI 316L heat exchanger plate (Figure 1.2(a)) which was exposed to two months of service in a laboratory corrosion test (cyclic exposure to sea water at 70 ºC, renewal of the fluid every 2 h), type 316L plates degrade substantially under the harsh conditions expected in the application. The corrosive failure is generally concentrated along the narrow crevice formed between the rubber gasket and the plate (detailed view in Figure 1.2(b)), the port area with limited fluid convection, or the contact points between the plates (detailed view in Figure 1.2(c)). The pronounced material failure triggers the need for new concepts to increase the lifetime of stainless steel plates in marine applications. Increasing of alloying may enable the application of highly alloyed stainless steels [2]; however, the associated significant increase in material cost may reduce the advantage towards the traditional technology, triggering the need for new strategies to overcome corrosive failure of common stainless steels in Cl^- containing media.

While traditional corrosion protection strategies, such as vitreous enamels or organic paints, are expected to impair the heat transfer over the plates, elaborate corrosion protection concepts, such as cathodic protection, are challenging due to the complex geometry of the component. As a promising alternative to the traditional concepts, thin film barrier coatings, which promise high barrier efficiency for corrosive species at a

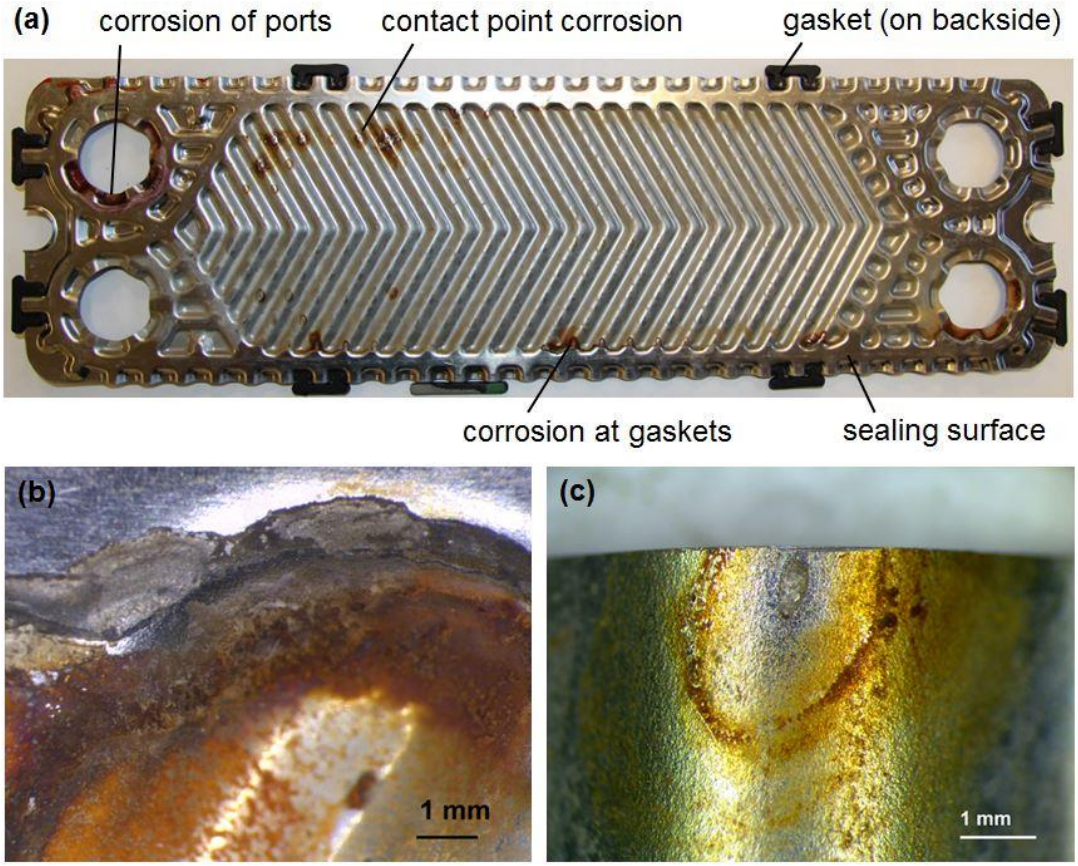

Figure 1.2: *Corrosive failure of AISI 316L heat exchanger plate after service in semi-accelerated laboratory corrosion test: (a) photograph of the plate showing severe corrosion at the gaskets, port area and contact points; (b) detailed view of corrosion site at the gasket area; (c) detailed view of a corroded contact point.*

minimum change in component geometry, have recently gained significant research focus. The coatings, which are frequently composed of ceramic compounds such as TiO_2 [3–6], Al_2O_3 [7] and SiO_x [8–12], are a viable solution to increase the lifetime of stainless steel heat exchanger plates, as they are neither expected to alter the plate geometry, nor impair the heat transfer considerably.

Recently, a novel approach for the coating deposition of thin films with stoichiometry close to SiO_2 has been introduced [13]. The approach is based on the deposition of a thin film of Hydrogen Silsesquioxane (HSQ) on a metallic substrate with subsequent thermal curing to crosslink the oligomeric precursor to an inorganic polymeric film [14,15], called spin-on-glass (SOG). The process has been successfully demonstrated for the coating deposition on metallic components [16–19] and is a promising solution to increase the lifetime of stainless steel plates in gasketed plate heat exchangers. In addition to an expected improvement in component lifetime, the technology has shown to significantly decrease the surface roughness of engineering components [16–18] and may yield in a significant decrease in biofilm adhesion or scaling when applied as surface finish for heat exchanger plates.

Since HSQ technology was traditionally used in microelectronics applications or nanolithography, only limited focused investigations have been carried out on HSQ as precursor for industrial surface coatings. Consequently, the present knowledge on the material, its microstructure, properties and performance as coating material is limited, triggering the need for a detailed investigation of HSQ-based barrier coatings on stainless steel substrates. Hence, the present dissertation will focus on the characterization of HSQ-based coatings on stainless steel substrates, the material interactions between coating and substrate and the assessment of the coating performance as corrosion barrier coatings. The dissertation will systematically study the industrially applicable coating deposition and will discuss the performance of the given coating system with respect to preexisting alternative coating processes.

1.1 Project organization

The project, funded by Innovation Fund Denmark, project name “Q-HEX, grant number 50-2014-1”, is a joint project of four major project partners. SiOx Aps, Espergærde, DK, constitutes the project leader and holder of the core patent application, US 2014/0154441 A1 [13]. Elplatek A/S, Espergærde, DK, is specialized on electrochemical surface finishing and holds extensive knowledge about electrochemical pretreatments for stainless steels. Alfa Laval AB, Lund, SE, is one of the world-leading producers of gasketed plate heat exchangers and holds extensive knowledge about heat exchanger design and testing. Finally, Technical University of Denmark (DTU), Department of Mechanical Engineering, Section of Materials and Surface Engineering, Kgs. Lyngby, DK, is a research group with a deep focus on the characterization of materials from the macroscopic to the nanoscopic length scale. Within the project organization, SiOx Aps holds the responsibility for the applied research on the coating process and its

implementation, Elplatek A/S for the electrochemical pretreatments of the substrate materials, Alfa Laval AB for the industrial-scale testing of coated heat exchanger components and DTU for the basic research on the coating materials, their properties, performance and their interactions.

1.2 Research objective

The present work focuses on the characterization of HSQ-based coating systems for the corrosion protection of stainless steels and on the assessment of the technology as suitable surface treatment to enable the application of stainless steel as alternative material for marine heat exchanger plates. The project aim is to gain a deeper understanding of the material in the technically relevant medium and the assessment and development of suitable processing conditions to produce functional and durable coating systems. Within this scope, the project aims at a fundamental understanding of the materials interaction between the coating and stainless steels and an assessment of the impact of the coating microstructure on the performance. Moreover, the project aims at a comprehensive understanding of the corrosion mechanisms of SiO_x coated stainless steel substrates and, based on this, a technologically relevant assessment of the protective performance of the systems.

1.3 Outline of the dissertation

The dissertation is structured in 14 individual chapters. A process chart showing the individual chapters and their logical connection is shown in Figure 1.3. Chapter 1 introduces the project and provides a formulation of the overall research objective. Chapter 2 gives a literature review of the relevant pre-existing knowledge on stainless steel corrosion, SiO_x thin film deposition, the performance of SiO_x films as barrier coatings and HSQ technology. Subsequently, chapter 3 gives a detailed overview of the experimental methods used during the experimental section of the dissertation and chapter 4 summarizes the key findings presented in the experimental chapters.

Detailed descriptions and discussions of the experimental work, based on six individual manuscripts and one technical report, are presented in chapters 5-11. As indicated in Figure 1.3, the experimental work may be divided into four logical blocks, being a proof of concept (chapter 5), followed by three blocks discussing curing under different curing conditions. The second block (chapters 6 and 7) explores the possibility of curing in air atmosphere and investigates the coating microstructure performance and properties of air-cured coatings. Based on the coating weaknesses identified in chapters 6 and 7, non-oxidatively cured coatings are further investigated in the third block (chapters 8-10). The block is started with a detailed investigation of the interfacial interactions between non-oxidatively cured SOG-coatings and stainless steel substrates (chapter 8) and continued with a focused investigation of the coating properties and the coating performance of non-oxidatively cured SOG-films in chloride containing aqueous solution (chapter 9). Subsequently, based on the issues identified in chapter 9, an improved version of non-

oxidatively cured coating is investigated in chapter 10 and benchmarked to a similar coating from a physical vapor deposition (PVD) process. Lastly, the experimental section is concluded by a technical note about electron beam curing of SOG-coatings as potential alternative to thermal curing.

The dissertation is continued with a comprehensive discussion of the experimental results (chapter 12), followed by the conclusions (chapter 13) and a proposal of further work (chapter 14).

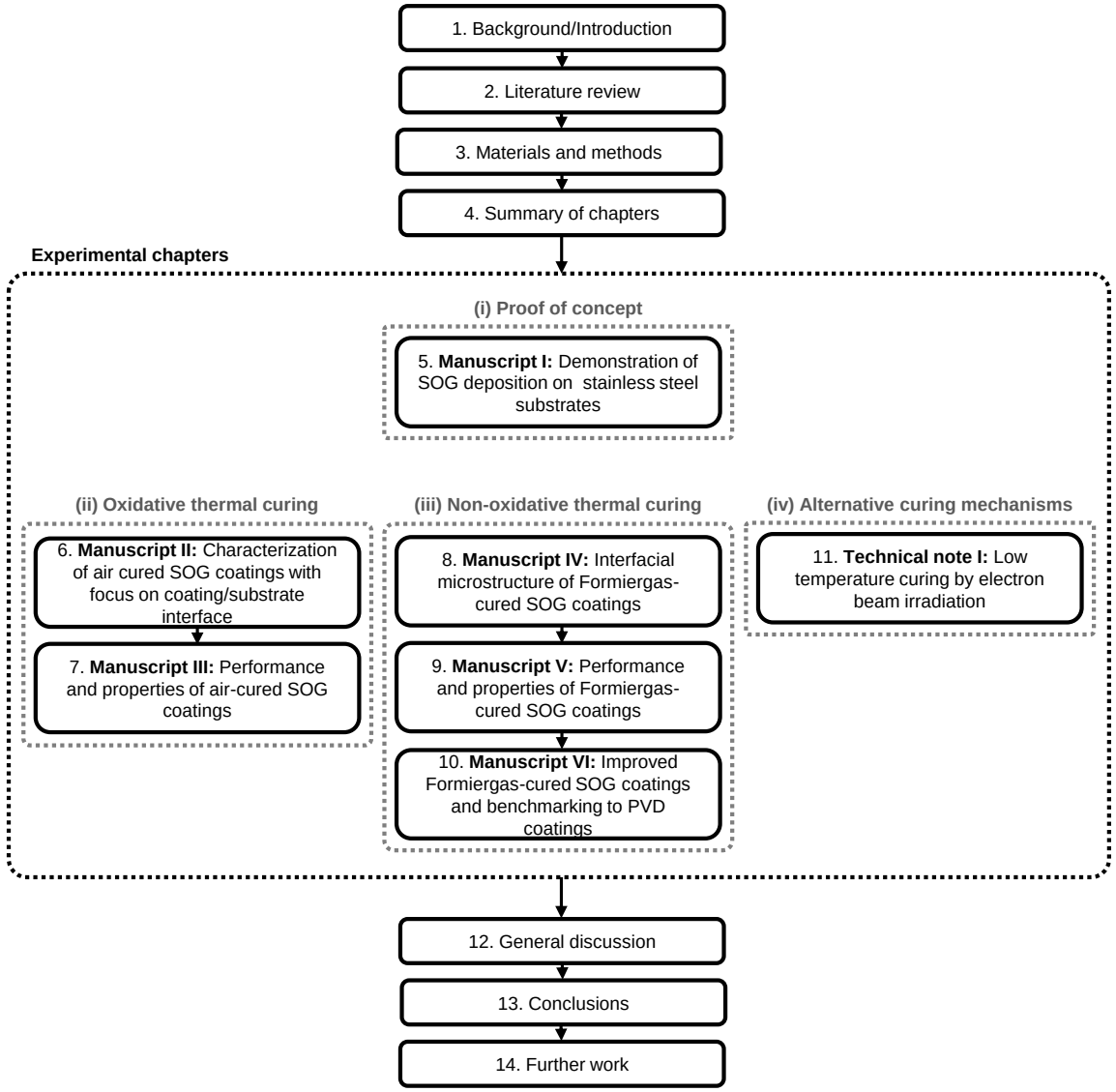

Figure 1.3: *Process-chart of the dissertation.*

References

[1] Alfa Laval Corporate AB, For Your Utility Heating and Cooling M-Series Plate Heat Exchangers, 2017. http://www.alfalaval.com/globalassets/documents/ products/heat-transfer/plate-heat-exchangers/gasketed-plate-and-frame-heat-exchangers/mline/pd-sheet---m-series-plate-heat-exchangers---en.pdf (accessed August 3rd, 2017).

[2] B. Leffler, Stainless-steels and their properties, 1996. https://www.tf.uni-kiel.de/matwis/amat/iss/kap_9/articles/stainless_steel.pdf (accessed March 1st, 2017).

[3] L. Ćurković, H.O. Ćurković, S. Salopek, M.M. Renjo, S. Šegota, Enhancement of corrosion protection of AISI 304 stainless steel by nanostructured sol–gel TiO2 films, Corros. Sci. 77 (2013) 176–184.

[4] S. Li, J. Fu, Improvement in corrosion protection properties of TiO2 coatings by chromium doping, Corros. Sci. 68 (2013) 101–110.

[5] S.T. Döşlü, B.D. Mert, B. Yazıcı, Polyindole top coat on TiO2 sol–gel films for corrosion protection of steel, Corros. Sci. 66 (2013) 51–58.

[6] S. Meth, N. Savchenko, M. Koltypin, D. Starosvetsky, F.A. Viva, A. Groysman, C.N. Sukenik, Corrosion studies of stainless steel protected by a TiO2 thin film deposited on a sulfonate-functionalized self-assembled monolayer, Corros. Sci. 52 (2010) 125–129.

[7] G. Ruhi, O.P. Modi, I.B. Singh, Pitting of AISI 304L stainless steel coated with nano structured sol–gel alumina coatings in chloride containing acidic environments, Corros. Sci. 51 (2009) 3057–3063.

[8] D.C.L. Vasconcelos, J.A.N. Carvalho, M. Mantel, W.L. Vasconcelos, Corrosion resistance of stainless steel coated with sol–gel silica, J. Non. Cryst. Solids. 273 (2000) 135–139.

[9] M. Atik, P. de Lima Neto, L.A. Avaca, M.A. Aegerter, J. Zarzycki, Protection of 316L stainless steel against corrosion by SiO2 coatings, J. Mater. Sci. Lett. 13 (1994) 1081–1085.

[10] O. de Sanctis, L. Gomez, N. Pellegri, C. Parodi, A. Marajofsky, A. Duran, Protective Glass Coatings on Metallic Substrates, J. Non. Cryst. Solids. 121 (1990) 338–343.

[11] T. Hwang, H. Lee, H. Kim, G. Kim, Two layered silica protective film made by a spray-and-dip coating method on 304 stainless steel, J. Sol-Gel Sci. Technol. 55 (2010) 207–212.

[12] D. Pech, P. Steyer, J.-P. Millet, Electrochemical behaviour enhancement of stainless steels by a SiO2 PACVD coating, Corros. Sci. 50 (2008) 1492–1497.

[13] H. Pranov, Reactive Silicon Oxide Precursor Facilitated Anti-Corrosion Treatment, US 2014/0154441 A1, USA, 2014.

[14] Y.K. Siew, G. Sarkar, X. Hu, J. Hui, A. See, C.T. Chua, Thermal Curing of Hydrogen Silsesquioxane, J. Electrochem. Soc. 147 (2000) 335.

[15] D. Többen, P. Weigand, M.J. Shapiro, S.A. Cohen, Influence of the cure process on the properties of hydrogen silsesquioxane spin-on-glass, Mater. Res. Soc. Somposium Proc. 443 (1997) 195–200.

[16] K. Mohaghegh, H.N. Hansen, H. Pranov, G. Kofod, A study on the surface roughness of a thin HSQ coating on a fine milled surface, in: 14th Euspen Int. Conf. - Dubrovink, 2014.

[17] K. Mohaghegh, H.N. Hansen, H. Pranov, G. Kofod, Verification of thickness and surface roughness of a thin film transparent coating, in: Proc. 13th Euspen Int. Conf., Berlin, 2013.

[18] J. Cech, H. Pranov, G. Kofod, M. Matschuk, S. Murthy, R. Taboryski, Surface roughness reduction using spray-coated hydrogen silsesquioxane reflow, Appl. Surf. Sci. 280 (2013) 424–430.

[19] T.C. Hobæk, M. Matschuk, J. Kafka, H.J. Pranov, N.B. Larsen, Hydrogen silsesquioxane mold coatings for improved replication of nanopatterns by injection molding, J. Micromechanics Microengineering. 25 (2015) 035018 (9pp).

2 Literature review

2.1 Corrosion of stainless steel

Localized corrosion, in particular crevice corrosion, is the main failure mechanism of the stainless steel engineering component under investigation. Generally, two different mechanisms for local passivity breakdown and subsequent localized corrosion of stainless steels are distinguished, namely pitting and crevice corrosion [1,2]. Recent advances, however, have indicated that crevice corrosion may be treated as a form of geometrically stabilized pitting corrosion [3,4], and therefore in this chapter both pitting and crevice corrosion will be treated in depth. The section commences with a general review about stainless steel passivity and continues with a detailed description of pitting corrosion of stainless steels, followed by a discussion of the major factors that influence the breakdown mechanism. The section is concluded with a review of crevice corrosion.

2.1.1 Passive layer

Stainless steels owe their resistance towards galvanic corrosion to their high Cr content and, resulting from this, a thin Cr-oxide/hydroxide -rich surface layer which protects the underlying material from chemical attack [1]. The oxide film on stainless steel, containing mostly Cr and Fe oxides/hydroxides, constitutes a native passivation with good barrier properties towards anodic dissolution. Further, the passivation is electrically conductive and allows cathodic reactions to take place on the surface at high rates [5].

The composition and nature of the native passivation is strongly dependent on the environmental conditions during oxide formation [6]. Compositions close to the stoichiometry of the base alloy have been reported for stainless steels which were oxidized in dry oxygen at room temperature [6,7], *i.e.* without influence of an aqueous solution. The passive film formed on the material under dry conditions does not exhibit a homogeneous elemental distribution, but rather shows an accumulation of Fe-rich oxides in the top-layer [8,9]. Similar observations have been made for samples that were mechanically ground in oxygenated water [10]. Prolonged exposure to aqueous solution, however, tended to enrich the surface film in alloying elements (particularly in Cr [6,10–14]), which was interpreted as selective dissolution of Fe from the oxide, leaving a Cr-enriched surface film [13,15–17]. There is wide agreement in the literature that the surface passivation formed in aqueous environment is not exclusively constituted from oxides, but rather a mix between oxides and hydroxides [6,8,10,12,13]. Further, the formation of a double layered passivation, which consists of an Cr-rich hydroxide with an underlying layer of Fe/Cr oxides, has been reported [6,10,12]. Similarly, an outer monolayer of Cr-hydroxide, followed by an inner layer of Fe-Cr oxides, has been identified after polarization in acidic media [18]. Further, the presence of a double layered passivation with an outer hydroxide and inner oxide layer has been confirmed by Tardio *et al.* [13], who have investigated the passivation formed on commercial grade AISI 316L

steel after oxidation in ambient air. The group concluded that air exposure of the material leads to water adsorption on the surface, followed by hydroxide formation.

2.1.2 Pitting corrosion of stainless steel

Pitting is a form of localized corrosion which frequently occurs on passivated metals in aggressive, typically halide-ion containing, environments such as sea water [1]. The corrosion mechanism is characterized by a small, anodic corrosion site which is surrounded by a large area which facilitates the cathode reaction. As described by Frankel [19], pitting can generally be divided into three stages: passivity breakdown, metastable pitting and pit growth.

Passivity breakdown

The initiation of active dissolution requires breakdown of the protective surface passivation. Passivity breakdown may occur by different mechanisms, depending on the particular corroding system or environmental conditions [20]. Generally three different mechanisms for passivity breakdown have been proposed [19,20]: Breakdown by ionic penetration (Figure 2.1(a)), adsorption of aggressive anions at the passive layer followed by thinning (Figure 2.1(b)) and film breaking (Figure 2.1(c)).

Hoar *et al.* [21] proposed the mechanism of ionic penetration (Figure 2.1(a)). Assisted by the high electric field (*i.e.* at the breakdown potential) in the passive film, aggressive anions, such as Cl^-, adsorb on the film and penetrate into the oxide, forming an "anion-contaminated oxide". The "contaminated oxide" is a more efficient cation-conductor with respect to the original passivating oxide and enables migration of cations from the substrate through the oxide film. It was suggested that the mechanism is strongest at irregularities in the passivation (*e.g.* grain boundaries or impurities) and accounts for preferential pit initiation at substrate defects.

The second proposed mechanism for pit initiation is based on the adsorption of aggressive anions on the passive film. The adsorption is suggested to lead to the formation of a surface complex with the oxide cations, which enables their separation from the oxide lattice, *i.e.* their dissolution [22]. Due to the anodic field, the oxide cations are replaced by cations from the substrate, which are subsequently dissolved by the previously described mechanism. As visualized in Figure 2.1(b), the mechanism leads to successive thinning of the oxide, and ultimately to breakdown of the passive film.

The last proposed mechanism by Vetter *et al.* [23] suggests that passivity breakdown results from the rupture of the passive film due to mechanical stresses, which allows the aggressive electrolyte to penetrate through the defect, and hence the initiation of pitting (Figure 2.1(c)). In analogy to mechanical stress, Sato [24] discussed the mechanical rupture of passive films due to electrostriction forces, assisted by the adsorption of anions at the film surface.

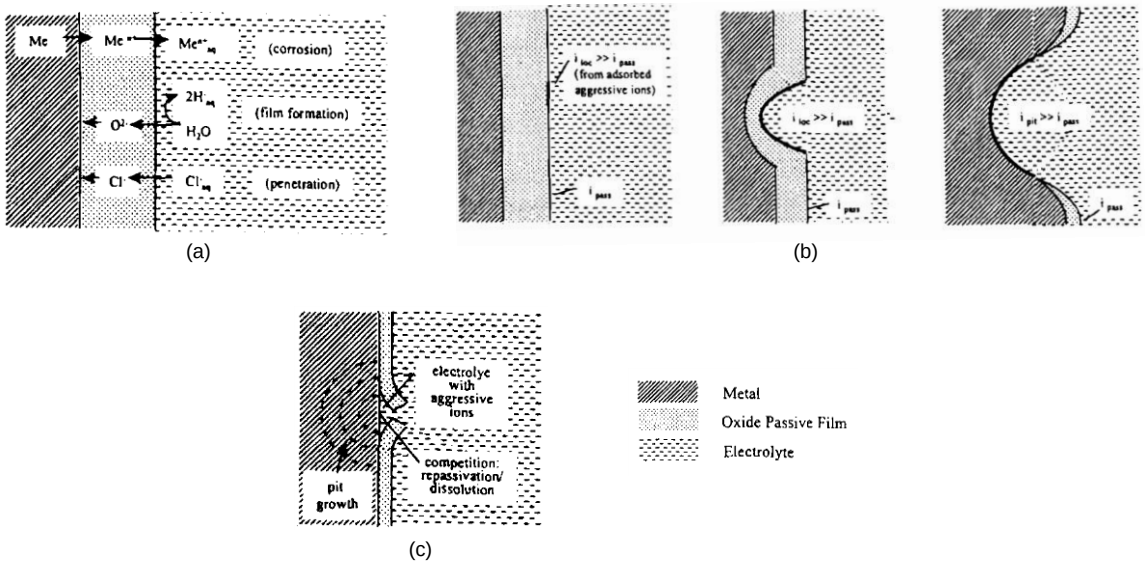

Figure 2.1: *Schematic diagrams representing pit initiation by: (a) penetration; (b) adsorption and thinning; (c) film breaking [19].*

In addition to the general mechanisms discussed in the previous section, pit initiation on stainless steels has been explained by pit formation at preexisting material defects, such as surface roughness or (Mn-) sulphide inclusions [25,26]. In a model proposed by Wranglén [26], MnS inclusions behave anodic with respect to the surrounding passive film and subsequently dissolve. In a consecutive step, the dissolution spreads to the unprotected metal below the inclusion, and thus initiates pitting corrosion. In an alternative approach, Pistorius *et al.* [25] discussed the initiation of pits at sulphide inclusions and suggested that pitting initiates at geometrically concealed inclusions such as sulphides occluded by *e.g.* surface roughness (Figure 2.2). In the model, the local electrolyte composition is changed by the dissolution of the inclusion, yielding increased dissolution rates in its vicinity. As stressed by the group, the effect may be amplified by the surface geometry surrounding the pit, leading to a lower pitting potential at inclusions situated in a geometrically occluded position (inclusion A in Figure 2.2) relative to inclusions at more open substrate defects (inclusion B in Figure 2.2).

Metastable pitting

Metastable pits are characterized as pits which grow for a short-lasting time and re-passivate before a sufficient pit size for stable pit growth is reached [19,27]. Usually, metastable pits reach a maximum size in the order of micrometers and have lifetimes in the order of seconds [19,28]. Pistorius *et al.* [25] describe the mechanism of metastable pitting in detail: Potentiostatically polarized stainless steel surfaces exhibit characteristic current transients with lifetimes of a few seconds (Figure 2.3). The slow increase and sudden decrease in current can be explained by the formation, growth and subsequent rapid passivation of metastable pits. The pits are stabilized by a pit cover, possibly a remnant of the surface oxide layer, which acts as diffusion barrier and thereby retains the

aggressive solution chemistry inside the pit. In case of rupture of the pit cover, the electrolyte inside the pit is diluted and the pit re-passivates.

Pit growth

For the transition from metastable pitting to stable pit growth, the conditions at the bottom of the pit need to be severe enough to prevent the re-passivation of the metal surface inside the pit [19,29]. As considered by Pistorius *et al.* [29], the aggressiveness inside a stable pit originates from a high acidity of the pit solution in combination with a high Cl^- concentration. Both the acidity of the solution and the Cl^- concentration are dependent on the metal cation content. Consequently, the concentration of the metal cations is a reliable measure of the pit-solution aggressiveness. Hence, to maintain a sufficiently aggressive pit environment, the diffusional transport of cations out of the pit has to be balanced by a sufficiently high cation dissolution speed. Pistorius *et al.* [29]

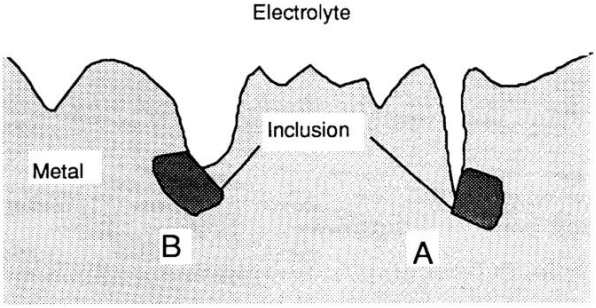

Figure 2.2: *Suggested pit initiation sites, which may account for the potential dependence of the number of available pit sites. An inclusion is exposed at the base of a depression in the surface of the metal. Dissolution of the inclusion changes the local electrolyte composition, but this change in composition is counteracted by diffusion. Since diffusion is more restricted from site "A", it can be activated at a lower potential than site "B". Site "B" can only grow into a pit at higher potentials, where the dissolution rate of the inclusion and of the metal, once activated, is higher [25].*

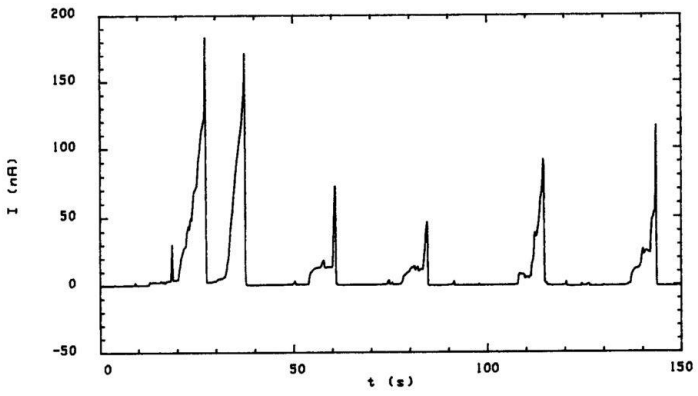

Figure 2.3: *Current transients which reflect the formation of metastable pits on a 50 µm electrode of type 304 stainless steel, held at 0.1 V vs. SCE in a solution of 1 M Cl^-, pH 0.7 [25].*

derived, based on a minimal cation concentration and the assumption of steady state cation diffusion out of the pit, a pit-geometry dependent minimal current density, the "pit stability product", which is necessary before a metastable pit can propagate into the active growth phase. In the group's considerations, no diffusion barrier except from the pit geometry itself is necessary to maintain stable pit growth after the transition from metastable to stable growth. In contrast to the theory outlaid by Pistorius *et al.* [29], Frankel *et al.* [28] have proposed pit growth mechanisms which require the formation of a stable pit cover such as the precipitation of a salt film, to maintain the aggressive pit electrolyte, and thus stable pit growth.

2.1.3 Assessment of susceptibility towards pitting corrosion

The susceptibility of stainless steels for localized corrosion is frequently characterized by the pitting or breakdown potential. Hereby the pitting potential is defined as the potential during an anodic potential sweep at which a steep increase in current becomes evident, *i.e.* at which passivity breakdown and subsequent initiation of pitting occurs [2]. Evaluation of the pitting resistance based on the pitting potential is one of the most widely applied methods to evaluate the electrochemical properties of stainless steels under different environmental conditions (such as temperature and chloride content [30,31] or for different stainless steel alloy compositions [30]).

An alternative approach to assessing the pitting resistance of stainless steels is the standardized test method for "Pitting and Crevice Corrosion Resistance of Stainless Steels and Related Alloys by Use of Ferric Chloride Solution", ASTM G 48 – 11 [32]. The approach relies on two methods to determine the pitting susceptibility of stainless steels. Method A, compares the relative susceptibility towards pitting corrosion after isothermal immersion in a solution of ~6 wt.% $FeCl_3$ aqueous solution, while method E describes a procedure to determine the critical pitting temperature, *i.e.* the minimum temperature at which pitting corrosion is observed after 24 h immersion in ~6 wt.% $FeCl_3$ aqueous solution. Although the accurate standard procedure is limited to the immersion in $FeCl_3$ aqueous solution as test electrolyte, the term critical pitting temperature has been transferred to other electrolytes and *e.g.* used for the minimum temperature of pitting initiation in neutral NaCl aqueous solutions [33].

2.1.4 Electrolyte temperature and chloride content

The susceptibility of stainless steels to localized corrosion is greatly influenced by the electrolyte composition and temperature. Since a major share of corrosion engineering failures of stainless steels are caused by chloride-induced corrosion, the effect of the chloride content on the susceptibility to pitting corrosion is well described in literature. Saithala *et al.* [30] determined a general increase in pitting susceptibility with increasing chloride solution concentration and solution temperature. Their investigations were based on the pitting potential of a variety of industrial grade stainless steels for various temperatures and chloride solutions ranging from 15-10000 ppm. Similarly, Wang *et al.*

[31] determined the susceptibility of AISI 304 stainless steel towards pitting corrosion based on the pitting potential for a variety of chloride concentrations and solution temperatures. The results from the respective study are summarized in Figure 2.4. As visible from Figure 2.4(a), the measured pitting potential significantly decreased with increasing Cl^- content for the entire investigated solution temperature range (20 – 200 ºC). In addition to increased Cl^- contents, increasing temperatures at constant Cl^--concentration led to decreasing pitting potentials, as visualized in Figure 2.4(b).

2.1.5 Effect of alloy composition on the sensitivity to pitting

Generally, steels with Cr contents above 11 wt.% possess the ability to form a continuous protective passivation [33]. The resistance to localized, Cl^- induced corrosion of stainless steels depends, apart from the Cr content, predominantly on the alloying with Mo and N. It is frequently approximated by the empirical pitting resistance equivalent (PRE_N) number defined by eq. (2.1), with the factor *x* commonly assumed as 16 for ferritic-austenitic and 30 for austenitic steels [1]. As elucidated by Leffler [33], the PRE_N value of a variety of austenitic stainless steels correlates with the critical pitting temperature (CPT) and critical crevice corrosion temperature (CCT) in a virtually linear relation, and hence gives a good empirical description of the Cl^- corrosion resistance of austenitic stainless steel grades. Figure 2.5 shows examples of diagrams of PRE_N vs. CPT or CCT in 1 M NaCl aqueous solution and 6 wt.% $FeCl_3$ aqueous solutions. It is evident that PRE_N and the pitting/crevice corrosion resistance of different steel grades follow an approximately linear relationship.

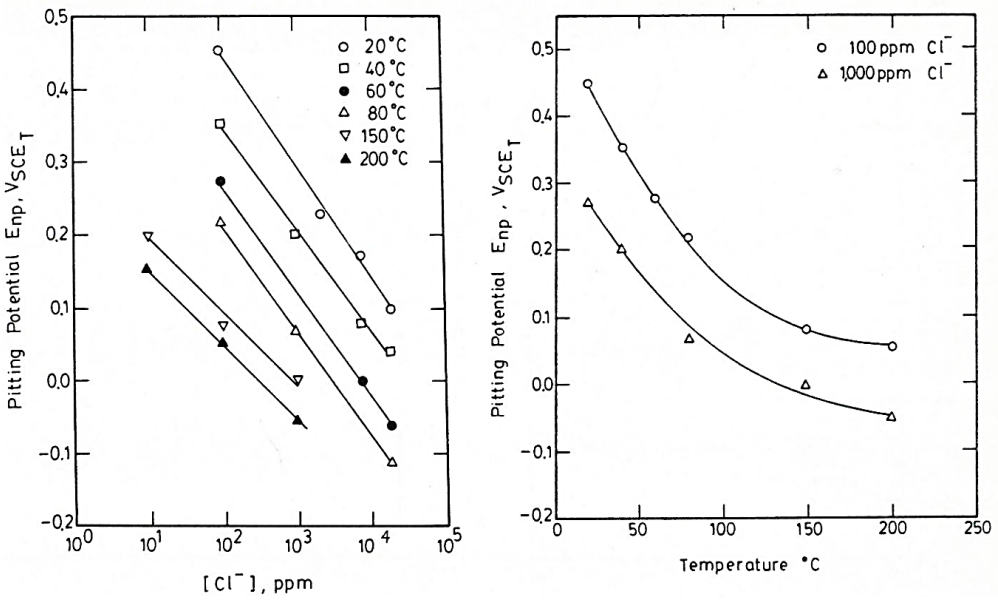

Figure 2.4: *(a) Pitting potential vs. log Cl^- concentration in aerated diluted (various degree of dilution) sea water at various temperatures; (b) Pitting potential vs. temperature in aerated diluted sea water with 100 and 1000 ppm Cl^-. The experiments were conducted on AISI 304 stainless steel [31].*

$$PRE_N = \%Cr + 3.3\ \%Mo + x * \%N \quad (2.1)$$

As described in section 2.1.1, stainless steels are capable of forming a Cr-rich passivation and Cr is clearly the main species that enables the passivation of the material [14,34]. However, as suggested by the PRE_N model, alloying with Mo and N play a vital role in the passive properties, in particular for highly corrosion resistant alloys [35].

Olefjord *et al.* [15], suggested that alloying with Mo decreases the defect density in the protective inner region of the passive layer, thereby decreasing the ionic conductivity. In contrast, Hashimoto *et al.* [36] demonstrated the beneficial effect of Mo addition to Fe-Cr steel and concluded that the improvement in corrosion resistance due to Mo addition originates from the formation of Mo oxy-hydroxide or molybdate on active sites, which consequently decreases the activity of the active surface. Similarly, Ogawa *et al.* [37] suggested, that the enhancement in corrosion resistance on Mo-bearing Cr-steels relies on

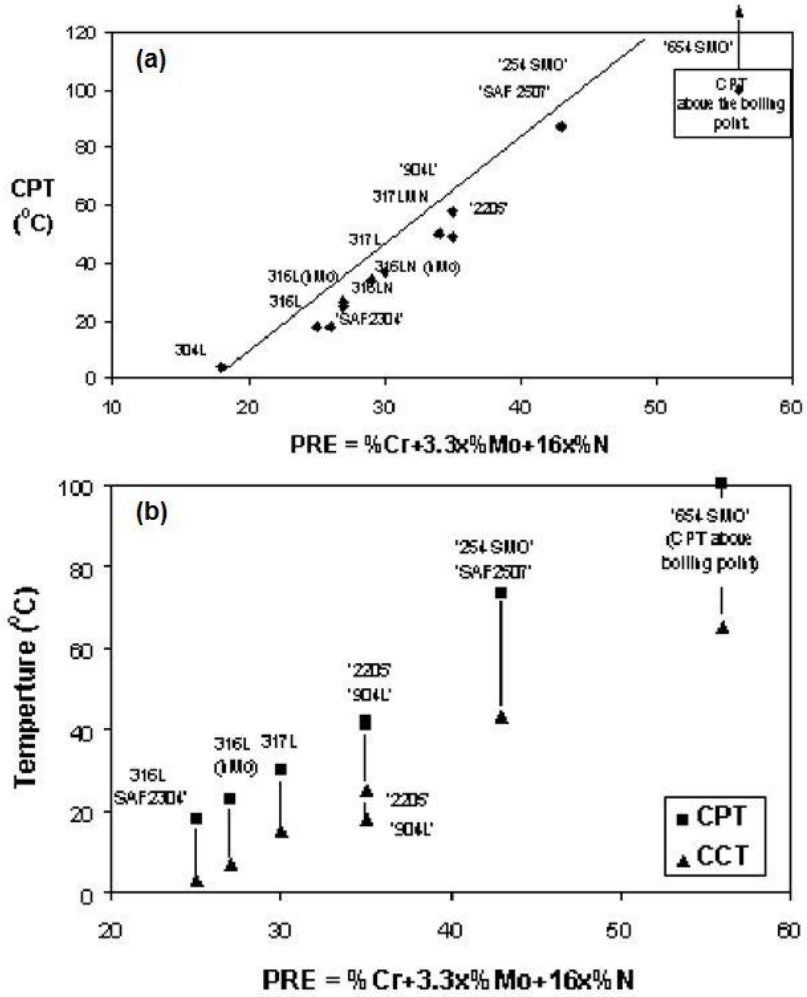

Figure 2.5: *Effect of PRE_N value on: (a) Critical pitting temperature (CPT) in 1 M NaCl aqueous solution; (b) CPT and critical crevice corrosion temperature (CCT) in 6 wt.% $FeCl_3$ aqueous solution [33].*

the adsorption of molybdate on active surface sites and other groups [38,39] suggested that the beneficial effect of Mo addition relies in the formation of stable Mo oxides which inhibit further attack of the substrate.

The positive effect of N addition on the corrosion resistance of stainless steels has been extensively studied and different mechanisms have been proposed to explain this behavior. N incorporation in the passive film was suggested as the prevailing mechanism for the performance enhancement in corrosion resistance [40]. However, surface-analytical studies [41–43] did not detect N incorporation into the oxide film and rather suggested that N segregates at the passive oxide/metal interface during metal dissolution. Consequently it was concluded, that the N segregation during the selective dissolution of metal atoms leads to the observable improvement in corrosion resistance [41]. Similarly, Olefjord *et al.* [44] detected N segregation at the interface; however, the group concluded that the N from the alloy compensates for the *p*H drop in forming pits via reaction with H^+ to form NH_3 or NH_4^+. The results were supported by research from Jargelius-Pettersson [45], who detected NH_4^+ as the dominant N species during the dissolution of N bearing steels and concluded that the improvement in corrosion resistance due to N alloying originates from *p*H buffering of the solution. In addition to the individual contributions on Mo and N alloying, an improvement in corrosion performance due to simultaneous Mo and N addition has been observed and synergetic effects of Mo and N alloying have been proposed [43,45,46].

2.1.6 Crevice corrosion

In contrast to pitting corrosion, the term crevice corrosion denotes a type of localized corrosion which occurs in restricted component areas such as *e.g.* gaskets, washers, bolt heads or under surface deposits [47]. Despite the technological relevance, there is at present no generally accepted mechanism for crevice corrosion [4] and different models for crevice corrosion initiation have been proposed:

One of the most common theories for crevice corrosion initiation is the passive dissolution model, which describes crevice corrosion initiation in four stages [48]. In the first stage, the cathodic reaction occurs homogeneously over the surface (in- and outside of the crevice). Since the crevice geometry restricts the inward diffusion of oxygen, the crevice is deoxygenated, which leads to a drop in electrochemical potential inside the crevice and consequently to the formation of a galvanic cell with the cathodic area outside and the anodic area inside the crevice. In the second stage, cation release from the alloy and subsequent cation-hydrolysis leads to an increase in solution acidity inside the crevice. To maintain electrical neutrality, Cl^- migrates into the crevice, yielding a highly aggressive, trapped solution. In the third stage, the crevice solution reaches a sufficiently high acidity together with sufficiently high Cl^- concentration to initiate a permanent breakdown of the passive film and the commencement of rapid corrosion inside the crevice. The fourth stage is characterized by propagation of active corrosion inside the

crevice, which is balanced by oxygen reduction on the large passive area outside the crevice.

As an alternative, thermodynamics based approach to explain the acidification of crevices and pits, Møller *et al.* [49] have formulated a model that describes the acidification by oxidation of divalent cations, as shown for iron in the reaction scheme below (reaction (2.2)-(2.4)). In a first step, a transition metal oxide is dissolved (reaction (2.2)), which leads to the subsequent oxidation of the base metal (reaction (2.3)).Then the divalent cations oxidize under the presence of O_2 at the crevice opening (reaction (2.4)), which leads to the local formation of H^+ and consequently acidification of the crevice.

$$Fe_2O_3 + 6H^+ + 4Cl^- \rightarrow 2FeCl_2^+ + 3H_2O \qquad (\Delta G = -168.0\ kJ) \qquad (2.2)$$

$$2FeCl_2^+ + Fe \rightarrow 3Fe^{2+} + 4Cl^- \qquad (\Delta G = -78.0\ kJ) \qquad (2.3)$$

$$4Fe^{2+} + O_2 + 4H_2O \rightarrow 2Fe_2O_3 + 8H^+ \qquad (\Delta G = -166.9\ kJ) \qquad (2.4)$$

In contradiction to the passive dissolution model [48], findings by Lott *et al.* [50] indicated that crevices do not acidify prior to passivity breakdown of the alloy and that acidification occurs after the initiation of active corrosion inside the crevice. These findings led to the proposal of a new model for crevice corrosion initiation based on the oxidation of MnS inclusions [51,52] to $S_2O_3^{2-}$ and H^+, whereby the locally increased concentration of $S_2O_3^{2-}$ and Cl^- leads to local breakdown of passivity, and thus initiation of active corrosion. Experiments by Brossia *et al.* [53], on the contrary, indicated that the predominant S species in crevices formed on AISI 304L-grade stainless steel was HS^-, contradicting the model of crevice corrosion initiation based on $S_2O_3^{2-}$. However, as outlaid by Newman *et al.* [54], HS^- is, similar to $S_2O_3^{2-}$, capable of inducing passivity breakdown in stainless steels and the initiation-model based on the oxidation of MnS inclusions may be applicable considering HS^- as electrochemically active species [4].

Another mechanism for crevice corrosion initiation was proposed by Pickering *et al.* [55,56], who found a significant decrease in corrosion potential inside crevices and pits due to Ohmic potential drop. As proposed by the group, the Ohmic drop found in crevices is sufficient to force the alloy from the passive to the active region, thereby initiating corrosion. Cho *et al.* [57] have shown, that the theory is applicable for the initiation of crevice corrosion in pure iron and that that crevice corrosion can be initiated without acidification of the crevice during the initiation period. However, as pointed out by Laycock *et al.* [4], significant changes in crevice chemistry are necessary to initiate passivity breakdown by the Ohmic potential drop mechanism in stainless steels, and hence the model is open to similar criticism as the passive dissolution model proposed by Oldfield *et al.* [48].

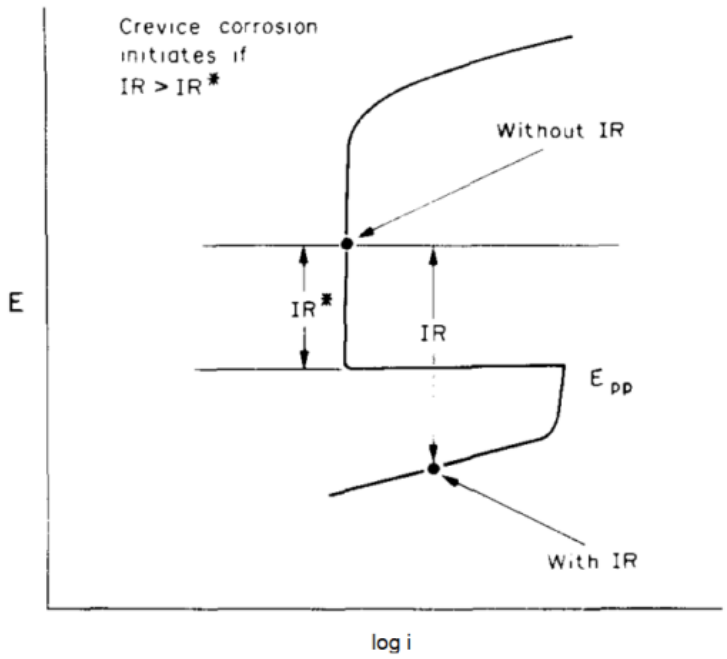

Figure 2.6: *Schematic illustration of IR induced crevice corrosion for iron in buffered acetic acid under anodic polarization [47]. (Modified figure)*

In addition to the previously outlaid theories, it was suggested to consider crevice corrosion as a particular case of pitting, whereby corrosion initiates in form of pits inside a crevice and propagates in form of crevice corrosion [58]. The hypothesis was supported by research from Stockert *et al.* [3], who found a direct correlation between the crevice corrosion susceptibility of stainless steels in aqueous NaCl solution and the metastable pitting activity. Based on this observation they extended the Ohmic potential drop model and proposed that the Ohmic potential drop in the crevice is sufficient to stabilize metastable pits, which would otherwise repassivate after breakdown of the pit-cover. According to their model, crevice corrosion initiation is a statistical phenomenon, which is based on the number of metastable pitting events, whereby stable crevice corrosion may be initiated by the growth of a single stabilized pit. The proposed mechanism has been experimentally supported by Laycock *et al.* [4], who validated the correlation between metastable pitting rate and crevice corrosion susceptibility.

2.2 Thin film deposition of silica

As pointed out in the previous section, stainless steels may be prone to corrosive failure in aggressive environments, necessitating highly alloyed stainless steels or advanced corrosion prevention strategies. In the present section, coating of stainless steels with thin films of silica is extensively reviewed as a novel corrosion prevention concept for stainless steels. In the first part of the section, the focus is set on the traditional processing routes, such as sol-gel processing, physical and chemical vapor deposition and liquid phase deposition. Subsequently, the application of silica deposition on steel substrates is

reviewed, starting with the general microstructural and morphological aspects of silica coatings and continuing with the application of silica films as corrosion barrier coatings. Finally, the section is concluded with a discussion about the chemical stability of silica films in aqueous environment.

2.2.1 Traditional processing routines

Sol-gel processes

The sol-gel synthesis of silica films is a common process to deposit silica from precursors such as functionalized silanes. Since the deposition from water-based sols constitutes the major share of sol-gel processes, the following section will solely focus on aqueous sol-gel processes. Within the synthesis, a solution of the precursor is transformed into a rigid network with siloxane backbone via hydrolysis and condensation of the precursor [59], whereby the most common precursors and silicon-sources for the synthesis of silica gels are monomeric alkoxysilanes such as tetramethylortosilicate (TMOS) or tetraethylortosilicate (TEOS). Within the process, the precursor is hydrolyzed via acid or base catalysis, forming reactive silanol moieties, as shown in the reaction schemes depicted in Figure 2.7. Conversely, polymerization of the sol occurs via a condensation reaction, *i.e.* acid or base catalyzed condensation, as visualized by the reaction schemes in Figure 2.8. Depending on the process parameters, sol-gel processes are versatile and suitable for the formation of films, fibers, particles or bulk glasses [60].

Common processes for the deposition of sol-gel-based films are dip-, spin-, or spray-coating. In particular dip-coating is of technological interest, since the process requires minimal processing equipment, allows for coating of complex geometries, is easily automatized and allows for batch processing. During the deposition, a substrate is immersed into a liquid precursor and withdrawn (usually vertically from the solution) with a controlled, constant speed, leaving a thin layer of precursor solution on the surface [62]. Consequently, excess liquid drains from the surface and the solvent evaporates from the precursor. For processes with high liquid viscosity η and withdrawal speed U_0, the final thickness h_0 is determined by the viscous drag (ηU_0) and the gravitational force (ρg), according to eq. (2.2) [62,63] (with the constant c_1 typically approximated as 0.8 for Newtonian liquids). For low withdrawal speeds (~1-10 mm/s) and liquid viscosities, as frequently observed in sol-gel films, eq. (2.2) needs to be adjusted for the ratio of viscous drag to liquid-vapor surface tension γ_{LV}, yielding eq. (2.3) [62,63]. However, deviations from the models based on the balance between viscous drag and gravitational force are found for systems where the progression of the drying line is faster than the withdrawal (at very low withdrawal speeds) such that the use of other models may become necessary for the estimation of the final film thickness [62].

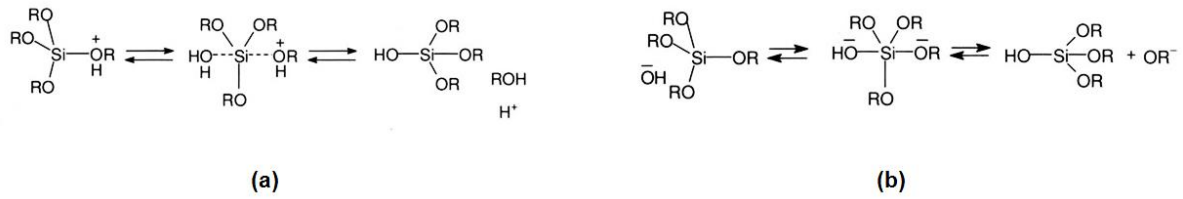

(a) (b)

Figure 2.7: *Reaction schemes for the hydrolysis of alkoxysilanes: (a) Acid catalyzed hydrolysis; (b) Base catalyzed hydrolysis [61].*

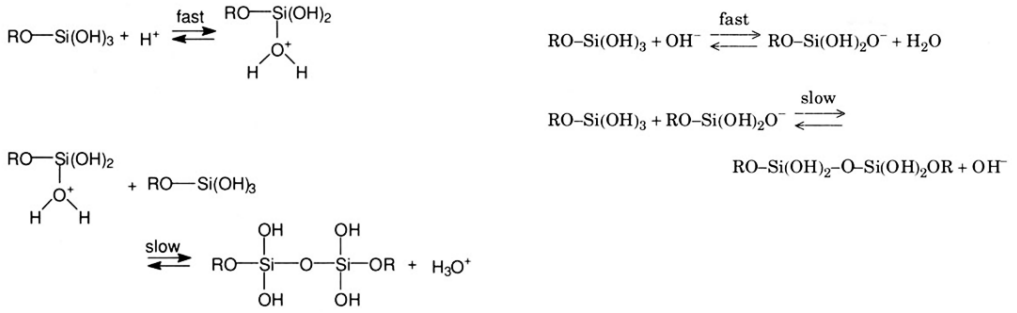

(a) (b)

Figure 2.8: *Reaction schemes for the condensation of silanol groups: (a) Acid catalyzed condensation; (b) Base catalyzed condensation [61].*

$$h_0 = c_1 \left(\eta U_0 / \delta \mathrm{g}\right)^{1/2} \tag{2.2}$$

$$h_0 = 0.94 \, \frac{(\eta U_0)^{2/3}}{\gamma_{\mathrm{LV}}^{1/6} (\delta \mathrm{g})^{1/2}} \tag{2.3}$$

During the sol-gel deposition of films, film-drying (*i.e.* solvent evaporation) overlaps with the polymerization of the material [60,64]. Once deposited on the surface, the sol condenses to a rigid solid skeleton filled with a continuous liquid phase (gelation), which prevents further draining [60]. Gelation is followed by continued solvent evaporation, leaving the skeleton as a porous surface deposit, termed xerogel [60]. Due to the short timespan for evaporation, excessive further polymerization of the wet films is hindered and the final xerogel-film structure depends largely on the degree of precursor polymerization and structure. Hence, the time given for sol-aggregation prior to deposition (aging) plays a vital role for the xerogel structure. Since the aggregation progresses during aging, longer aging times yield more porous xerogels [64]. Higher film densities can be achieved by heating of the films [65–67]. During heating, the xerogel film may densify by contraction due to capillary pressure, progressing condensation or oxidation of organic groups, structural relaxation of the rigid matrix (*i.e.* isotropic

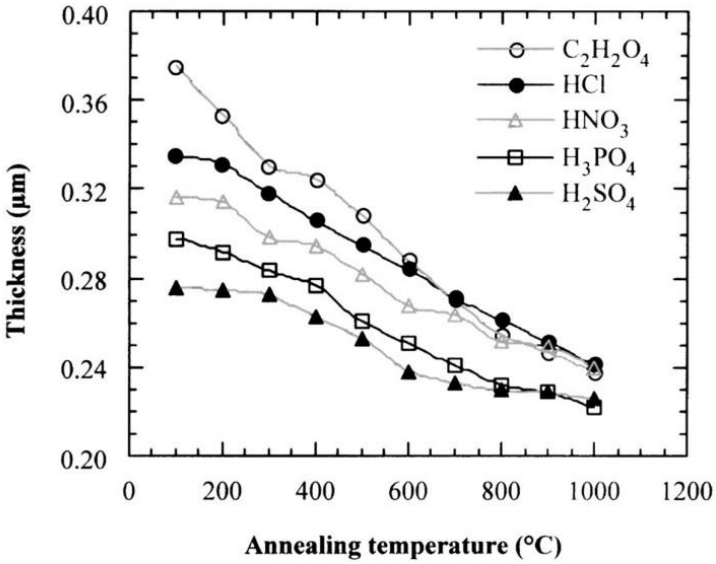

Figure 2.9: *Film thickness vs. annealing temperature (measured in dry N_2 atmosphere). The experiments were conducted on a TEOS-based sol, which was aged for 24 h before deposition and under application of different catalysts (indicated in the figure) [68].*

shrinkage) or viscous sintering [66,67]. Generally, drying and the thermal treatment, as visualized in Figure 2.9, is associated with shrinkage of the sol [68]. Since the shrinkage is geometrically constrained by the substrate, sol-gel films are inherently under tensile stress after drying or densification [65]. Consequently, sol-gel films have a critical thickness, which largely depends on the sol chemistry and processing or curing conditions and often lies in the magnitude of 0.5-1 µm for inorganic films [69].

Chemical vapor deposition (CVD)

Chemical vapor deposition (CVD) is a group of common thin film deposition processes, which are applicable to a multitude of substrates and have a broad range of operation temperatures. The processes rely on the reaction of one or more gaseous species on a solid surface, yielding one or more solid phase reaction products [70]. CVD of silica is a common process for the fabrication of dielectric films in semiconductor devices [71].

Initially, silica films were deposited in an atmospheric pressure (APCVD) reactor by the simultaneous injection of SiH_4 and O_2 onto a heated wafer (typically at 400 ºC) [71]. Due to problems associated with insufficient step coverage, new precursors were introduced for APCVD, yielding improved step coverage at high deposition rates for the deposition from *e.g.* TEOS with O_3 [72]. The deposition speed of APCVD is vastly controlled by the deposition temperature with applicable temperatures between 300-500 ºC for SiH_4/O_2 (100-300 nm/min) and 300-450 ºC for $TEOS/O_3$ (100-200 nm/min) precursor [71]. A decrease in reactor pressure, as in low pressure CVD (LPCVD), limits the transport of reactant to the surface. Under low pressure conditions, the reactant reaches the substrate rather by diffusion than direct flow, leading to increased surface homogeneity and

improved step coverage at the expense of a low deposition speed, limiting the process throughput [73]. Hence, the process is predominantly applicable for the deposition of high quality films with low thickness.

The technology of plasma enhanced CVD (PECVD) relies on the promotion of the chemical reaction on the surface by a radio frequency (RF) -induced plasma operated in vacuum, which may yield improved deposition rates and denser films with respect to APCVD [71]. In analogy to APCVD, early PECVD deposition of silica was based on SiH_4/O_2 precursor and process improvements (film conformity and improved step coverage) were possible by employing TEOS as silicon-bearing precursor in combination with O_2 as reactant. As a further alternative to create SiO_2 films at low processing temperature, without the threat of substrate degradation due to damage from energetic ions, laser induced CVD has been introduced [74,75]. Apart from a low processing temperature, the process offers the option of localized deposition due to precise focusing of the laser. As shown by Rieger *et al.* [75], the process can be run with various precursors, such as SiH_4 or TEOS; however, the resulting films may contain traces of organics when using organosilane precursors.

Physical vapor deposition (PVD)

PVD is a common process for the deposition of thin films, where a source is evaporated and subsequently deposited on a substrate. A variety of PVD processes for the deposition of SiO_2 thin films, such as various evaporation techniques [76–79] or atomic layer deposition [80] have been reported in literature. Due to the immediate importance for this work, the following section focuses on magnetron sputtering. For a detailed review of the other PVD processes, the reader is referred to Møller *et al.* [81].

Generally, it is distinguished between reactive and non-reactive sputter processes. While in non-reactive sputtering, a source material is evaporated and deposited in a controlled atmosphere (*i.e.* vacuum with an inert working gas such as Ar), a reactive process relies on the introduction of a reactive gas to the atmosphere (such as O_2 or N_2). The introduction of a reactive gas allows a gas-phase reaction before deposition, and hence the deposition of *e.g.* ceramic materials from metallic targets [81]. To increase the plasma efficiency, the basic sputtering configuration can be modified by a magnetic field, which increases the pathway of the charged particles. This increases the number of collisions in the plasma, enabling lower working pressures at increased deposition rates [81,82]. In a balanced magnetron, magnets of similar field strength are placed with one magnetic pole in the center of the sputter-target and the other pole arranged in a ring of magnets at the outer edge of the target (Figure 2.10(a)). In this setup, the plasma is confined to the immediate vicinity of the target (~60 mm from the target), leading to either changes in the structure and properties of the growing films when the substrate is placed inside the plasma region [83] or inherently low ion currents when the substrate is placed outside of the region [82]. Increasing the negative bias to the substrate may increase the ion current, but is often detrimental to the film properties [82].

The shortcomings of a balanced magnetron can be overcome by increasing the magnetic strength of the outer magnetic ring, as in the case of a (type-2) unbalanced magnetron (Figure 2.10(b)). In this magnet arrangement, some of the magnetic field lines are directed towards the substrate, allowing the plasma to extend further outward, and thus yielding higher ion currents at the substrate. Introduction of multiple sources into a system, as shown for the closed field configuration in Figure 2.10(c), enables the film deposition with higher uniformity on complex component geometries. Furthermore, the use of different source materials allows for the co-deposition of multi-element materials [82].

Oxides or ceramics can be deposited by reactive magnetron sputtering of a metallic (*i.e.* conductive) target. Alternatively, a radio frequency (RF) excitation instead of a direct current can be applied, which allows for the deposition from non-conductive targets [82]. Magnetron sputtering of highly insulating materials such as oxides or ceramics is prone to "target poisoning", *i.e.* the buildup of insulating material on the target, which breaks down during deposition and causes defects in the growing films due to incorporation of ejected material [82,84]. The issues associated with the deposition of insulating materials can be overcome by pulsed magnetron sputtering. In this process, the magnetron discharge is pulsed, which greatly reduces the charge buildup on the target. Thus the amount of breakdown events is reduced, allowing for the deposition of insulating films at higher rates [82,84]. Generally, it is distinguished between unipolar pulsed magnetron sputtering, where the target voltage is pulsed between the operating voltage and ground and bipolar pulsed sputtering, where the target voltage is pulsed to positive values during operation [82,84].

Different magnetron processes have been reported for the deposition of both stoichiometric and non-stoichiometric SiO_2/SiO_x. Seifarth *et al.* [85] reported the

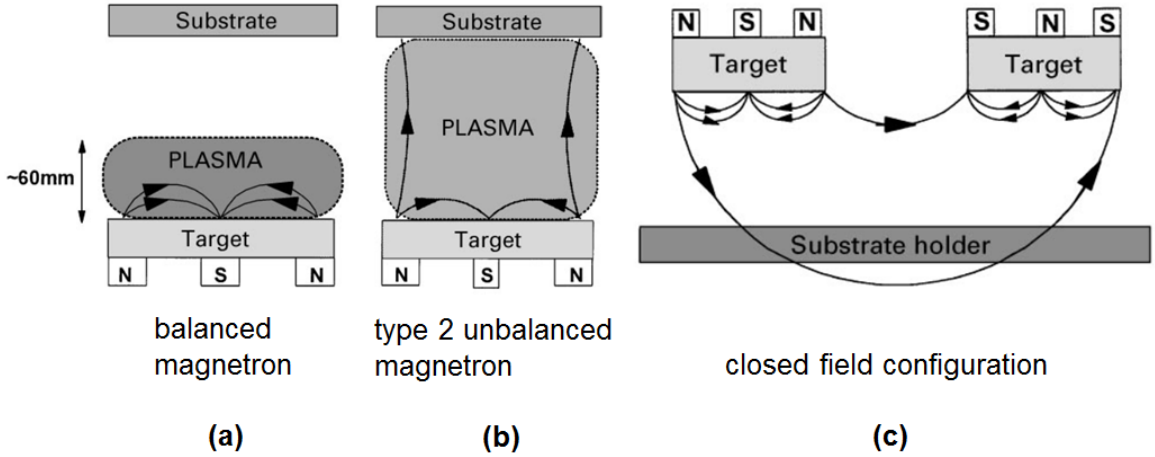

Figure 2.10: *Schematic representation of the plasma confinement observed in magnetrons: (a) balanced magnetron; (b) unbalanced magnetron; (c) closed field configuration of a multiple magnetron system [82].*

deposition of SiO_x via reactive RF magnetron sputtering of Si. Further, He *et al.* [86] demonstrated that the stoichiometry of RF magnetron sputtered SiO_x films can be controlled by the reactive/inert gas ratio. Similarly, Howson *et al.* [87] reported the deposition of high quality SiO_2 films from an unbalanced RF magnetron with Si target and O_2 as reactive gas at a deposition rate of 42 nm/min for stoichiometric films with a refractive index of 1.46. Further, Schreiber *et al.* [88] compared reactive and non-reactive RF magnetron deposition of SiO_2 from SiO_2 targets and reported oxygen vacancies in the films deposited by the non-reactive process, which could be avoided by dosing ~3% O_2 into the inert gas. These results are in agreement with data reported by Jeong *et al.* [89], who found an improvement in both film morphology and resistance to water absorption for films deposited by reactive RF magnetron sputtering on a SiO_2 target with respect to films deposited by a non-reactive process.

The properties of unipolar and bipolar magnetron sputtered SiO_2 films from Si targets with respect to RF magnetron sputtered films from SiO_2 targets has been investigated [90,91]. The groups reported deposition rates of 231 and 156 nm/min for unipolar and bipolar magnetron sputtering in contrast to 15 nm/min for RF sputtering, while the electrical properties of the pulsed magnetron sputtered films were close to the ones obtained by RF sputtering. Zywitzki *et al.* [92] compared SiO_x films deposited by unipolar reactive magnetron sputtering of a Si target in an Ar/O_2 environment to films deposited by plasma activated electron beam evaporation. With ~300 nm/min, the group obtained an inferior deposition rate of the magnetron process with respect to the electron beam evaporation process, which yielded a deposition rate of 36 µm/min. However, the electron beam evaporation process led to significant formation of micro-porosity, while the magnetron process yielded significantly better mechanical integrity of the films.

Liquid phase deposition (LPD)

LPD relies on the immersion of a substrate in a supersaturated aqueous solution of a precursor, which consequently precipitates on the substrate in form of a thin film. The research focus of LPD of silica films has primarily been set to microelectronic applications [93–95]; however, the process has also shown to be applicable for the deposition of coatings on Cu [96] or stainless steel substrates (under cathodic protection of the substrate) [97]. Moreover, the process is particularly interesting for processes which require a low thermal budget, since the deposition is usually carried out at temperatures below approx. 50 °C [93].

Common processing routines rely on the precipitation from a hexafluorsilic acid (H_2SiF_6) which is supersaturated with a precursor such as silicic acid [93–95] or SiO_2 powder [93,98]. A common reaction scheme, as proposed by Nagayama *et al.* [98], is shown in Figure 2.11: SiO_2 is dissolved in H_2SiF_6 aqueous solution and then saturated with SiO_2 (according to reaction (2.4)). Addition of boric acid changes the equilibrium conditions in solution (see reaction (2.5)), leaving the solution in supersaturated condition. The

subsequent immersion of a substrate (in case of Figure 2.11 “Glass”) consequently leads to precipitation of SiO_2 on the substrate.

$$H_2SiF_6 + 2H_2O \rightleftarrows 6HF + SiO_2 \tag{2.4}$$

$$H_3BO_3 + 4HF \rightleftarrows BF_4^- + H_3O^+ + 2H_2O \tag{2.5}$$

With deposition rates of approx. 40 to 120 nm/h [94] the process can be considered as slow compared to the previously discussed processes. In addition, the use of hydrofluoric acid in the process incorporates risk for human health as well as the environment, making the process unattractive for industrial-scale production. Usami *et al.* [99,100] have shown that the environmental issues of traditional LPD processing can be overcome by a novel process, which relies on the hydrolysis/condensation of silicon alkoxides such as TEOS [99] and TMOS [100], however their process was comparably slow to H_2SiF_6-based processes with reported deposition rates below 40 nm/h.

2.2.2 Silica as coating material for steel substrates

SiO_x-based thin films are widely applied as gas barrier coating in packaging applications [101–103], but have also been reported as surface finishes or coatings for iron-based substrates. Due to the broad applicability of the processes, most reported coatings are deposited by the sol-gel method or PECVD, but also coatings from LPCVD [104,105] or laser induced CVD [106] have been reported.

PECVD and sol-gel-based SiO_x coatings have been applied to stainless steel substrates to improve the anti-fouling properties of the substrate in the food processing industry [107,108]. Further, the impact of the substrate surface finish, based no. 2R (bright annealed) and no. 2B finished surfaces, on the coating properties was investigated (the

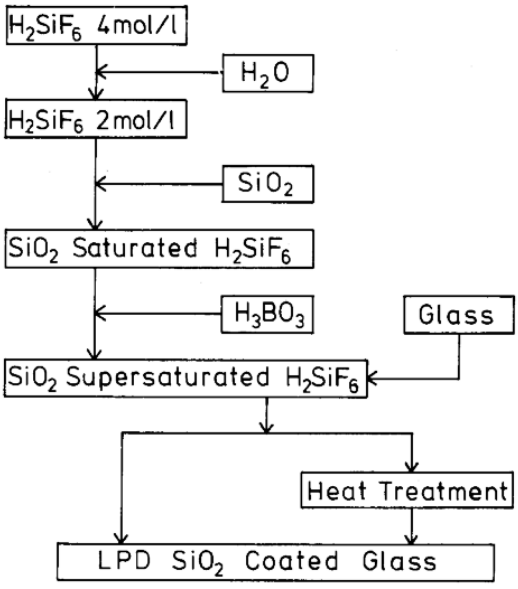

Figure 2.11: *Schematic diagram of LPD SiO_2 coating process [98].*

surface finishes are defined in section 3.1.3). The processes yielded significantly different surface properties, as shown in the atomic force micrographs of a no. 2B finished test coupon in unmodified and coated conditions (Figure 2.12). Further, the group investigated the impact of the substrate finish on the film roughness. While the roughness of the CVD coating was largely dependent on the substrate finish, the sol-gel process leveled substrate roughness and yielded smooth surfaces irrespective of the substrate finish [107]. In this perspective, the group evaluated the surface roughness of the two processes by atomic force microscopy and measured a roughness average R_a of 23 nm vs. 206 nm for the CVD film on the no. 2R vs. the no 2B finished substrate, respectively. Conversely, the R_a roughness determined on the sol-gel film was approx. constant ranging from 35 to 38 nm. Similarly, the two processes yielded varying wettability in water with contact angles between 67 vs. 15 º for the CVD process and 66-61 º for the sol-gel process (coatings on no. 2R vs. 2B substrates, respectively). Both SiO_x treatments were tested for their susceptibility to biofouling (calcium phosphate adhesion) whereby the CVD SiO_x showed an increased susceptibility to calcium phosphate film formation with respect to a no. 2R finished stainless steel surface [108]. Conversely, a decrease in calcium phosphate film formation and adhesion was observed for the sol-gel SiO_x coating.

Pin-on-disc testing of SiO_x films deposited by ion beam assisted deposition on an AISI 329 grade substrate showed that SiO_x films of ~2 µm thickness can improve the wear resistance against a 100Cr6 pin in unlubricated sliding wear [109]. Similarly, Gallardo *et al.* [110] observed an increase in resistance against fretting wear (determined in bi-

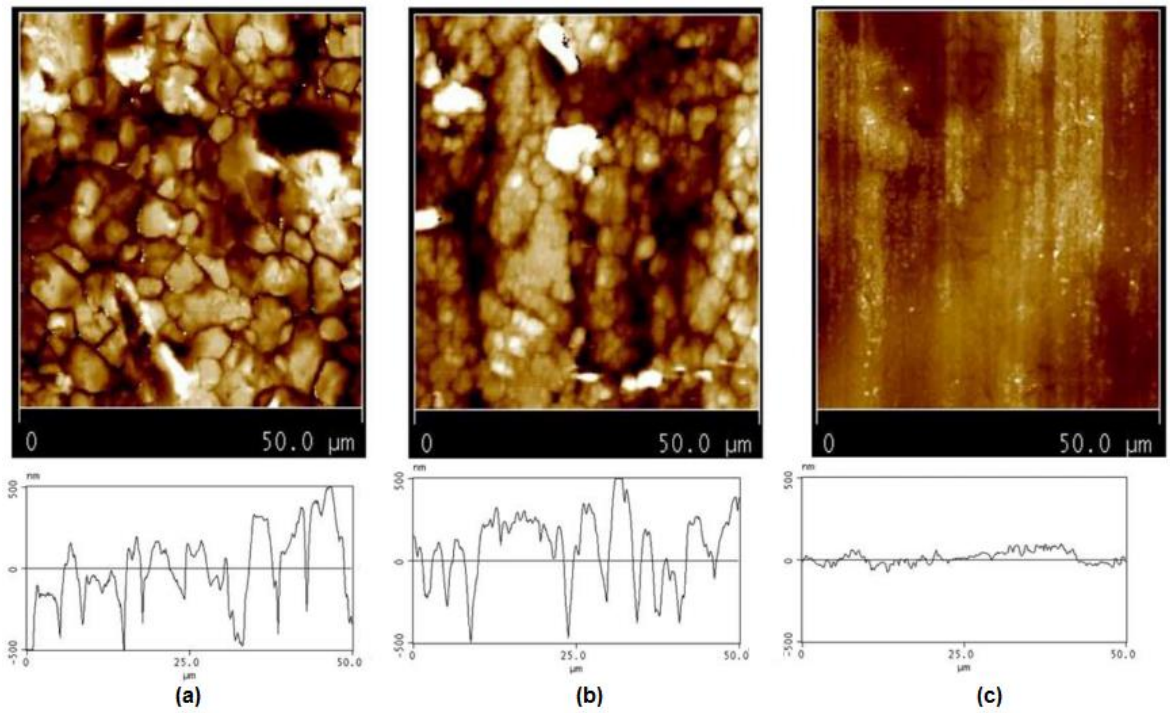

Figure 2.12: *Atomic force microscopy height maps and profiles of the surfaces on an AISI 316 substrate, no. 2B finish. (a) unmodified; (b) PECVD SiO_x; (c) sol-gel SiO_x. [107].*

directional sliding wear against a 10 mm Al_2O_3 ball with 500 µm displacement amplitude) for sol-gel coated AISI 316L substrates. The group investigated the stability of a fully calcined sol-gel coating from silicon alkoxide precursor and determined a stable coefficient of friction (indicating an intact coating) for ~20.000 cycles at 2 N load. Furthermore, the group demonstrated the addition of soda lime glass fillers to the sol and the simultaneous deposition of a suspension of sol and filler. Doping of the coatings with fillers led to an improvement in coating properties: The critical crack-free thickness was increased from ~0.5 µm for un-doped to ~4 µm for coatings doped with 10 % fillers. Hereby the coating thickness was predominantly limited by the increased SiO_2-matrix thickness around the suspended particles, which may reach the critical thickness, as schematically shown in Figure 2.13. In addition to the beneficial effect on critical thickness, the coating lifetime in the wear test was increased to ~80.000 cycles for coatings containing 5 and 10 % fillers. In contrast, Marsal *et al.* [111] investigated the wear performance of ~1 µm thick sol-gel silica coatings on AISI 304 L substrate by pin-on-disc testing against an AISI 316L ball at 2 N normal force. The group could neither observe an initial run-in period, nor a decrease in friction coefficient with respect to an uncoated substrate. After 250 m of unlubricated sliding wear, the coating was worn off and it was concluded that coating with sol-gel silica was an inefficient method to increase the wear properties of the substrate.

Hänni *et al.* [105] demonstrated the deposition of SiO_2 from TEOS precursor by LPCVD. Since the group could not obtain crack-free coatings by dry processing, water vapor or isopropanol (which decomposes with water as a byproduct at the process temperature) was added to the gas phase to yield crack free coatings. The group proposed that the addition of water to the reactive environment leads to an incomplete TEOS decomposition, yielding sub-stoichiometric SiO_2, which subsequently prevents the fracture of the coating.

2.2.3 Adhesion and interface formation between silica and stainless steel

While the adhesion of thick glass films, as in the case of vitreous enameling, is largely dependent on the mechanical interlocking of the coating [112], thin film coatings are often applied on smooth substrates, and thus require chemical adhesion. Findings from

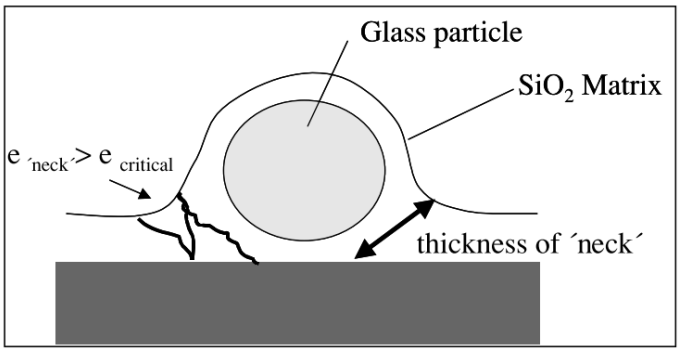

Figure 2.13: *Scheme of coating with particles and neck formation [110].*

Benjamin *et al.* [113] indicated that the adhesion between metal and glass is primarily dependent on the oxygen affinity of the metal and that good adhesion is guaranteed by the formation of an intermediate transition layer of oxide. Consequently, oxygen-affine metals such as Fe and Cr show good adhesion to glass. Similarly, Jiang *et al.* [114] characterized the interfacial interaction between Cr and alkaline earth modified silicate glass by analytical transmission electron microscopy and observed a ~5 nm thick interface zone ("diffusion layer" in Figure 2.14). Since the interface zone contained Cr, Si and O, the group concluded that Cr diffused into the glass and chemically bonded with it. Further, the group hypothesized on the function of the interface zone and pointed out that the thick interface may be responsible for the adhesion between the glass and the metal, however, may also introduce high stress gradients, leading to fracture at low applied stress levels, or even without externally applied stress.

In contrast to the chemical adhesion hypothesis, Lee *et al.* [115] proposed an adhesion mechanism between RF-sputtered SiO_2 films and stainless steel substrates based on mechanical interlocking in microscopical substrate defects. The group investigated the adhesion of SiO_2 deposits by constant load scratch testing and found an increase in critical load, *i.e.* an increase in adhesion, for ion etched surfaces with respect to mechanically polished surfaces. Further, the group identified an increase in thickness of the film/substrate interaction zone and consequently concluded that the etching-induced increase in substrate defects (*e.g.* vacancies and micro-cavities) had led to increasing mechanical interlocking between the film and substrate, and thus increased adhesion.

Benayoun *et al.* [116] demonstrated the applicability of increasing load scratch testing to determine the adhesion of 0.66 µm thick PECVD SiO_2 films on AISI 316L substrates. The group quantified the adhesion between the films and substrates which had been plasma cleaned before deposition and substrates which had only been cleaned in organic solvent and sonication. Their results stressed the importance of the surface pretreatment on the adhesion of the films, showing that sequential hydrogen and oxygen plasma cleaning enhanced the adhesion up to 25 %.

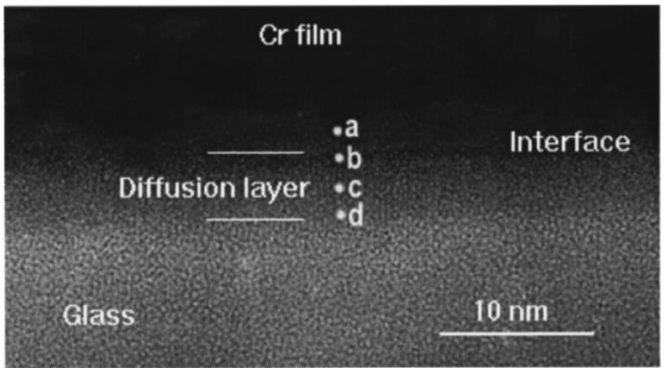

Figure 2.14: *Transmission Electron Microscopy bright field image showing a Cr film deposited on alkaline earth boroaluminosilicate glass 2 weeks after deposition. A blurred diffusion layer is indicated [114].*

Several groups have speculated about the interaction at the coating/substrate interface and its effect on the coating performance. Pech *et al.* [117] emphasized that a potential interaction of the coating with the native passivation may impact its efficiency to maintain substrate passivity at microscopic coating defects. Similarly, Vasconcelos *et al.* [118] determined a smooth transition between a sol-gel silica and a stainless steel substrate by Rutherford backscattering spectrometry (Figure 2.15), which was interpreted as intermediate layer between the coating and the substrate. The group further hypothesized that the intermediate layer positively influenced the corrosion behavior.

Stoch *et al.* [119] studied the formation of an interfacial zone between sol-gel silica and a stainless steel substrate after a thermal treatment at 700 ºC by X-ray photoelectron spectroscopy. The group reported elemental segregation of Fe and Mn at the interface and hypothesized that the silica layer accelerated the outwards transport of the elements, resulting in the formation of an intermediate layer of amorphous silicates. Further, Takemori [120,121] discussed the interaction between sol-gel silica films and AISI 304 substrates. The films were deposited by a non-aqueous sol-gel process [122], which involved several heat treatment stages at temperatures up to 190 ºC, followed by a final heat treatment at 500 ºC for 2 h in air. Generally, the coatings showed a high density with respect to aqueous sol-gel silica and an inconsistent thickness between 350 and 1000 nm; however, the coatings showed failure in form of crack formation, exfoliation and spallation due to, presumably, buildup of thermal stresses during cooling [120]. In addition to different modes of cracking, the formation of a several tens of nanometer-thick multilayer-interface between the silica-film and the substrate was observed (Figure 2.16). The interface chemistry was analyzed by EDS and an outer, iron-rich region (B, C in Figure 2.16) was found on top of a Cr-rich inner layer (C, D in Figure 2.16). Coating delamination, caused by lateral propagation of cracks underneath the coating, was found to propagate between the coating and the outer interface film, as visualized in Figure 2.17.

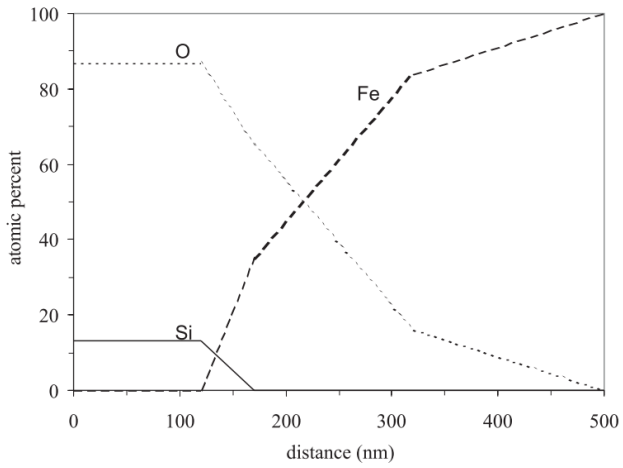

Figure 2.15: *Rutherford backscatter spectrometry depth profile for sol-gel silica coated AISI 304 heated at 600 ºC [118].*

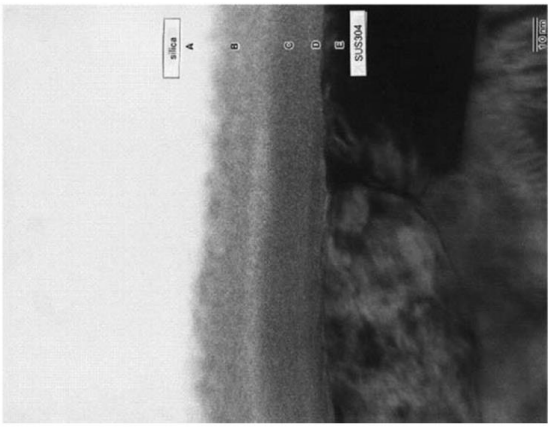

Figure 2.16: *Cross-sectional TEM image of silica coating on AISI (SUS) 304 [120].*

Figure 2.17: *Cross-sectional TEM image of silica coating on AISI 304, showing the lateral propagation of a crack along the outer interface layer [120].*

2.2.4 Corrosion protection of steels via SiO_x barrier coatings

The application of HSQ-based thin films as corrosion barrier coating is not reported in the literature, whereas thin film deposition by traditional methods such as the sol-gel method and CVD has been investigated. Thin film SiO_x coatings have shown positive results as stand-alone coating systems [117,118,123,124] or as adhesion layers for further coating systems such as thick organic coatings [125,126]. Furthermore, SiO_x-based coatings have found interest as surface treatment to increase the lifetime or biocompatibility of stainless steel-based implants [127–129].

Sol-Gel silica coatings have been tested in media such as salt water [118,124,128,130], acid [118,131] and artificial body fluids [127]. Vasconcelos *et al.* [118] investigated the corrosion properties of sol-gel silica coatings from TEOS calcinated at temperatures up to 600 ºC on stainless steel substrates. Sol gel coatings cured at up to 200 ºC significantly increased the corrosion potential in 1 N H_2SO_4 and coatings cured at 80 ºC were reported to increase both the pitting and corrosion potential in 3.5 wt.% NaCl solution (Figure 2.18). The results were in agreement with other studies, which found an improvement in the acid-corrosion [131,132] and chloride-induced corrosion [130] resistance of stainless steels when coated with sol-gel silica. Moreover, Hwang *et al.* [124] demonstrated the deposition of sol-gel silica coatings as efficient ionic barrier coatings on AISI 304 substrates and showed that thin silica coatings are capable of impeding chloride transport to the substrate as well as decrease the corrosion current by approx. one order of magnitude. Gallardo *et al.* [110] investigated the coating barrier properties of sol-gel SiO_2 from silicon alkoxide precursors cured at different temperatures (*i.e.* retaining different degrees of organic character). Coatings cured at 400 ºC retained a considerable amount of organic groups, and hence showed high coating flexibility and hydrophobicity, yielding efficient barrier coatings in 3.5 wt.% NaCl aqueous solution. Coatings cured at 550 ºC, on the contrary, were fully inorganic, showing less flexibility and a higher defect density,

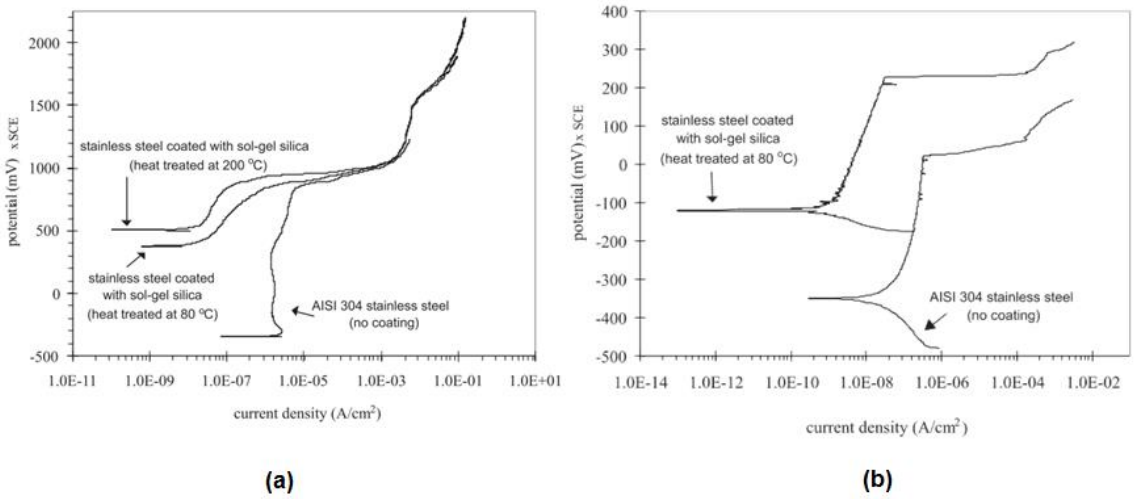

***Figure 2.18**: (a) Polarization curves in 1 N H_2SO_4 solution for stainless steel with and without sol-gel silica coating. (b) Polarization curves in 3.5 NaCl for stainless steel with and without sol-gel silica coating [118].*

and consequently smaller barrier efficiency; however, all coatings irrespective of the curing temperature were found to improve the corrosion properties in an anodic CP experiment. Moreover, Ono *et al.* [133] deposited silica films (200 nm) from TEOS precursor on AISI 304 substrates by the sol-gel method and investigated the corrosion performance by a 17 h long immersion test in 6 % $FeCl_3$ aqueous solution at 50 ºC. The group determined a clear reduction in weight loss with respect to an uncoated reference and concluded that the corrosion resistance of the system was remarkably improved by the process. Similarly, 100 nm thick silica coatings were deposited on AISI 304 substrate and evaluated by the $FeCl_3$ immersion test [134]. Curing of the coatings at temperatures between 350 and 500 ºC led to a significant decrease in corrosion rate.

In contradiction with the previously described results, de Damborenea *et al.* [135] did not observe an improvement in corrosion resistance of stainless steels in both 2 M NaCl and 2 M HCl aqueous solution. For their experiments, the group pre-oxidized test coupons of AISI 304 and coated them with sol-gel silica from TEOS pre-cursor with a curing cycle at 500 ºC. Samples tested in 2 M NaCl showed a significant decrease in OCP while no alteration in corrosion potential was observed in 2 M HCl. The group concluded that coating defects such as cracks or pores allow electrolyte penetration and allow for the initiation of localized corrosion, which subsequently advances under the coating.

Pech *et al.* [117,123] described the effect of 600 nm thick PACVD silica films, which had been deposited from TEOS precursor at a temperature of 100 ºC, on the corrosion protection of both mirror-polished M2 tool steel and AISI 304 austenitic steel. The groups showed that the passive current density was strongly decreased for coated samples (Figure 2.19(a)), which was correlated with the small electrode area that was exposed through pores and defects in the coating. The pitting potential fluctuated between the typical value of uncoated AISI 304 and the dielectric breakdown potential of the surface

film, which indicated unpredictable local differences in coating quality, but an improvement in corrosion resistance for virtually defect free coatings. In addition, since the pitting potential never shifted to more cathodic values, it was shown that the coating did not deteriorate the passive character of the substrate. Impedance measurements, as shown in Figure 2.19(b) indicated purely capacitive behavior of the surface, *i.e.* the coated sample acted as a blocking electrode which could be modeled with an -R-C- equivalent circuit.

Similarly, PECVD SiO_x coatings have been investigated by Delimi *et al.* [136] as corrosion barrier coatings for carbon steels. The group deposited films from SiH_4 and N_2O precursor at 300 ºC with up to 200 nm thickness and investigated the films by quasi-steady state linear polarization measurements and impedance spectroscopy. The results showed a decrease in corrosion current density of up to 96 % for 200 nm thick coatings, which was interpreted as a considerable decrease in actively corroding area. In contrast to the films reported by Pech *et al.* [117], the group found two distinct capacitive features in electrochemical impedance spectroscopy, which indicates that the coating allowed ionic transport to the substrate and acted as an imperfect barrier coating. In agreement, two capacitive features were observed during EIS measurements of CVD-silica coated low carbon steel by Pech *et al.* [123] and the data were fitted with the electrical equivalent circuit illustrated in Figure 2.20(a). As pointed out by the authors, the value of the coating resistance R_{coat} is extremely high with respect to the other resistive circuit elements, and thus the element can be neglected. EIS data acquisition and subsequent analysis by electrical equivalent circuit fitting allows for a precise determination of both the resistive and capacitive elements of the circuit. Due to the non-destructive nature of the technique, it allows for continuous monitoring of corrosion processes and coating degradation. Consequently, the effect of immersion in 3 % NaCl aqueous solution on the evolution of the equivalent circuit elements shown in Figure 2.20(a) was monitored for 100 h immersion time. As visualized in Figure 2.20(b), the charge transfer resistance decreased over time, while the double layer capacitance increased, indicating an increasingly

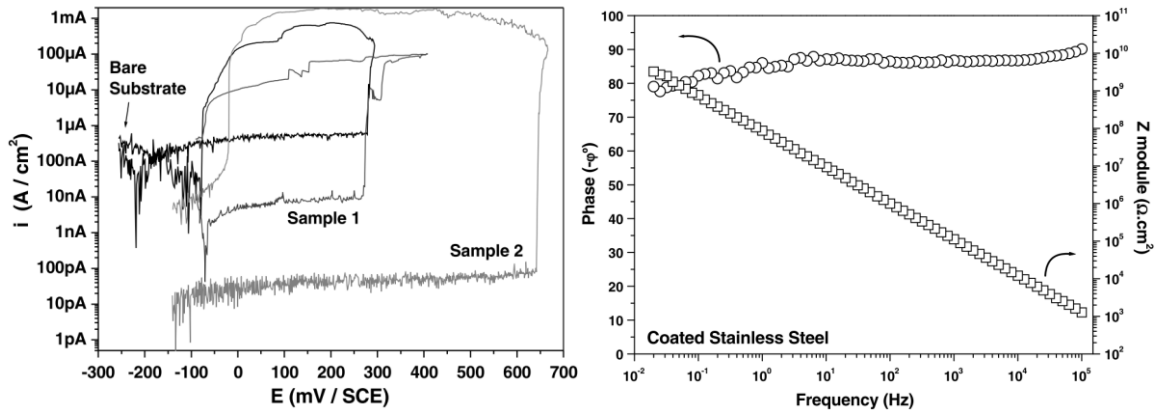

Figure 2.19: *Electrochemical studies of PACVD silica on AISI 304 substrate: (left) Cyclic potentiodynamic polarization curves of bare sample and coated samples (Samples 1 and 2); (right) Bode plot of coated sample [117].*

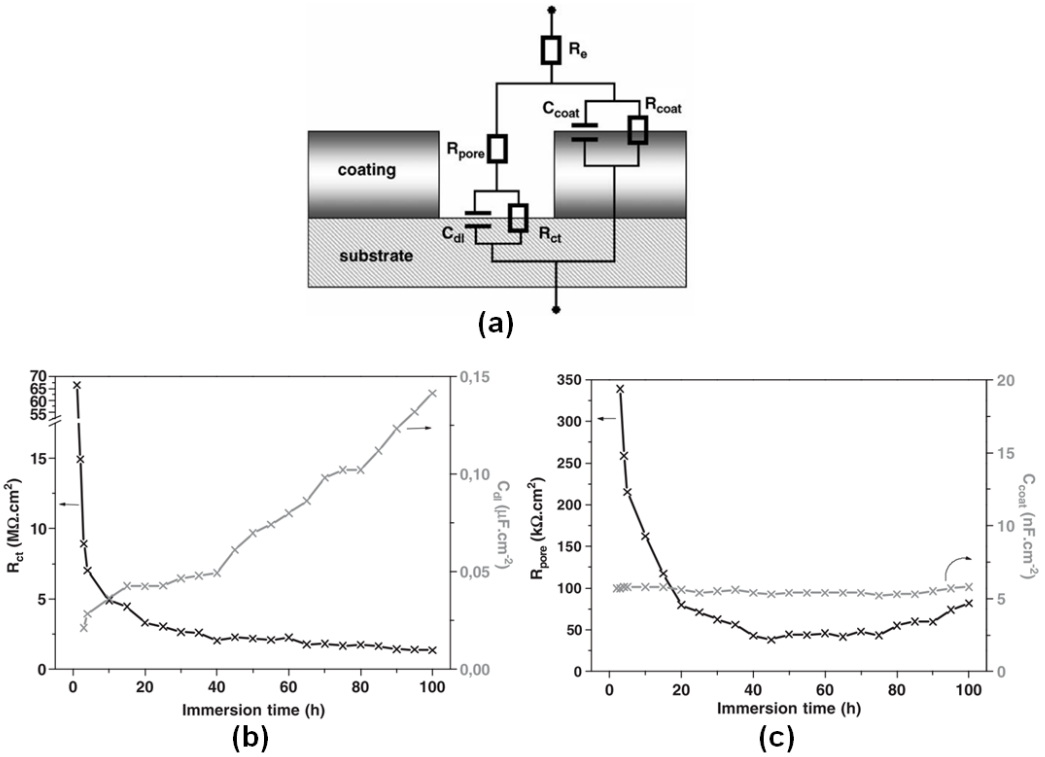

***Figure 2.20**: EIS analysis of CVD SiO_x film on mirror-polished tool steel. (a) Schematic cross-section of a coated conductive substrate showing a pore and corresponding electrical equivalent circuit used to model the system; (b) Time dependence of charge transfer resistance (R_{ct}) and double layer capacitance (C_{dl}) during immersion in 3% NaCl solution; (c) Time dependence of pore resistance (R_p) and coating capacitance (C_{coat}) during immersion in 3% NaCl solution [123].*

exposed substrate surface. Similarly, prolonged immersion led to a decrease in pore resistance at constant coating capacitance (Figure 2.20(c)), indicating gradually increasing ionic transport over the coating at excellent inertness of the coating material.

Hausbrand *et al.* [126] investigated the corrosion mechanism of flame assisted CVD thin film silica coatings on carbon steel and concluded on the corrosion mechanism. The group found that corrosion initiates at coating defects such as pinholes and is kinetically controlled by the rate of oxygen reduction. Moreover, the group showed that CVD silica coated surfaces strongly inhibit oxygen reduction as cathode reaction at defect-free sites, however, do not impede hydrogen reduction as strongly. Further, the effect of ion beam assisted plasma CVD silica on the acid corrosion of stainless steel has been studied by Baba *et al.* [137], who found that the thin coatings successfully impeded anodic dissolution in H_2SO_4.

Apart from the corrosion resistance in aqueous media, SiO_2 coated stainless steels have been investigated for their high temperature corrosion resistance. Both, coating of stainless steel substrates with sol-gel-based [130,131] and ion beam assisted plasma CVD

[137,138] coatings showed significant improvements in the oxidation resistance of the substrate. In addition to oxidation resistance, sol-gel SiO_2 coatings have shown to form efficient barrier coatings to improve the resistance against nitration in dry ammonia at elevated temperatures [139].

2.2.5 Chemical stability of SiO_2 thin films

As stated by Deltomee *et al.* [140], Si is a powerful reducing agent and decomposes water under evolution of silane and hydrogen gas to form silica or silicates. This reaction is often not apparent, since Si tends to passivate irreversibly by a SiO_2 film, which is virtually inert in most aqueous environments up to a *p*H of ~11 (Figure 2.21). However, as indicated in Figure 2.21, the dissolution of SiO_2 to various forms of silicic acid (only monosilic acid was considered) has a negative free energy and SiO_2 dissolution may occur even at neutral *p*H [140]. Further, as shown in Figure 2.22, the solubility of SiO_2 in water is strongly dependent on the polymorph as well as the solution *p*H. All polymorphs show a constant solubility between *p*H 0 and ~*p*H 9 and a progressively increasing solubility for higher alkalinity. Moreover, the dependence on the polymorph yields lower dissolution rates for the considered crystalline polymorphs and significantly higher rates for the amorphous polymorphs. This relation was empirically studied by Icenhower *et al.* [141], who investigated the dissolution kinetics of quartz and amorphous SiO_2 in the temperature interval from 40-250 ºC in near neutral environment. Generally, the group found a strong correlation between the polymorph and the dissolution rate, whereby amorphous silica showed increased dissolution rates with respect to quartz. Furthermore, the group showed that addition of low concentrations ($\leq$ 0.05 molal) of NaCl leads to a significant increase in dissolution rate.

Delimi *et al.* [136] investigated the stability of PACVD SiO_x films by immersion testing for 2 days in aqueous solution at a *p*H between 1 and 13 and found the homogeneous dissolution of the oxide in the alkaline solution and film stability in the neutral and acidic solutions. Further, Klause *et al.* [142] investigated the dissolution kinetics of thin silica films on polymer substrate in near neutral solution (phosphate buffer at *p*H 5.5 and *p*H 7.0) at temperatures of 60 and 90 ºC. The group found a significant decrease in layer thickness over immersion time and concluded that SiO_2 coatings dissolve in near neutral solutions via the surface controlled reaction proposed by Knauss *et al.* [143] (reaction (2.5)-(2.6); * denotes an activated complex in the reaction schemes). In their experiment, the dissolution rate was controlled by the solution acidity and temperature, as well as the coating quality. Higher solution temperatures and less perfect coatings led to higher dissolution rates (Figure 2.23) and higher solution alkalinity led to an accelerated coating dissolution yielding dissolution rates between 0.1 nm/h up to >50 nm/h within the range of experimental conditions.

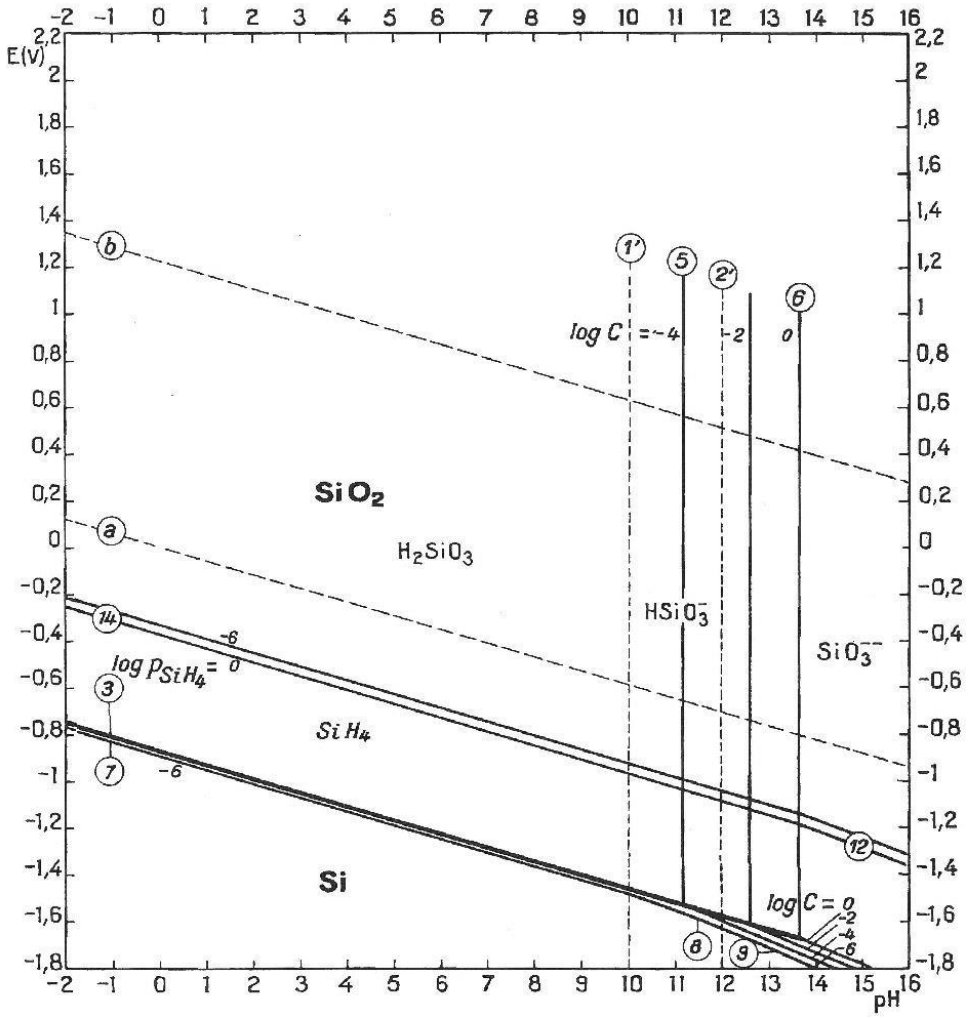

Figure 2.21: *Potential-pH equilibrium diagram for the system silicon-water, at 25 ºC. (Considering SiO_2 in the form of quartz. Approximate diagram) [140].*

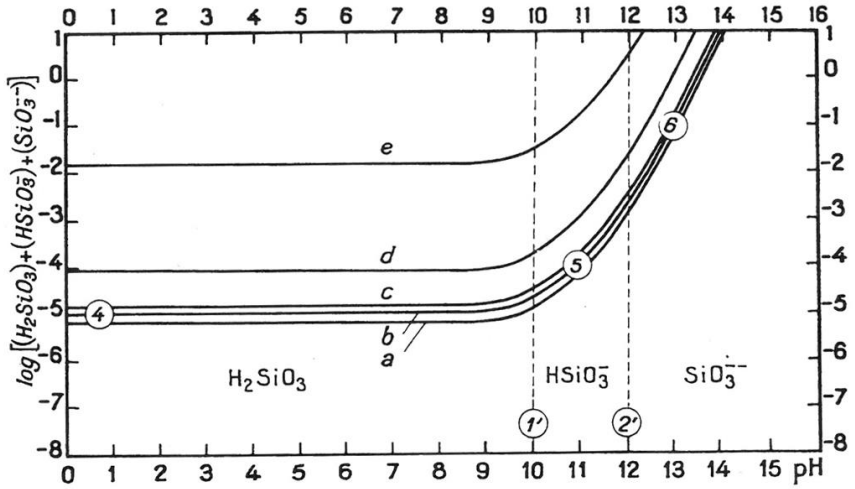

Figure 2.22: *Influence of pH on the solubility of silica SiO_2, at 25 ºC. a, quartz; b, cristobalite; c. tridymite; d. vitreous silica; e, amorphous silica [140].*

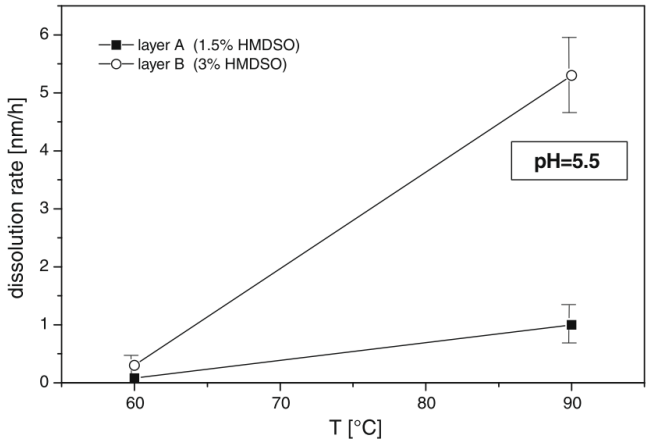

Figure 2.23: *Dissolution rate of thin film silica coating on polymer substrate in phosphate buffer at pH 5.5. Layer A denotes a dense structure, whereas layer B denotes a less polymerized film with defects [142].*

$$SiO_2 + H_2O \rightarrow (SiO_2 * 2H_2O)^* \tag{2.6}$$

$$(SiO_2 * 2H_2O)^* \rightarrow H_4SiO_4 \tag{2.7}$$

Similar observations have been made by Kang *et al.* [144], who investigated the dissolution kinetics of various types of thin film Si-oxides, such as thermal, PECVD and electron beam evaporated oxides, in near-neutral and alkaline environments. The group found that the dissolution kinetics are mainly determined by the oxide density (active surface area due to microscopic porosities), solution temperature and alkalinity where an increased solution temperature and alkalinity led to an increased dissolution rate. Moreover, the group found that the investigated oxide films dissolved in a uniform and gradual fashion and without accelerated dissolution due to fragmentation or release of fragmented pieces.

2.3 Hydrogen Silsesquioxane technology

It was shown in the previous section that coating with silica films can be a viable concept to enhance the corrosion resistance of stainless steels in harsh environments. In the current section, the deposition from Hydrogen Silsesquioxane (HSQ) precursor is demonstrated as an alternative to the previously introduced traditional processes. HSQ, as a member of the class of silsesquioxane oligomers [145], can be used as a molecular precursor for spin-on-glass (SOG), which traditionally finds application in microelectronics production as interlayer dielectric [146–148] or as negative electron beam resist [149,150]. The molecule is used due to its capability to cross-link, thereby forming an inorganic polymer with siloxane backbone and potentially SiO_2-like character [146,151]. In the following, the existing literature on HSQ-technology is reviewed in detail. At first, the HSQ oligomer and the commercially available solvents are described. Hereafter, the different curing mechanisms are reviewed and conclusions about the respective film properties are drawn. The section is concluded with a summary of the

existing applications with focus on novel processes, which utilize HSQ as precursor for surface coatings on metallic substrates.

2.3.1 Commercial HSQ solutions

The HSQ oligomer

The simplest member of the class of silsesquioxanes ($(RSiO_{3/2})_n$) is HSQ with the stoichiometric formula $(HSiO_{3/2})_n$ [145]. Silsesquioxanes are oligomeric units of the monomer $RSiO_{3/2}$ with the degree of polymerization *n*. The molecule is often depicted as the cage-like T_8 oligomer with $n = 8$ (Figure 2.24); however, the precise molecular weight distribution of commercial HSQ solutions may differ and solutions may contain various oligomeric compounds.

Solvents for HSQ

Even though HSQ, as a non-polar molecule, is insoluble in water, it is susceptible to hydrolysis in water containing environment, owing to its reactive Si-H corner moieties [59]. Hence, the mono/oligomer is usually solvated in a non-polar organic solvent at low temperature. The molecule is commercially available from Dow Corning in two different solvents (due to different legislation in different countries), namely in Methyl Isobutyl Ketone, $C_6H_{12}O$, or a blend of Hexamethyldisiloxane, $C_6H_{18}OSi_2$, and Octamethyltrisiloxane, $C_8H_{24}O_2Si_3$, in a ratio of 3:1. The commercially available solvents have boiling points between 99 °C (Hexamethyldisiloxane) [152] and 152 °C (Octamethyltrisiloxane) [153], which guarantees complete evaporation of the solvent before the onset of precursor polymerization at ~190 °C - 250 °C [154–156].

Polymerization below the boiling point of the solvent on the contrary has been investigated as a measure to introduce porosity into HSQ-based thin films to decrease the film density and dielectric constant [157–160]. For this a high boiling point solvent such as tetradecane [157,158], $C_{14}H_{30}$, is introduced into the solution as porogen (in this case Methyl Propyl Ketone is used as the primary low boiling point solvent). Tetradecane, with a comparably high molecular weight, has a boiling point of 254 °C [152] and will therefore not evaporate during drying of the film. The solid parts of the film are cross-linked via ammonia catalyzed hydrolysis and condensation, transforming the film into a

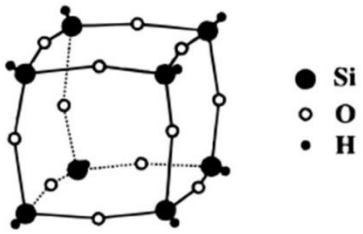

Figure 2.24: *Schematic representation of the molecular structure of HSQ as eight-corner oligomer (T_8) [148].*

porous, semi-networked structure. Finally, further pyrolysis of the film at temperatures well above the boiling point of tetradecane transforms the film into a cross-linked, porous structure with a low dielectric constant.

2.3.2 Infrared spectroscopy of HSQ-based resin

In technological applications, Fourier transform infrared spectroscopy (FT-IR) is commonly used to analyze the structure of HSQ-based spin-on-glass. Figure 2.25 shows a typical FT-IR absorption spectrum of a film deposited from a commercial HSQ solution before and after curing. The positions of the most commonly reported and discussed FT-IR bands are annotated in the figure and summarized in Table 2.1. Generally, polymerization of HSQ resin leads to an increase of the Si-O asymmetric stretching mode at 1070 cm^{-1} at the expense of the Si-O asymmetric stretching mode at 1130 cm^{-1}. This shift in peak position is well described in literature [145] and indicates a distinct change in Si-O absorption of from the cage-like, oligomeric precursor to a polymeric resinous material. In addition to bands from Si-O asymmetric stretching, an absorption feature at 830 cm^{-1}, indicating Si-O bending vibrations, is apparent from the spectrum [155]. The shift in Si-O stretching absorption is accompanied by a decrease in Si-H stretching absorption (2256 cm^{-1}) and Si-H bending absorption (890 cm^{-1}) due to loss of Si-H moieties during curing. In technical applications, the quality or degree of polymerization of HSQ-based films is frequently assessed based on the loss in integrated Si-H stretching absorption intensity [148,155,161], which gives an accurate indication of the remaining Si-H bond density [148] or the ratio between the integrated Si-H stretching and Si-O asymmetric stretching intensities [146,151].

In addition to the clearly visible IR-features denoted in Table 2.1, the FT-IR spectrum of HSQ reveals further bands, which will be discussed in the following. Polymerization of the films may yield the formation of SiH_2 linkages [155], leading to a shift in vibrational bond frequency and the appearance of a second, low-frequency Si-H stretching band at 2200 cm^{-1}. The formation of the SiH_2 stretching band at 2200 cm^{-1} is visualized in Figure 2.26. Further, depending on curing conditions, curing temperature or residual Si-H content, HSQ-based films may be susceptible to moisture absorption, leading to the formation of a broad IR-feature above ~3000 cm^{-1} wavenumber [161–163]. Similar broad IR features have been observed for sol-gel silica films [164,165] and identified as complex superposition of OH-stretching absorptions of both silanol and water. As discussed by Pliskin [166], the integrated intensity of the –OH feature is proportional to the quantity of the –OH present and may be utilized for the quantification of the –OH content. In addition to Si-O asymmetric stretching at 1075 and 1140 cm^{-1}, a high frequency shoulder around 1250 cm^{-1} is frequently reported in literature [150,155,167]. The shoulder has been interpreted as the transverse optical (TO) splitting component of the asymmetric stretching vibration, arising from the oscillation perpendicular to the direction of wave propagation [168].

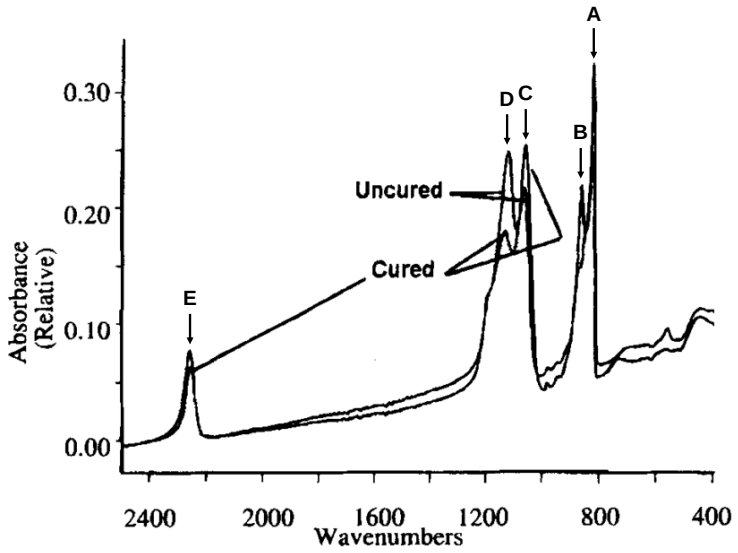

Figure 2.25: *The (FT-IR) absorbance of cage HSQ, post bake and post cure [155]. (with annotations)*

Table 2.1: *Interpretation of FT-IR spectra shown in Figure 2.25.*

Designation in Figure 2.25	Position/Wavenumber [cm^{-1}]	Description	Reference
A	830	Si-O bending	[145]
B	870	Si-H bending	[145]
C	1075	Si-O asymmetric stretching of incompletely closed cage moieties	[145]
D	1140	Si-O asymmetric stretching of closed HSQ cages	[145]
E	2260-2285	Si-H stretching in $HSiO_{3/2}$	[145]

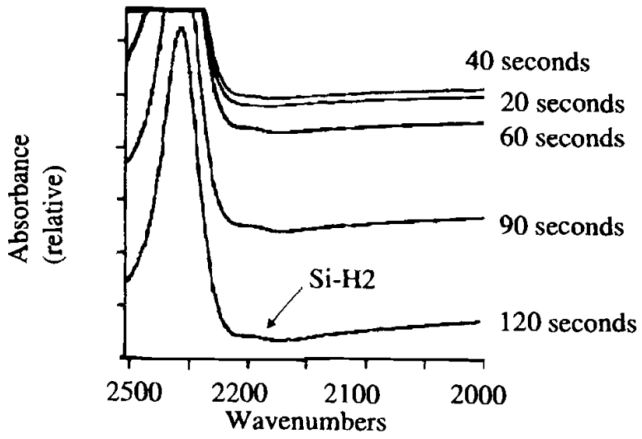

Figure 2.26: *The development of the SiH_2 stretch band at 2200 cm^{-1} on baking at 350 ºC for 20-120 s in N_2 atmosphere [155].*

2.3.3 Cross-linking of HSQ thin films

Thermal curing in non-oxidizing atmosphere

Thermally induced polymerization (often referred to as "cage to network transformation") of HSQ in fully inert curing atmosphere is generally described as redistribution reaction between neighboring HSQ cage molecules. Belot *et al.* [169] characterized redistribution reactions (also "exchange" or "disproportonation" reactions) of polysiloxanes as equilibrium reactions in which two substituents on two central moieties are exchanged. The redistribution reaction of hydrogenated polysiloxanes, as found in the corner moieties of HSQ oligomers, is schematically illustrated in Figure 2.27. The group found redistribution reactions of hydrogenated polysiloxane resins to occur at considerably lower temperatures (approximately 300 °C) compared to other organofunctional polysiloxanes, *i.e.* methylated polysiloxanes).

Siew *et al.* [148] proposed a 3 stage model (neglecting solvent loss at low temperatures), based on the observable film weight loss during a dynamic temperature sweep, for the curing reactions of HSQ thin films in the temperature regime below 500 °C under the absence of oxygen. Annealing in the low temperature region between 250 and 350 °C predominantly leads to a cage to network redistribution [148,170] between neighboring oligomers, according to reaction (2.8), which is graphically displayed for complete HSQ cage molecules in Figure 2.28. In addition to the pure bond redistribution, the commencement of silane (SiH_4) and hydrogen (H_2) gas desorption can be observed [147,170,171]. Hereby silane evolution can be explained by the continuation of the redistribution reaction according to the reaction scheme shown by reactions (2.8)-(2.10) [156]. Further research on the effect of low temperature annealing (240-340 °C) of HSQ films has been carried out by Yang *et al.* [170]. Apart from an increase in film thickness during annealing, the group observed a decrease in refractive index over the entire temperature range from ~1.4 for the uncured precursor to ~1.369 for the film cured at 340 ºC (Figure 2.29). The change in film properties during the low-temperature transformation was explained by the buildup of free volume due to the lower packing density of the HSQ-network structure with respect to the cage structure, together with the formation of porosities due to the outgassing of reaction by-products or solvent.

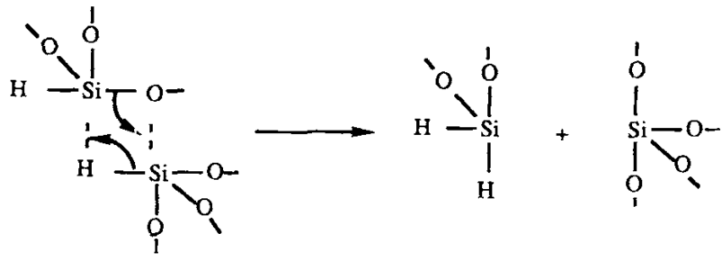

Figure 2.27: *Schematic representations of Si-H / Si-O bonds exchange [169].*

$$2HSiO_{3/2} \rightarrow SiO_{4/2} + H_2SiO_{2/2} \quad (2.8)$$

$$H_2SiO_{2/2} + HSiO_{3/2} \rightarrow SiO_{4/2} + H_3SiO_{1/2} \quad (2.9)$$

$$H_3SiO_{1/2} + HSiO_{3/2} \rightarrow SiO_{4/2} + SiH_4 \quad (2.10)$$

For temperatures between 350 °C and 435 °C a medium temperature regime is observable [148], which is, in addition to the redistribution reaction in the low temperature regime, characterized by a higher Si-H dissociation rate and a high weight loss. The high Si-H dissociation was explained by an increased silane and hydrogen gas desorption [147,156] according to the continued redistribution reaction described previously and the formation of hydrogen gas according to reaction (2.11) [148]. For annealing temperatures above 435 °C a film contraction, accompanied with a strong degree of weight loss can be observed [148]. Above these temperatures, the porous film structure (which has built up at lower temperatures) collapses [148,170], resulting in denser films with higher refractive indices and dielectric constants.

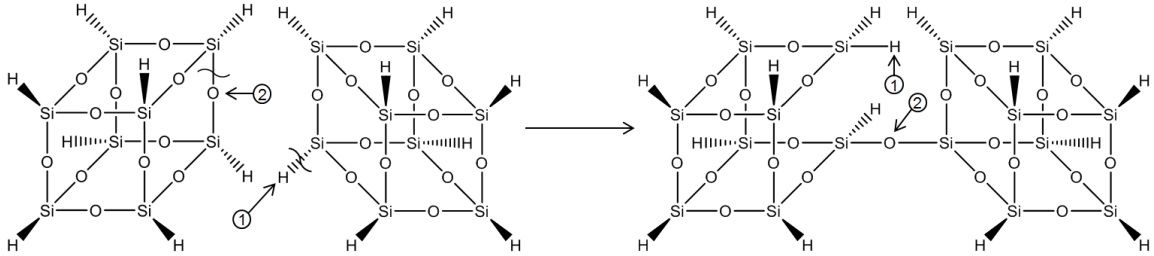

Figure 2.28: *Cage to network redistribution of HSQ (based on the redistribution reaction by Siew et al. [148]).*

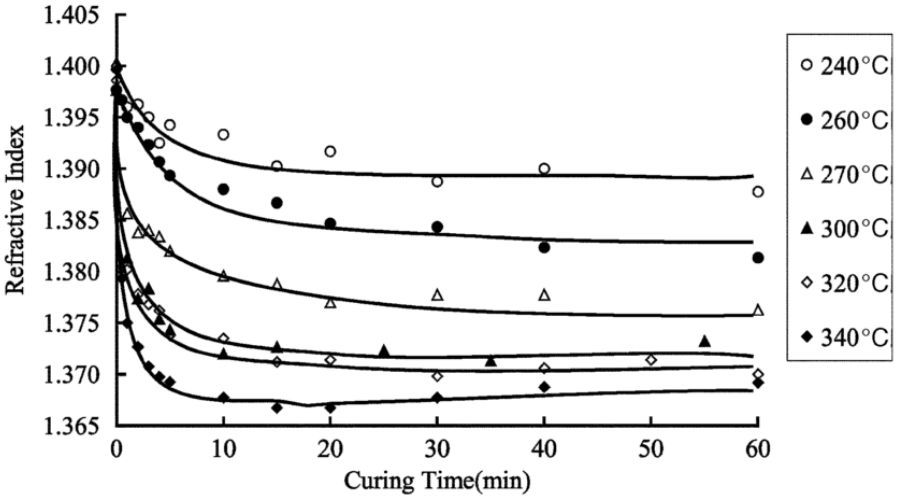

Figure 2.29: *Variation of the refractive index of the HSQ films with different curing temperatures and curing times [170].*

$$2H_2SiO_{2/2} \rightarrow 2H_2 + Si_2O_{2/2} \quad (2.11)$$

A further increase in curing temperature leads to advances in film shrinkage [146] (Figure 2.30(a)). This shrinkage is accompanied by a further decrease in Si-H content and the relative amount of Si-H decreases to 0 for annealing temperatures of > 600 °C [151] (Figure 2.30(b)). Moreover, a loss in hydrophobicity and consequently adsorption of water was detected in films annealed at 600 ºC, which resulted in an increased refractive index and dielectric constant compared to silica from chemical vapor deposition (CVD) [151]. It was concluded that Si-H depleted films are more hydrophilic than Si-H containing films, leading to water adsorption on the surface. This conclusion is in agreement with observations by other groups [161,172], who found HSQ films with low Si-H content to be susceptible to moisture adsorption. A further increase in temperature, as for annealing at temperatures of 850 °C (in O_2 ambient), was shown to transform HSQ films to water-free oxides with properties similar to CVD oxides. Apart from the pure densification of the films, an increase in mechanical integrity with increasing curing temperature can be observed: Both the hardness and modulus [146,173] increase due to the more advanced networking of the films, yielding similar mechanical properties to SiO_2 for curing above 650 °C [146]. For a detailed discussion of the mechanical properties, the reader is referred to section 2.3.4.

Liou *et al.* [146] investigated the inherent stress of HSQ-based film as a function of curing temperature by Si-wafer curvature measurements and their results are visualized in Figure 2.31(a). The films stress was tensile and increased in magnitude with temperature

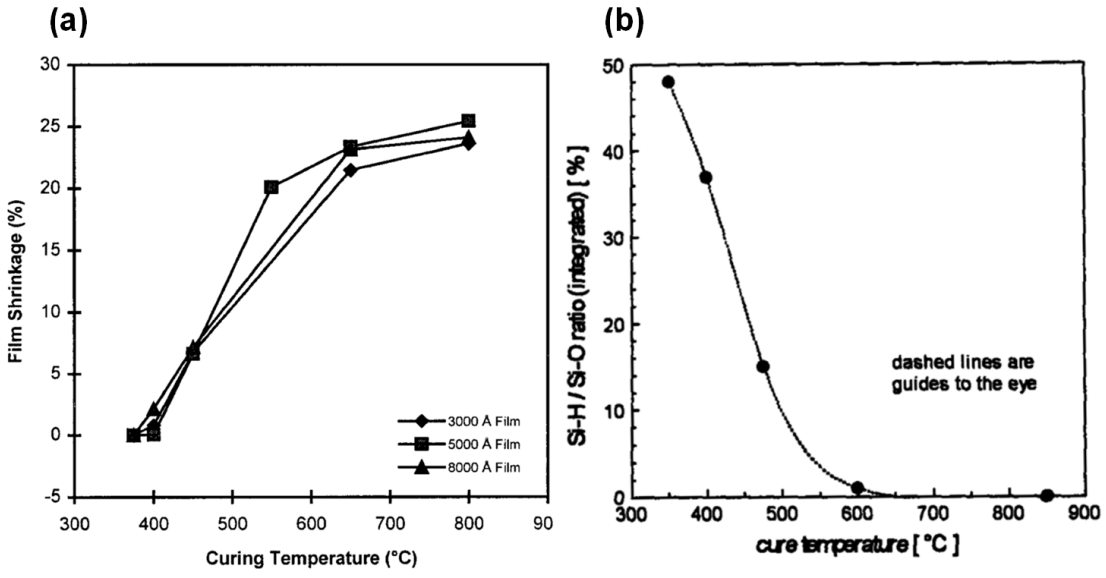

Figure 2.30: *HSQ film properties as function of curing temperature (at curing for 1 h in N_2 ambient): (a) Film shrinkage determined for films of different thickness vs. curing temperature (curing at 800 ºC was performed in O_2 ambient)* [146]*; (b) Si-H/Si-O ratio vs. curing temperature [151].*

for films cured up to 450 ºC. However, the stress of the films was found compressive for films cured above 650 ºC, which was explained by a temperature induced change in coefficient of thermal expansion (CTE) of the HSQ-based films. The CTE (Figure 2.31(b)) decreased with increasing curing temperatures and transits the value for Si (3 ppm/ºC) between 450 and 650 ºC curing temperature. As a result, the stress in the film, originating from the thermal expansion mismatch between Si-substrate and film changes from tensile to compressive stress when the material is cured above 650 ºC. Associated with curing stress, SOG is increasingly prone to fracture with increasing film thickness, leading to a reported cracking threshold of ~1200 nm film thickness for HSQ-based films (cured at 400 - 425 ºC in inert atmosphere) [162,174]; however, the cracking threshold is largely dependent on the curing temperature and annealing time and results from Bremmer *et al.* [175] indicated, that a film thickness of 1200 nm can be exceeded when the films are cured within a temperature dependent time frame.

In addition to thermally induced polymerization, Hessel *et al.* [176,177] observed the formation of Si nano-domains for curing temperatures above 450 ºC in reducing atmosphere [176,177]. The group studied HSQ-based films after curing at various temperatures by X-ray photoelectron spectroscopy (XPS) and observed a low oxidation state Si $2p_{3/2}$-emission at 99.3-99.5 eV binding energy in addition to the dominating Si $2p_{3/2}$-emission of SiO_x (103.3-104 eV binding energy). A representative XPS spectrum of a film cured at 600 ºC, showing the Si 2p emission corresponding to SiO_2 and its lower valent sub-oxides (dominant emission at high binding energy) together with the Si 2p emission corresponding to Si^0 (low binding energy shoulder) is shown in Figure 2.32. The nano-domains appeared amorphous for temperatures below 900 ºC, but showed long-range order in XRD after curing above 900 ºC [176]. It was proposed that Si nano-domains form due to thermal decomposition of the reaction by-product SiH_4 to Si and H_2.

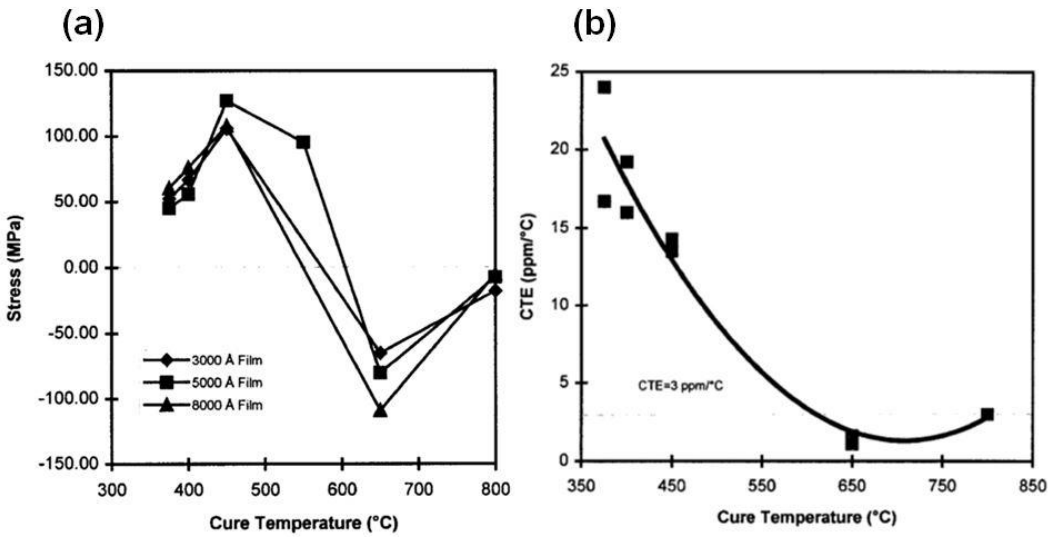

Figure 2.31: *(a) The stress level of HSQ films vs. curing temperature (on Si-wafer substrate); (b) The coefficient of thermal expansion (CTE) of HSQ films vs. curing temperature [146].*

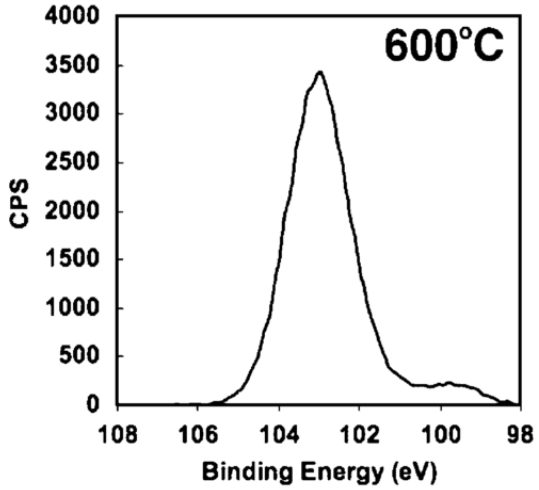

Figure 2.32: *Shirley background-subtracted high-resolution XPS spectrum of the Si 2p region for Si/SiO_2 composites obtained from HSQ-processing at 600 ºC [177].*

Thermal curing in oxidizing atmosphere

If oxygen is introduced to the system, the amount of Si-H dissociation due to oxidation increases strongly with respect to inert curing [147,178]. It has been shown that HSQ is sensitive to oxygen containing atmospheres above temperatures of approximately 350 °C [147,161], while the investigated HSQ films were insensitive to oxygen when cured below 340 °C. At increased temperatures of 650 °C, curing in oxygen can lead to a full conversion of HSQ to silica [147]. The mechanism of oxidative curing relies on the oxidation of Si-H bonds to silanol, *i.e.* is characterized by a strong decrease in Si-H and an increase in refractive index, originating from a densification of the films and an increase in polar bonds [161]. The curing mechanism is visualized in Figure 2.33. As shown by Bremmer *et al.* [161], the normalized Si-H bond density decreases (and thus film density of oxidatively cured films) correlates with both the temperature and oxygen partial pressure. The complex relation between the normalized Si-H bond density, the curing temperature and the oxygen partial pressure is visualized in Figure 2.34(a). Further, the effect of curing temperature and oxygen partial pressure on the film density is plotted in Figure 2.34(b). However, within the investigated curing conditions, the film density remained clearly below the density reported for thermal SiO_2 (2.2 g/cm^3). Moreover, the group investigated the relation between the normalized Si-H bond density and the film density and shrinkage. Their results are summarized in Figure 2.35. In the investigated temperature domain, the respective Si-H bond densities were proportional to both the film density and the film shrinkage.

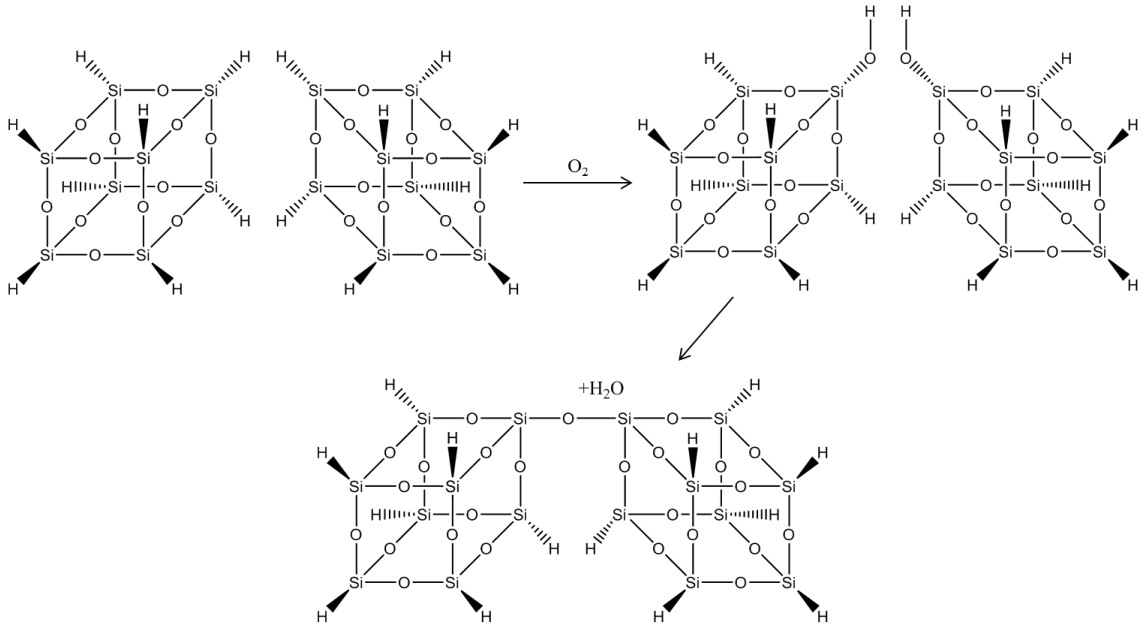

Figure 2.33: *Oxidative curing mechanism of HSQ (Based on the findings by Bremmer et al. [161]).*

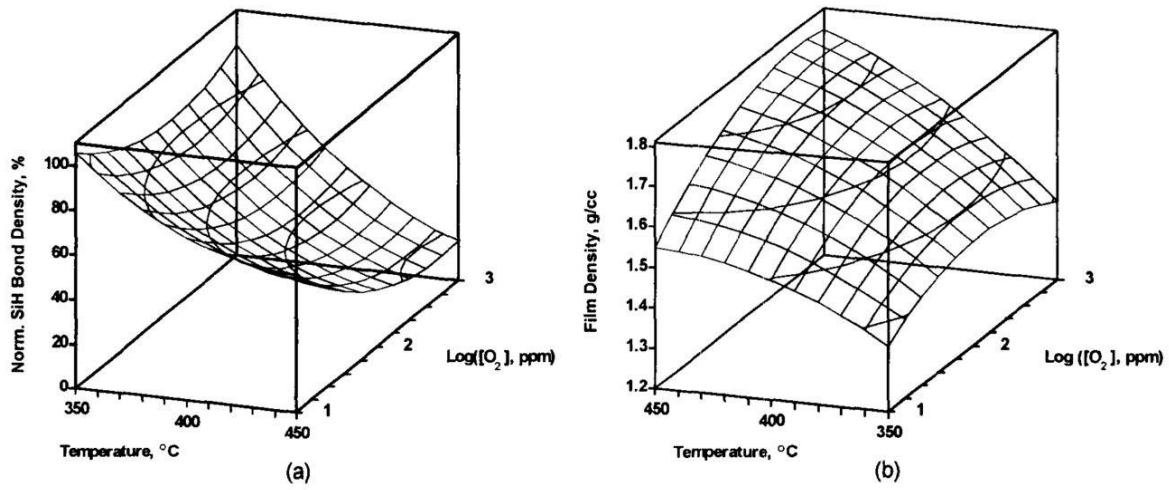

Figure 2.34: *Effect of cure process temperature and oxygen concentration on structure of hydrogen silsesquioxane for (a) normalized Si-H bond density (%); (b) film density (g/cubic centimeter (cc)) [161].*

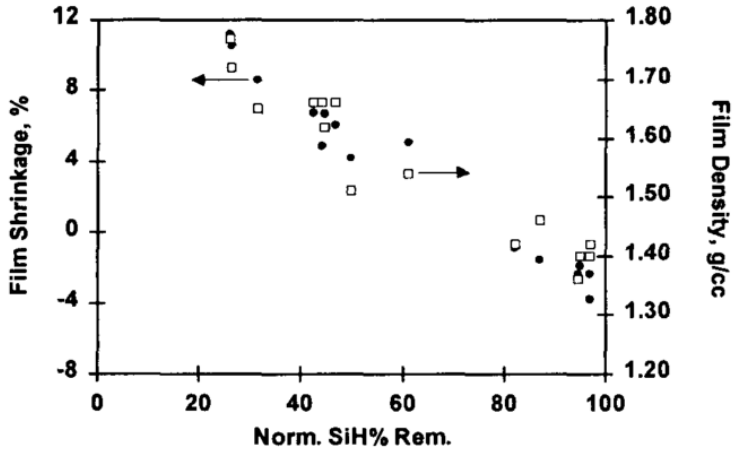

Figure 2.35: *Influence of hydrogen silsesquioxane structure on film shrinkage [161].*

Results by Gentle [179] indicated that the oxidative transformation of HSQ films by Rapid Thermal Processing (RTP) with arc and tungsten-halogen lamps is more efficient with respect to furnace curing. It has been suggested that this effect is due to the prevention of a "skinover"–effect (densification of the film in the utmost surface layer), which may limit oxygen diffusion into the film during furnace curing. Since in RTP the films are heated from the substrate, the process allows for more homogeneous curing, and thus for higher curing efficiencies.

Electron beam curing

Electron beam curing is mostly known from nanolithography, where nano-sized patterns are "printed" onto silicon wafers. Since the process is common in nanotechnology, it is well described in literature; however, different models for the transformation from cage to network structure due to electron beam irradiation have been proposed:

Namatsu *et al.* [180] proposed a cross-linking mechanism for HSQ by electron beam irradiation by a 3 step reaction: In the first step Si-H bonds in the film are broken and radical sites are formed. In the second step, these sites react with water to form silanol groups, which subsequently link with water production as a by-product. The experiments by Namatsu *et al.* were carried out with electron beam exposure at 70 kV. A reaction scheme of the curing mechanism as proposed by the group is shown in Figure 2.36.

A detailed investigation of the curing mechanism due to electron beam irradiation by Olynick *et al.* [181] has led to a different proposal of curing mechanism: The group investigated electron beam irradiated films by Raman spectroscopy and found that, similar to thermally cured HSQ resin, both SiH_2 and SiH_3 peaks were present. Hereby the Si-H peaks gradually evolved into SiH_2 and SiH_3 with longer exposure times / higher electron doses, suggesting that a redistribution reaction similar to the reaction induced by thermal curing (Figure 2.28) occurs. In contrast to thermal curing, the bond scissoring (indicated in the figure) is induced by the ionizing electron beam irradiation.

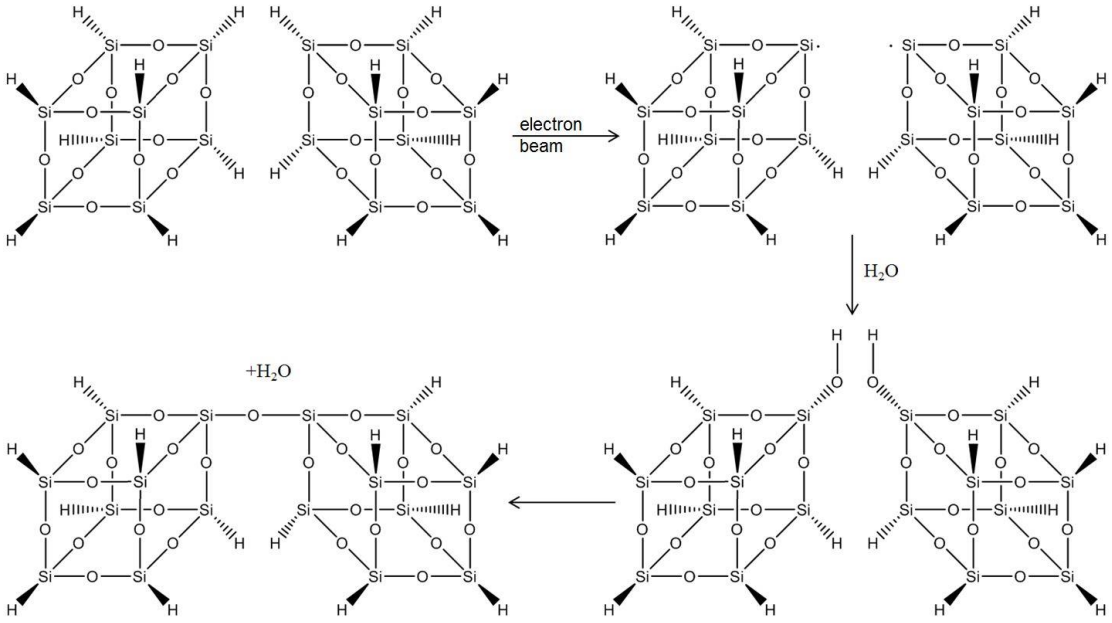

Figure 2.36: *Electron beam curing mechanism as proposed by Namatsu et al. [180].*

Nakamura *et al.* [162] assessed the effect of electron beam curing (at 150 kV accelerating voltage/10 mA beam current) with different intensities on HSQ-based films on silicon wafers and compared the results to conventional thermal curing at 400 °C. Electron beam curing was found to decrease the Si-H concentration with increasing beam dosage to levels comparable to thermal curing for dosages of 4 MGy and further raise the cracking threshold thickness to ~3 µm. Due to the high degree of similarity between the FT-IR spectra of the thermally and the electron beam cured film the group concludes that HSQ is oxidatively cured by electron beam irradiation.

The chemical changes (based on FT-IR analysis) induced by electron beam processes are similar to the changes induced by thermal curing [181,182]. However, Choi *et al.* [182] observed differences in the degree of densification, induced by the different curing mechanisms. X-ray reflectivity measurements showed that thermal annealing at temperatures above 400 °C leads to more dense layers than electron beam curing in the applied irradiation doses. The group suggested that curing with higher irradiation doses than applied in their experiment (> 1200 µC/cm^2) may lead to more dense layers.

While electron beam curing at low temperatures yields low film densities [182], Lee *et al.* [183] have shown that electron beam curing at elevated temperatures can improve the curing efficiency of electron beam processes: The group has observed electron beam cured films with cross-linking close to thermally cured films at 750 ºC when the irradiation curing is performed at a temperature of 400 ºC. The group's results indicated that thermally enhanced electron beam curing leads to the formation of more Si-Si bonds, which in turn improved the chemical stability of the film during HF wet etching and led to a significant increase in refractive index.

Curing with other types of ionizing radiation

It has been demonstrated that HSQ is, apart from electron beam radiation, sensitive to different kinds of ionizing irradiation, such as UV-, X-ray, H^+ and He^+ -irradiation [184–186]. Peuker *et al.* [184] investigated the sensitivity of HSQ-based films to different types of irradiation, ranging from photons with a visible wavelength to X-rays, electron and He^+ irradiation. The outcome of their investigation is summarized in Table 2.2. Clearly, negative tone in alkaline developer, indicating cross-linking under the applied type of irradiation, was observed for photon wavelengths below 157 nm and the other investigated types of irradiation.

Plasma treatment

Apart from ionizing irradiation, HSQ can be densified by different plasma treatments. Yuan *et al.* [187] postulated that oxygen plasma treatments cure HSQ films in analogy to thermal treatments in oxygen ambient (Figure 2.33). Oxygen plasma is capable of breaking the Si-H bonds, forming Si-OH bonds of which some will furthermore form stable Si-O-Si links between the cages. The group has shown that oxygen plasma treatment leaves the films partially hydrolyzed and concludes that oxygen plasma cured films are prone to water uptake. Penaud *et al.* [188] densified HSQ by oxygen plasma treatment and compared the results to thermally cured HSQ. The group has shown by FT-IR analysis that long high power oxygen plasma treatments, transform cage-like structures to network structures similar to thermal treatments. In their study, the transformation from cage to network structure becomes more efficient with increasing plasma energies and exposure times and the group was able to induce (based on FT-IR measurements) similar degrees of transformation for high power plasma treatments with respect to thermal curing at 700 ºC in inert atmosphere. Furthermore, the group investigated the effect of various plasma treatments on the etch rate in 1 % HF and found

Table 2.2: *Sensitivity of HSQ for various types of irradiation [184].*

Radiation	**Sensitivity**	**Dose (mJ/cm^2)**
Photon wavelength (nm)		
800-400	-	< 1000
365	-	< 1000
248	-	< 1000
193	-	< 150
157	Negative tone	> 650
13.5	Negative tone	> 50
1.3	Negative tone	> 400
0.154	Negative tone	unknown
Electrons at 50 keV	Negative tone	> 5000
He^+ ions at 75 keV	Negative tone	> 75

that the plasma-treatment reduced the etch rate significantly with respect to an uncured film, however, showed inferior etch resistance with respect to the thermally cured film (Figure 2.37). Generally, the group observed a non-linear curing behavior over plasma exposure time, leading to rapid cage to network structure transformation during the initial period of plasma treatment, followed by a slowly progressing transformation with further plasma exposure. Moreover, as shown in Figure 2.37, the plasma treated films exhibited, in contrast to the thermally cured film, slow etching kinetics during initial exposure to the HF solution and faster kinetics during further etching. Consequently, the group proposed that the plasma treatment led to a preferential densification of the top layer of the films, while the film volume remained largely unaffected.

A detailed study of the effect of curing HSQ in N_2 plasma was conducted by Lee *et al.* [163]. The group characterized the depth-dependent densification of the films by X-ray reflectivity measurements. In agreement with the suggestions by Penaud *et al.* [188], the group found a densified surface layer in the films, which grew in thickness with increasing exposure time and plasma power. The results indicated that the plasma treatment densifies the film at the film/air interface and the thickness of the densified layer increases with increasing exposure time or plasma powers. The group assigned the changes to cleavage of the HSQ cages and the transformation of Si-H bonds into Si-O bonds. Despite the absence of oxygen during plasma curing, the films contained a significant amount of Si-OH. The group suggested that the plasma-induced bond cleavages leave a significant amount of dangling bonds, making the films prone to water absorption after exposure to ambient air.

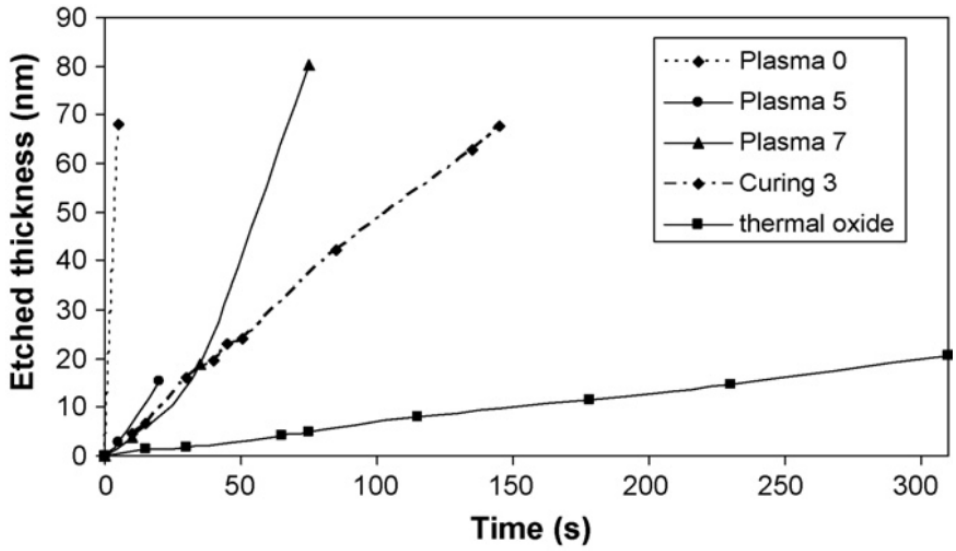

Figure 2.37: *HF etched thickness of HSQ submitted to various treatments vs. etching time. Plasma 0: uncured; Plasma 5: O_2 plasma at 290 W for 5 min; Plasma 7: O_2 plasma at 290 W for 20 min; Curing 3: Thermal curing in N_2 at 700 ºC for 1h [188].*

Curing via gelation

Deis *et al.* [189] demonstrated that exposure to moist ammonia prior to thermal curing in N_2 atmosphere strongly influences the mechanical properties of the cured films. This was shown by an increase in modulus from 6 GPa (control group of a nonporous HSQ film after curing in N_2 atmosphere at 400 °C) to 30 GPa for films which were subjected to a moist ammonia treatment. Similarly, an increase in toughness due to wet ammonia treated films compared to the control group was observed. These observations were interpreted with the gelation of the films via base catalyzed hydrolysis and condensation of the films prior to the heat treatment. Similarly, Cheng *et al.* [158] investigated the ammonia-catalyzed sol-gel transition of porous HSQ-based films and found a progressing polymerization with increasing exposure to wet ammonia. Apart from progressing polymerization, the group detected a significant amount of uncondensed silanol in the films.

2.3.4 Mechanical properties

The mechanical properties of HSQ-based films cured over a broad temperature range have been extensively studied by Liou *et al.* [146]. The group investigated both hardness and elastic modulus of HSQ-based films on Si-wafer substrates and found both an increase in hardness and modulus with increasing curing temperature for films cured for 1 h in N_2 ambient (exception: films cured at 850 °C were cured in O_2 ambient). Their results (based on a Berkovich nanoindentation test) are displayed in Figure 2.38. Both the elastic modulus and the hardness of the films cured at low temperatures (375-450 °C) were significantly decreased when compared with thermal SiO_2, however, reached values comparable to fused silica when cured at 800 °C [190]. The values reported by Liou *et al.* [146] are in agreement with a study by Toivola *et al.* [173], who investigated the impact of thermal curing in the temperature range of 375 - 450 °C on the mechanical properties of HSQ-based films and reported an elastic modulus between ~6 – ~14 GPa and a respective hardness between ~1.1 – ~2.1 GPa. Changes in the curing mechanism may lead to substantial change in the mechanical properties of the material, as shown by Lanniel *et al.* [191], who investigated the impact of electron beam curing on the elastic modulus up to irradiation doses of 5000 $\mu C/cm^2$ for solely electron beam cured material. The group determined a maximum elastic modulus of 1 GPa, *i.e.* a significantly lower value with respect to thermally cured films. Moreover, the mechanical properties of HSQ-based films after sol-gel transition have been analyzed by Cheng *et al.* [158]. From nanoindentation measurements, the group determined a maximum hardness of ~0.8 GPa together with a Young's modulus of ~5.55 GPa. Even lower values for the stiffness of HSQ-based films have been reported for electron beam cured films [191]. As visualized in Figure 2.39, the Young's modulus (determined by indentation with an atomic force microscope) increases with electron beam dosage; however, a maximum Young's modulus of ~1 GPa was reported within the investigated dose-range.

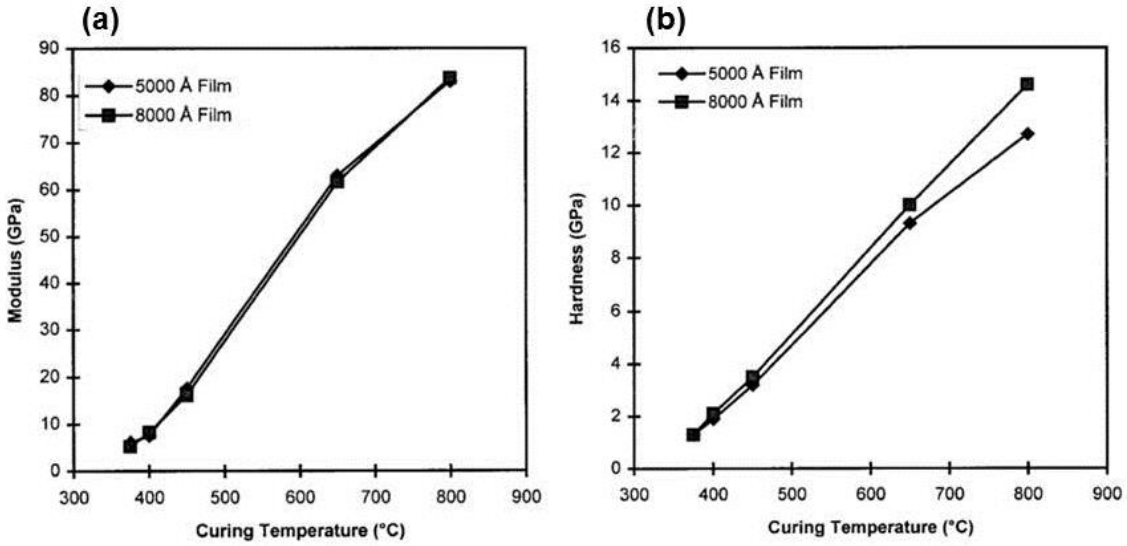

Figure 2.38: *The (a) elastic modulus and (b) hardness of HSQ films at different curing temperatures [146].*

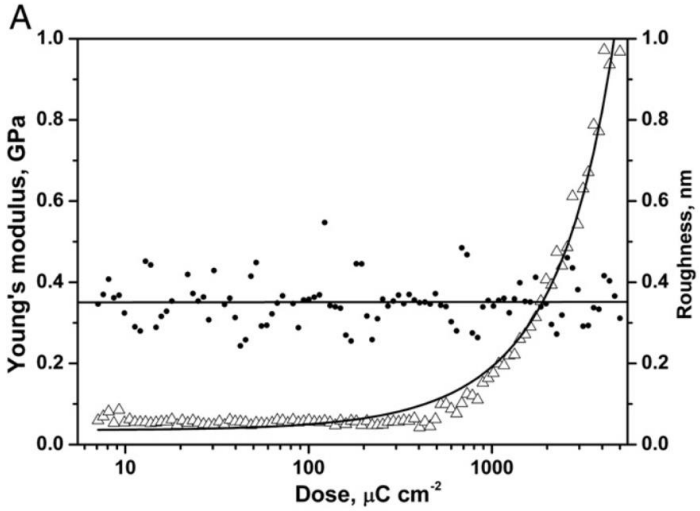

Figure 2.39: *Young's modulus (Δ) and root mean squared roughness (·) of HSQ array as function of electron beam exposure [191].*

2.3.5 Stress corrosion cracking

Several groups have demonstrated that SOG-films are susceptible to stress corrosion cracking in moist environments [173,192,193]. It has been found that SOG films on Si-wafer substrates, which are inherently under tensile stress from both curing strain and thermal expansion mismatch with the substrate [192], show advanced cracking velocities when exposed to moist environment. This was interpreted as the hydrolysis of bridging Si-O-Si bonds in the SOG at strained crack tips, leading to rapid, chemically assisted propagation of cracks. Films which were initially crack free fragmented when exposed to

moist environment and surface cracks initiated by micro indentation showed advanced propagation velocities when immersed in water (compared to dry environment). Their results on the tendency to fracture of various films cured at 400 ºC in inert environment are summarized in Table 2.3. In the table, the films are benchmarked by the approximate timeframe for film fracture or fracture kinetics at an indentation flaw. The results indicated that the driving force for crack initiation in moist environment is dependent on the film stress (controlled by curing conditions and film thickness) and the networking. Consequently, the lowest crack propagation velocities were observed for films with a high degree of polymerization combined with a low film thickness.

2.3.6 Applications of HSQ

Interlayer dielectric

Microelectronic systems are frequently composed of integrated circuits which contain many layers of wiring separated by insulating material (interlayer dielectric) [194], as visualized in Figure 2.40. The output voltage of the integrated circuit and the signal velocities are functions of the interlayer capacitance, making materials with a low capacitive response desirable [194]. Since the capacitance of the interlayer dielectric in turn is proportional to the dielectric constant, *k*, low-*k* materials are desirable as interlayer dielectrics.

HSQ-resin, with the appropriate heat treatment, exhibits a significantly lower dielectric constant/refractive index than CVD silica [161]. Siew *et al.* [148] have shown that a refractive index as low as 1.372 can be achieved by curing at 400 ºC in inert atmosphere, compared to 1.457 for thermal SiO_2 [195]. Based on this, the group proposed an optimal curing routine of curing below 435 ºC for 60 min for interlayer dielectric applications. To decrease the dielectric constant even further, curing in the presence of a porogen has been subject of recent research [157–160] and dielectric constants as low as 1.5 have been reported [157,159].

Table 2.3: *HSQ-film cracking observations (Films were cured at 400 ºC in N_2 for 1h) [192].*

Thickness (µm)	Treatment conditions		
	Air	**Water**	**Indent/water**
1.5	Unstable	-	-
1	Days	Hours	Unstable
0.85	Month	Days	Rapid extension (> 10 µm/s)
0.55	Stable	Month	Slow extension (< 10 µm/s)

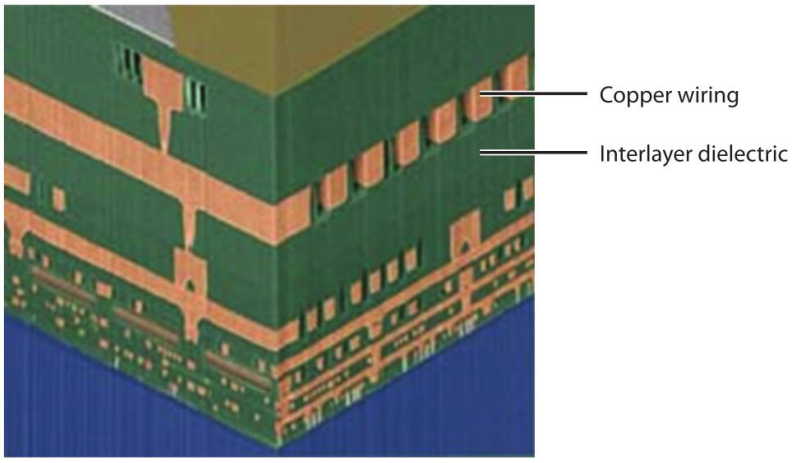

Figure 2.40: *Cross-sectional view of an integrated circuit with many layers of copper wiring [194].*

Electron beam resist

Due to its sensitivity to ionizing irradiation, HSQ finds application in the field of nanolithography and nanofabrication. As negative electron beam resist [196], a thin film of HSQ-solution is deposited on a surface, the solvent is evaporated and nano-features are written with an electron beam [180]. The polymerized material is more resistant towards dissolution in a developer solution [196], leaving only the irradiated portion of the film on the substrate. Features written in HSQ are generally developed in alkaline developer such as tetramethylammonium hydroxide [180,196–199], potassium hydroxide [180] or sodium hydroxide [200], yielding high resolution nano-patterns, as exemplarily shown in Figure 2.41.

Wafer bonding agent

HSQ-based spin-on-glass was successfully demonstrated as wafer bonding agent in nano-fabrication processes. Lee *et al.* [202] demonstrated HSQ as a bonding agent between Si-wafer and hydrogen implanted SiC-wafer for the fabrication of micro electro-mechanical systems. In their processing sequence the SiC-wafer needed to be bonded to a Si-wafer substrate to enable further processing of the SiC-wafer. The group demonstrated that the

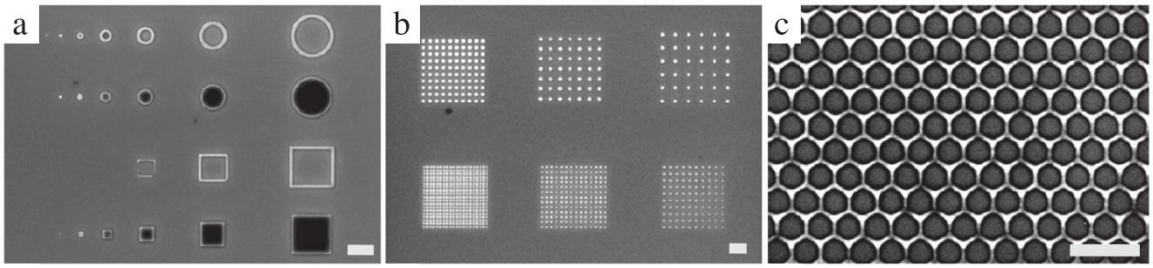

Figure 2.41: *SEM images of HSQ patterns on Si substrates. All scale bars are 500 nm [201].*

use of HSQ as bonding agent can minimize both the roughness requirements of the wafers and the annealing requirements for the processing compared to previous studies on directly bonded wafers. Similarly, in the manufacturing of high electron mobility resistors HSQ has been applied as a bonding agent between AlGaN/GaN layer grown on Si(111)-wafer and a Si(100) wafer [203,204], to guarantee mechanical stability of the AlGaN/GaN layer during further processing.

HSQ-based thin films as surface coating for metallic substrates

While HSQ is traditionally applied as interlayer dielectric or electron beam resist, the precursor has recently gained industrial focus as surface coating on metallic substrates [205,206], with a particular interest in the surface levelling ability of the coatings [207–209]. While the material is traditionally deposited by spin-coating (onto a Si-wafer substrate) [148,161], spray-coating from an ultrasonic nozzle has been introduced as a more applicable deposition procedure on industrial components [208,209]. As demonstrated by Cech *et al.* [209], spray-coating, reflow of the coating by solvent re-saturation and subsequent thermal curing of the HSQ precursor can lead to the formation of a uniform coating on rough metallic substrates (Figure 2.42). The coatings deposited by the group were primarily of interest due to their excellent levelling ability and in this perspective, the group reported a peak to valley roughness reduction of a factor of 20 for mechanically ground and more than 10 for mechanically polished Al 1050 surfaces. The effect of HSQ deposition on the surface roughness of a sandpaper polished Al 1050 substrate is shown in Figure 2.43.

HSQ-based surface treatments have primarily found application in molding tools, where a low mold cavity surface roughness is required to mold “optically smooth” polymer components. In this application the surface treatment has shown to endure more than 10,000 injection molding cycles without detectable degradation [209]. Apart from the smoothening ability, HSQ-based coatings have been investigated as a surface treatment that carries nano-patterns which can subsequently be transferred to a plastic component by injection molding [210]. To transfer nano-patterns into a HSQ coated surface, the surface was embossed by a nanostructured stamp prior to polymerization, leaving a nanostructure on the mold cavity which could be replicated onto the polymer part during molding. Moreover, the surface energy of the HSQ-based coating was modified by the deposition of an anti-sticking monolayer, which improved the release of the replica from the mold.

Recently, HSQ has come into focus as precursor for an anti-corrosion barrier coatings: In US2014/015441 A1 [206] the process of HSQ-thin film deposition as anti-corrosion treatment for metallic substrates is described. In the process description, a liquid solution of $RSiO_x$, *i.e.* HSQ or more complex silsesquioxanes, is deposited on a surface and thermally cured to form a silicon oxide with a stoichiometry between (Si:O) 1:1 and 1:2. The curing ambient is not clearly stated in the patent application; however, both curing in inert and oxygen-containing atmospheres are considered.

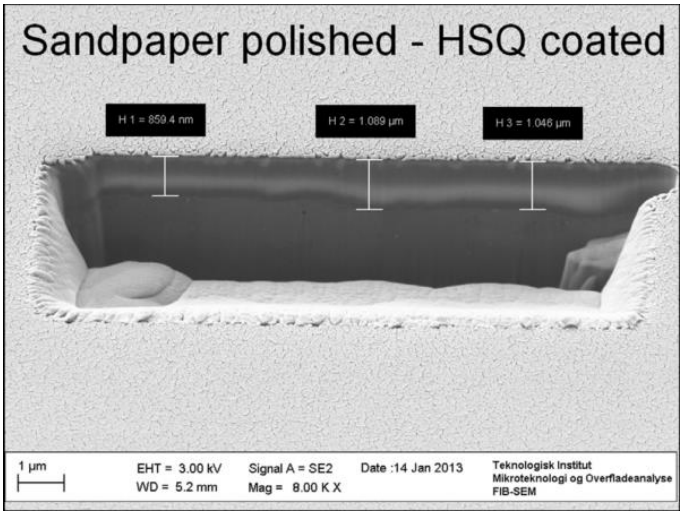

Figure 2.42: *Focused ion beam milled cross-sectional micrograph showing a sandpaper polished Al 1050 surface with a HSQ surface film [209].*

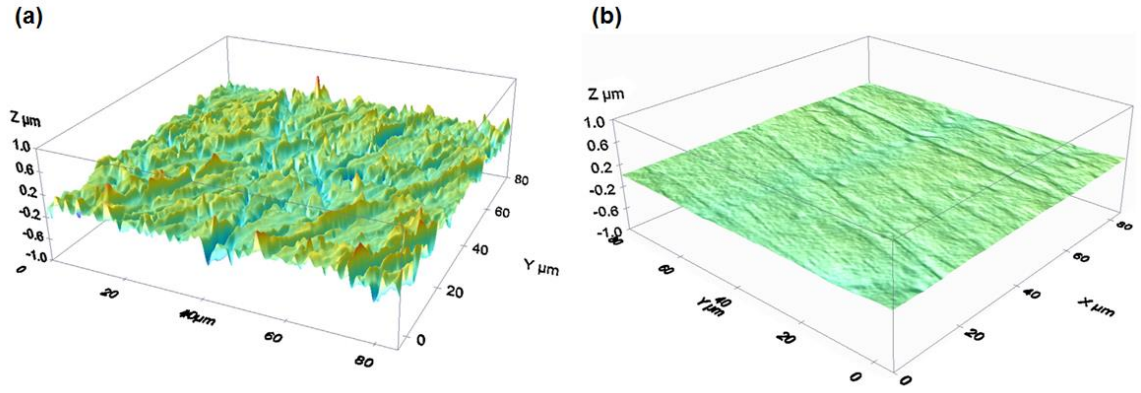

Figure 2.43: *Optical profiler data showing the topography of superfine sandpaper polished sample surfaces: (a) Uncoated surface; (b) HSQ-glass coated surface. The surface roughness is strongly reduced [209].*

2.4 Summary

Stainless steels naturally passivate due to their high alloying with Cr and form a Cr-rich oxide/hydroxide surface film, which constitutes a physical barrier between the substrate and corrosive species from the environment. The efficiency of the passivation is dependent on the alloy composition, whereby an increasing Cr, Mo and N content generally yields a more efficient passivation. Further, the ability to sustain an efficient passivation may be compromised in halide (often Cl^-)-containing media, whereby an increase in Cl^- content, together with an increase in electrolyte temperature yields increasingly corrosive media. Corrosive failure of stainless steels in Cl^--containing media may be observed in form of localized corrosion which is often observed in conjunction with pre-existing surface defects such as Mn-sulphide inclusions. Restricted system/component geometries such as crevices from gaskets, washers, bolt heads or

surface deposits constitute preferred initiation points for localized corrosion and may lead to accelerated failure of the component.

Sub-micrometer or micrometer-thick SiO_x films can be deposited by various techniques, whereby the traditional techniques are wet processes such as sol-gel deposition or LPD and vapor phase processes such as CVD and PVD. The traditional processes are applicable to stainless steel substrates, whereby the vapor phase processes show drawbacks due to the need for complex processing equipment (need for reactor/vacuum equipment) with respect to the wet processes. Further, LPD is restricted to low deposition rates, compromising the suitability of the process for large-scale industrial production. Sol-gel processes, on the contrary, are versatile and do not require complex processing equipment; however, SiO_x films deposited from aqueous sol are porous in nature and require high-temperature sintering to densify. Generally, SiO_x films are applicable as coating material for steel substrates and may show improvements in surface roughness, hardness, wear resistance, biocompatibility or cleanability with respect to uncoated surfaces. Further, SiO_x coatings have been successfully demonstrated as corrosion barrier coatings and may show beneficial effects on the wet corrosion behavior of stainless steel substrates. SiO_2 constitutes a thermodynamically metastable phase in aqueous environment, but high quality amorphous silica such as fused silica or crystalline silica (e.g. quartz) show inherently low dissolution rates. Poor quality SiO_x films may, on the contrary, dissolve in aqueous solutions at increased rates.

HSQ is a versatile thin film precursor, which can be polymerized to form both hydrogenated and non-hydrogenated inorganic polymers with siloxane backbone. Most commonly, the precursor is polymerized by a thermal treatment, whereby the curing efficiency is largely dependent on the curing temperature and the oxygen content of the curing ambient. Generally, non-oxidative curing relies on a bond exchange reaction with silane and hydrogen gas as a reaction by-product, while the presence of oxygen in the curing ambient results in oxidation of the precursor, leading to an accelerated polymerization. Apart from a thermal treatment, the precursor is sensitive to different types of ionizing irradiation of plasmas and can be polymerized by these. Traditionally, the precursor is applied as interlayer dielectric, since it can sustain a significant amount of molecular porosity or hydrogenation, leading to an inherently low dielectric constant. Further, the precursor is applied in the field of nanolithography, since it can be polymerized by irradiation treatments and gives a negative tone after development. Recently, the precursor has immerged into the field of industrial surface finishing and was applied as planarization treatment of rough metallic substrates, leading to an increase in performance of *e.g.* injection molding tools. Reports on the efficiency as anti-corrosion barrier coating are absent.

References

[1] E. Bardal, Corrosion and Protection, Springer-Verlag London Ltd., London, 2004.

[2] B.N. Popov, Pitting and Crevice Corrosion, in: Corros. Eng. Princ. Solved Probl., Elsevier B.V., 2015: pp. 289–325.

[3] L. Stockert, H. Böhni, Susceptibility to Crevice Corrosion and Metastable Pitting of Stainless Steels, Mater. Sci. Forum. 44–45 (1989) 313–328.

[4] N.J. Laycock, J. Stewart, R.C. Newman, The Initiation of Crevice Corrosion in Stainless Steel, Corros. Sci. 39 (1997) 1791–1809.

[5] U. Rohles, H.D. Schulze, Possibilities of corrosion prevention and removal in seawater exposed structures and desalination plants, Desalination. 55 (1985) 283–296.

[6] I. Olefjord, B.O. Elfström, The Corrosion Resistance of Fe-Cr Alloys as Studied by ESCA, in: React Solids, Proc Int Symp, 8th, 1977: pp. 791–796.

[7] C. Leygraf, S. Ekelund, G. Schon, ESCA and Electron Microscopy Studies of Oxide Films on an 18/8 Stainless Steel, Scand. J. Metall. 2 (1973) 313–320.

[8] I. Olefjord, ESCA-Studies of the Composition Profile of Low Temperature Oxide Formed on Chromium Steels - I. Oxydation in Dry Oxygen, Corros. Sci. 15 (1975) 687–696.

[9] H. Fischmeister, I. Olefjord, Elektronenspektroskopische Untersuehung der natürlichen Oxidhaut eines rosffreien Stahls, Monatshefte Für Chemie. 102 (1971) 1486–1498.

[10] I. Olefjord, B.O. Elfström, Investigation by ESCA of the Passive Film Formed on Austentic Stainless Steel in Oxygenated Water, 6th Eur. Congess Met. Corros. - EUROCORR ’77. (1977) 19–28.

[11] I. Olefjord, B.O. Elfström, The Composition of the Surface during Passivation of Stainless Steels, Corros. - NACE. 38 (1982) 46–52.

[12] I. Olefjord, H. Fischmeister, ESCA Studies of the Composition Profile of Low Temperature Oxide Formed on Chromium Steels - II. Corrosion in Oxygenated Water, Corros. Sci. 15 (1975) 697–707.

[13] S. Tardio, M.-L. Abel, R.H. Carr, J.E. Castle, J.F. Watts, Comparative study of the native oxide on 316L stainless steel by XPS and ToF-SIMS, J. Vac. Sci. Technol. A Vacuum, Surfaces, Film. 33 (2015) 05E122-1-05E122-14.

[14] T. Hong, T. Ogushis, M. Nagumo, The Effect of Chromium Enrichment in the Film Formed by Surface Treatments on the Corrosion Resistance of Type 430 Stainless Steel, Corros. Sci. 38 (1996) 881–888.

[15] I. Olefjord, B. Brox, U. Jelvestam, Surface Composition of Stainless Steels during Anodic Dissolution and Passivation Studied by ESCA, J. Electrochem. Soc. 132 (1985) 2854–2861.

[16] I. Olefjord, The Passive State of Stainless Steels, Mater. Sci. Eng. 42 (1980) 161–171.

[17] B.O. Elfström, The Effect of Chloride Ions on Passive Layers on Stainless Steels, Mater. Sci. Eng. 42 (1980) 173–180.

[18] I. Olefjord, L. Wegrelius, Surface analysis of passive state, Corros. Sci. 31 (1990) 89–98.

[19] G.S. Frankel, Pitting Corrosion of Metals A Review of the Critical Factors, J. Electrochem. Soc. 145 (1998) 2186.

[20] H.H. Strehblow, Breakdown of Passivity and Localized Corrosion: Theoretical concepts and fundamental results, Werkstoffe Und Korrosion. 35 (1984) 437–448.

[21] T.P. Hoar, D.C. Mears, G.P. Rothwell, The relationships between anodic passivity, brightening and pitting, Corros. Sci. 5 (1965) 279–289.

[22] T.P. Hoar, W.R. Jacob, Breakdown of Passivity of Stainless Steels by Halide Ions, Nature. 216 (1967) 1299–1301.

[23] D. Der Mischungswarme, J. Vetter, Vetter, K.J. Strehblow, H.H., Berichte Der Bunsen-Gesellschaft. 74 (1970) 1024–1035.

[24] N. Sato, A theory for breakdown of anodic oxide films on metals, Electrochim. Acta. 16 (1971) 1683–1692.

[25] P.C. Pistorius, G.T. Burstein, Detailed Investigation of Current Transients from Metastable

Pitting Events on Stainless Steel - The Transition to Stability, Mater. Sci. Forum. 111–112 (1992) 429–452.
[26] G. Wranglén, Pitting and Sulphide Inclusions in Steel, Corros. Sci. 14 (1974) 331–349.
[27] G.T. Burstein, P.C. Pistorius, S.P. Mattin, The Nucleation and Growth of Corrosion Pits on Stainless Steel, Corros. Sci. 35 (1993) 57–62.
[28] G.S. Frankel, L. Stockert, F. Hunkeler, H. Boehni, Metastable Pitting of Stainless Steel, Corros. - NACE. 43 (1987) 429–436.
[29] P.C. Pistorius, G.T. Burstein, Metastable pitting corrosion of stainless steel and the transition to stability, Philos. Trans. R. Soc. Ser. A. 341 (1992) 531–559.
[30] J.R. Saithala, S. McCoy, A. Houghton, J.D. Atkinson, Pitting Corrosion of Stainless Steels in Chloride Solutions at Elevated Temperatures, in: Eur. Corros. Congr. Manag. Corros. Sustain. EUROCORR 2008, 2008.
[31] J.-H. Wang, C.C. Su, Z. Szklarska-Smialowska, Effects of Cl- Concentration and Temperature on Pitting of AISI 304 Stainless Steel, Corros. Sci. 44 (1988) 732–737.
[32] ASTM G48-11 Standard Test Methods for Pitting and Crevice Corrosion Resistance of Stainless Steels and Related Alloys by Use of Ferric Chloride Solution, 3 (2011).
[33] B. Leffler, Stainless-steels and their properties, 1996. https://www.tf.uni-kiel.de/matwis/amat/iss/kap_9/articles/stainless_steel.pdf (accessed 01.03.2017).
[34] K. Asami, K. Hashimoto, An X-ray Photo-Electron Spectroscopic Study of Surface Treatments of Stainless Steels, Corros. Sci. 19 (1979) 1007–1017.
[35] C.R. Clayton, I. Olefjord, Passivity of Austenitic Stainless Steels, in: P. Marcus (Ed.), Corros. Mech. Theory Pract. Third Ed., CRC Press, 2011: pp. 327–347.
[36] K. Hashimoto, K. Asami, K. Teramoto, An X-ray Poto-Electron Spectroscopic Study on The Role of Molybdenunm in Increasing the Corrosion Resistance of Ferritic Stainless Steels in HCl, Corros. Sci. 19 (1979) 3–14.
[37] H. Ogawa, H. Omata, I. Itoh, H. Okada, Auger Electron Spectroscopic and Electrochemical Analysis of the Effect of Alloying elements on the Passivation Behavior of Stainless Steels, Corros. - NACE. 34 (1978) 52–60.
[38] A. Pardo, M.C. Merino, A.E. Coy, F. Viejo, R. Arrabal, E. Matykina, Effect of Mo and Mn additions on the corrosion behaviour of AISI 304 and 316 stainless steels in H2SO4, Corros. Sci. 50 (2008) 780–794.
[39] L. Jinlong, L. Tongxiang, W. Chen, Surface enriched molybdenum enhancing the corrosion resistance of 316L stainless steel, Mater. Lett. 171 (2016) 38–41.
[40] J.E. Truman, M.J. Coleman, K.R. Pirt, Note on the Influence of Nitrogen Content on the Resistance to Pitting Corrosion of Stainless Steels, Br. Corros. J. 12 (1977) 236–238.
[41] Y.C. Lu, R. Bandy, C.R. Clayton, R.C. Newman, Surface Enrichment of Nitrogen during Passivation of a Highly Resistant Stainless Steel, J. Electrochem. Soc. 130 (1983) 1774–1776.
[42] S. Ahila, B. Reynders, H.J. Grabke, The evaluation of the repassivation tendency of Cr-Mn and Cr-Ni steels using scratch technique, Corros. Sci. 38 (1996) 1991–2005.
[43] C.-O.A. Olsson, The influence of nitrogen and molybdenum on passive films formed on the austeno-ferritic stainless steel 2205 studied by AES and XPS, Corros. Sci. 37 (1995) 467–479.
[44] I. Olefjord, L. Wegrelius, The Influence of Nitrogen on the Passivation of Stainless Steels, Corros. Sci. 38 (1996) 1203–1220.
[45] R.F.A. Jargelius-Pettersson, Electrochemical investigation of the influence of nitrogen alloying on pitting corrosion of austenitic stainless steels, Corros. Sci. 41 (1999) 1639–1664.
[46] R. Bandy, D. Van Rooyen, Pitting-Resistant Alloys in Highly Concentrated Chloride Media, Corros. - NACE. 39 (1983) 227–236.
[47] B.A. Shaw, P.J. Moran, P.O. Gartland, The role of Ohmic potential drop in the initiation of crevice corrosion on alloy 625 in seawater, Corros. Sci. 32 (1991) 707–719.
[48] J.W. Oldfield, W.H. Sutton, Crevice Corrosion of Stainless Steels I. A Mathematical Model, Br. Corros. J. 13 (1978) 13–22.

[49] P. Møller, L.P. Nielsen, Introduction To Corrosion, in: Adv. Surf. Technol. Vol 1, 2013: pp. 37–70.
[50] S.E. Lott, R.C. Alkire, The variation of solution composition during the initiation of crevice corrosion on stainless steel, Corros. Sci. 28 (1988) 479–484.
[51] S.E. Lott, R.C. Alkire, The Role of Inclusions on Initiation of Crevice Corrosion of Stainless Steel: 1. Experimental Studies, J. Electrochem. Soc. 136 (1989) 973–979.
[52] R.C. Alkire, S.E. Lott, The Role of Inclusions on Initiation of Crevice Corrosion of Stainless Steel: 2. Theoretical Studies, J. Electrochem. Soc. 136 (1989) 3256–3262.
[53] C.S. Brossia, R.G. Kelly, On the Role of Alloy Sulfur in the Initiation of Crevice Corrosion in Stainless Steel, Proc. Symp. Crit. Factors Localized Corros. II. 95 (1995) 201–217.
[54] R.C. Newman, H.S. Isaacs, B. Alman, Effects of Sulfur Compounds on the Pitting Behavior of Type 304 Stainless Steel in Near-neutral Chrloride Solutions, Corros. - NACE. 38 (1982) 261–265.
[55] H.W. Pickering, R.P. Frankenthal, On the Mechanism of Localized Corrosion of Iron and Stainless Steel: 1. Electrochemical Studies, J. Electrochem. Soc. 10 (1967) 1297–1304.
[56] H.W. Pickering, R.P. Frankenthal, On the Mechanism of Localized Corrosion of Iron and Stainless Steel: 2. Morphological Studies, J. Electrochem. Soc. 119 (1972) 1304–1310.
[57] K. Cho, H.W. Pickering, Demonstration of Crevice Corrosion in Alkaline Solution Without Acidification, J. Electrochem. Soc. 137 (1990) 3313–3314.
[58] Z. Szklarska-Smialowska, J. Mankowski, Crevice Corrosion of Stainless Steels in Sodium Chloride Solution, Corros. Sci. 18 (1978) 953–960.
[59] C.J. Brinker, G.W. Scherer, Hyrdolysis and Condensation of Silicon Alkoxides, in: Sol-Gel Sci., Academic Press, Inc., San Diego, 1990: pp. 108–216.
[60] C.J. Brinker, Sol-Gel Processing of Silica, Adv. Chem. Ser. 234 (1994) 361–402.
[61] A.M. Buckley, M. Greenblatt, The Sol-Gel Preparation of Silica Gels, J. Chem. Educ. 71 (1994) 599–602.
[62] J. Brinker, Dip Coating, in: T. Schneller, R. Waser, R. Kosec, D. Payne (Eds.), Chem. Solut. Depos. Funct. Oxide Thin Film., Wien, 2013: pp. 233–261.
[63] C.J. Brinker, G.C. Frye, A.J. Hurd, C.S. Ashley, Fundamentals of sol-gel dip coating, Thin Solid Films. 201 (1991) 97–108.
[64] C.J. Brinker, A.J. Hurd, G.C. Frye, K.J. Ward, C.S. Ashley, Sol-Gel Thin Film Formation, J. Non. Cryst. Solids. 121 (1990) 294–302.
[65] G.W. Scherer, Sintering of Sol-Gel Films, J. Sol-Gel Sci. Technol. 8 (1997) 353–363.
[66] C.J. Brinker, G.W. Scherer, E.P. Roth, Sol -> Gel -> glass: II. Physical and Structural Evolution During Constant Heating Rate Experiments, J. Non. Cryst. Solids. 72 (1985) 345–368.
[67] G.W. Scherer, C.J. Brinker, E.P. Roth, Sol -> Gel -> Glass: III. Viscous Sintering, J. Non. Cryst. Solids. 72 (1985) 369–389.
[68] M.A. Fardad, Catalysts and the structure of SiO 2 sol-gel films, J. Mater. Sci. 35 (2000) 1835–1841.
[69] C.J. Brinker, G.W. Scherer, Drying, in: Sol-Gel Sci., San Diego, 1990: pp. 453–513.
[70] A. Bagolini, A.S. Savoia, A. Picciotto, LPCVD against PECVD for micromechanical applications, J. Micromechanics Microengineering. 6 (1996) 1–13.
[71] J. Foggiato, Chemical Vapor Deposition of Silicon Dioxide Films, in: Handb. Thin Film Depos. Process. Tech. (Second Ed., 2nd ed., Elsevier B.V., 2001: pp. 111–149.
[72] K. Fujino, Y. Nishimoto, N. Tokumasu, K. Maeda, Low Temperature and Atmospheric Pressure CVD Using Polysiloxane, OMCTS, and Ozone, J. Electrochem. Soc. 138 (1991) 3727–3732.
[73] B. Mattson, CVD Films for Interlayer Dielectrics, Solid State Technol. 23 (1980) 60–64.
[74] P. González, D. Fernández, J. Pou, E. García, J. Serra, B. León, M. Pérez-Amor, Photo-induced chemical vapour deposition of silicon oxide thin films, Thin Solid Films. 218 (1992) 170–181.
[75] D. Rieger, F. Bachmann, ArF laser induced CVD of SiO2 films: a search for the best

suitable precursors, Appl. Surf. Sci. 54 (1992) 99–107.
[76] M. Sasaki, T. Ehara, Silicon Oxide Thin Films Prepared by Vacuum Evaporation and Sputtering Using Silicon Monoxide, J. Phys. Conf. Ser. 417 (2013) 12028.
[77] H. Sakata, K. Aikawa, Abrasive wear of thick silica films prepared by vacuum evaporation, J. Mater. Sci. 19 (1984) 2671–2676.
[78] M.R. Amirzada, A. Tatzel, V. Viereck, H. Hillmer, Surface roughness analysis of SiO2 for PECVD, PVD and IBD on different substrates, Appl. Nanosci. 6 (2015) 215–222.
[79] S.M. Baumann, C.C. Martner, D.W. Martin, R.J. Blattner, A.J. Braundmeier, A study of electron beam evaporated SiO2, TiO2, and Al2O3 films using RBS, HFS, and SIMS, Nucl. Instruments Methods Phys. Res. Sect. B. 45 (1990) 664–668.
[80] D. Hiller, R. Zierold, J. Bachmann, M. Alexe, Y. Yang, J.W. Gerlach, A. Stesmans, M. Jivanescu, U. Müller, J. Vogt, H. Hilmer, P. Löper, M. Künle, F. Munnik, K. Nielsch, M. Zacharias, Low temperature silicon dioxide by thermal atomic layer deposition: Investigation of material properties, J. Appl. Phys. 107 (2010) 1–10.
[81] P. Møller, L.P. Nielsen, Physical Vapor Deposition, in: Adv. Surf. Technol. Vol 1, 2013: pp. 457–482.
[82] P. J. Kelly, R. D. Arnell, Magnetron sputtering: a review of recent developments and applications, Vacuum. 56 (2000) 159–172.
[83] M. Taguchi, S. Hamaguchi, Molecular dynamics study on Ar ion bombardment effects in amorphous SiO2 deposition processes, J. Appl. Phys. 100 (2006).
[84] P.J. Kelly, J.W. Bradley, Pulsed magnetron sputtering – process overview and applications, J. Optoelectron. Adv. Mater. 11 (2009) 1101–1107.
[85] H. Seifarth, R. Grötzschel, A. Markwitz, W. Matz, P. Nitzsche, L. Rebohle, Preparation of SiO2 films with embedded Si nanocrystals by reactive r.f. magnetron sputtering, Thin Solid Films. 330 (1998) 202–205.
[86] L.-N. He, J. Xu, Properties of amorphous SiO2 films prepared by reactive RF magnetron sputtering method, Vacuum. 68 (2003) 197–202.
[87] R.P. Howson, N. Danson, G.W. Hall, Reactive magnetron sputtering of silicon to produce silicon oxide, Nucl. Instruments Methods Phys. Res. Sect. B Beam Interact. with Mater. Atoms. 121 (1997) 90–95.
[88] H.-U. Schreiber, E. Fröschle, High Quality RF-Sputtered Silicon Dioxide Layers, J. Electrochem. Soc. Solid-State Sci. Technol. 123 (1976) 30–33.
[89] S.-H. Jeong, J.-K. Kim, B.-S. Kim, S.-H. Shim, B.-T. Lee, Characterization of SiO2 and TiO2 films prepared using rf magnetron sputtering and their application to anti-reflection coating, Vacuum. 76 (2004) 507–515.
[90] H. Bartzsch, D. Glöß, B. Böcher, P. Frach, K. Goedicke, Properties of SiO2 and Al2O3 films for electrical insulation applications deposited by reactive pulse magnetron sputtering, Surf. Coatings Technol. 174–175 (2003) 720–724.
[91] P. Frach, H. Bartzsch, D. Glöß, M. Fahland, F. Händel, Electrically insulating Al2O3 and SiO2 films for sensor and photovoltaic applications deposited by reactive pulse magnetron sputtering, hollow cathode arc activated deposition and magnetron-PECVD, Surf. Coatings Technol. 202 (2008) 5680–5683.
[92] O. Zywitzki, H. Sahm, M. Krug, H. Morgner, M. Neumann, Comparison of structure and properties of SiOx coatings deposited by reactive pulsed magnetron sputtering (PMS) and by hollow cathode activated EB evaporation (HAD), Surf. Coatings Technol. 133 (2000) 555–560.
[93] M. Manhas, T.J. Pease, R. Cross, S.C. Bose, D.P. Oxley, M.M. De Souza, E.M. Sankara Narayanan, Device Quality SiO2 Films By Liquid Phase Deposition (LPD) at 48 °C, Mater. Res. Soc. Somposium Proc. 716 (2002) B7.9.1-B7.9.7.
[94] L. Wang, S. Yu, J. Cho, Properties of Liquid-Phase Deposited Silica Films for Low- k Dielectric Applications, J. Am. Ceram. Soc. 92 (2009) 2388–2391.
[95] J.-S. Chou, S.-C. Lee, Improved process for liquid phase deposition of silicon dioxide, Appl. Phys. Lett. 64 (1994) 1971.
[96] C. Ning, L. Mingyan, Z. Weidong, Fouling and Corrosion Properties of SiO2 Coatings on

Copper in Geothermal Water, ACS Ind. Eng. Chem. Res. 51 (2012) 6001–6017.
[97] S. Nitta, Y. Kimura, Formation of SiO2 Thin Film on SUS304 Stainless Steel by Liquid Phase Deposition (in Japanese), J. Soc. Matierals Sci. Japan. 43 (1994) 1437–1443.
[98] H. Nagayama, H. Honda, H. Kawahara, A New Process for Silica Coating, J. Electrochem. Soc. 135 (1988) 2013–2016.
[99] K. Usami, S. Hayashi, Y. Uchida, M. Matsumura, Liquid-Phase Deposition of Silicon-Dioxide Films using Tetra-Ethyl Orthosilicate, Jpn. J. Appl. Phys. 37 (1998) L97–L99.
[100] K. Usami, S. Sugahara, K. Sumimura, M. Matsumura, Liquid-Phase Deposition of Low-K Organic Silicon-Oxide Films, MRS Proc. 511 (1998) 27–32.
[101] M. Creatore, F. Palumbo, R. D'Agostino, Diagnostics and insights on PECVD for gas-barrier coatings, Pure Appl. Chem. 74 (2002) 407–411.
[102] D.G. Howells, B.M. Henry, Y. Leterrier, J.A.E. Månson, J. Madocks, H.E. Assender, Mechanical properties of SiOx gas barrier coatings on polyester films, Surf. Coatings Technol. 202 (2008) 3529–3537.
[103] G.H. Lee, J. Yun, S. Lee, Y. Jeong, J.H. Jung, S.H. Cho, Investigation of brittle failure in transparent conductive oxide and permeation barrier oxide multilayers on flexible polymers, Thin Solid Films. 518 (2010) 3075–3080.
[104] B. Delperier, F. Maury, R. Calsou, R. Morancho, Silica CVD from TEOS on Fe/Cr/Ni Alloy, in: Proc. Tenth Int. Conf. Chem. Vap. Depos., 1987: pp. 1139–1146.
[105] W. Hänni, H.E. Hintermann, D. Morel, A. Simmen, Silica Coatings on Strongly Passivated Substrates, Surf. Coatings Technol. 36 (1988) 463–470.
[106] J. Pou, P. Gonzales, E. Garcia, D. Fernandez, J. Serra, B. Leon, S.R.J. Saunders, M. Perez-Amor, Ceramic coatings for high-temperature corrosion protection by laser-CVD processes, Appl. Surf. Sci. 79/80 (1994) 338–343.
[107] O. Santos, T. Nylander, R. Rosmaninho, G. Rizzo, S. Yiantsios, N. Andritsos, A. Karabelas, H. Müller-Steinhagen, L. Melo, L. Boulangé-Petermann, C. Gabet, A. Braem, C. Trägårdh, M. Paulsson, Modified stainless steel surfaces targeted to reduce fouling—surface characterization, J. Food Eng. 64 (2004) 63–79.
[108] R. Rosmaninho, O. Santos, T. Nylander, M. Paulsson, M. Beuf, T. Benezech, S. Yiantsios, N. Andritsos, A. Karabelas, G. Rizzo, H. Müller-Steinhagen, L.F. Melo, Modified stainless steel surfaces targeted to reduce fouling – Evaluation of fouling by milk components, J. Food Eng. 80 (2007) 1176–1187.
[109] G.A. Garzino-Demo, F.L. Lama, Friction and wear of uncoated or SiO2-coated 329 stainless steel and of uncoated or A1N-coated aluminium surfaces, Surf. Coatings Technol. 68/69 (1994) 507–511.
[110] J. Gallardo, A. Duran, I. Garcia, J.P. Celis, M.A. Arenas, A. Conde, Effect of Sintering Temperature on the Corrosion and Wear Behavior of Protective SiO2-Based Sol-Gel Coatings, J. Sol-Gel Sci. Technol. 27 (2003) 175–183.
[111] A. Marsal, F. Ansart, V. Turq, J.P. Bonino, J.M. Sobrino, Y.M. Chen, J. Garcia, Mechanical properties and tribological behavior of a silica or/and alumina coating prepared by sol-gel route on stainless steel, Surf. Coatings Technol. 237 (2013) 234–240.
[112] F.S. Shieu, M.J. Deng, K.C. Lin, J.C. Wong, J.Y. Wu, Effect of surface pretreatments on the adherence of porcelain enamel to a type 316L stainless steel, J. Mater. Sci. 34 (1999) 5265–5272.
[113] P. Benjamin, C. Weaver, The Adhesion of Evaporated Metal Films on Glass, Proc. R. Soc. London. Ser. A, Math. Phys. 261 (1961) 516–531.
[114] N. Jiang, J. Silcox, Observations of reaction zones at chromium/oxide glass interfaces, J. Appl. Phys. 87 (2000) 3768–3776.
[115] G.H. Lee, M. Cailler, C. Constantinescu, S.C. Kwon, Adhesion studies of radio-frequency sputtered SiO2 films on Ti, stainless steel, Ni and Inconel substrates. Effects of substrate surface ion bombardment etching, J. Adhes. Sci. Technol. 4 (1990) 481–501.
[116] S. Benayoun, L. Fouilland-Paille, J.J. Hantzpergue, Microscratch test studies of thin silica films on stainless steel substrates, Thin Solid Films. 352 (1999) 156–166.
[117] D. Pech, P. Steyer, J.-P. Millet, Electrochemical behaviour enhancement of stainless steels

by a SiO2 PACVD coating, Corros. Sci. 50 (2008) 1492–1497.
[118] D.C.L. Vasconcelos, J.A.N. Carvalho, M. Mantel, W.L. Vasconcelos, Corrosion resistance of stainless steel coated with sol–gel silica, J. Non. Cryst. Solids. 273 (2000) 135–139.
[119] A. Stoch, J. Stoch, A. Rakowska, An XPS and SEMS study of silica sol-gel/metal substrate interaction, Surf. Interface Anal. 22 (1994) 242–247.
[120] M. Takemori, Crack formation, exfoliation, and ridge formation in 500 ^{o}C annealed sol-gel silica coatings on stainless steel SUS304: Part I. Microscopic observations and elemental analysis, Ceram. Int. 35 (2009) 1731–1746.
[121] M. Takemori, Crack formation, exfoliation, and ridge formation in 500 °C annealed sol–gel silica coatings on stainless steel SUS304: Part II Spectroscopic and mechanical analyses and insights into mechanisms controlling coating characteristics, Ceram. Int. 35 (2009) 1747–1755.
[122] M. Takemori, Low temperature synthesis of a silica-based glass-like adherent film by a sol-gel method, J. Mater. Sci. Lett. 20 (2001) 151–154.
[123] D. Pech, P. Steyer, A.-S. Loir, J.C. Sánchez-López, J.-P. Millet, Analysis of the corrosion protective ability of PACVD silica-based coatings deposited on steel, Surf. Coatings Technol. 201 (2006) 347–352.
[124] T. Hwang, H. Lee, H. Kim, G. Kim, Two layered silica protective film made by a spray-and-dip coating method on 304 stainless steel, J. Sol-Gel Sci. Technol. 55 (2010) 207–212.
[125] R. Hausbrand, T. van der Donck, J.-P. Celis, F. Clarysse, Properties of FA-CVD silica coated steel sheet after deformation: coating integrity and corrosion related forming limit curve, Corros. Eng. Sci. Technol. 48 (2013) 530–536.
[126] R. Hausbrand, B. Bolado-Escudero, A. Dhont, J. Wielant, Corrosion of flame-assisted CVD silica-coated steel sheet, Corros. Sci. 61 (2012) 28–34.
[127] W. Walke, Z. Paszenda, M. Basiaga, P. Karasinski, M. Kaczmarek, EIS Study of SiO2 Oxide Film on 316L Stainless Steel for Cardiac Implants, in: E. Piętka, J. Kawa, W. Wieclawek (Eds.), Inf. Technol. Biomed. Vol 4., Springer International Publishing, Cham, 2014: pp. 403–410.
[128] W. Walke, Z. Paszenda, T. Pustelny, Z. Opilski, S. Drewniak, M. Ko, M. Basiaga, Evaluation of physicochemical properties of SiO2-coated stainless steel after sterilization, Mater. Sci. Eng. C. 63 (2016) 155–163.
[129] P. Galliano, J.J. De Damborenea, M.J. Pascual, A. Durán, Sol-Gel Coatings on 316L Steel for Clinical Applications, J. Sol-Gel Sci. Technol. 13 (1998) 723–727.
[130] B. Nikrooz, M. Zandrahimi, H. Ebrahimifar, High temperature oxidation resistance and corrosion properties of dip coated silica coating by sol gel method on stainless steel, J. Sol-Gel Sci. Technol. 63 (2012) 286–293.
[131] O. de Sanctis, L. Gomez, N. Pellegri, C. Parodi, A. Marajofsky, A. Duran, Protective Glass Coatings on Metallic Substrates, J. Non. Cryst. Solids. 121 (1990) 338–343.
[132] M. Atik, P. de Lima Neto, L.A. Avaca, M.A. Aegerter, J. Zarzycki, Protection of 316L stainless steel against corrosion by SiO2 coatings, J. Mater. Sci. Lett. 13 (1994) 1081–1085.
[133] S. Ono, Y. Nishi, S. Hirano, Chromium-Free Corrosion Resistance of Metals by Ceramic Coating, J. Am. Ceram. Soc. 84 (2001) 3054–3056.
[134] S. Ono, H. Tsuge, Y. Nishi, S.I. Hirano, Improvement of corrosion resistance of metals by an environmentally friendly silica coating method, J. Sol-Gel Sci. Technol. 29 (2004) 147–153.
[135] J. de Damborenea, N. Pellegri, O. Sanctis, A. Duran, Electrochemical Behaviour of SiO2 Sol-Gel Coatings on Stainless Steel, J. Sol-Gel Sci. Technol. 4 (1995) 239–244.
[136] A. Delimi, Y. Coffinier, B. Talhi, R. Boukherroub, S. Szunerits, Investigation of the corrosion protection of SiOx-like oxide films deposited by plasma-enhanced chemical vapor deposition onto carbon steel, Electrochim. Acta. 55 (2010) 8921–8927.
[137] K. Baba, R. Hatada, S. Nagata, H. Fujiyama, G.K. Wolf, W. Einsinger, SiO2 coatings produced by ion beam assisted ECR-plasma CVD, Surf. Coatings Technol. 75 (1995) 292–296.

[138] M.J. Bennett, M.R. Houlton, R.W.H. Hawes, The Improvement by a CVD Silica Coating of the Oxidation Behavior of a 20%Cr25%Ni Niobium Stabilized Stainless Steel in Carbon Dioxide, Corros. Sci. 22 (1981) 111–133.
[139] O. de Sanctis, L. Gomez, N. Pellegri, A. Duran, Behaviour in hot ammonia atmosphere of SiO2-coated stainless steels produced by a sol-gel procedure, Surf. Coatings Technol. 70 (1995) 251–255.
[140] E. Deltomee, N. de Zoubov, M. Pourbaix, Silicon, in: Atlas Electrochem. Equilibria Aqueous Solut., Houston, 1996: pp. 458–463.
[141] J.P. Icenhower, P.M. Dowe, The dissolution kinetics of amorphous silica into sodium chloride solutions : Effects of temperature and ionic strength, Geochemica Cosmochem. Acta. 64 (2000) 4193–4203.
[142] M. Klause, U. Rothhaar, M. Bicker, W. Ohling, Dissolution of thin SiO2-coatings – Characterization and evaluation, J. Non. Cryst. Solids. 356 (2010) 141–146.
[143] K.G. Knauss, T.J. Wolery, The dissolution kinetics of quartz as a function of pH and time at 70 ° C, Geoch. 52 (1988) 43–53.
[144] S.-K. Kang, S.-W. Hwang, H. Cheng, S. Yu, B.H. Kim, J.-H. Kim, Y. Huang, J.A. Rogers, Dissolution Behaviors and Applications of Silicon Oxides and Nitrides in Transient Electronics, Adv. Funct. Mater. 24 (2014) 4427–4434.
[145] C.L. Frye, W.T. Collins, The Oligomeric Silsesquioxanes, (HSiO3/2)n, J. Am. Chem. Soc. 92 (1970) 5586–5588.
[146] H. Liou, J. Pretzer, Effect of curing temperature on the mechanical properties of hydrogen silsesquioxane thin films, Thin Solid Films. 335 (1998) 186–191.
[147] M.J. Loboda, C.M. Grove, R.F. Schneider, Properties of a-SiOx:H Thin Films Deposited form Hydrogen Silsesquioxane Resins, J. Electrochem. Soc. 145 (1998) 2861–2866.
[148] Y.K. Siew, G. Sarkar, X. Hu, J. Hui, A. See, C.T. Chua, Thermal Curing of Hydrogen Silsesquioxane, J. Electrochem. Soc. 147 (2000) 335.
[149] D. Lauvernier, S. Garidel, C. Legrand, J.-P. Vilcot, Realization of sub-micron patterns on GaAs using a HSQ etching mask, Microelectron. Eng. 77 (2005) 210–216.
[150] D.-H. Kim, S.-K. Kang, G.-Y. Yeom, J.-H. Jang, Nanometer-Scale Fabrication of Hydrogen Silsesquioxane (HSQ) Films with Post Exposure Baking, J. Nanosci. Nanotechnol. 13 (2013) 1918–1922.
[151] D. Többen, P. Weigand, M.J. Shapiro, S.A. Cohen, Influence of the cure process on the properties of hydrogen silsesquioxane spin-on-glass, Mater. Res. Soc. Somposium Proc. 443 (1997) 195–200.
[152] PubChem, Information, National Center for Biotechnology, (2017). http://pubchem.ncbi.nlm.nih.gov/ (accessed 01.03.2017).
[153] Dow Corning, GPS SAFETY REPORT Octamethyltrisiloxane, (2015). https://www.dowcorning.com/content/about/aboutehs/EHSPortalFiles/GPS_Safety_Report_107-51-7.pdf (accessed November 4, 2015).
[154] A.G. Caster, S. Kowarik, A.M. Schwartzberg, O. Nicolet, S.-H. Lim, S.R. Leone, Observing hydrogen silsesquioxane cross-linking with broadband CARS, J. Raman Spectrosc. 40 (2009) 770–774.
[155] M.G. Albrecht, C. Blanchette, Materials Issues with Thin Film Hydrogen Silsesquioxane Low K Dielectrics, J. Electrochem. Soc. 145 (1998) 4019–4025.
[156] V. Belot, R.J.P. Corriu, D. Leclercq, P.H. Mutin, A. Vioux, Redistribution reactions in silsesquioxane gels, J. Mater. Sci. Lett. 9 (1990) 1052–1054.
[157] H. Lee, E.K. Lin, H. Wang, W. Wu, W. Chen, E.S. Moyer, Structural Comparison of Hydrogen Silsesquioxane Based Porous Low- k Thin Films Prepared with Varying Process Conditions, Chem. Mater. 14 (2002) 1845–1852.
[158] Y.Y. Cheng, C.J. Chang, C.C. Chang, K.M. Peng, C.A. Dai, Preparation and Characterization of Porous Hydrogen Silsesquioxane by Sol-gel Process, Solid State Phenom. 111 (2006) 115–118.
[159] H. Lee, E.K. Lin, H. Wang, W. Wu, W. Chen, T.A. Deis, Correlations between Structural Characteristics and Process Conditions of HSQ Based Porous Low-k Thin Films, Mater.

Res. Soc. Somposium Proc. 714 (2001) L7.11.1-L7.11.7.
[160] H.-J. Lee, Structural characterization of porous low-k thin films prepared by different techniques using X-ray porosimetry, J. Appl. Phys. 95 (2004) 2355.
[161] J.N. Bremmer, Y. Liu, K.G. Gruszynski, F.C. Dall, Cure of Hydrogen Silsesquioxane for Intermetal Dielectric Applications, Mater. Res. Soc. Symp. Proc. 476 (1997) 37–44.
[162] T. Nakamura, M. Sasaki, A. Kobayashi, K. Sawa, K. Mine, Oxidative Curing of Hydrogen Silsesquioxane Resin Films by Electron Beam Irradiation without Additional Heatings and Characterization of the Cured Films, Jpn. J. Appl. Phys. 40 (2001) 6187–6191.
[163] H.J. Lee, E.K. Lin, W.L. Wu, B.M. Fanconi, J.K. Lan, Y.L. Cheng, H.C. Liou, Y.L. Wang, M.S. Feng, C.G. Chao, Investigation of N2 Plasma Effects on the Density Profile of Hydrogen Silsesquioxane Thin Films, MRS Proc. 714 (2011) L7.10.1.
[164] C.J. Brinker, G.W. Scherer, 2.4.3. IR-Raman investigations of gel dehydroxylation, in: Sol Gel Sci. Phys. Chem. Sol-Gel Process., 1990: pp. 582–588.
[165] P. Innocenzi, Infrared spectroscopy of sol-gel derived silica-based films: A spectra-microstructure overview, J. Non. Cryst. Solids. 316 (2003) 309–319.
[166] W.A. Pliskin, Comparison of properties of dielectric films deposited by various methods, J. Vac. Sci. Technol. 14 (1977) 1064.
[167] W.-C. Liu, C.-C. Yang, W.-C. Chen, B.-T. Dai, M.-S. Tsai, The structural transformation and properties of spin-on poly(silsesquioxane) films by thermal curing, J. Non. Cryst. Solids. 311 (2002) 233–240.
[168] I.P. Lisovskii, V.G. Litovchenko, V.G. Lozinskii, G.I. Steblovskii, IR spectroscopic investigation of SiO2 film structure, Thin Solid Films. 213 (1992) 164–169.
[169] V. Belot, R.J.P. Corriu, D. Leclercq, P.H. Mutin, A. Vioux, Thermal Redistribution Reactions in Crosslinked Polysiloxanes, J. Polym. Sci. Part A Polym. Chem. 30 (1992) 613–623.
[170] C.-C. Yang, W.-C. Chen, The structures and properties of hydrogen silsesquioxane (HSQ) films produced by thermal curing, J. Mater. Chem. 12 (2002) 1138–1141.
[171] V. Belot, R. Corriu, D. Leclercq, P.H. Mutin, A. Vioux, Thermal reactivity of hydrogenosilsesquioxane gels, Chem. Mater. 3 (1991) 127–131.
[172] B.K. Hwang, J.H. Choi, H.J. Lee, J.S. Goo, U.-I. Chung, Y. Lee, Moon, Simple and Low Thermal Budget Planarization Process for Premetal Dielectric Based Spin-on Hydrogen Silsesquioxane (HSQ), in: VLSI Multilevel Interconnect. Conf., Santa Clara, CA, USA, 1996: pp. 623–625.
[173] Y. Toivola, J. Thurn, R.F. Cook, Structural, Electrical, and Mechanical Properties Development during Curing of Low-k Hydrogen Silsesquioxane Films, J. Electrochem. Soc. 149 (2002) F9–F17.
[174] S.A. Wheelock, J.N. Bremmer, D.S. Schwab, L. Moore, K. Kozel, G. Bujouves, J. Lommel, D. Rast, Spin-On Inter-Metal Dielectric Materials: Hydrogensilsesquioxane versus Methylsiloxane, Semicon China. (2003).
[175] J.N. Bremmer, K. Chung, C.K. Saha, M.J. Spaulding, EP 0 833 165 A2 - Method for producing thick crack-free coatings from hydrogen silsesquioxane resin, 1998.
[176] C.M. Hessel, E.J. Henderson, J.G.C. Veinot, An Investigation of the Formation and Growth of Oxide-Embedded Silicon Nanocrystals in Hydrogen Silsesquioxane-Derived Nanocomposites, J. Phys. Chem. C. 111 (2007) 6956–6961.
[177] C.M. Hessel, E.J. Henderson, J.G.C. Veinot, Hydrogen Silsesquioxane: A Molecular Precursor for Nanocrystalline Si-SiO2 Composites and Freestanding Hydride-Surface-Terminated Silicon Nanoparticles, Chem. Mater. 18 (2006) 6139–6146.
[178] M.J. Loboda, G.A. Toskey, Understanding hydrogen silsesquioxane-based dielectric film processing, Solid State Technol. (1998).
[179] T.E. Gentle, Oxidation of Hydrogen Silsesquioxane, (HSiO3/2)n, by Rapid Thermal Processing, in: SPIE Vol. 1595 Rapid Therm. Integr. Process., 1991: pp. 146–164.
[180] H. Namatsu, Y. Takahashi, K. Yamazaki, T. Yamaguchi, M. Nagase, K. Kurihara, Three-dimensional siloxane resist for the formation of nanopatterns with minimum linewidth fluctuations, J. Vac. Sci. Technol. B. 16 (1998) 69.

[181] D.L. Olynick, B. Cord, A. Schipotinin, D.F. Ogletree, P.J. Schuck, Electron-beam exposure mechanisms in hydrogen silsesquioxane investigated by vibrational spectroscopy and in situ electron-beam-induced desorption, J. Vac. Sci. Technol. B Microelectron. Nanom. Struct. 28 (2010) 581–587.
[182] S. Choi, M.J. Word, V. Kumar, I. Adesida, Comparative study of thermally cured and electron-beam-exposed hydrogen silsesquioxane resists, J. Vac. Sci. Technol. B. 26 (2008) 1654–1659.
[183] H.-J. Lee, J. Goo, S.-H. Kin, J.-G. Hong, H.-D. Lee, H.-K. Kang, S.-I. Lee, M.Y. Lee, A New, Low-Thermal-Budget Planarization Scheme for Pre-Metal Dielectric Using Electron- Beam Cured Hydrogen Silsesquioxane in Device, Jpn. J. Appl. Phys. 39 (2000) 3924–3929.
[184] M. Peuker, M.H. Lim, H.I. Smith, R. Morton, A.K. van Langen-Suurling, J. Romijn, E.W.J.M. van der Drift, F.C.M.J.M. van Delft, Hydrogen SilsesQuioxane, a high-resolution negative tone e-beam resist, investigated for its applicability in photon-based lithographies, Microelectron. Eng. 61–62 (2002) 803–809.
[185] S. Gorelick, F. Zhang, J.A. van Kan, H.J. Whitlow, F. Watt, Adhesion of proton beam written high aspect ratio hydrogen silsesquioxane (HSQ) nanostructures on different metallic substrates, Nucl. Instruments Methods Phys. Res. Sect. B Beam Interact. with Mater. Atoms. 267 (2009) 3314–3318.
[186] S. Gorelick, F. Zhang, P.G. Shao, J. a. van Kan, H.J. Whitlow, F. Watt, Proton beam written hydrogen silsesquioxane (HSQ) nanostructures for Nickel electroplating, Nucl. Instruments Methods Phys. Res. Sect. B Beam Interact. with Mater. Atoms. 267 (2009) 2309–2311.
[187] Q. Yuan, G. Yin, Z. Ning, Effect of Oxygen Plasma on Low Dielectric Constant HSQ (Hydrogensilsesquioxane) Films, Plasma Sci. Technol. 15 (2013) 86–88.
[188] J. Penaud, F. Fruleux, E. Dubois, Transformation of hydrogen silsesquioxane properties with RIE plasma treatment for advanced multiple-gate MOSFETs, Appl. Surf. Sci. 253 (2006) 395–399.
[189] T.A. Deis, C. Saha, E. Moyer, K. Chung, Y. Liu, M. Spaulding, J. Albaugh, W. Chen, J. Bremmer, Ultra Low-K Inorganic Silsesquioxane Films with Tunable Electrical and Mechanical Properties, Mater. Res. Soc. Somposium Proc. 612 (2000) D5.18.1-D5.18.6.
[190] T.P. Weihs, S. Hong, J.C. Bravman, W.D. Nix, Mechanical deflection of cantilever microbeams : A new technique for testing the mechanical properties of thin films, J. Mater. Res. 3 (1988) 931–942.
[191] M. Lanniel, B. Lu, Y. Chen, S. Allen, L. Buttery, P. Williams, E. Huq, M. Alexander, Patterning the mechanical properties of hydrogen silsesquioxane films using electron beam irradiation for application in mechano cell guidance., Thin Solid Films. 519 (2011) 2003–2010.
[192] R.F. Cook, E.G. Liniger, Stress-Corrosion Cracking of Low-Dielectric-Constant Spin-On-Glass Thin Films, J. Electrochem. Soc. 146 (1999) 4439–4448.
[193] E.P. Guyer, R.H. Dauskardt, Fracture of nanoporous thin-film glasses., Nat. Mater. 3 (2004) 53–7.
[194] P. Kohl, Low-dielectric constant insulators for future integrated circuits and packages, Annu. Rev. Chem. Biomol. Eng. 2 (2011) 379–401.
[195] I.H. Malitson, Interspecimen Comparison of the Refractive Index of Fused Silica, Interspecimen Comp. Refract. Index Fused Silica. 55 (1965) 1205–1209.
[196] S.K. Choi, Nanolitography and Nanofabrication using Hydrogen Silsesquioxane Resists (Dissertation), University of Illinois, 2009.
[197] H.-S. Lee, J.-S. Wi, S.-W. Nam, H.-M. Kim, K.-B. Kim, Two-step resist-development process of hydrogen silsesquioxane for high-density electron-beam nanopatterning, J. Vac. Sci. Technol. B Microelectron. Nanom. Struct. 27 (2009) 188.
[198] M.J. Word, I. Adesida, P.R. Berger, Nanometer-period gratings in hydrogen silsesquioxane fabricated by electron beam lithography, J. Vac. Sci. Technol. B Microelectron. Nanom. Struct. 21 (2003) L12.

[199] J. Kim, W. Chao, B. Griedel, X. Liang, M. Lewis, D. Hilken, D. Olynick, Understanding the base development mechanism of hydrogen silsesquioxane, J. Vac. Sci. Technol. B Microelectron. Nanom. Struct. 27 (2009) 2628.
[200] J. Katherine, S. Strobel, J.K.W. Yang, In situ study of hydrogen silsesquioxane dissolution rate in salty and electrochemical developers, J. Vac. Sci. Technol. B Microelectron. Nanom. Struct. 29 (2016) 06FJ01.
[201] Z. Zhang, H. Duan, Y. Wu, W. Zhou, C. Liu, Y. Tang, H. Li, Improving the adhesion of hydrogen silsesquioxane (HSQ) onto various substrates for electron-beam lithography by surface chemical modification, Microelectron. Eng. 128 (2014) 59–65.
[202] J.-H. Lee, I. Bargatin, J. Park, K.M. Milaninia, L.S. Theogarajan, R. Sinclair, R.T. Howe, Smart-cut layer transfer of single-crystal SiC using spin-on-glass, J. Vac. Sci. Technol. B Microelectron. Nanom. Struct. 30 (2012) 42001.
[203] J.W. Chung, E.L. Piner, T. Palacios, N-Face GaN / AlGaN HEMTs Fabricated Through Layer Transfer Technology, IEEE Electron Device Lett. 30 (2009) 113–116.
[204] J.W. Chung, J. Lee, E.L. Piner, T. Palacios, Seamless On-Wafer Integration of Si (100) MOSFETs and GaN HEMTs, IEEE Electron Device Lett. 30 (2009) 1015–1017.
[205] H. Pranov, Spin-on-glass assisted polishing of rough substrates, WO 2013/083129 A1, 2013.
[206] H. Pranov, Reactive Silicon Oxide Precursor Facilitated Anti-Corrosion Treatment, US 2014/0154441 A1, USA, 2014.
[207] K. Mohaghegh, H.N. Hansen, H. Pranov, G. Kofod, A study on the surface roughness of a thin HSQ coating on a fine milled surface, in: 14th Euspen Int. Conf. - Dubrovink, 2014.
[208] K. Mohaghegh, H.N. Hansen, H. Pranov, G. Kofod, Verification of thickness and surface roughness of a thin film transparent coating, in: Proc. 13th Euspen Int. Conf., Berlin, 2013.
[209] J. Cech, H. Pranov, G. Kofod, M. Matschuk, S. Murthy, R. Taboryski, Surface roughness reduction using spray-coated hydrogen silsesquioxane reflow, Appl. Surf. Sci. 280 (2013) 424–430.
[210] T.C. Hobæk, M. Matschuk, J. Kafka, H.J. Pranov, N.B. Larsen, Hydrogen silsesquioxane mold coatings for improved replication of nanopatterns by injection molding, J. Micromechanics Microengineering. 25 (2015) 035018 (9pp).

3 Materials and methods

The following chapter reviews the materials and experimental methods that have been used within the experimental chapters (5-11) of this dissertation. This chapter is intended as a general overview of the applied methods and further, detailed descriptions of the specific use of the methods can be found in the respective experimental chapters.

3.1 Materials and coating technology

3.1.1 HSQ precursor solution

All films were deposited from "Dow Corning FOx (R) 25" flowable oxide [1], containing 22-23 wt.% of HSQ ("solid content") in a blend of a siloxane-based solvent with 50-70 wt.% octamethyltrisiloxane, 20-30 wt.% hexamehtyldisiloxane and a minor quantity of toluene (1-5 wt.%).

3.1.2 Si-wafer substrate

For infrared spectroscopy, ellipsometry, nanoindentation and the determination of the coating dissolution rate, HSQ-based thin films were deposited on Si-wafer. The used wafers were single crystalline Topsil FZ silicon wafers with 150 mm diameter, 675 µm thickness and polished/etched front-/backside, respectively. For dip-coating, the wafers were diced into 30 mm wide strips on a wafer dicing saw. Prior to coating deposition, the wafers were ultrasonically cleaned in ethanol, cleaned in acetone and dried.

In exceptional cases, different wafers were used (*e.g.* growth of a thermal oxide). The used wafer formats are specified in the respective chapters.

3.1.3 Stainless steel substrate

Metallic substrates were generally type 316L stainless steel with the nominal standard composition shown in Table 3.1. The material was chosen in its low C variant to avoid substrate sensitization due to intergranular carbide precipitation [2]. Since different batches were used in the course of the experiments, the exact substrate compositions are documented in the experimental sections of the respective experimental chapters. (The substrates used in chapter 5 were from the same batch of the substrates used in chapters 8 and 9). The standard test coupons had an area of 100×50 mm^2 and a thickness between 0.5 and 1 mm (specified in the respective experimental sections). The sheet metal was delivered in two different surface conditions, *i.e.* no. 2B finish and BA (bright annealed) finish, as specified by ASTM A480/A480M – 16b [3]. "no. 2B" refers to a smooth, moderately reflective cold rolled annealed and pickled/descaled finish and "BA" to a smooth, bright and reflective finish, produced by cold rolling followed by annealing in a protective atmosphere and a final mild cold rolling. Within the experiments, the appropriate finish was chosen according to the particular experimental requirements on

Table 3.1: *Chemical composition of type 316L steel (according to ASTM A959 – 16 [4]).*

Element	C	Mn	P	S	Si	Cr	Ni	Mo
Composition (wt.%)	≤ 0.030	≤ 2	0.045	0.03	≤ 1	16-18	10-14	2-3

the substrate roughness. Prior to the experimental use (*e.g.* as reference or substrate for coatings), the coupons were degreased in the commercial solution Schlötter Slotoclean AK 90, anodically degreased in the commercial solution Schlötter Slotoclean EL DCG and activated in the commercial solution Schlötter Slotoclean Decasel 5.

In exceptional cases, deviating surface finishes or pretreatment routines were applied. Deviations are specified in the respective experimental chapters.

3.1.4 HSQ-based coatings

Thermal processing

The deposition process of thermally cured, HSQ-based coatings is graphically visualized in Figure 3.1. The HSQ-solution was deposited on the various substrates by dip-coating on a Thorlabs LTS300 linear stage with 300 mm travel range. After dip-coating, the solvent was evaporated at 160 ºC in an open furnace and the specimens were subjected to further heat treatment either in air atmosphere in an open furnace or Formiergas (blend of 10 vol.% H_2 in Ar gas) in a retort furnace. The heat treatment duration was generally kept constant at 2 h.

Electron beam processing

For electron beam curing, films were deposited similar to thermally processed films. After soft-baking, the films were subjected to electron beam curing on a Comet EBLab low energy accelerator in ambient atmosphere. The equipment was operated at 100 kV accelerating voltage and a beam current of 5.281 mA. The irradiation dose of a single irradiation cycle was 38.6 kGy (as determined by a dosimetry measurement) and higher irradiation doses were achieved by multiple irradiation cycles.

3.1.5 Physical vapor deposition (PVD) coatings

PVD coatings were deposited by reactive bipolar sputtering in a Polyteknik Cryofox Discovery 500 magnetron sputter deposition unit, which was fitted with two Testbourne Ltd. Si P-type targets of 99.999% purity with diameter of 76.2 mm and thickness of 6.35 mm. The chamber was fitted with four substrates and rotated at three revolutions/minute. Prior to deposition, the substrates were pretreated in analogy to SOG deposition and plasma etched for 9 min at 400 mA plasma current under flow of 20 cm^3/min Ar and 20 cm^3/min O_2 at a pressure of 8 x 10^{-2} mbar. Subsequently, the chamber pressure was

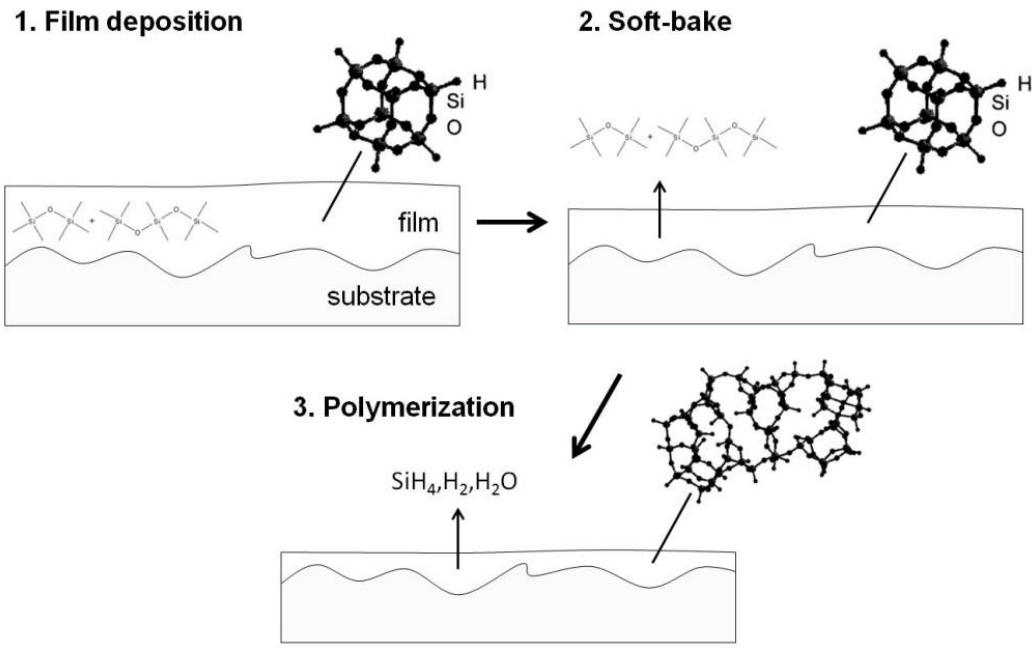

Figure 3.1: *Schematic illustration of HSQ-film deposition. Illustrations of the HSQ-molecules from Bremmer et al. [5].*

reduced to 2 x 10^{-5} mbar base pressure. The deposition was carried out under flow of 30 vol.% O_2 dosed into Ar working gas at a process pressure of 7 x 10^{-3} mbar yielding a deposition rate of ~3 Å/s.

3.2 Microstructural and chemical characterization

3.2.1 Light optical microscopy (LOM)

LOM was used to acquire top view images of surfaces under low magnification. Due to the inherently low thickness of the coatings, an investigation of coating cross-sections by LOM was not possible.

3.2.2 Spectroscopic ellipsometry

Film thickness was measured on a VASE ellipsometer on coated Si wafers. The measured positions were chosen in center of the wafers and 15 mm from the drop-off edge of the wafer. All spectra were acquired at angles of 50, 55 and 60 º for acquisition times of 3 s and the measured dispersions were analyzed with a Cauchy-model on a Si-substrate. The acquisition on metallic substrates was not possible due to roughness of the substrates and formation of interfacial films that had too high uncertainties to be modelled with the known dispersion models.

3.2.3 Fourier transform infrared spectroscopy (FT-IR)

Conclusions on the chemical composition of the coatings were drawn based on FT-IR analysis. FT-IR spectra were acquired on a ThermoScientific Nicolet iN10 MX in both transmittance mode on films deposited on Si-wafers (chapters 5, 7 and 9) and by attenuated total reflectance (ATR) on coated steel substrates (chapter 10). The data acquisition was carried out in ambient air and without further subtraction of atmospheric artefacts. For background subtraction during transmittance measurements, background spectra were determined on a clean reference Si-wafer and digitally subtracted. In chapter 11 it was deviated from this background subtraction routine. Here, the infrared (IR) spectrum was acquired on an air-background and the typical curved background of the Si substrate was digitally subtracted. Peaks were analyzed according to the data available in the literature (summarized in chapter 7) and quantitative peak analysis was carried out by numerical integration of the relevant IR-absorption feature on a linear background with the commercial software OriginLab OriginPro 9.0.

3.2.4 Water contact angle measurements

The water contact angle was measured on two different contact angle meters. Initially, the water contact angle was measured on a Ramé-hart instrument co. contact angle meter, which required a manual placement of the droplet from a pipette. Subsequent measurements were conducted on an Attension Theta contact angle meter, which was fitted with an automated pipette. All contact angle measurements were conducted with a 10 µl droplet of MilliQ water by the sessile droplet method.

3.2.5 Atomic force microscopy (AFM)

AFM was performed on a Bruker dimension edge AFM in tapping mode. The microscope was fitted with a Bruker model RTESP probe with a Sn doped Si cantilever with ~300 kHz resonance frequency. Data analysis was carried out with the commercial software Bruker NanoScope Analysis v. 1.5.

3.2.6 Adhesion testing

Coating adhesion was assessed both by cross cut testing and scratch testing. Cross cut testing [6] was performed with a single-bladed cutting tool and a cross cut pattern with six parallel cuts of 1 mm distance and manual tape lift-off at ~60 º angle. Scratch testing was performed on a ST Instruments Micro Scratch Tester on a STeP 4 Platform. The scratch was performed with a stylus with Rockwell-C indenter diamond tip with 100 µm tip radius. Within the experiments, the profiler load was linearly increased from 10 mN to 500 mN at 8 mm/min scratch speed on a 2 mm scratch track.

3.2.7 Nanoindentation

Nanoindentation was performed on a CSM instruments NHT^2 nanoindentation tester fitted with a diamond Berkovich-shape indenter tip on films deposited on Si wafer. The technique relies on measuring a load vs. indenter displacement curve at a constant loading rate and a maximum indentation load P_{max}, as schematically shown in Figure 3.2. The experimental data were automatically analyzed with the commercial software Anton Paar Indentation 6.1.19, which utilizes the method for load and displacement sensing indentation experiments proposed by Oliver *et al.* [7] and calculates the indentation modulus according to ISO 14577-1 [8]. The indenter area function was calibrated on a fused silica slide and the indentation experiments were conducted with a maximum load (P_{max}) of 0.5 mN at a linear loading/unloading rate of 1 mN/min. To match a minimum ratio between the indenter displacement at peak load h_{max} and the film thickness of 1/10 [8], the film thickness was adjusted for films with different stiffness.

3.2.8 Scanning electron microscopy (SEM)

SEM imaging

SEM imaging was primarily performed on a FEI Helios NanoLAB 600 SEM equipped with a Field Emission Gun (FEG) electron source. Low and medium resolution images were taken with an Everhart-Thornley Secondary Electron Detector (ETD). For high resolution imaging, a Through Lens Detector (TLD) was used. To guarantee charge transfer on the dielectric materials, samples were Au or C sputter coated before SEM investigation. Generally, Au was used as a conductive coating for samples which were further processed by focused ion beam (FIB) milling. Due to fracture of the conductive

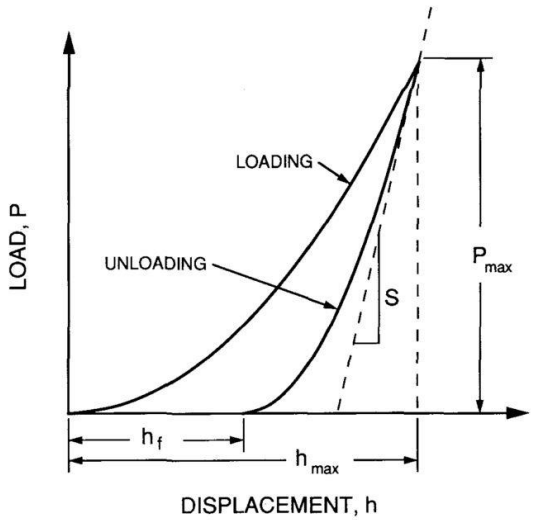

Figure 3.2: *A schematic representation of load versus indenter displacement data for an indentation experiment. The quantities shown are: P_{max}, the peak indentation load; h_{max}, the indenter displacement at peak load; h_f, the final depth of the contact impression after unloading and S: the initial unloading stiffness [7].*

film, leading to a characteristic pattern on the surface, Au sputter coatings are, not suitable for high resolution top-view investigations and for this purpose, specimens were prepared with C coating.

In exceptional cases (specified in the respective experimental sections), data were acquired on a JEOL JSM-5900 SEM fitted with a LaB_6 filament electron source and Oxford Instruments EDS detector. For EDS acquisition on stainless steel substrates, the instrument was operated at 20 kV accelerating voltage.

Focused Ion Beam (FIB) milling

The coatings investigated in this study were hard and brittle and artefacts from mechanical preparation (such as cracks) were observed after the metallurgical preparation of cross-sections. Hence, coating cross-sections were solely prepared by FIB cross-sectioning on a FEI Helios NanoLAB 600 SEM. The microscope was fitted with a Ga^+ ion source and a gas injection system for the injection of precursor gas for *e.g.* CVD Pt deposition. The ion source was generally operated with an accelerating voltage of 30 kV for milling. Moreover, to prevent ion beam damage in the vicinity of the site of interest, a double layer (electron beam CVD followed by ion beam CVD) of Pt was deposited prior to milling. A schematic drawing of the FIB-SEM setup is shown in Figure 3.3. For cross-sectioning the sample was tilted to 52 º, yielding a FIB direction perpendicular to the specimen surface. Cross-sectional images were taken under 52 º tilt to the electron beam, leading to a vertical compression of the images.

3.2.9 Transmission electron microscopy (TEM)

For TEM imaging, different microscopes were used, depending on the resolution and analytical techniques that were applied.

TEM specimen preparation

All TEM specimens were prepared by in-situ lift out on a FEI Helios NanoLab 600 dual beam SEM fitted with a Ga^+ ion beam source and an Oxford Instruments OmniProbe micromanipulator. The rough sample geometry was cut by ion beam milling at 30 kV FIB

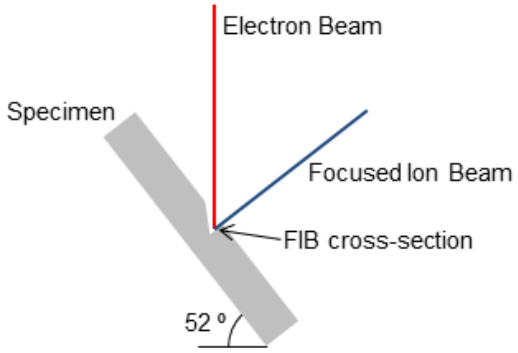

Figure 3.3: *Schematic drawing of FIB cross-sectioning.*

accelerating voltage and the lamella was lifted out with the micromanipulator. Subsequently, the lamella was deposited on a Cu TEM-grid and thinned by ion beam milling (30 kV accelerating voltage) to electron transparency (~100 nm thickness). In a final cleaning step, the ion source was set to 2 kV accelerating voltage and amorphization was removed by milling in an oblique angle. For high resolution electron energy loss spectroscopy (EELS) analysis (chapter 8) the lamella was further thinned by Ar^+ etching on a Fischione NanoMill precision Ar-ion mill.

Tecnai T20 G2

Intermediate resolution bright field imaging was carried out on a FEI Tecnai T20 G2 TEM fitted with a LaB_6 filament electron source, which was operated at 200 kV accelerating voltage.

Jeol 3000F

Intermediate resolution bright field imaging combined with Energy Filtered TEM (EFTEM) and Energy Dispersive Spectroscopy (EDS) was carried out on a Jeol 3000F fitted with a FEG electron source operated at 300 kV accelerating voltage, an Oxford Instruments EDS detector and a Gatan Image Filter (GIF). EFTEM imaging requires a background subtraction which is commonly carried out by the three window or the jump-ratio method [9]. Due to the complex alloy, and hence the superposition of energy loss peaks from the various elements with the background, background subtraction with the three window method was not possible and the background subtraction was generally carried out by the jump ratio method. The analysis of Mo was not possible, since the $L_{2,3}$ major edges lay outside the energy range of the image filter. Further, the analysis of Ni was omitted due to artefacts induced by the overlap from the Fe L_1 and Ni $L_{2,3}$ edges.

FEI Titan Analytical 80-300ST

Scanning TEM (STEM) analysis, high angle dark field (HADF) and high resolution TEM (HRTEM) imaging as well as EELS were performed on a FEI Titan Analytical 80-300ST instrument which was fitted with a monochromated FEG electron source and a Gatan 865 Tridem GIF. The instrument was operated at 300 kV accelerating for HRTEM imaging and at 120 kV accelerating voltage in STEM mode and during EELS acquisition.

3.2.10 X-ray photoelectron spectroscopy (XPS)

XPS analysis was performed on a ThermoScientific K-alpha instrument under 10^{-7}-10^{-8} mbar pressure with an Al Kα (1486.7 eV photon energy) X-ray source on an area with a diameter of 400 µm. Binding energies in high resolution spectra were acquired with 50 eV pass energy at an energy step size of 0.1 eV under use of a flood gun to compensate for surface charging. For depth profiling, material was removed by Ar^+ etching with 2 kV accelerating voltage. High resolution spectra were deconvoluted with the commercial

peak fitting software ThermoScientific Avantage V. 5.949 using a pseudo Voigt–type peak function on a Shirley-type background. The asymmetries of the metallic peaks were determined by the method suggested by Fredriksson *et al.* [10], *i.e.* Ar^+ etching to the subsurface region (showing only metallic peaks) and subsequent determination of the peak shape of the asymmetric metallic peaks. Chemical compositions were determined by analysis of the normalized peak areas with the sensitivity factors reported by Scofield [11].

To enable the acquisition of sharp interfaces during depth profiling, the substrate roughness was decreased from the as-received 2B-finish to a mechanically ground, mirror-like finish. For this, the surface was successively ground and polished on emery paper and diamond paste to a 1 µm diamond paste polished finish before the coating deposition.

3.3 Electrochemical studies / corrosion tests

3.3.1 Anodic linear cyclic polarization (CP)

CP measurements were performed on an ACM Instruments GillAC potentiostat with the sweep rates and stabilization times indicated in the respective experimental chapters. The tests were generally conducted in 3.5 wt.% NaCl aqueous solution. Since the breakdown potential of the bright annealed substrates was strongly increased, the test solution for the bright annealed samples was adjusted to *p*H 2.5 by dropwise addition of H_2SO_4 (Sigma Aldrich, 97% purity). For measurements in acidified solutions, the solutions were deaerated with N_2 before and throughout the experiments. Due to the severe impact of chloride-induced crevice corrosion between gasket and substrate, leading to significant uncertainties in the breakdown potential, the measurements were conducted in a flat cell with the cell-design from Qvarfort [12] (schematically shown in Figure 3.4). Throughout the measurement, the buildup of an aggressive crevice solution was prevented by a continuous dilution of the crevice solution with deionized water. As stated by Qvarfort [12], due to the lower density of the distilled water with respect to a saline solution, the deionized water immediately flows upwards after leaving the crevice, preventing a significant dilution of the electrolyte at the sample surface. In this work, a corrosion cell with a solution volume of 400 ml, exposed sample area of 1 cm^2, and Pt-rod auxiliary electrode was used. The potential was measured vs. a KCl saturated Ag-AgCl reference electrode. The cell was operated with a water-inflow of 7.4 ml/h and without compensation for bulk solution salinity. Consequently, the bulk solution was diluted throughout the experiment, limiting measurements in the given setup to short experiments under the assumption of constant salinity.

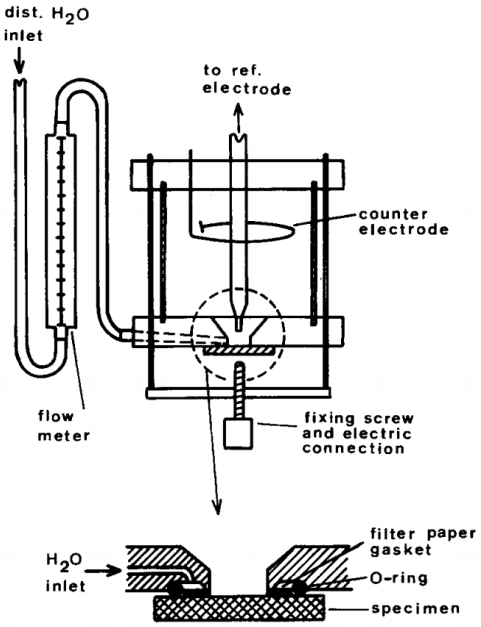

Figure 3.4: *Schematic illustration of the corrosion cell design from Qvarfort [12].*

3.3.2 Electrochemical impedance spectroscopy (EIS)

EIS data acquisition was carried out with Gamry Ref 600 potentiostat and a flat corrosion cell with the design shown in Figure 3.5. Since all measurements were conducted at the open circuit potential (OCP), *i.e.* far below the breakdown potential in this cell geometry, the preferential initiation of crevice corrosion at the O-ring gasket was not observed. The solution container had a solution volume of 15 ml and an exposed sample surface area of 2.1 cm^2. During data acquisition, the entire corrosion cell was shielded from external electromagnetic fields by a fully closed Faraday cage while the system was operated with fully shielded leashes. The potential was measured against a Saturated Calomel Electrode (SCE) and the system was excited by a Pt-wire auxiliary electrode with a sinusoidal excitation signal of 10 mV amplitude after a sufficiently long cell settle-time to guarantee pseudo-linearity of the system [13]. Analysis and quantification of the experimental data was conducted with the commercial software Gamry Echem Analyst V6.31. All reported impedance-datasets were validated by an automatic Kramers Kroning test. The EIS experiments were initially conducted in 0.5 M Na-acetate buffered solution (*p*H 6) to exclude the effects from chloride induced corrosion during the measurement and, after validation of the equivalent circuit model, further experiments were performed in 3.5 wt.% NaCl aqueous solution.

For EIS analysis, the capacitive response was modeled by a constant phase element (CPE) to account for time constant dispersion [14] caused by imperfections such as roughness and local inhomogeneity in the resistive and capacitive behavior of the coatings. Conversion between the CPE parameters, Q_0 and α, was conducted by the relation reported by Hsu *et al.* [15] (eq. (3.1)) with the maximum radial frequency ω_{max}.

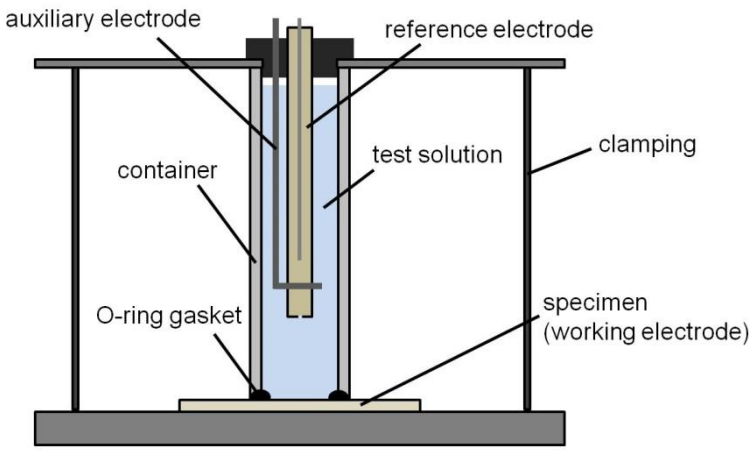

Figure 3.5: *Schematic illustration of the corrosion flat cell used for EIS.*

$$C_{eq} = Q_0(\omega_{max})^{\alpha-1} \tag{3.1}$$

Since ω_{max} is the inverse of the time constant τ, substitution of ω_{max} with eq. (3.2) yields the description of C_{eq} as function of Q_0, α and the resistive pathway in parallel to the CPE, R (eq. (3.3)).

$$\omega_{max} = \frac{1}{\tau} = \frac{1}{RC_{eq}} \tag{3.2}$$

$$C_{eq} = Q_0^{1/\alpha}\left(\frac{1}{R}\right)^{\left(1-\frac{1}{\alpha}\right)} \tag{3.3}$$

3.3.3 Scanning vibrating electrode technique (SVET)

In this work, an Applicable Electronics system, fitted with a Pt/Ir -alloy vibrating probe and Pt/Ir –alloy reference/ground electrodes and an optical microscope with digital CCD, was used. Before data acquisition, all electrodes were plated according to manufacturer specification in 10 vol.% Pt chloride + 1 vol.% lead acetate aqueous solution. The vibrating probe was plated to a final probe diameter of ~30 µm and the probe capacitance was regularly tested and kept above 2 nF. The samples were masked with a varnish and the solution container with a volume of 2 ml was directly glued to the sample. The probe working distance was aligned with the optical focal point of the microscope and set to an average probe distance of 100 µm from the sample surface. Since the signal quality depends on the solution conductivity, data acquisition in 3.5 wt.% NaCl aqueous solution was not possible. On the contrary, measuring in more diluted NaCl aqueous solution did not lead to detectable initiation of localized corrosion and 1 wt.% $FeCl_3$*$6H_2O$ aqueous solution was chosen as test-electrolyte to compromise between high corrosivity and moderately low solution conductivity (82.03 Ω*cm, as determined on a Radiometer

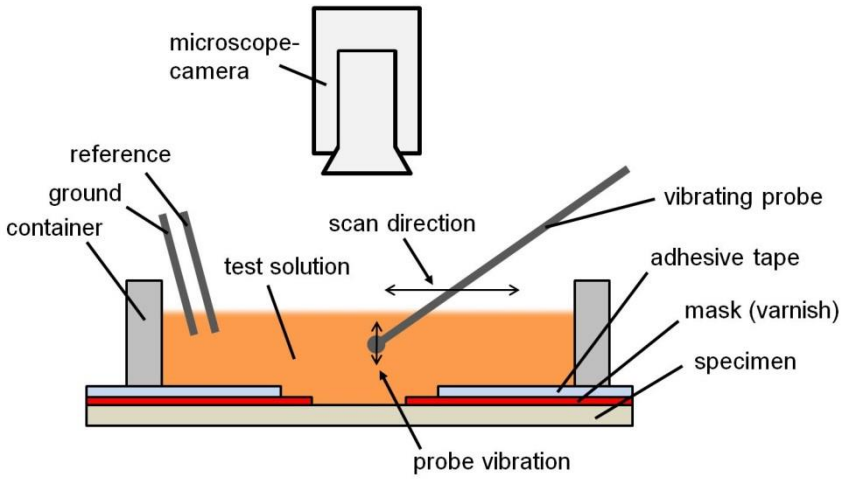

Figure 3.6: *Schematic illustration of the setup used for SVET.*

Copenhagen CDM conductivity meter). A schematic cross-sectional view of the SVET setup used in this work is shown in Figure 3.6.

3.3.4 Spot testing

Spot testing was performed with a solution of 5 g/l $K_3Fe(CN)_6$ in 3.5wt.% NaCl aqueous solution. During the experiment, the solution was deposited on the surface with a pipette and soaked for 5 min. Subsequently the liquid was removed with a pipette and the surface was allowed to dry in air before further microscopic investigation.

3.3.5 Neutral salt spray testing

The long-term corrosion performance of various coatings was assessed by neutral salt spray testing according to the standard EN ISO 9227 – "Corrosion tests in artificial atmosphere, Salt spray tests" [16].

References

[1] Dow Corning, Safety Data Sheet Fox(R) 25 Flowable Oxide, 12.04.2016. http://www.dowcorning.com/DataFiles/09027701829d323b.pdf.

[2] P.P. Trazaskoma-Paulette, A. Nazeri, Effects of Sol-Gel Coatings on the Localized Corrosion Behavior of 304 Stainless Steel, J. Electrochem. Soc. 144 (1997) 1307–1310.

[3] ASTM Standard A480/A480M 14b: Standard Specification for General Requirements for Flat-Rolled Stainless and Heat- Resisting Steel Plate, Sheet, and Strip, (2016) 1–26.

[4] Designation: A959-16 Standard Guide for Specifying Harmonized Standard Grade Compositions for Wrought Stainless Steels, 2016.

[5] J.N. Bremmer, Y. Liu, K.G. Gruszynski, F.C. Dall, Cure of Hydrogen Silsesquioxane for Intermetal Dielectric Applications, Mater. Res. Soc. Symp. Proc. 476 (1997) 37–44.

[6] ISO 2409:2007(E) Paints and varnishes - Cross-cut test, 2007.

[7] W.C. Oliver, G.M. Pharr, An improved technique for determining hardness and elastic modulus using load and displacement sensing indentation experiments, J. Mater. Res. 7 (1992) 1564–1583.

[8] E.C. for Standardization, ISO 14577-1:2002 E Metallic materials - Instrumented indentation test for hardness and materials parameters - Part 1: Test method, (2003) 1–25.

[9] D.B. Williams, C.B. Carter, 39.4.B Background Subtraction, in: Transm. Electron Microsc. Part1 Basics, 2009: pp. 726–728.

[10] W. Fredriksson, K. Edström, C.-O.A. Olsson, XPS analysis of manganese in stainless steel passive films on 1.4432 and the lean duplex 1.4162, Corros. Sci. 52 (2010) 2505–2510.

[11] J.H. Scofield, Hartree-Slater Subshell Photoionization Cross-Sections at 1254 and 1487 eV, J. Electron Spectros. Relat. Phenomena. 8 (1976) 129–137.

[12] R. Qvarfort, New Electrochemical Cell for Pitting Corrosion Testing, Corros. Sci. 28 (1988).

[13] M.E. Orazem, B. Tribollet, 8.2.2 Linearity, in: Electrochem. Impedance Spectrosc., John Wiley& Sons, Inc., Hoboken, New Jersey, 2008: p. 134.

[14] M.E. Orazem, B. Tribollet, 13 Time Constant Dispersion, in: Electrochem. Impedance Spectrosc., Hoboken, New Jersey, 2008: pp. 233–263.

[15] C.H. Hsu, F. Mansfeld, Technical Note: Concerning the Conversion of the Constant Phase Element Parameter Y0 into a Capacitance, Corrosion. 57 (2001) 747–748.

[16] EN ISO 9227:2012 Corrosion tests in artificial atmospheres - Salt spray tests, (2012).

4 Summary of the experimental chapters

This section summarized the key-findings presented in the articles/manuscripts which were presented in chapters 5-11.

4.1 Manuscript I

Hydrogen Silsesquioxane based silica glass coatings for the corrosion protection of austenitic stainless steel

In the first article, the basic working principle of HSQ-based spin-on-glass (SOG) is reviewed and the process is introduced as an efficient and cost-effective alternative to the existing processes. The article aims at a conceptual study of SOG-coating deposition on industrially finished (no. 2B) substrates in Formiergas curing environment and an initial characterization of the coating properties together with an interpretation of the coating impedance in aqueous environment. Dip-coating was demonstrated as a viable process to deposit HSQ-based films, whereby the obtained film thickness on smooth substrates correlates, in analogy to films from aqueous sols during sol-gel processing, with the withdrawal rate by a power-law relation. Film deposition and subsequent non-oxidative curing led to the formation of a transparent surface deposit, showing green/blue discoloration due to thin film interference. Investigations of the coatings by SEM revealed that the material penetrates into surface voids and decreases the substrate roughness ("levelling"). Since the coating topography does not follow the substrate topography, the coating thickness appears largely inhomogeneous and may, for coatings deposited with 1 mm/s withdrawal speed, vary between ~200 nm to ~1.4 µm. The coatings appear well adherent after cross-cut testing and show mixed (both adhesive and cohesive) failure in the close vicinity of the cross-cut scribe marks. Chemical analysis by FT-IR demonstrated that the applied curing routine has only led to partial transformation from HSQ to SiO_2, leaving significantly hydrogenated deposits. Impedance spectroscopy in *p*H-buffered solution revealed imperfect blockage of the electrode, indicating ionic pathways through the coating due to *e.g.* coating defects or pores. Based on the observed behavior of SOG coated stainless steel and observations on similar coating systems by other groups, an impedance equivalent circuit was proposed which allows the distinction between coating and substrate impedance.

4.2 Manuscript II

Interfacial interaction of oxidatively cured hydrogen silsesquioxane spin-on-glass enamel with stainless steel substrate

The manuscript focuses on the microscopical interaction of HSQ-based coatings and stainless steel substrates after curing in air. In the study, HSQ-resin is deposited on 316L substrates and thermally cured in air ambient at 450 ºC. The interface region between the

coating and the substrate was investigated by XPS, SEM, and TEM. Additionally the effect of the interfacial interaction was discussed based on an evaluation of the coating adhesion via cross-cut testing.

In contrast to non-oxidative curing, curing in air led to a significant yellow/golden discoloration of the coating/substrate system. Investigation of a coated substrate with (FIB-)SEM identified an interfacial layer between the coating and the substrate. Adhesion testing by cross-cut testing indicated excellent coating adhesion and SEM analysis of the scribe-marks revealed microscopic delamination in their close vicinity. Ion beam cross-sectioning of the delaminated area revealed that the major portion of the film had delaminated by adhesive failure (delamination between the interface film and the substrate); however, the analysis also indicated that delamination may take place as cohesive failure between the interfacial layer and the coating. Consequently, it was concluded that the interface may guide cracks and poses a potential weakness for the coating adhesion/performance.

The nature of the interface layer was further investigated by XPS, which identified oxidized states of Fe and Cr in the interfacial layer. The analysis by XPS depth-profiling indicated a double layered interface with an outer $Fe^{3+/2+}$ and inner $Fe^{3+/2+}/Cr^{3+}$ -rich region. In addition to the metal-ion rich interface, the depth profile showed a distinct depression in Cr content in the surface of the substrate alloy. In agreement with the compositional depth profile, TEM bright field imaging together with EDS spot analysis indicated an outer Fe-enriched region of the interface together with an inner Cr-enriched region. To gain information at higher spatial resolution and to gain further insight into the interface chemistry, the region was investigated by EELS in STEM. The compositional quantification on an EELS line scan across the interface confirmed the presence of a double layered interface with an outer region which only showed Fe signal and an inner interface which showed both Cr and Fe. Analysis of the oxidation states of the most abundant elements indicated the presence of Fe^{3+} in the outer interface together with the simultaneous presence of Fe^{2+} and Cr^{3+} in the inner interface. In addition to Fe and Cr, traces of Mn were detected in the interfacial region. The presence of Si over the entire interface layer was shown by probing the Si $L_{2,3}$ edge and analysis of its ELNES did not indicate chemical bonding between Si and transition metal anions from the substrate. Lastly, the elemental distribution over the interface was visualized by EFTEM, showing the clear presence of O and Si over the entire interface and further, the enrichment of the outer interface in Fe together with the enrichment of the inner interface with Cr and Mn.

Due to the chemical similarity to medium temperature thermal oxides on stainless steels, a mechanism based on substrate oxide growth into coating porosity was proposed. Furthermore, it was pointed out that the formation of a thermal oxide at the interface in combination with the formation of a Cr-depleted zone in the subsurface region may decrease the ability of the alloy to form a stable passivation, and thus may be detrimental for the substrate passivity.

4.3 Manuscript III

Corrosion resistance of AISI 316L coated with an air-cured hydrogen silsesquioxane based spin-on-glass enamel in chloride environment

The article focuses on a holistic study of the corrosion resistance and the potential failure mechanisms of air-cured SOG-coatings on 316L substrates in chloride containing electrolyte. For the study, SOG-films were deposited on no. 2B finished 316L substrates and cured in air at temperatures between 400 and 550 ºC. The coating microstructure and chemistry was studied by (FIB-)SEM and FT-IR and the effect of the coating chemistry on the coating hydrophobicity was analyzed by water contact angle measurements. The electrochemical response of the SOG coated substrates was investigated by EIS, anodic CP measurements and the SVET. Further, the long term performance of the coating was examined by neutral salt spray testing.

Cross-sectional analysis by (FIB-)SEM revealed that curing in air led to the formation of an interface layer, which increases in thickness with increasing curing temperature. Further, the formation of thick interface layers at elevated curing temperatures had led to void formation between the coating and the substrates. FT-IR analysis indicated full polymerization (full loss of hydrogenation) at 550 ºC, together with significant hydroxylation of the coatings. All coatings were hydrophilic; however, the coating cured at 400 ºC was significantly less hydrophilic with respect to the other coatings. This was explained by the lesser extend of hydroxylation and the higher degree of retained hydrogenation.

Anodic CP measurements in neutral 3.5 wt.% NaCl solution clearly indicated full loss in substrate passivity for coatings cured above 450 ºC, while coating systems cured at 450 ºC were compromised in their substrate passivity. The barrier performance, based on the coating's pore resistance in EIS experiments, decreased with increasing curing temperature and it was concluded that the resistance towards ionic transport does not primarily depend on the coating density, but rather on a complex relation between coating density, hydrophobicity and coating adhesion. The corrosion mechanism of a coating system cured at 450 ºC was further investigated by the SVET in 1 wt.% $FeCl_3*6H_2O$ solution, which indicated stable cathodic sites together with transient anodic sites at continuously changing positions. (FIB-)SEM analysis of the electrochemically active sites revealed major coating defects as possible cathodic sites. Anodic sites were found as local corrosion pits which have spread underneath the coating and it was suggested that the coating may act as stable pit cover, thereby enhancing the susceptibility to pitting corrosion.

An accelerated corrosion test by neutral salt spray testing confirmed an increased susceptibility to localized corrosion after curing of the coating at high temperatures. Further, the test indicated chemical instability of the coating material during the accelerated corrosion test: This instability was increased for the coatings cured at the

lowest temperatures and, in agreement with results from previous studies, it was proposed that the coating instability originated from material defects due to imperfect polymerization, molecular porosity or hydroxylation of the material.

4.4 Manuscript IV

Probing the chemistry of adhesion between a 316L substrate and spin-on-glass coating

The manuscript focuses on the interface characterization of Formiergas-cured SOG on 316L substrate after curing at 600 ºC. The interfacial zone was investigated by TEM and EELS analysis and the results were discussed based on a simulation of the thermodynamic oxygen/metal phase equilibrium at the interfacial zone.

The analysis revealed, similar to manuscript II, an interface region between the coating and the substrate; however, the thickness of the layer was only 5-10 nm, *i.e.* strongly decreased with respect to the air-cured system. Elemental analysis revealed that the thin interface layer consisted of Si, O, Cr and Fe. Analysis of the ELNES indicated that Fe was predominantly present in divalent state, while Cr was present in both tri- and divalent states. Analysis of high resolution TEM images of the interface region by fast Fourier transformation (FFT) of the image indicated crystallinity of the interface, and the FFT-pattern was matched with a crystalline olivine-type Fe_2SiO_4 phase. The possible phase formation at the interface was discussed based on the simulated oxygen/metal phase equilibrium in the interface and it was suggested that the interface consisted predominantly of Cr_2O_3 in the immediate vicinity of the substrate surface, followed by an olivine-phase-rich intermediate zone and a spinel-phase-rich outer region of the interface.

4.5 Manuscript V

Properties and performance of spin-on-glass coatings for the corrosion protection of stainless steel

The manuscript focuses on an assessment of the coating properties and performance as barrier coating of HSQ-based SOG-coatings which were cured in Formiergas-atmosphere. SOG-films were deposited on no. 2B finished 316L substrates and cured between 400 and 800 ºC. The coating properties, microstructure and morphology was analyzed by AFM, TEM, FT-IR, XPS, contact angle measurements, depth-sensing nanoindentation and (FIB-)SEM. The coating performance as a corrosion barrier coating was studied by EIS, potentiodynamic cyclic polarization and $K_3Fe(CN)_6$ spot-testing in aqueous NaCl solution. The dissolution kinetics of SOG-films during artificial corrosion testing by salt spray testing were investigated by probing of the residual film thickness during cyclic inspection of the test samples.

The AFM measurements indicated that the coating levelled the no. 2B finished substrate significantly, yielding a reduction in R_a roughness from 38.9 nm to 15.4 nm. Further, the roughness of the coating without substrate influence was investigated and an overall SOG-coating roughness of R_a = 0.19 nm was determined. TEM bright field analysis showed that the formation of a thick interfacial layer was suppressed by curing in Formiergas and FT-IR analysis showed that curing above 800 ºC is necessary to fully remove hydrogenation. Further, hydroxyl formation, presumably due to hydroxylation and water absorption of the hydrophilic and incompletely polymerized coatings, was observed for coatings cured at 600 and 700 ºC. XPS analysis of a SOG-film cured at 800 ºC showed, apart from the Si^{4+} peak expected for SiO_2, a lower binding energy peak, presumably due to the formation of Si nano-domains during film curing. Apart from Si^{4+} and Si^0, the high resolution XP spectrum of the SOG indicated the presence of lower valent Si (*e.g.* Si^{2+}), indicating the presence of Si-suboxides. These observations were in agreement with mechanical testing by depth sensing nanoindentation, which showed an increasing indentation modulus with increasing curing temperatures. Overall, all investigated HSQ-based films exhibited a distinctly more compliant behavior with respect to fused silica. In analogy, the film hardness increased with curing temperature; however, the maximum nanoindentation hardness obtained for the SOG-films was 6.3 GPa, and thus significantly lower with respect to a fused silica reference, where a nanoindentation hardness of 10.8 GPa was measured. The water contact angle was primarily dependent on the amount of residual hydrogenation, showing hydrophobic behavior for films cured at 400-500 ºC and hydrophilic behavior for films cured at 600-800 ºC.

EIS analysis indicated that the barrier performance was mostly unaffected by the curing temperature. The exception was a local minimum in pore resistance for the coating system cured at 700 ºC, presumably due to a disadvantageous combination of low coating hydrophobicity and imperfect polymerization. Anodic CP measurements indicated that the SOG-coatings can significantly increase the breakdown potential in some cases; however, it was observed that coating may induce the adverse effect, *i.e.* a decrease in the breakdown potential. The variations in breakdown potential appeared adventitious and it was hypothesized that the presence of arbitrarily spread coating defects may have caused the fluctuating breakdown potential. The presence of coating defects was investigated by spot testing in NaCl aqueous solution with addition of $K_3Fe(CN)_6$ indicator. The test revealed voids caused by the microscopic delamination of the coating at surface voids (caused by *e.g.* surface roughness), which may have acted as micro-crevices, and thus assisted the initiation of localized corrosion.

In addition to the electrochemical performance of the system, the chemical inertness of the coating material was systematically studied as function of the curing temperature. The results indicated that the chemical stability of SOG during salt spray testing was strongly affected by the curing temperature, whereby increasing the curing temperature led to increasing chemical stability. Even films cured at the maximum temperature (800 ºC) exhibited a dissolution rate of ~0.13 nm/h, indicating significantly decreased chemical

stability of the SOG-coating with respect to thermally grown SiO_2, where dissolution was insignificant within the experimental timeframe. The increased susceptibility to chemical attack of the SOG was explained by the high degree of imperfection of the oxide, allowing for accelerated dissolution.

4.6 Manuscript VI

Corrosion properties of SiO_x-like thin film coatings from spin-on-glass and reactive bipolar PVD on bright annealed stainless steel substrate

The manuscript focuses on potential a solution to the problems associated with surface roughness addressed in manuscript V. The failure mechanism outlaid in manuscript V is prevented by increasing the substrate smoothness and the performance of the coating on bright annealed substrates is tested. In addition to the effect of an improved substrate smoothness, the manuscript assesses the functionality of a PVD-based SiO_2 film to conclude on the general failure mechanisms of stainless steels after coating with an inert film and to benchmark the SOG process to preexisting technologies. For this, SOG-coatings of different thickness were deposited on bright annealed 316L substrates and cured at 800 ºC in Formiergas atmosphere, while PVD coatings of different thickness were deposited by reactive bipolar sputtering of Si targets. The films were investigated by attenuated total reflection (ATR-)FT-IR, (FIB-)SEM, increasing load scratch testing, EIS, linear potentiodynamic anodic polarization measurements and neutral salt spray testing.

Surface analysis indicated good coverage for both processes; however, inhomogeneities in film thickness were present for the PVD coatings, which originated from the PVD chamber geometry. FT-IR indicated a clearly SiO_x-like structure for the PVD coating, while the SOG-coating appeared mildly hydrogenated. Both coatings were found hydroxylated. Scratch testing indicated better adhesion of the SOG-coating with respect to the PVD coating, which, presumably, originated from the chemical interaction, and thus increased bonding between SOG and the substrate (manuscript IV).

EIS analysis showed imperfect barrier behavior for all coatings, *i.e.* two clearly separable capacitive features, irrespective of the coating thickness. Linear potentiodynamic anodic polarization measurements showed that the breakdown potential of SOG coated samples is frequently shifted to more anodic values, however, may also remain in the expected range for uncoated substrates. The breakdown potential for PVD coated samples did never show an anodic shift and fluctuated between the expected range for uncoated substrates and significantly more cathodic values. Failure analysis of the PVD coated sample identified bulging and coating spallation as the primary failure mode and it was suggested that, in analogy to manuscript V, crevice corrosion at the bulged or delaminated coating was responsible for the decrease in breakdown potential. Conversely, it was suggested that the increase in breakdown potential originated from either a chemical conversion of the native passivation throughout processing or the good barrier properties of the coating.

Both coatings were aged by neutral salt spray testing for 1000 h. While the previously described coating dissolution (manuscript V) was the predominant failure observed on the SOG-coatings, the PVD coating suffered from extensive failure due to coating spallation. Further, dissolution of the PVD coating at ~0.05 nm/h was observed. Despite the material deterioration after ageing, the coated samples retained their characteristic breakdown behavior, *i.e.* an anodic shift in breakdown potential for the SOG coated samples together with a cathodic shift of the PVD coated samples. Failure analysis of aged and polarized PVD samples showed that pitting failure occurred site specific along the coating spallation. It was shown that pitting corrosion evolves at the brink of the observed coating spallation and grows underneath the coating, indicating that inert deposits on stainless steel may act as stable pit cover and thereby increase failure by pitting corrosion.

4.7 Technical note I

Low temperature curing of hydrogen silsesquioxane films by electron beam curing

The technical note focuses on the effect and achievable degree of polymerization by electron beam curing. It was shown that electron beam curing up to 12 MGy irradiation dose leads to inferior polymerization to thermal curing at 450 ºC in air (2 h). Due to the inferior cross-linking, electron beam curing in the applied irradiation dose was found inadequate to guarantee sufficient chemical stability of the coatings.

5 Manuscript I

Hydrogen Silsesquioxane based silica glass coatings for the corrosion protection of austenitic stainless steel*

Felix Lampert[a], Annemette Hindhede Jensen[b], Rameez Ud Din[a], Per Møller[a]

[a] Technical University of Denmark, Department of Mechanical Engineering, 2800 Kgs. Lyngby, Denmark

[b] SiOx ApS, Bybjergvej 7, 3600 Espergærde, Denmark

Abstract

The application of stainless steels in hostile environments, such as concentrated acid or hot sea water, requires additional surface treatments, considering that the native surface oxide does not guarantee sufficient corrosion protection under these conditions. In the present work, silica-like thin-film barrier coatings were deposited on AISI 316L grade austenitic stainless steel with 2B surface finish from Hydrogen Silsesquioxane (HSQ) spin-on-glass precursor and thermally cured to tailor the film properties. Results showed that curing at 500 ˚C resulted in a film-structure with a polymerized siloxane backbone and a reduced amount of Si-H moieties. The coatings showed good substrate coverage and the average thickness was between 200 and 400 nm on the rough substrate surface, however, film thicknesses of more than 1400 nm were observed at substrate defects. Deposition of these films significantly improved the barrier properties by showing a 1000 times higher modulus while an ionic transport over the coating was also observed.

* published work: F. Lampert, A.H. Jensen, R.U. Din, P. Møller, Surface & Coatings Technology 307 (2016) 879-885. The format of the article has been edited to match the dissertation.

5.1 Introduction

Stainless steels owe their resistivity against galvanic corrosion to a high Cr content, which triggers the formation of a thin, Cr-rich surface-oxide with a low ionic conductivity and solubility, that protects the underlying material from chemical attack in neutral and alkaline environments [1]. However, the native oxide becomes unstable at low *p*H (*p*H below approx. 4) [2] and consequently corrosion of stainless steels can be initiated under acidic conditions. Apart from uniform breakdown of the native oxide film, stainless steels are susceptible to localized corrosion in form of pitting and crevice corrosion in chloride containing electrolytes such as sea water [3,4], and therefore the application of stainless steels in acidic or chloride containing environments may require further protection of the material.

Vitreous enamel coatings find wide industrial application as barrier coatings to increase the corrosion resistance of materials [5–7]. Traditionally, porcelain or glass coatings are applied from powdered precursors and fired at elevated temperatures, thereby fusing the solid particles and forming an envelope-type coating which acts as a corrosion barrier between substrate and corrosive medium. However, this technology is limited to rather thick, brittle coatings, which alter the optical appearance and geometry of the substrate and are prone to brittle fracture. In this regard, thin coating systems can potentially overcome the drawbacks of traditional enamels, while retaining their protective properties. It has been reported in literature [8–14], that SiO_2 thin film coatings can substantially increase the aqueous as well as high temperature corrosion resistance of stainless steel substrates and high quality SiO_2 thin films have been successfully deposited on stainless steel substrates by Physical Vapor Deposition (PVD) [15], Chemical Vapor Deposition (CVD) [8,9,14,16–18] and Liquid Phase Deposition (LPD) [19]. However, the cost of processing equipment for vapor phase processes is high, while LPD processes rely on highly hazardous precursors such as H_2SiF_6 [19].

As an economically feasible and non-hazardous alternative, SiO_2 deposition on stainless steel from liquid precursors by the sol-gel method has been demonstrated [10,11,13,20]. Within common sol-gel processing, a tetrafunctional alkoxide precursor with the alkyl group R, such as tetraethyl orthosilicate (TEOS), is hydrolyzed according to reaction (5.1) and subsequently condensed to form siloxane bonds via alcohol or water condensation according to reactions (5.2),(5.3) [21].

$$\equiv SiOR + H_2O \rightarrow \equiv SiOH + ROH \qquad \textit{(hydrolysis)} \qquad (5.1)$$

$$\equiv SiOR + \equiv SiOH \rightarrow \equiv SiOSi\equiv + ROH \qquad \textit{(alcohol condensation)} \qquad (5.2)$$

$$2 \equiv SiOH \rightarrow \equiv SiOSi\equiv + H_2O \qquad \textit{(water condensation)} \qquad (5.3)$$

The main advantage of these processes is the ease of their application, *i.e.* deposition by high throughput processes such as spray or dip-coating and curing in simple heating

equipment. However, sol-gel SiO_2 from aqueous solution is porous in nature and high temperature sintering is required to densify and convert porous films to continuous SiO_2 films [22]. In this perspective, the aqueous corrosion properties of sol-gel coated stainless steels cured at medium temperature are under discussion: Vasconcelos *et al.* [10] tested sol-gel SiO_2 coated stainless steel samples and observed a decrease in corrosion rate in sulfuric acid as well as an increase in pitting potential combined with a decrease in passive current in aqueous NaCl solution. Moreover, de Sanctis *et al.* [11] found an improvement in resistance to corrosion in hot nitric acid for sol-gel SiO_2 coated stainless steel and Nikrooz *et al.* [13] demonstrated an improvement of the high temperature oxidation resistance as well as wet corrosion resistance ferritic stainless steel after dip-coating with sol-gel silica. On the contrary, Damborenea *et al.* [20] reported results, which did not indicate an improvement in corrosion resistance in acid or aqueous NaCl solution. Recent studies by Takemori [23,24] reported a sol-gel process from non-aqueous solution to deposit non-porous SiO_2 films on stainless steel substrate. However, the coatings produced by their method showed cracking and defoliation and consequently cannot be evaluated as suitable candidates for corrosion barrier coatings.

As an alternative approach to deposit SiO_2 from wet precursor, thin SiO_2-like films based on Hydrogen Silsesquioxane (HSQ) technology have been reported in literature [25–27]. HSQ is an oligomeric molecule with the formula $(HSiO_{3/2})_n$, which, under the appropriate heat treatment, is capable of cross-linking via a multi-step bond redistribution under reaction (5.4) [28] or dissociation of Si-H bonds under reaction (5.5) [25] to form SiO_2-like films [25,29].

$$4HSiO_{3/2} \rightarrow 3SiO_{4/2} + SiH_4 \quad (5.4)$$

$$2H_2SiO_{2/2} \rightarrow 2H_2 + Si_2O_{2/2} \quad (5.5)$$

Thereby, heat treatment at higher temperatures leads to more advanced degrees of curing and may result in the formation of films with similar properties to SiO_2 deposited via CVD processes [26]. Moreover, HSQ-based thin films have gained particular interest as interlayer dielectric in microelectronics, since the thin film properties can be precisely tailored to achieve low dielectric constants [25,26,29], which can enhance the performance of integrated circuits [30]. In recent years, HSQ has come into focus as material applied on metallic substrates, due to its ability to level rough substrates [31–34], induce nano-patterns in injection molding [35] or act as corrosion barrier coating [36,37]. The material can be spin- [25,38], spray- [32,34] or dip- [37] coated, *i.e.* is, similar to sol-gel coatings, capable for high-throughput processing. In the present study, HSQ spin-on-glass was investigated as a novel precursor to form thin film SiO_2 coatings for the corrosion protection of stainless steel. Further, the microstructure, chemical composition and corrosion properties of these films were characterized in detail by using Field Emission Gun (FEG) and Focused Ion Beam (FIB) scanning electron microscopy (SEM), Fourier Transformed Infrared Spectroscopy (FT-IR), Spectroscopic Ellipsometry and Electrochemical Impedance Spectroscopy (EIS).

5.2 Materials and methods

5.2.1 Coating deposition

AISI 316L test coupons (sheet material, area of 50 x 100 mm^2, thickness 1 mm, 2B surface finish) and Si wafers (thickness 675 µm, front side polished, backside etched) were partially dip-coated with 1 mm/s withdrawal speed in a solution of HSQ in silanol-based solvent (Dow Corning FOx 25) in a single dip-cycle. Afterwards the test coupons were subjected to a heat treatment in order to form silica-like thin film coatings within 24 h after the precursor deposition. The applied heat treatment consisted of a soft-bake at 160 ºC for 30 min to evaporate the solvent and a subsequent calcination at 500 ºC for 2 h in oxygen depleted atmosphere under flow of 0.45 l/min Ar with addition of 0.05 l/min H_2 gas to avoid oxidation of the films/substrate. Further, to determine the relation between the film thicknesses vs. dipping speed, Si-wafers were coated with varying dipping speed and subjected to the soft-bake without additional calcination.

5.2.2 Characterization

Microstructural analysis

The coated substrates have been investigated with a Helios Nanolab 600 dual beam Scanning Electron Microscope (SEM) with Ga^+ Focused Ion Beam (FIB) source and Pt deposition system. Before FIB cross-sectioning, a double layer of CVD Pt was deposited to avoid beam-induced artifacts on the surface. Images on FIB cross-sections have been taken under 52 º sample-tilt and no digital tilt correction was applied. To avoid artifacts from surface charging, SEM specimens have been sputter-coated with a conductive Au film of a few nm thickness prior to investigation.

Adhesion testing

The coating adhesion test was conducted according to ISO 2409:2007(E) “Paints and varnishes – Cross-cut test” [39]. The test was carried out with 6 parallel scribes of 1 mm spacing, resulting in the formation of a “hatch pattern”. The area with the “hatch pattern” was analyzed by optical microscopy as well as SEM, followed by cross-sectional investigation via (FIB)-SEM. As per standard requirement, the test was repeated three times at different locations.

Chemical compositional analysis

Fourier Transform Infrared Spectroscopy (FT-IR) was carried out on films deposited on silicon wafer. The HSQ film on the backside of the wafer was removed before curing to avoid artefacts. FT-IR spectra were recorded on a Thermo Scientific Nicolet iN 10 MX in transmittance mode, whereby the background was collected on a reference silicon wafer of similar type.

Thickness measurements

The film thickness was measured optically by Spectroscopic Ellipsometry on a VASE ellipsometer. Only films deposited on Si-wafers in soft-baked condition were investigated.

Corrosion performance

Electrochemical Impedance Spectroscopy (EIS) was implemented to assess the barrier-properties of the coating by using a Gamry Ref 600 potentiostat in 0.5 M Na-acetate buffer solution at *p*H 6. EIS measurements were carried out after an open circuit measurement of 3600 s in a solution volume of 15 ml and on an area of 2.1 cm^2. Potentials were determined with a Standard Calomel Electrode and the system was perturbed with a Pt wire auxiliary electrode. The experiment was repeated on three samples for consistency.

5.3 Results and discussion

5.3.1 Film thickness

Figure 5.1 shows the film thickness on a polished Si-wafer substrate at different dipping speeds. The reported film thickness corresponds to the film thickness after solvent evaporation, *i.e.* the remaining solids of the HSQ solution before curing. Although not shown here, similar film thicknesses were achieved at higher dipping speeds when the HSQ solution was diluted to lower solid content. Furthermore, it was evident that the log of the film thickness linearly depends on log of the dipping speed, suggesting a relation similar to the power-law relation between film thickness and dipping rate as described by

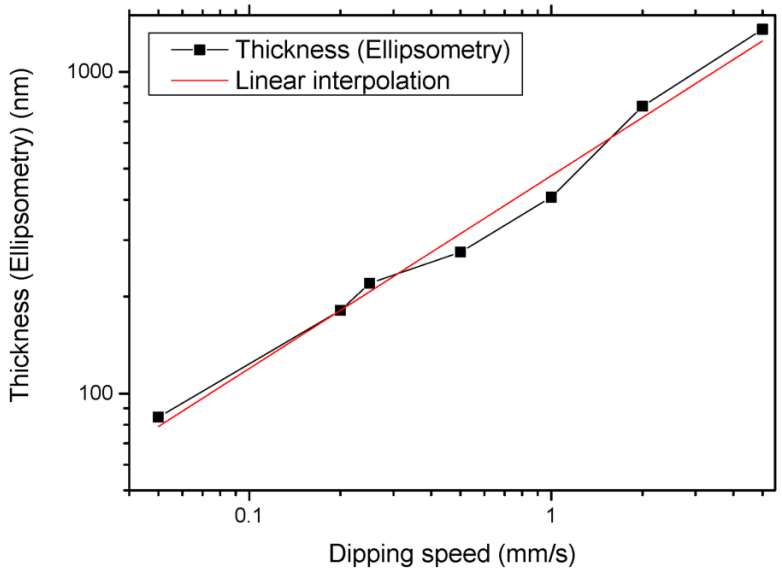

Figure 5.1: *Film thickness vs. dipping speed after solvent evaporation (on polished Si-wafer).*

Brinker *et al.* [40] for dip-coating of SiO_2 sol-gel films. Since HSQ films undergo shrinkage during curing, the direct determination of the final film thickness from Figure 5.1 is not possible. Under the given curing conditions, HSQ films are expected to shrink by 10-15 % of the initial thickness [29] and the values reported in Figure 5.1 have to be corrected for shrinkage when concluding on the final film thickness.

5.3.2 Optical appearance

The optical appearance of the test coupon after curing of the material is shown in Figure 5.2. The coating deposition led to the formation of a transparent surface film, which, depending on the film thickness, showed slight blue/violet discoloration from thin film interference. In general, the film was homogeneous and no island formation was observed. Although not presented here, there was no significant optical appearance difference in the coated area before and after curing.

5.3.3 Surface morphology and cross-sectional analysis

The detailed microstructure of the film was analyzed by SEM and FIB-SEM, as presented in Figure 5.3. Comparison between top view micrographs of a reference coupon (Figure 5.3(a)) and coated sample (Figure 5.3(b)) shows that the coating covers the surface and smoothens out the substrate grain boundary cavities from the 2B finish. Furthermore, there was no visible evidence of cracking or spallation of the coating at the top surface. The cross sectional analysis by FIB-SEM (Figure 5.3(c)) confirmed that the coating was well adherent to the substrate and neither showed cavities under the coating nor exfoliation. Moreover, film formation in substrate voids, in particular in the 2B grain-boundary trenches was observed, which resulted in the leveling of present undulations and roughness of the substrate. These results are in agreement with previous studies, where the leveling effect of HSQ surface treatments on metallic polymer molding tools [31–34] was investigated and reduction of peak to valley roughness up to a factor of 20 for mechanically ground aluminum surfaces was reported [34]. As visible from the micrograph, the simple thickness/dipping speed relation described in section 5.3.1 does

Figure 5.2: *Digital photograph of test coupon after curing.*

not apply for coatings on rough substrates, where the thickness is determined by the inhomogeneous influence of substrate undulations, rather than the dipping speed. In this perspective, a precise value of film thickness could not be determined from Figure 5.3(c). However, the minimum thickness of the film at the substrate surface was approximately 200 nm and on voids and undulations areas showed a maximum thickness of approximately 1000 - 1400 nm.

5.3.4 Adhesion testing

Figure 5.4 shows the results of the adhesion test. In general, no evidence of delamination (Figure 5.4(a)) was observed from the optical analysis and the coating was assessed as "0" according to standard test classification [39]. However, coating delamination in the close vicinity of the scribe was visible from SEM analysis, as shown in Figure 5.4(b). To further investigate the nature of the delamination, the vicinity of the scribe was investigated by FIB-SEM cross-sectioning, as presented in Figure 5.4(c). It was evident that the delaminated segment of the coating was completely removed from the surface during the test. Further, the coating delamination showed a mixed behavior by both

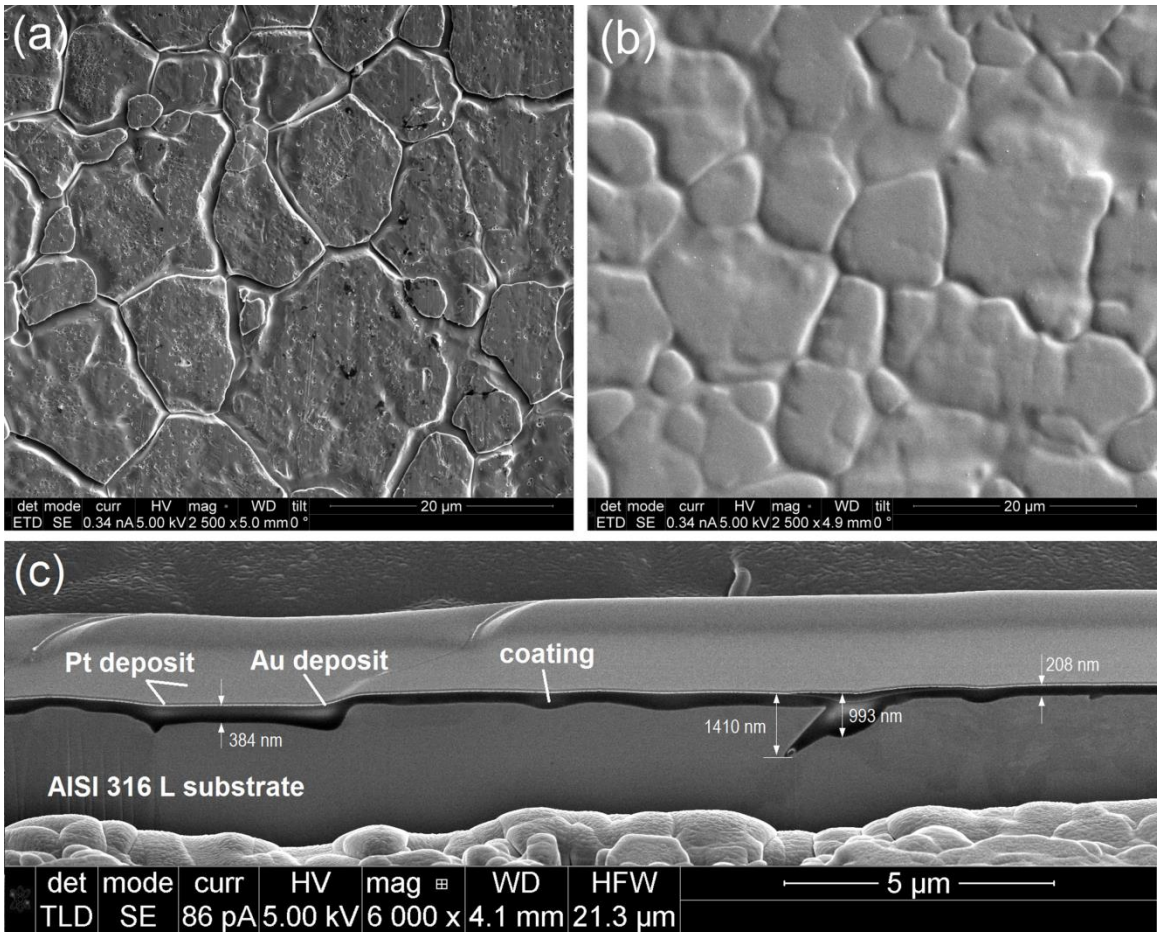

Figure 5.3: *SEM images of (a) uncoated reference (top view); (b) coated specimen (top view); (c) FIB-SEM cross section of coated sample. Au and Pt depositions are artifacts from the specimen preparation.*

adhesive and, to a minor extend, cohesive failure, as visible from the detail in Figure 5.4(c).

5.3.5 Chemical compositional analysis

The chemical composition of soft-baked (uncured) and cured films were analyzed by FT-IR, which is a well-established characterization technique to gain semi-quantitative information about the cage to network transformation and Si-H loss in HSQ films [38,41]. The FT-IR absorption spectra of the HSQ films on Si-wafer before and after curing are shown in Figure 5.5.

Non-polymerized HSQ is a cage-like oligomer with a siloxane backbone and Si-H corner moieties [41], as indicated by A and B in Figure 5.6, respectively, and shows distinct FT-IR absorption bands from the Si-O asymmetric stretching of siloxane cages at 1140 cm^{-1} and Si-H stretching from corner moieties at 2260 cm^{-1}, as shown in Figure 5.5. During the

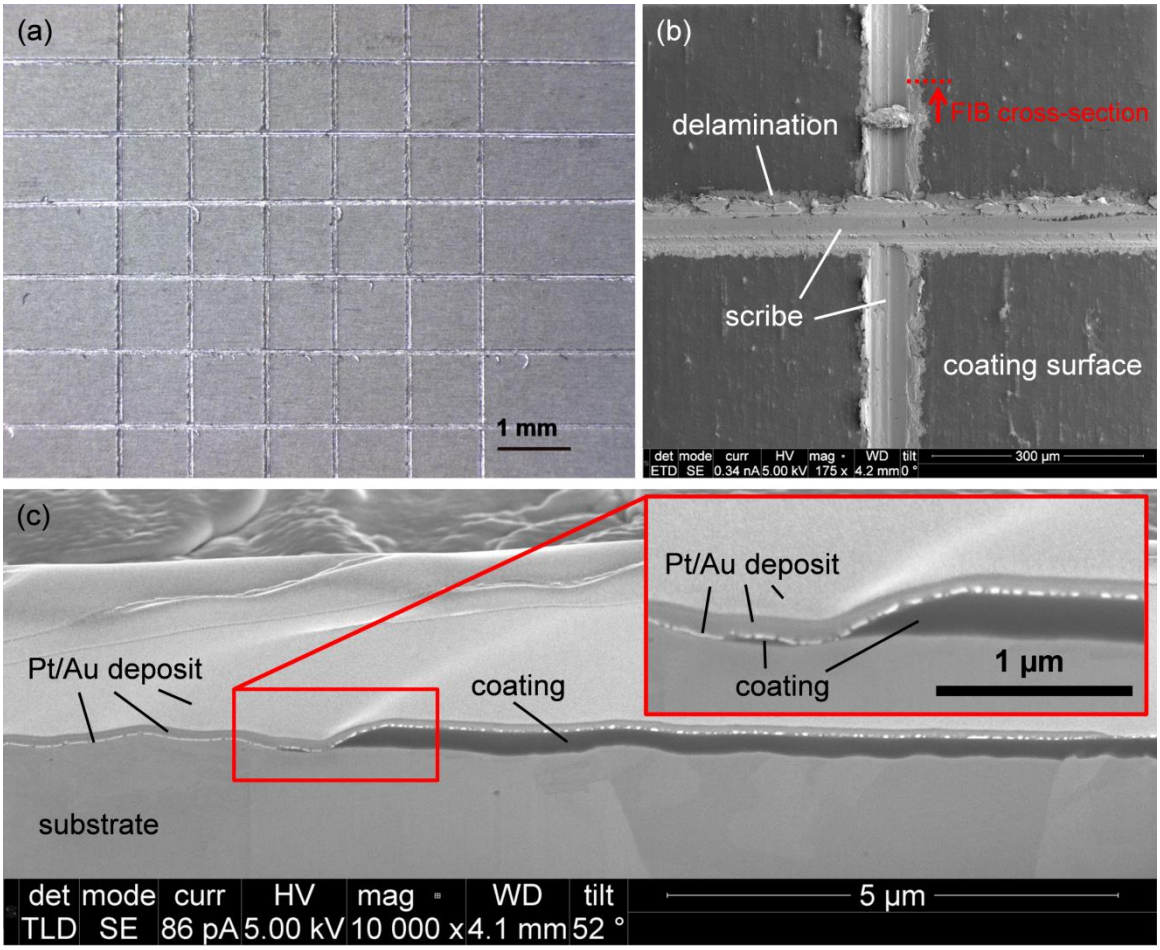

Figure 5.4: *Cross-cut test of coating: (a) Optical micrograph of coating surface after the test; (b) SEM micrograph of scribe junction. The marker in the micrograph indicates the location of the FIB-SEM cut shown in Figure 5.4(c); (c) FIB-SEM cross section across delaminated coating, where Au and Pt depositions are artifacts from the specimen preparation.*

heat treatment the cage oligomers polymerize via a multi-step redistribution reaction [25], forming networked siloxane bonds between cages, as indicated by notation "C" in Figure 5.6. In general, Si-O asymmetric stretching of networked siloxane shows an absorption peak shift in FT-IR, leading to the Si-O asymmetric stretching edge at 1075 cm^{-1} as presented in Figure 5.5. Apart from Si-H stretching at 2260 cm^{-1}, another lower intensity absorption from Si-H stretching caused by $H_2SiO_{2/2}$ [42] was observed at 2200 cm^{-1}, which is indicated by notation "D" in Figure 5.6. The presence of $H_2SiO_{2/2}$ bands indicate the formation of an intermediate reaction product in the multi-step cage to network redistribution reaction, as described by Siew *et al.* [25], and are therefore indicative for an incomplete polymerization of the HSQ film. Overall, these results showed that the applied heat treatment cycle led to a partial transformation from HSQ to SiOx, *i.e.* to the formation of a networked structure with a siloxane backbone and some remaining Si-H.

These findings are in well agreement with earlier studies [26,29], where curing at 500 ºC led to an incomplete cage to network transformation, while temperatures of 650-800 ºC fully transformed HSQ into a ceramic with virtually no remaining Si-H and a stoichiometry close to SiO_2. High remaining Si-H ratios have shown to positively influence the film properties and the films reported in this study are expected to show low film stress as well as a high stability to moisture adsorption [38].

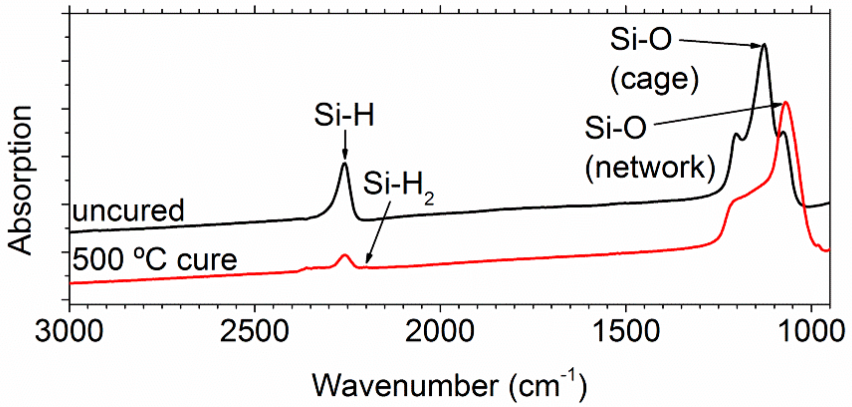

Figure 5.5: *FT-IR absorption spectra of films deposited on Si-wafer.*

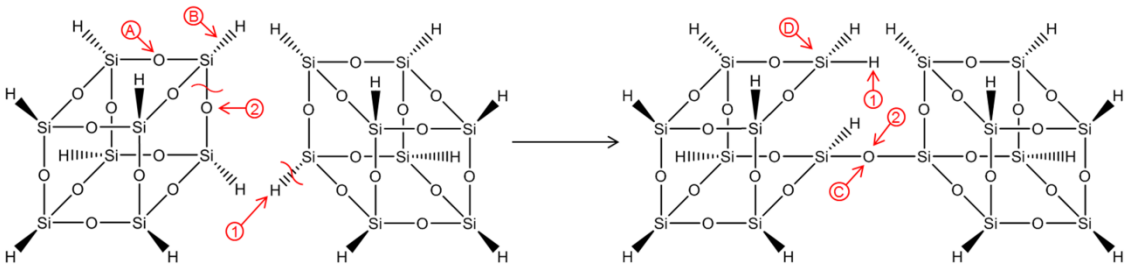

Figure 5.6: *Redistribution reaction of HSQ cage oligomers to a more networked structure (based on the redistribution reaction by Siew et al. [25]). 1 and 2 indicate atoms which are exchanged between the two neighboring cage oligomers.*

5.3.6 Electrochemical impedance spectroscopy

A widely used method to assess the barrier properties of inert thin film ceramic coatings is Electrochemical Impedance Spectroscopy (EIS) [8,9,13,43–45]. A Bode plot of the measured impedance spectra of an uncoated AISI 316L reference coupon and a coated test coupon is shown in Figure 5.7. The reference sample shows one capacitive maximum, indicating a simple charge transfer reaction over a double layer, while the spectrum acquired for the coated sample can be separated into two distinct capacitive maxima, indicating a charge transfer mechanism over the film that involves two capacitances of different origin as well as Ohmic transport.

The quantitative interpretation of EIS data requires fitting with a correct equivalent circuit model. Thus, the interpretation of a charge transfer over a double layer, as it was observed for a bare electrode immersed into an electrolyte, can be described by a Randle's equivalent circuit as shown in Figure 5.8(a) [46]. In contrast, various equivalent circuits have been proposed for steel substrates covered with SiO_2 thin films [8,9,44,45]. Pech *et al.* [9] discussed pore and pinhole free SiO_2 coatings as blocking electrodes, which can be modelled as a solution resistance in series with a capacitive element. However, their model is only applicable for systems showing a single capacitive plateau and therefore is applicable to systems, which indicate ohmic charge transport over the coating. Others [8,44,45] observed impedance responses with two capacitive maxima and applied different equivalent circuits to analyze their data. Walke *et al.* [44,45] analyzed sol-gel SiO_2 on stainless steel substrate with a R-(QR)-(QR) -type model, whereas, Pech *et al.* [8] applied a R-(Q(R-(QR))) -type model to conclude on the impedance response of PACVD SiO_2 coatings on M2 high speed steel.

Despite their mathematical equivalency, the equivalent circuits may have a different physical meaning [47] and the appropriate choice of the equivalent circuit depends on the physical properties of the system. It has been reported in literature [8,18,43,48], that similar coating systems generally decrease the corroding substrate surface, however, allow electrolyte penetration via coating defects such as pores, cracks or pinholes. Therefore, the exposed substrate double layer is in parallel to the dielectric coating and hence, assuming electrolyte penetration via coating defects, we propose a R-(Q(R-(QR))) –type model for the further analysis of the coating impedance. As shown in Figure 5.7 and Figure 5.9, the equivalent circuit showed good results in the high frequency region ($f < 10$ Hz). The addition of a semi-infinite diffusional impedance (semi-infinite Warburg impedance) could improve the fitting, yielding a R-(Q(R-(Q(W-R)))) -type circuit, as presented in Figure 5.7 and Figure 5.9, which was in agreement with reported literature [43]. A graphic representation of the equivalent circuit for the coated system is shown in Figure 5.8(b). The proper circuit fit of the data from Figure 5.7 with the equivalent circuits shown in Figure 5.8, using the relation described by Hsu *et al.* [49] for the conversion between constant phase element and equivalent capacitance, yielded the results displayed in Table 5.1. Overall, the coated specimen showed high barrier

efficiency by exhibiting a pore resistance R_p of 907 kΩ*cm^2 as well as an increase in total modulus *IZI* of the test coupons from 983 kΩ*cm^2 for the reference to 214 MΩ*cm^2. Moreover, the coated test coupon showed a decrease in equivalent double layer capacitance $C_{eq,dl}$ by three orders of magnitude, which indicates a significant decrease in electrolyte-exposed surface [8], *i.e.* a high degree of coating coverage.

Overall, the coating showed characteristics similar to silica coatings obtained by other methods such as CVD [8] or sol-gel [13], namely a highly a high resistance to ionic

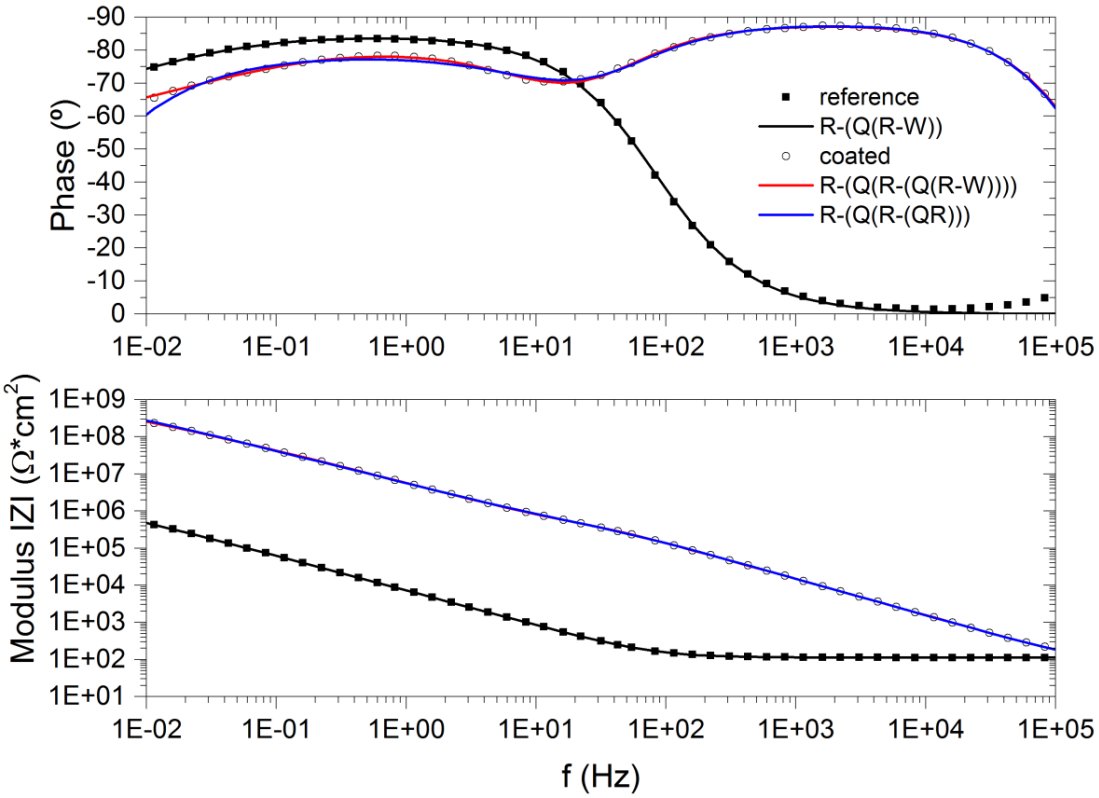

Figure 5.7: *Bode plots of coated and uncoated AISI 316L in Na-acetate buffer solution.*

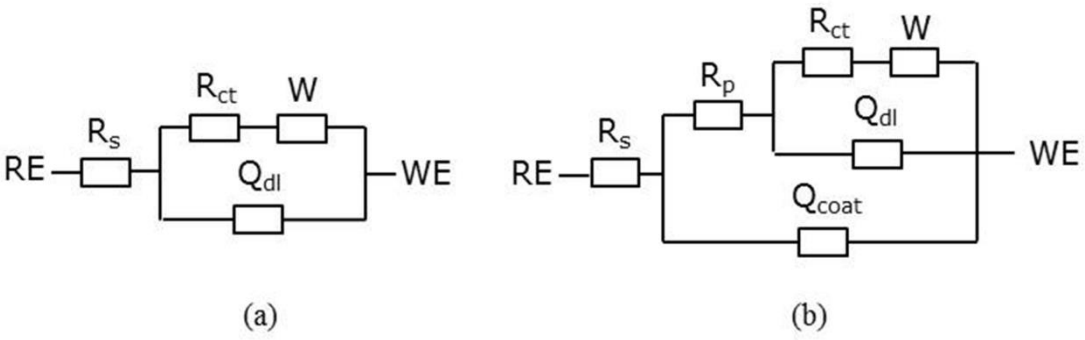

Figure 5.8*: Equivalent circuit models for: (a) reference; (b) coated sample. With solution resistance R_s, charge transfer resistance R_{ct}, pore resistance R_p, CPE of double layer Q_{dl}, CPE of coating Q_{coat}, reference electrode RE and working electrode WE.*

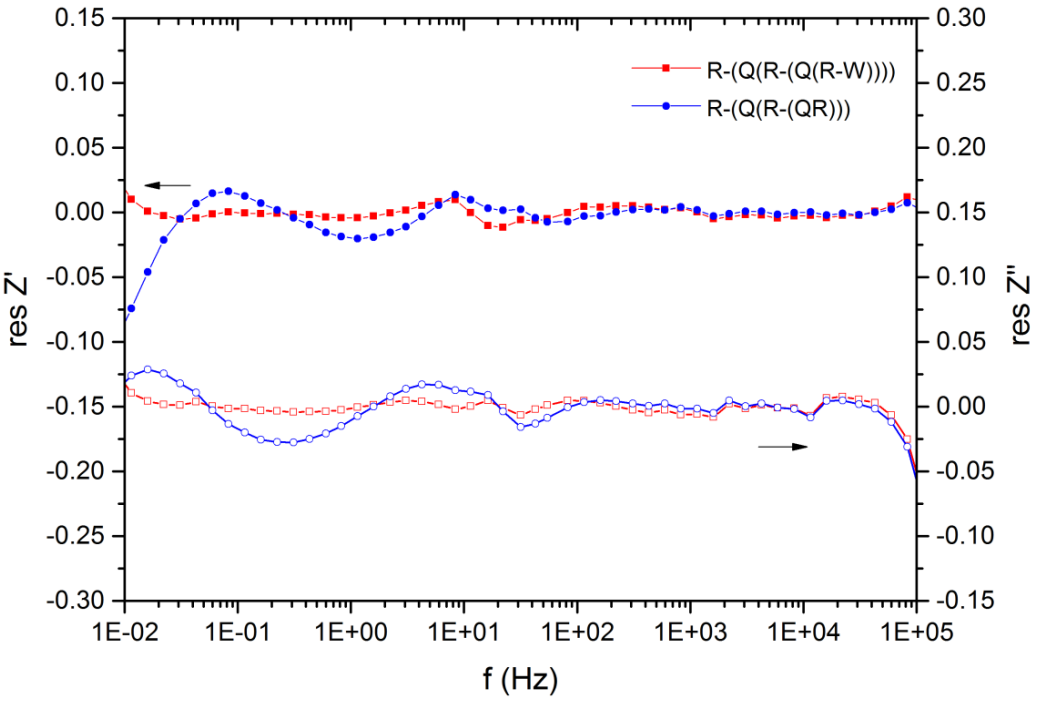

Figure 5.9: *Residuals of impedance fits shown in Figure 5.7.*

Table 5.1: *Fitting results from EIS measurements.*

Sample	R_p (Ω*cm^2)	$Q_{0,coat}$ (Ss$^{\alpha}$/cm^2)	α_{coat}	$C_{eq,coat}$ (F/cm^2)	R_{ct} (Ω*cm^2)	$Q_{0,dl}$ (Ss$^{\alpha}$/cm^2)	α_{dl}	$C_{eq,dl}$ (F/cm^2)
reference	-	-	-	-	2.33E6	2.61E-05	0.926	3.33E-05
coated	7.95E+05	1.15E-08	0.982	1.15E-08	9.29E+08	2.36E-08	0.817	4.70E-08

transport through coating defects combined with a high degree of coating coverage. However, since the previous studies were based on an assessment of the coating performance in NaCl solution, a quantitative assessment of the performance of the HSQ-based coating in respect to other coating systems is not possible solely based on this study. Further investigations have to be conducted to conclude on the barrier efficiency of the coating in technically relevant media such as chloride solutions, which are well known to induce localized failure in stainless steels [1].

5.4 Conclusions

1. HSQ-based thin film coatings can be applied to stainless steels by dip-coating to form crack free thin film enamels. Further, the deposited coatings showed good leveling abilities, adhesion and did not show any interfacial cracking or spallation.
2. The thickness of the deposited film on a rough substrate was approx. 200-400 nm, which could not be estimated by interpolation of data collected on smooth substrates.

3. Film curing at 500 ºC led to a significant polymerization of the HSQ precursor, yielding cross-linked films with a siloxane backbone and some remaining Si-H.
4. The electrochemical impedance response of the coating system could be modelled by an R-(Q(R-(Q(W-R)))) -type model, which accounts for ionic transport over the coating and compensates for diffusion in the test setup.
5. The coating indicated high barrier properties and a high substrate coverage, by exhibiting a pore resistance of 907 kΩ*cm^2 and a decrease in double layer capacitance by 3 orders of magnitude.

Acknowledgements

The authors acknowledge SiOx Aps for the deposition of coatings and all other project partners. Further, Innovation Fund Denmark is acknowledged for providing financial support for the project Q-HEX [grant number 50-2014-1].

References

[1] E. Bardal, Corrosion and Protection, Springer-Verlag London Ltd., London, 2004.

[2] E. Deltomee, N. de Zoubov, M. Pourbaix, 10.1 Chromium, in: Atlas Electrochem. Equilibria Aqueous Solut., NACE, Houston, 1996: pp. 256–271.

[3] K.M. Deen, M. a. Virk, C.I. Haque, R. Ahmad, I.H. Khan, Failure investigation of heat exchanger plates due to pitting corrosion, Eng. Fail. Anal. 17 (2010) 886–893.

[4] Z. Szklarska-Smialowska, J. Mankowski, Crevice Corrosion of Stainless Steels in Sodium Chloride Solution, Corros. Sci. 18 (1978) 953–960.

[5] H.C. Wilson, Acid Resisting Properties of Porcelain Enamels, Symp. Porc. Enamels Ceram. Coatings as Eng. Mater. 1954 (1954) 26–28.

[6] P. Møller, L.P. Nielsen, Vitreous Enamel, in: Adv. Surf. Technol. Vol 2, 2013: pp. 645–654.

[7] H. Laithwaite, Some Properties of Vitreous Enamels and their practical Significance, Sheet Met. Ind. 31 (1954) 775–780.

[8] D. Pech, P. Steyer, A.-S. Loir, J.C. Sánchez-López, J.-P. Millet, Analysis of the corrosion protective ability of PACVD silica-based coatings deposited on steel, Surf. Coatings Technol. 201 (2006) 347–352.

[9] D. Pech, P. Steyer, J.-P. Millet, Electrochemical behaviour enhancement of stainless steels by a SiO2 PACVD coating, Corros. Sci. 50 (2008) 1492–1497.

[10] D.C.L. Vasconcelos, J.A.N. Carvalho, M. Mantel, W.L. Vasconcelos, Corrosion resistance of stainless steel coated with sol–gel silica, J. Non. Cryst. Solids. 273 (2000) 135–139.

[11] O. de Sanctis, L. Gomez, N. Pellegri, C. Parodi, A. Marajofsky, A. Duran, Protective Glass Coatings on Metallic Substrates, J. Non. Cryst. Solids. 121 (1990) 338–343.

[12] O. de Sanctis, L. Gomez, N. Pellegri, A. Duran, Behaviour in hot ammonia atmosphere of SiO2-coated stainless steels produced by a sol-gel procedure, Surf. Coatings Technol. 70 (1995) 251–255.

[13] B. Nikrooz, M. Zandrahimi, H. Ebrahimifar, High temperature oxidation resistance and corrosion properties of dip coated silica coating by sol gel method on stainless steel, J. Sol-Gel Sci. Technol. 63 (2012) 286–293.

[14] K. Baba, R. Hatada, S. Nagata, H. Fujiyama, G.K. Wolf, W. Einsinger, SiO2 coatings produced by ion beam assisted ECR-plasma CVD, Surf. Coatings Technol. 75 (1995) 292–296.

[15] G.A. Garzino-Demo, F.L. Lama, Friction and wear of uncoated or SiO2-coated 329 stainless steel and of uncoated or A1N-coated aluminium surfaces, Surf. Coatings Technol. 68/69 (1994) 507–511.

[16] W. Hänni, H.E. Hintermann, D. Morel, A. Simmen, Silica Coatings on Strongly Passivated Substrates, Surf. Coatings Technol. 36 (1988) 463–470.

[17] S. Benayoun, L. Fouilland-Paille, J.J. Hantzpergue, Microscratch test studies of thin silica films on stainless steel substrates, Thin Solid Films. 352 (1999) 156–166.

[18] A. Delimi, Y. Coffinier, B. Talhi, R. Boukherroub, S. Szunerits, Investigation of the corrosion protection of SiOx-like oxide films deposited by plasma-enhanced chemical vapor deposition onto carbon steel, Electrochim. Acta. 55 (2010) 8921–8927.

[19] S. Nitta, Y. Kimura, Formation of SiO2 Thin Film on SUS304 Stainless Steel by Liquid Phase Deposition (in Japanese), J. Soc. Matierals Sci. Japan. 43 (1994) 1437–1443.

[20] J. de Damborenea, N. Pellegri, O. Sanctis, A. Duran, Electrochemical Behaviour of SiO2 Sol-Gel Coatings on Stainless Steel, J. Sol-Gel Sci. Technol. 4 (1995) 239–244.

[21] C.J. Brinker, G.W. Scherer, Hyrdolysis and Condensation of Silicon Alkoxides, in: Sol-Gel Sci., Academic Press, Inc., San Diego, 1990: pp. 108–216.

[22] C.J. Brinker, G.W. Scherer, Sintering, in: Sol-Gel Sci., Academic Press, Inc., San Diego, 1990: pp. 675–742.

[23] M. Takemori, Crack formation, exfoliation, and ridge formation in 500 °C annealed sol-gel silica coatings on stainless steel SUS304: Part I. Microscopic observations and elemental analysis, Ceram. Int. 35 (2009) 1731–1746.
[24] M. Takemori, Crack formation, exfoliation, and ridge formation in 500 °C annealed sol–gel silica coatings on stainless steel SUS304: Part II Spectroscopic and mechanical analyses and insights into mechanisms controlling coating characteristics, Ceram. Int. 35 (2009) 1747–1755.
[25] Y.K. Siew, G. Sarkar, X. Hu, J. Hui, A. See, C.T. Chua, Thermal Curing of Hydrogen Silsesquioxane, J. Electrochem. Soc. 147 (2000) 335.
[26] H. Liou, J. Pretzer, Effect of curing temperature on the mechanical properties of hydrogen silsesquioxane thin films, Thin Solid Films. 335 (1998) 186–191.
[27] W.-C. Liu, C.-C. Yang, W.-C. Chen, B.-T. Dai, M.-S. Tsai, The structural transformation and properties of spin-on poly(silsesquioxane) films by thermal curing, J. Non. Cryst. Solids. 311 (2002) 233–240.
[28] V. Belot, R.J.P. Corriu, D. Leclercq, P.H. Mutin, A. Vioux, Redistribution reactions in silsesquioxane gels, J. Mater. Sci. Lett. 9 (1990) 1052–1054.
[29] D. Tobben, P. Weigand, M.J. Shapiro, S.A. Cohen, Influence of the cure process on the properties of hydrogen silsesquioxane spin-on-glass, Mater. Res. Soc. Somposium Proc. 443 (1997) 195–200.
[30] P. Kohl, Low-dielectric constant insulators for future integrated circuits and packages, Annu. Rev. Chem. Biomol. Eng. 2 (2011) 379–401.
[31] K. Mohaghegh, H.N. Hansen, H. Pranov, G. Kofod, A study on the surface roughness of a thin HSQ coating on a fine milled surface, in: 14th Euspen Int. Conf. - Dubrovink, 2014.
[32] K. Mohaghegh, H.N. Hansen, H. Pranov, G. Kofod, Verification of thickness and surface roughness of a thin film transparent coating, in: Proc. 13th Euspen Int. Conf., Berlin, 2013.
[33] H. Pranov, Spin-on-glass assisted polishing of rough substrates, WO 2103/083129 A1, 2013.
[34] J. Cech, H. Pranov, G. Kofod, M. Matschuk, S. Murthy, R. Taboryski, Surface roughness reduction using spray-coated hydrogen silsesquioxane reflow, Appl. Surf. Sci. 280 (2013) 424–430.
[35] T.C. Hobæk, M. Matschuk, J. Kafka, H.J. Pranov, N.B. Larsen, Hydrogen silsesquioxane mold coatings for improved replication of nanopatterns by injection molding, J. Micromechanics Microengineering. 25 (2015) 035018.
[36] H. Pranov, Reactive Silicon Oxide Precursor Facilitated Anti-Corrosion Treatment, US 2014/0154441 A1, 2014.
[37] F. Lampert, A.H. Jensen, P. Møller, Low Temperature Curing of Hydrogen Silsesquioxane Surface Coatings for Corrosion Protection of Aluminum, NASF Surf. Technol. White Pap. 80 (2016) 1–8.
[38] J.N. Bremmer, Y. Liu, K.G. Gruszynski, F.C. Dall, Cure of Hydrogen Silsesquioxane for Intermetal Dielectric Applications, Mater. Res. Soc. Symposium Proc. 476 (1997) 37–44.
[39] ISO 2409:2007(E) Paints and varnishes - Cross-cut test, (2007).
[40] C.J. Brinker, G.W. Scherer, Physics of Film Formation, in: Sol-Gel Sci., 1990: pp. 788–797.
[41] C.L. Frye, W.T. Collins, The Oligomeric Silsesquioxanes, (HSiO3/2)n, J. Am. Chem. Soc. 92 (1970) 5586–5588.
[42] M.G. Albrecht, C. Blanchette, Materials Issues with Thin Film Hydrogen Silsesquioxane Low K Dielectrics, J. Electrochem. Soc. 145 (1998) 4019–4025.
[43] C. Liu, Q. Bi, A. Leyland, A. Matthews, An electrochemical impedance spectroscopy study of the corrosion behaviour of PVD coated steels in 0.5 N NaCl aqueous solution: Part I. Establishment of equivalent circuits for EIS data modelling, Corros. Sci. 45 (2003) 1243–1256.
[44] W. Walke, Z. Paszenda, T. Pustelny, Z. Opilski, S. Drewniak, M. Ko, M. Basiaga, Evaluation of physicochemical properties of SiO2-coated stainless steel after sterilization, Mater. Sci. Eng. C. 63 (2016) 155–163.

[45] W. Walke, Z. Paszenda, M. Basiaga, P. Karasinski, M. Kaczmarek, EIS Study of SiO2 Oxide Film on 316L Stainless Steel for Cardiac Implants, in: E. Piętka, J. Kawa, W. Wieclawek (Eds.), Inf. Technol. Biomed. Vol 4., Springer International Publishing, Cham, 2014: pp. 403–410.
[46] F. Mansfeld, H. Shih, H. Greene, C.H. Tsai, Analysis of EIS Data for Common Corrosion Processes, in: Electrochem. Impedance Anal. Interpret., 1993: pp. 37–53.
[47] M.E. Orazem, B. Tribollet, 4 Electrical Circuits, in: Electrochem. Impedance Spectrosc., John Wiley& Sons, Inc., Hoboken, New Jersey, 2008: pp. 61–72.
[48] T. Hwang, H. Lee, H. Kim, G. Kim, Two layered silica protective film made by a spray-and-dip coating method on 304 stainless steel, J. Sol-Gel Sci. Technol. 55 (2010) 207–212.
[49] C.H. Hsu, F. Mansfeld, Technical Note: Concerning the Conversion of the Constant Phase Element Parameter Y0 into a Capacitance, Corrosion. 57 (2001) 747–748.

6 Manuscript II

Interfacial Interaction of Oxidatively Cured Hydrogen Silsesquioxane Spin-On-Glass Enamel with Stainless Steel Substrate*

Felix Lampert[a], Shima Kadkhodazadeh[b], Annemette H. Jensen[c], Rameez Ud Din[a], Per Møller[a]

[a] Technical University of Denmark, Department of Mechanical Engineering, Produktionstorvet 425, 2800 Kgs. Lyngby, Denmark
[b] Technical University of Denmark, Center for Electron Nanoscopy (CEN), Fysikvej 307, 2800 Kgs. Lyngby, Denmark
[c] SiOx ApS, Bybjergvej 7, 3600 Espergærde, Denmark

Abstract

Thin film silica coatings have proven to be efficient barrier coatings to protect stainless steels from corrosion in aggressive environments. The deposition of sub-µm silica films from liquid hydrogen silsesquioxane precursor has previously been demonstrated on metallic substrates, whereby the films were thermally cured in inert atmosphere, which required complicated processing equipment, such as gas or vacuum furnaces. In contrast, curing in air is a promising routine to simplify the curing process, reduce curing cost and increase the curing efficiency. In the present work, silica-like thin films were deposited on 316L grade austenitic stainless steel and oxidatively cured at 450 ºC in ambient air. Oxidative curing yielded well adherent films which solely showed microscopic delamination after standardized adherence testing. Further, the oxidative curing led to the formation of a pronounced interfacial duplex-oxide with an outer zone composed of Fe_2O_3 in a SiO_{2-x} matrix and an inner zone composed of complex (Cr^{3+},Fe^{2+},Mn^{2+})-oxides. Moreover, a Cr depletion of the substrate in the immediate vicinity of the surface was observed. It was concluded that the interfacial formation is controlled by the kinetic limitation of Cr transport to the interface, which consequently led to the Cr-depletion of the sub-surface region.

* published work: F. Lampert, S. Kadkhodazadeh, A.H. Jensen, R.U. Din, P. Møller, Journal of the Electrochemical Society, 164(6) (2017) C1-C9. The format of the article has been edited to match the dissertation.

6.1 Introduction

Stainless steels belong to the most widely used engineering materials in corrosion sensitive applications. The material is highly corrosion resistant in a multitude of chemical environments due to its high Cr content, which triggers the formation of a Cr-rich, passive surface layer [1–3]. However, their corrosion resistance can be compromised in highly acidic [4] or halogen-ion containing media [5]. In particular, chloride-induced localized corrosive failure, such as pitting and crevice corrosion, limits the applicability of the material and unpredicted and premature failure of stainless steel engineering components is frequently observed in chloride containing media [6–10]. The localized corrosive failure is often concealed by the component geometry (*e.g.* in crevices) or hidden in form of large subsurface pits with a small pit mouth [5,10], and thus the corrosion-site often remains undetected until component failure.

Motivated by the limitations in the corrosion resistivity of stainless steel, the deposition of protective coatings, *e.g.* thin layers of SiO_x, has been attempted [11–15]. The coatings have been found to strongly decrease the passive current density [11–14] or increase the pitting potential [11], and thus reduce the susceptibility to corrosive attack in both chloride [11–13] and acid media [13,14]. Recently, the deposition of SiO_x thin film coatings on metallic substrates using hydrogen silsesquioxane (HSQ) as a precursor has been demonstrated [16–22] and the process allowed the deposition of high quality coatings for applications such as microinjection molding tools, where a particularly good surface finish in combination with a high geometrical stability is required [16,17,19]. In addition to the roughness reduction, our earlier studies [22] have shown that the coating system has excellent ionic barrier properties in aqueous media, and thus constitutes a highly promising alternative to the more traditional SiO_x deposition methods, such as sol-gel or CVD processes.

The technology of silica-like thin films from HSQ precursor originates from the semiconductor industry, where HSQ-based “spin-on-glass” films have found great interest as interlayer dielectrics, owing to their good insulating properties combined with a low dielectric constant [23–25]. In conventional HSQ processing, the precursor is deposited on a substrate and thermally polymerized to form an amorphous thin film [23,25]. Bremmer *et al.* [24] have discussed that the oxygen content of the curing ambient has a crucial effect on the curing process and thin film properties, as their investigations of oxidatively cured films showed both a more advanced degree of curing, and oxidation of the thin films (*i.e.* formation of silanol moieties). Both effects increase the dielectric constant of the deposits, and thus oxidative curing is categorically excluded in the processing of HSQ-based interlayer dielectrics, where low refractive indices are a basic requirement.

The same practice has so far been adopted as curing routine for HSQ-based coating systems [16–22]. However, in contrast to interlayer dielectric applications, barrier coatings do not require low dielectric constants, and subsequently, the oxygen induced

increase in dielectric constant can be neglected. It is thus highly relevant to investigate curing HSQ films in oxygen ambient for HSQ-based coating applications, as it can combine improvements in barrier properties with decrease in thermal budget, increased applicability and cost reduction in the production process of SiO_x thin film coatings. In particular, the coating/substrate interaction is of fundamental interest for thin film coating systems, since it is expected to influence both the coating adhesion [26–28] and the corrosion properties [13]. It has been shown that firing thin film silica coatings on stainless steel substrates at elevated temperatures leads to the formation of a complex interfacial film between the coating and the substrate [13,26–29]. However, despite the high technological relevance of the interface, its chemical nature, morphology and the mechanism of formation is not yet fully understood. In the present study, the adhesion properties and interfacial structure of HSQ thin films deposited on a commercial AISI 316L -grade substrate and cured in air ambient at 450 ºC have been characterized using analytical electron microscopy and X-ray photoelectron spectroscopy (XPS). The results provide novel insight into interface formation and its role on coating adhesion and substrate corrosion resistance in air-cured HSQ-based silica coating systems on stainless steel.

6.2 Experimental

6.2.1 Thin film deposition

AISI 316L substrates (Composition (wt.%): 17.5 Cr, 10.5 Ni, 2.2 Mo, 1.2 Mn, 0.5 Si, bal. Fe; determined by Energy dispersive X-ray spectroscopy (EDS) at 20 kV acceleration voltage on a JEOL JSM-5900 Scanning Electron Microscope (SEM) with Oxford Instruments EDS detector) with an area of 100 x 50 mm^2 and a thickness of 1 mm were partially coated with the commercial hydrogen silsesquioxane ($[HSiO_{3/2}]_n$) solution Dow Corning FOx 25 by dip coating at 1 mm/s withdrawal speed. Substrates used for visual and microscopical investigation had a 2B surface finish (as received) whereas for XPS analysis the substrate surface was ground/polished to a mirror-like surface with a 1 µm diamond polish in the final step. All substrate surfaces were immersion degreased in Schlötter Slotoclean AK 90, followed by anodic degreasing in Schlötter Slotoclean EL DCG at 8 A/dm^2 and acid pickling in Schlötter Slotoclean Decasel 5 prior to coating deposition. The solvent was evaporated via heat treating at 160 ºC for 30 min, followed by a polymerization of the deposited HSQ in air ambient at 450 ºC for 2 h.

6.2.2 Film adhesion

Film adhesion was tested using standardized cross-cut testing according to ISO 2409:2007(E) “Paints and varnishes – Cross-cut test” [30] with 6 parallel cuts at a spacing of 1 mm. After the adhesive test, the cross-cuts were examined for adhesive failure using optical microscopy and SEM. The test was repeated three times on different locations of the test coupon to ensure consistency.

6.2.3 Characterization

X-ray photoelectron spectroscopy (XPS)

The XPS data acquisition was carried out on a Thermo Scientific XPS with a monochromated Al K-Alpha X-ray source at a photon energy of 1486.7 eV under ultrahigh vacuum and with the use of a flood gun to compensate for charging. Depth-profiling measurements were performed using iterative Ar^+ etching at 2 kV on a circular area with a diameter of 400 µm. High-resolution spectra were recorded with 50 eV pass energy at an energy step-size of 0.1 eV. Each high-resolution spectrum was acquired with 5 individual scans. The peak fitting was performed using the commercial software Thermo Avantage 5.949 with a Shirley-type background. Further, the asymmetries for the metal peaks [31] were determined on a surface sputtered down to the bulk, as suggested by others [32]. The quantitative compositional analysis was performed from the analysis of normalized peak areas using the sensitivity factors reported by Scofield [33].

Electron microscopy

SEM imaging and Focused Ion Beam (FIB) milling of specimens were carried out using a Helios NanoLAB 600, fitted with a Field Emission Gun (FEG), Ga^+ ion source and an Omniprobe micro-manipulator. Specimens were sputter-coated with ~20-30 nm of Au to avoid surface charging under the beam. Cross-sectional SEM images were recorded under a 52 º specimen tilt at the beam currents and acceleration voltages indicated directly in the figures. Lamellae in cross-sectional geometry for examination with transmission electron microscopy (TEM) were cut by FIB milling, lifted out with the Omniprobe, mounted on a Cu TEM grid and further FIB milled to electron transparency. The initial FIB milling was carried out at 30 kV ion beam accelerating voltage, followed by final polishing at 2 kV and 0.44 nA ion beam accelerating voltage and current, respectively, to remove residual FIB damage [34]. Specimen surfaces were protected from ion beam irradiation damage by depositing a Pt layer prior to FIB milling.

The prepared lamellae were examined using a variety of TEM imaging and analysis techniques. EDS and energy-filtered TEM (EFTEM) imaging were carried out in a JEOL 3000F instrument operated at 300 kV accelerating voltage and fitted with a FEG electron source, Oxford Instruments EDS detector and a Gatan image filter (GIF). Background subtraction in EFTEM was performed using the jump ratio method [35]. Slit sizes and acquisition times were adjusted accordingly for each energy-loss feature. Scanning TEM (STEM) imaging and electron energy-loss spectroscopy (EELS) were performed in a FEI Titan instrument fitted with a FEG electron source and a monochromator. The instrument was operated at 120 kV accelerating voltage and with the monochromator excited, giving spatial and energy resolutions of ~5 Å and ~0.15 eV.

6.3 Results

6.3.1 Coating appearance and adhesion

A photograph of a half-coated substrate is shown in Figure 6.1. The coated side of the sample shows a straw/golden appearance compared to the uncoated side, which appears metallic-red. The coating also has a good surface coverage and does not show any flaking or cracking. Due to the brittleness of the coating, specimen cross-sections were prepared using FIB-SEM, instead of metallographic methods. A FIB-SEM cross-section of the coating containing a typical surface undulation of the 2B finished substrate is presented in Figure 6.2. The coating has a minimum thickness of approx. 200 nm at the surface, while thicker coating coverage is found due to substrate surface defects, *e.g.* in connection with surface roughness. Another noteworthy feature is a distinct interfacial layer between the coating and substrate (denoted as interface in the image) clearly visible in Figure 6.2.

Figure 6.1: *A digital photograph of half-coated test coupon after curing. The coated portion of the coupon shows a straw yellow/golden color while the uncoated portion shows red/golden discoloration.*

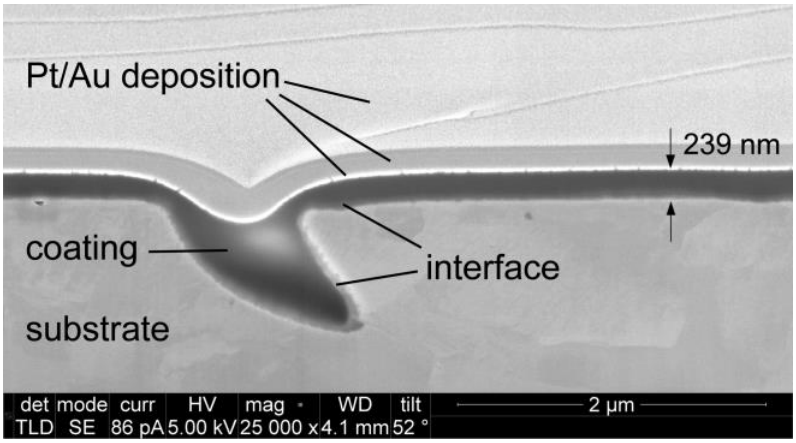

Figure 6.2: *SEM image of a FIB-milled cross-section. The area has been coated with Au and Pt prior to milling. Substrate defects are leveled by the coating.*

Optical micrographs after the standardized cross-cut test of a coated coupon are presented in Figure 6.3(a,b). The micrographs indicate that the coating remains intact after the test, since no macroscopic delamination on the surface or near the marks made by the scribe can be seen. The coating adhesion is, thus, classified with "0", according to the standard specifications of the test [30]. The micrographs of the test coupons displayed in Figure 6.3(b,c), reveal pronounced ridges present at the edge of the scribe marks formed by the cross-cuts. A closer SEM examination of the coating near the ridge (area indicated in Figure 6.3(c)) in cross-sectional view (Figure 6.3(d)) shows that the ridge protrudes above the coated surface and that microscopic coating delamination and flaking is present into an area approx. 10 µm from the ridge. This includes both adhesive failure, *i.e.* delamination of the coating and interface from the substrate, and cohesive failure, *i.e.* delamination of the coating from the interface, as seen in the detail in Figure 6.3(d).

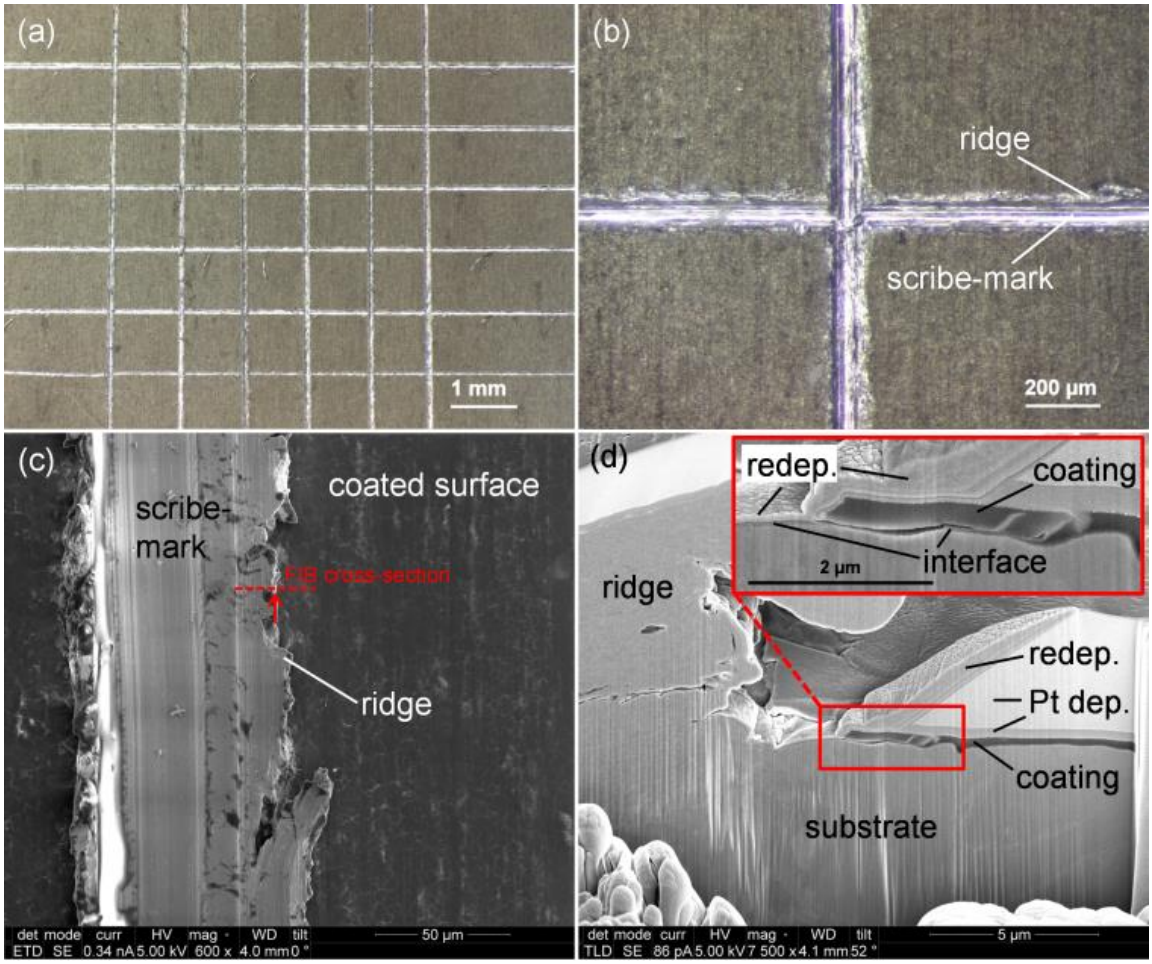

Figure 6.3: *Cross-cut test of coating: (a), (b) Top view image of cross-cuts in stereo light optical microscope; (c) Top view SEM image of the scribe test. The red inscription in the micrograph indicates the location of the FIB-SEM cut shown in Figure 6.3(d); (d) SEM image of FIB milled cross-section of ridge area. The vertical lines on the substrate are due to the so-called curtaining, artefact typically induced by FIB milling. The area has been coated with Pt (Pt dep.) prior to FIB milling. An additional FIB-milling artefact present is material redeposition (redep.) into the void underneath the ridge.*

6.3.2 Compositional depth profiling by XPS

XPS depth-profiling was carried out to gain quantitative information about the distribution and oxidation state of the elements across the interface. Typical high-resolution XPS spectra, acquired in the interface region, and their deconvolution into their constituent peaks are displayed in Figure 6.4. All profiles shown in Figure 6.4 were acquired at the maximum integrated area of the O^{2-} peak originating from metal oxides (O^{2-}_{MeOx}), *i.e.* after 1445 s of Ar^{+} etching. In general, a shift of ionic peaks over the film/interface from higher to lower binding energies was observed, which is an experimental artefact induced by the charging in non-conductive materials.

Deconvolution of high resolution spectra

Figure 6.4(a) shows the Ni $2p_{3/2}$-edge as superposition of Ni^{0} and a distinctive satellite feature [36,37], indicating that Ni is only found in the metallic state. Deconvolution of the Fe $2p_{3/2}$-edge (Figure 6.4(b)) identifies Fe^{0} [38], Fe^{+2} [39] and Fe^{+3} [40,41]. Since Ar^{+} sputtering of Fe-oxides is well known to induce reduction of metal oxides to a lower

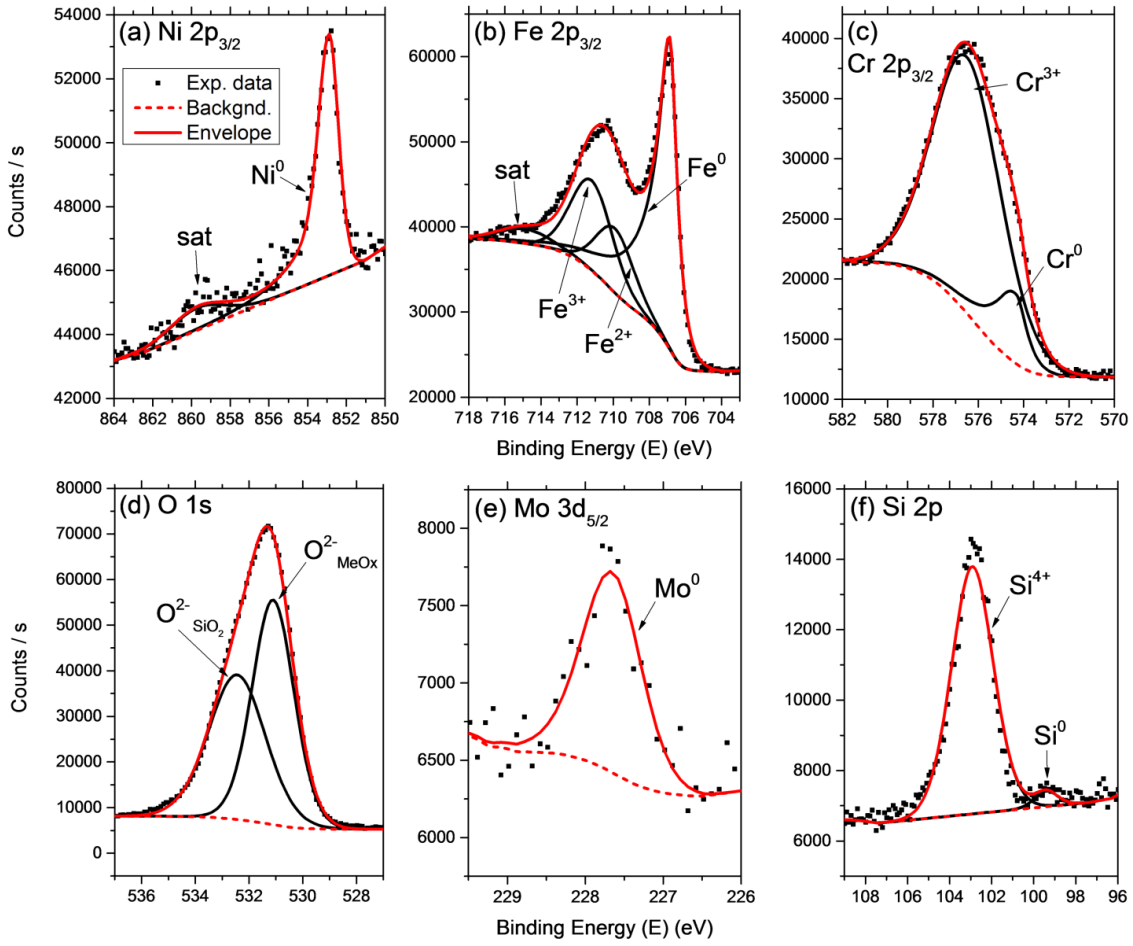

Figure 6.4: *Deconvoluted high-resolution XPS spectra of (a) Ni 2p3/2; (b) Fe 2p3/2; (c) Cr 2p 3/2; (d) O 1s; (e) Mo 3d5/2; (f) Si 2p. Spectra acquired after 1455 s sputtering.*

oxidation state [42–44], a definitive conclusion about the oxidation states cannot be drawn from the acquired XPS spectra and a quantitative differentiation between Fe^{2+} and Fe^{3+} is thus not included in the analysis in the following section. Cr 2 $p_{3/2}$ consists of contributions from Cr^0 and Cr^{3+} [45], as shown in Figure 6.4(c).

The O 1s edge (Figure 6.4(d)) is fitted with two peaks, one at higher binding energy, characteristic for O^{2-} in amorphous SiO_2 [46], and a second contribution at lower binding energy from O^{2-} in metal oxides [47]. Similar to Ni, Mo is only present in metallic state [48], as evident by the Mo $3d_{5/2}$ spectrum in Figure 6.4(e). The spectrum containing Si 2p shows a major feature at high binding energy, which has previously been identified as Si^{4+} in HSQ-based glasses [49–51], and a second feature at lower binding energy, which indicates the formation of Si nano-domains [49–51].

Quantitative XPS depth profiling

Based on the depth profiles, three distinct regions are identified and indicated in Figure 6.5: the coating, showing solely signal from Si and O, the interface, with a strong contribution from oxidized Fe and Cr, and the bulk containing a pronounced contribution from the alloying elements in metallic state. Interface roughness and the interaction volume of the measurements render the transitions between the regions gradual, as is clear in Figure 6.5.

A constant composition of 64 at.% O^{2-} and 36 at.% Si^{4+} is measured in the coating, which is indicative of cross-linked HSQ. The concentration profiles of $Fe^{2+,3+}$ and Cr^{3+} reveal a double-layer interface, divided into an outer $Fe^{2+,3+}$-rich region (outer interface) and an inner Cr^{3+}-rich region (inner interface). In addition to oxidized Fe and Cr, O^{2-}_{MeOx} is present and reaches a maximum within the interfacial region. The cumulative Fe and Cr

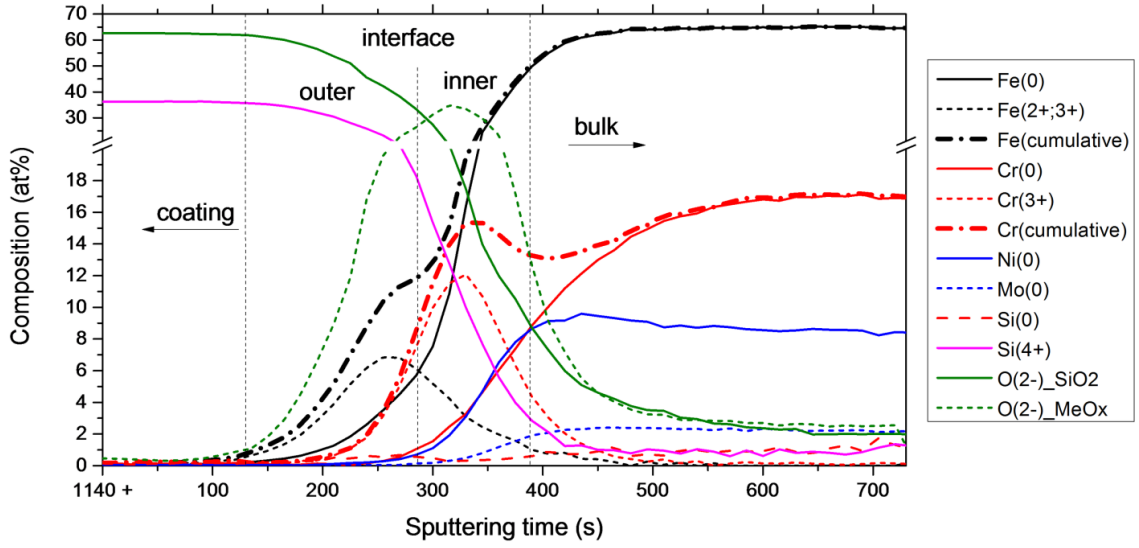

Figure 6.5: *XPS sputter depth-profile of HSQ/substrate interface. Cumulative curves are sums of the metallic and oxidized curves.*

concentration profiles (sums of the respective oxidized and metallic species) in Figure 6.5 show a local maximal Fe(cumulative) content in the outer interface and a local peak in the Cr(cumulative) content in the inner interface. Moreover, a depression in Cr(cumulative) content compared to the bulk composition is visible at the interface/substrate transition. Upon approaching the substrate from the inner interface, Ni and Mo are detected in metallic state, whereby the Ni^0 content shows a local maximum in in the Cr-depleted zone.

6.3.3 Transmission electron microscopy analysis

EDS chemical analysis

In order to acquire detailed information about the adhesion and the chemical composition across the coating, interface and substrate, the coating system was investigated by TEM. A typical bright-field TEM image of the coating in cross-sectional view is shown in Figure 6.6(a). Similar to the SEM cross-section, the micrograph shows a diffuse contrast between the coating and substrate, labelled as interface. In order to determine whether the observed varying TEM image contrast arises from chemical composition inhomogeneities, EDS line scans were recorded across the interface. The results of the EDS composition profile along the line marked in Figure 6.6(a) are plotted in Figure 6.6(b). Signals from Mo and Mn were negligible and were excluded from the analysis. The composition of the coating is measured to be ~64 at.% O and ~36 at.% Si (average over points 1 – 4; standard deviation of 0.47 at.%). Moreover, the results suggest a double-layer interface: the outer interface (spectra 5-6) shows enrichment in Fe, while the concentration of the main alloying elements Ni and Cr remains minimal. The Fe profile peaks at point 7, combined with a first noticeable increase in Cr content, indicating the

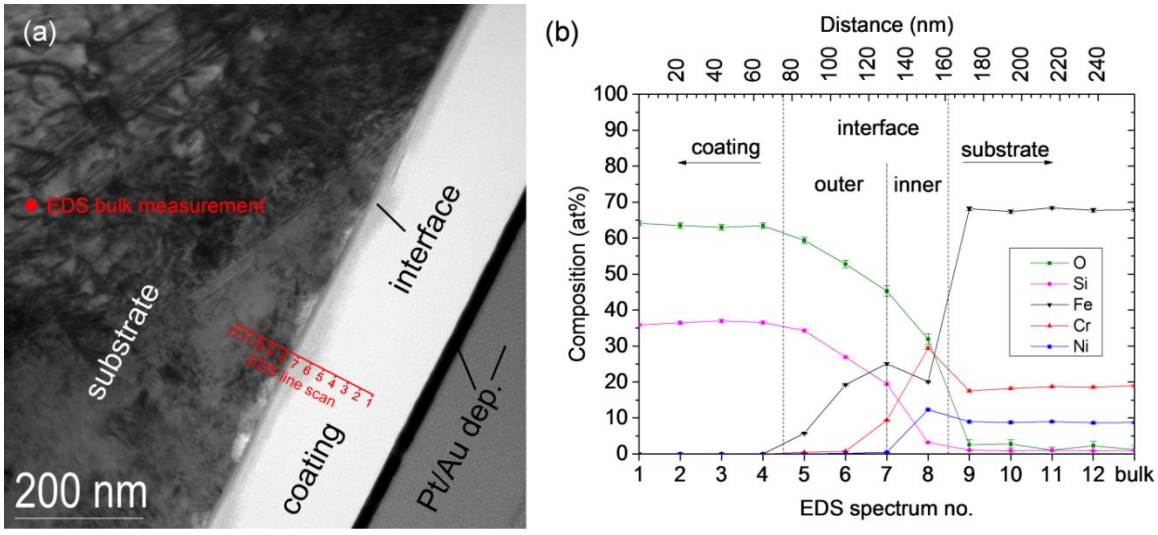

Figure 6.6: *(a) Bright field TEM cross-sectional image of coating on AISI 316L substrate; (b) Quantification of the EDS line-scan indicated in Figure 6.6(a). The dimension of the condensed beam for EDS analysis was ~20 nm. Error-bars indicate the statistical error of the EDS measurement.*

transition between the outer and inner interfaces. At the inner interface (spectrum 8), a decrease in Fe content in combination with an increase in Cr and Ni contents is observed. Upon entering the substrate (spectrum 9) the Cr-content is decreased compared to the bulk composition. No significant change in chemical composition is observed within the subsurface region probed by spectra 10-12.

Analysis of oxidation states by EELS

In order to gain additional information about the chemistry of the interface, EELS analysis of the specimens was carried out. Besides allowing chemical composition analysis with very high spatial resolution, the energy-loss near-edge fine-structure (ELNES) in EELS has been shown to be a powerful tool in probing the local chemistry, such as chemical bonding, oxidation state, crustal structure and coordination number [52–54]. Figure 6.7(a,b) shows a dark-field STEM image of the interface structure and the relative composition of these elements across the interface. EELS spectra containing the O K, Cr $L_{2,3}$, Mn $L_{2,3}$, and Fe $L_{2,3}$ and Si $L_{2,3}$ edges are shown in Figure 6.8. The analysis of the Ni $L_{2,3}$ edge was not possible due to overlap with the Fe L_1 edge. Our experimental set-up did not allow recording single EELS spectra containing signals from all elements of interest and hence, spectra containing the Si $L_{2,3}$ edge had to be recorded separately. Moreover, due to electron beam irradiation damage to the sample, it was not possible to record the spectra in Figure 6.7(a) and Figure 6.7(b) from exactly the same regions. However, the measurements were repeated across different regions of the specimen and the results were found to be reproducible.

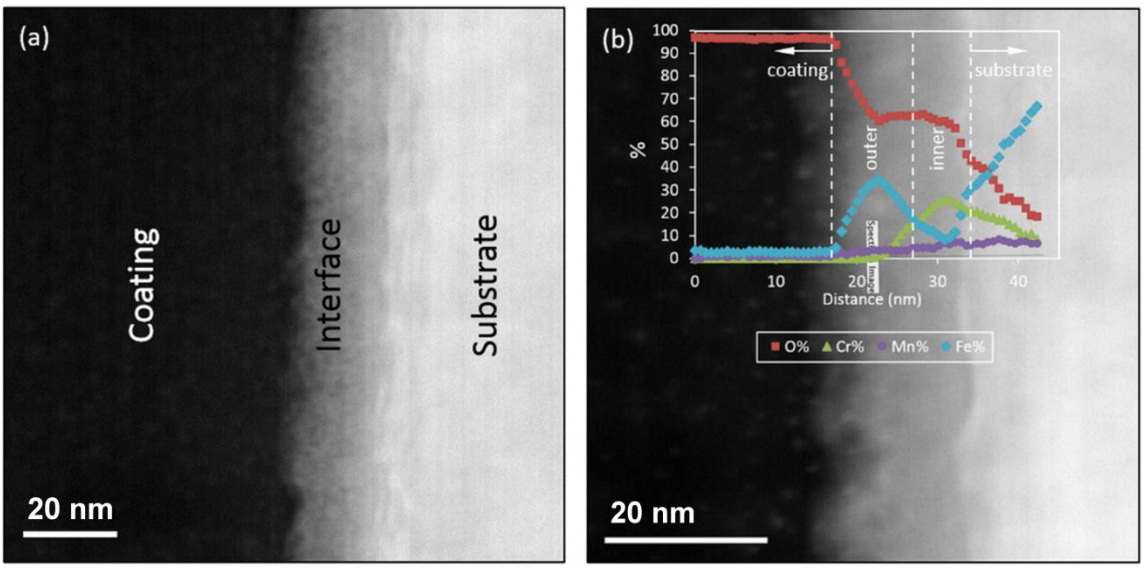

Figure 6.7: *(a) Dark-field STEM cross-sectional image of the coating on AISI 316L substrate. (b) at.% EELS composition line profile of elements O, Cr, Mn and Fe across the interface.*

The relative composition profile across the interface obtained from the EELS data in Figure 6.7(b) confirms a double-layer interface structure, characterized by a Fe-rich (outer interface), followed by a Cr- and Mn-rich (inner interface) region. The signal from the coating includes Si $L_{2,3}$-edge with onset energy of 103 eV and O K-edge with onset energy of ~534 eV, as shown in Figure 6.8(a) and Figure 6.8(b), respectively. Both the onset energies and the shape of these edges indicate that the coating is SiO_2-glass [55]. When approaching the interface from the coating, the intensity of the Si $L_{2,3}$-edge begins

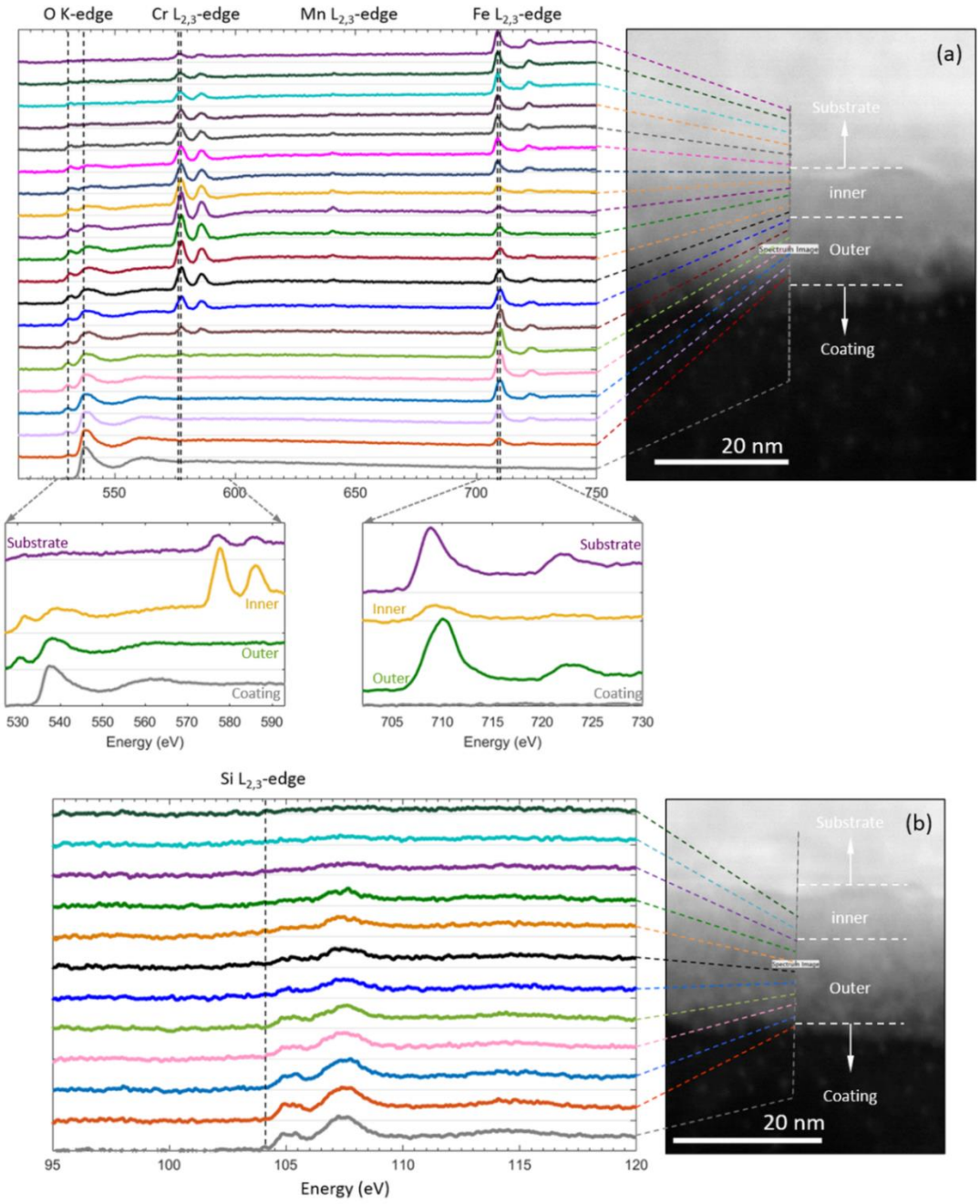

Figure 6.8: *EELS signal containing (a) the O K, Cr $L_{2,3}$, Mn $L_{2,3}$ and Fe $L_{2,3}$-edges and (b) the Si $L_{2,3}$ edge across the interface.*

to decrease without showing any noticeable changes in fine-structure. In contrast, a clear change can be observed between the fine-structure of the O K-edge recorded from the coating and the interface. Most notable is the appearance of a pre-edge at ~528 eV within the entire interface region, which is typical for the ELNES of the O K-edge in transition-metal oxides [56,57].

An additional interesting feature is the position of the Fe, Cr and Mn $L_{2,3}$-edges in the EEL spectra along the line scan in Figure 6.8(a). The position of the L-edge in transition metals has been shown to be sensitive to the their oxidation state, with increase in oxidation state often resulting in shift of L-edges to higher energies [58]. Here, both the Fe and Cr $L_{2,3}$-edges acquired from within the interface are positioned at higher energies than those from the substrate. The peak position of the Fe L_3-edge in the outer interface at 710 eV (positioned at 709 eV in the substrate) is indicative of the presence of Fe^{3+} in this region and a shift in Fe L_3-edge position to 709 eV in the inner interface indicates the presence of Fe^{2+} in this region [59,60]. Similarly, the Cr L_3-edge in the inner interface resembles that of Cr^{3+} [61,62], while the peak position of the Mn L_3- edge signal in the inner interface suggests the presence of Mn^{2+} in this layer [63]. Beside the peak position, the fine structure of the Fe, Cr and O edges also contain information regarding the nature of the interface. The L_3 edge in transition metals typically exhibits a splitting due to crystal field effects, which is influenced by the transition metal's oxidation number and coordination [53,64]. Although this splitting is not fully resolved in the spectra in Figure 6.8(a), the asymmetric profile of the Fe L_3-edge in the outer interface (having a longer tail on the left) combined with the position of its maxima and the fine structure of the O K-edge are indicative of the abundance of Fe_2O_3 in this region [59,60,64]. The Fe L_3-edge in the inner interface shows a different profile (having a longer tail on the right), matching the profile of Fe^{2+}. Both the profile of the Cr L_3-edge and the fine structure of the O K-edge in the inner interface suggest the abundance of Cr_2O_3 in this region [61,64].

Elemental distribution over the interface by EFTEM

EFTEM images, demonstrating the distribution of O, Si, Fe, Cr and Mn across the interface, are presented in Figure 6.9. Analogous to the EELS analysis, the acquisition of EFTEM images for Ni was not possible, due to artefacts from the overlap of the Fe L_1 and Ni $L_{2,3}$ edges. Moreover, specimen radiation damage from the 300 kV electron beam prohibited acquisition of multiple EFTEM images from the same region, making it necessary to move to new regions of the specimen after every acquisition. The results are in general in good agreement with the XPS, EDS and EELS findings: O and Si signals are present in the coating and, to a minor extent, within the interface (Figure 6.9(a,b)), followed by a double-layer interface structure containing mutually exclusive Fe-rich outer and Cr-rich inner layers Figure 6.9(c,d). Further, the EFTEM image of Mn, shown in Figure 6.9(e) shows an enrichment of Mn in the subsurface, as well as in the inner interface.

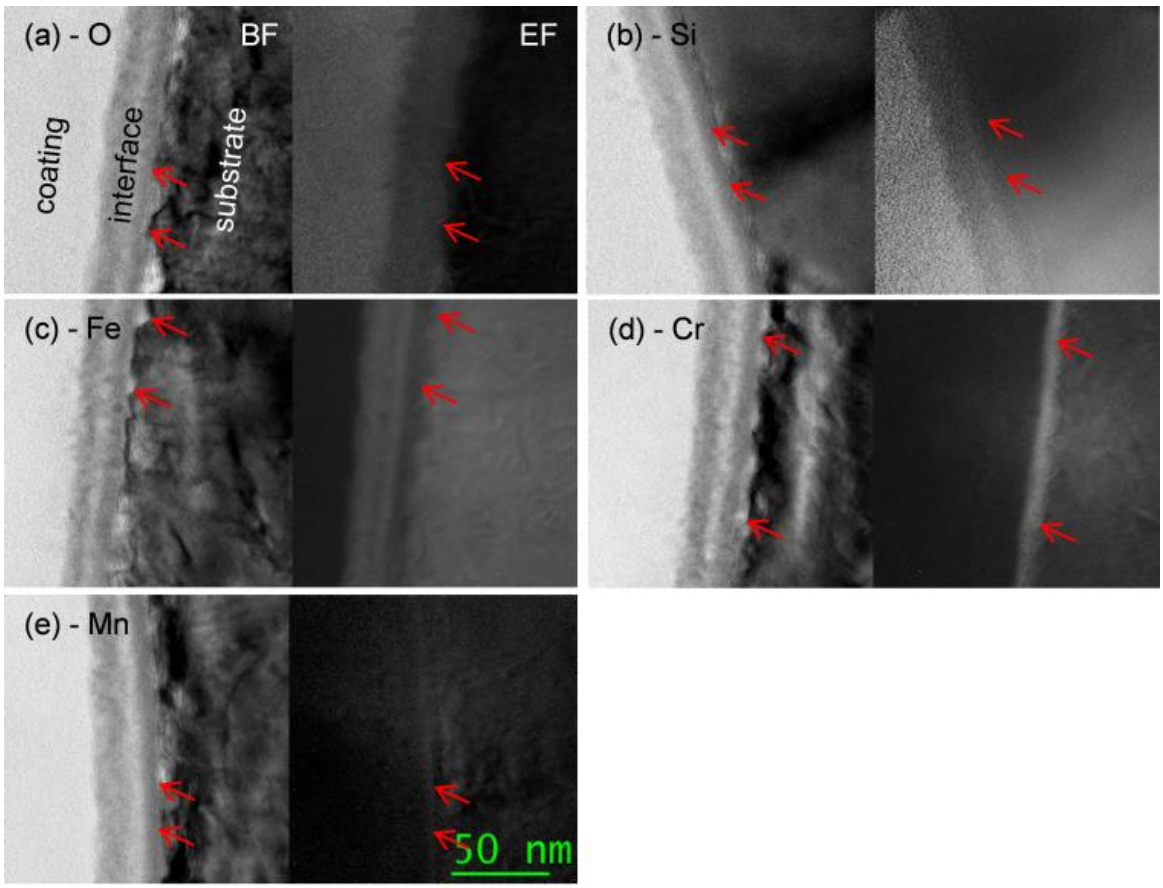

Figure 6.9: *Bright-field (BF) TEM (left) / Energy filtered (EF) TEM (right) images of interfacial region. The scale bar in subfigure (f) is representative for all micrographs. The arrows indicate same positions on the substrate surface on the bright-field/EFTEM images. Images are energy filtered for: (a) O K major edge (532 eV); (b) Si K major edge (1839 eV); (c) Fe L3 major edge (708 eV); (d) Cr L3 major edge (575 eV); (e) Mn L3 major edge (640 eV).*

6.4 Discussion

6.4.1 Chemical composition of the coating

The results indicate a coating stoichiometry of SiO_{2-x}, without incorporation of alloying elements from the substrate. Under the applied curing temperature and atmosphere, cross-linking predominantly takes place by a redistribution reaction [65] and oxidative curing [24], which both yield a gradual reduction of the Si:O ratio from 2:3 in the precursor to 1:2 in a completely polymerized HSQ-based glass [66]. Hence, the observed excess in Si can be associated with an incompletely polymerized coating. In addition to Si^{4+} from the SiO_{2-x} matrix, the film contains a minor quantity of Si^0 that was previously interpreted as Si nano-domains, which form as a byproduct of the thermal decomposition of HSQ [49–51] and contributes to the observed excess in Si. In addition to Si and O, Bremmer *et al.* [24] detected a significant amount of H from residual Si-H and non-condensed Si-OH

moieties in oxidatively cured HSQ films. In analogy, we expect residual H in the film, which was, however, not analyzed in this study.

6.4.2 Chemical composition of the interface

The results show a ~20 nm wide, interface, with an outer Fe-rich zone (outer interface) and an inner Cr-rich zone (inner interface) between the coating and the substrate. The immediate substrate surface shows a distinct depletion in Cr-content. A schematic model of the interface, based on the experimental results and the following discussion, is shown in Figure 6.10(d).

The Si signal in both the EELS fine structure and the XPS peak fitting does not show significant changes from the coating to the interface, suggesting that Si is not chemically bonded to metal oxides. Similarly, the EELS fine structure and the deconvolution of the XPS high resolution spectra of O show the presence of transition-metal oxides in the interface. In consequence, we suggest that the interface is built up as a multi-phase region consisting of SiO_{2-x} and transition-metal oxides. The chemical state analysis of Fe by XPS and EELS show conflicting results in the outer interface: while XPS indicates the presence of both, Fe^{2+} and Fe^{3+}, only the presence of Fe^{3+} can be confirmed via EELS. The validity of XPS for the chemical state analysis of iron after Ar^{+}-ion etching is under discussion [42,43], since ion etching evidently induces the reduction of Fe^{3+} to lower oxidation states [42–44]. Thus, we suggest that the conflict between XPS and EELS originates from the reduction of Fe^{3+} to lower oxidation states and that the outer interface is predominantly composed of SiO_{2-x} and Fe_2O_3. In contrast, the inner interface is predominantly composed of Cr^{3+}-rich oxides with the simultaneous presence of Fe^{2+} and Mn^{2+}, suggesting the formation of a complex (Cr^{3+},Fe^{2+},Mn^{2+})-oxide or a multi-phase oxide region. In addition to oxide formation at the interface, a Cr depleted zone can be observed in the subsurface region of the substrate.

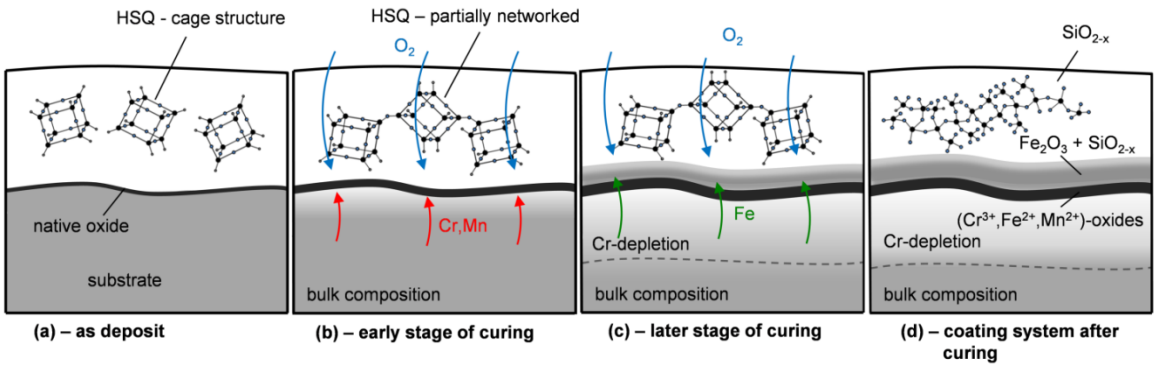

Figure 6.10: *Schematic drawing of coating/substrate interface formation: (a) As-deposit HSQ layer on substrate; (b) Early stage of curing: The easily oxidized substrate elements are oxidized at the coating/substrate interface; (c) Later stage of curing: A Cr depleted zone has formed and Cr diffusion to the interface is hindered. Fe diffuses to the interface and forms an Fe-rich outer interface; (d) Coating system after curing.*

Our results do not agree with findings from Stoch *et al.* [26], who concluded that the interfacial segregation of substrate elements in a sol-gel-based coating system annealed at 700 ºC was driven by the formation of transition metal silicates. This disagreement, may originate from the significantly lower curing temperature applied in this work. On the contrary, our results agree with the findings presented by Takemori [27,28], who detected a complex interfacial film with an outer Fe-rich and an inner Cr-rich interface in a sol-gel-based coating system cured at 500 ºC in air. However, since their analysis was solely based on EDS data without the identification of oxidation states, no unambiguous mechanism for interface formation could be proposed. The herein observed coating/substrate interface resembles the typical double-layered oxide structures found after medium temperature dry oxidation of stainless steels, with a double layered surface oxide [67–70] and a Cr-depleted subsurface zone [71–73] and thus, we suggest that the oxide formation occurs in analogy to stainless steel dry oxidation, as outlaid by Olefjord [71]: The formation of the double layered thermal oxide derives from a competition between thermodynamic driving force for oxidation and kinetic availability of substrate elements. Cr, with a higher thermodynamic driving force for oxidation with respect to Fe [74], is easily oxidized in the initial stage of the heat treatment (Figure 6.10(a,b)), however, cannot be sufficiently supplied from the bulk via diffusion, which retards the formation of a thick Cr-oxide and effectuates a depletion of Cr in the subsurface region (Figure 6.10(b,c)). Fe, as the most abundant substrate element, can be sufficiently supplied to facilitate the growth of an Fe-oxide layer on top of the Cr-rich oxide (Figure 6.10(c)). As model for the two phase formation in the outer interface we propose a growth mechanism of Fe_2O_3 into the incompletely polymerized coating: As reported by others [23,24,75], incompletely polymerized HSQ-based films retain molecular porosity and we conclude that the SiO_{2-x}/Fe_2O_3 two-phase region originates from growth of Fe_2O_3 into the rigid, porous SiO_{2-x}-matrix. Since Ni did not participate in the interfacial formation, the observed increase in relative Ni concentration likely originated from the selective removal of other alloying elements in the subsurface region.

6.4.3 Coating performance

The coating shows good adherence after standardized cross-cut testing and the delamination of the coating is limited to the immediate vicinity of the induced defect. Similar to the investigation by Takemori [27,28], cohesive failure between coating and the outer interfacial oxide is observed and, thus, the air-cured films showed substantially different delamination behavior with respect to films without a pronounced interfacial oxide, where delamination mostly took place as adhesive failure and to a minor extend as cohesive failure directly in the coating material [22]. The results indicate the possibility of crack-propagation between interface and coating and we suggest, in analogy to Takemori [27,28], that the outer interface guides cracks along the surface and, thus, poses a potential weakness in the coating adhesion. However, this work can only give a qualitative assessment of coating adhesion and further dedicated investigations are necessary to conclude on the impact of interfacial oxidation on the coating adhesion.

As stated by Pech *et al.* [11] the ability of silica-coated stainless steel substrates to maintain passivity after coating is of utmost importance for the performance of the coating system in aggressive environments. However, the high temperature oxidation of stainless steels, leading to Cr-depletion of the subsurface region, has shown to sensitize the material for localized corrosion in Cl^- containing electrolytes and decrease resistance to pitting [70,73] and crevice corrosion [72]. Overall, the observed Cr-depletion of the subsurface poses a potential threat for an increased susceptibility to localized corrosion at physical coating defects such as cracks, pinholes or microscopic porosities and a detailed assessment of the consequence of the Cr-depletion on the corrosion performance of the coating system is crucial for the application of HSQ-based SiO_x barrier-coatings and will be the subject of upcoming investigations.

6.5 Conclusion

In summary, we have successfully demonstrated the deposition of HSQ-based thin film coatings on AISI 316L substrate with curing in air ambient. Curing at 450 ºC led to polymerization of the film to a continuous surface layer with a stoichiometry close to SiO_2 in excess of Si, while no long-range diffusion of substrate elements into the coating was observed. The curing process led to the formation of a double layered interfacial oxide between coating and substrate with an Fe^{3+}-rich outer and a Cr^{3+}-rich inner oxide layer. Apart from Cr^{3+}, the inner layer was enriched in Mn^{2+} and Fe^{2+}. Moreover, no formation of a pronounced transition metal silicate region at the coating/substrate boundary was observed. The interface formation was driven by the availability of oxygen at the metal/coating interface and resembles a mechanism similar to medium temperature dry oxidation of stainless steels. A Cr depleted zone was detected below the substrate surface, which could potentially sensitize the material for Cl^- induced corrosion.

Acknowledgements

This work is funded by Innovation Fund Denmark under the grant number 50-2014-1. The authors acknowledge SiOx Aps for the deposition of coatings and all other project partners. The A. P. Møller and Chastine Mc-Kinney Møller Foundation is gratefully acknowledged for their contribution towards the establishment of the Centre for Electron Nanoscopy at the Technical University of Denmark.

References

[1] I. Olefjord, B.O. Elfström, The Composition of the Surface during Passivation of Stainless Steels, Corros. - NACE. 38 (1982) 46–52.

[2] I. Olefjord, H. Fischmeister, ESCA Studies of the Composition Profile of Low Temperature Oxide Formed on Chromium Steels - II. Corrosion in Oxygenated Water, Corros. Sci. 15 (1975) 697–707.

[3] I. Olefjord, B.O. Elfström, Investigation by ESCA of the Passive Film Formed on Austentic Stainless Steel in Oxygenated Water, 6th Eur. Congess Met. Corros. - EUROCORR '77. (1977) 19–28.

[4] E. Deltomee, N. de Zoubov, M. Pourbaix, 10.1 Chromium, in: Atlas Electrochem. Equilibria Aqueous Solut., NACE, Houston, 1996: pp. 256–271.

[5] B.N. Popov, Pitting and Crevice Corrosion, in: Corros. Eng. Princ. Solved Probl., Elsevier B.V., 2015: pp. 289–325.

[6] M. Torkar, F. Tehovnik, M. Godec, Crevice corrosion of stainless-steel fastening components in an indoor marine-water basin, Mater. Technol. 46 (2012) 423–427.

[7] K.M. Deen, M. a. Virk, C.I. Haque, R. Ahmad, I.H. Khan, Failure investigation of heat exchanger plates due to pitting corrosion, Eng. Fail. Anal. 17 (2010) 886–893.

[8] J. Smiderle, J.M. Pardal, S.S.M. Tavares, A.C.N. Vidal, Premature failure of superduplex stainless steel pipe by pitting in sea water environment, Eng. Fail. Anal. 46 (2014) 134–139.

[9] P. Sharma, H. Roy, Pitting corrosion failure of an AISI stainless steel pointer rod, Eng. Fail. Anal. 44 (2014) 400–407.

[10] S. Kaewkumsai, S. Auampan, K. Wongpinkaew, E. Viyanit, Root cause analysis for 316L stainless steel tube leakages, Eng. Fail. Anal. 37 (2014) 53–63. d.

[11] D. Pech, P. Steyer, J.-P. Millet, Electrochemical behaviour enhancement of stainless steels by a SiO2 PACVD coating, Corros. Sci. 50 (2008) 1492–1497.

[12] S. Meth, N. Savchenko, F.A. Viva, D. Starosvetsky, A. Groysman, C.N. Sukenik, Siloxane-based thin films for corrosion protection of stainless steel in chloride media, J. Appl. Electrochem. 41 (2011) 885–890.

[13] D.C.L. Vasconcelos, J.A.N. Carvalho, M. Mantel, W.L. Vasconcelos, Corrosion resistance of stainless steel coated with sol–gel silica, J. Non. Cryst. Solids. 273 (2000) 135–139.

[14] M. Atik, P. de Lima Neto, L.A. Avaca, M.A. Aegerter, J. Zarzycki, Protection of 316L stainless steel against corrosion by SiO2 coatings, J. Mater. Sci. Lett. 13 (1994) 1081–1085.

[15] J. de Damborenea, N. Pellegri, O. Sanctis, A. Duran, Electrochemical Behaviour of SiO2 Sol-Gel Coatings on Stainless Steel, J. Sol-Gel Sci. Technol. 4 (1995) 239–244.

[16] K. Mohaghegh, H.N. Hansen, H. Pranov, G. Kofod, A study on the surface roughness of a thin HSQ coating on a fine milled surface, in: 14th Euspen Int. Conf. - Dubrovink, 2014.

[17] K. Mohaghegh, H.N. Hansen, H. Pranov, G. Kofod, Verification of thickness and surface roughness of a thin film transparent coating, in: Proc. 13th Euspen Int. Conf., Berlin, 2013.

[18] H. Pranov, Spin-on-glass assisted polishing of rough substrates, WO 2013/083129 A1, 2013.

[19] J. Cech, H. Pranov, G. Kofod, M. Matschuk, S. Murthy, R. Taboryski, Surface roughness reduction using spray-coated hydrogen silsesquioxane reflow, Appl. Surf. Sci. 280 (2013) 424–430.

[20] T.C. Hobæk, M. Matschuk, J. Kafka, H.J. Pranov, N.B. Larsen, Hydrogen silsesquioxane mold coatings for improved replication of nanopatterns by injection molding, J. Micromechanics Microengineering. 25 (2015) 35018.

[21] H. Pranov, Reactive Silicon Oxide Precursor Facilitated Anti-Corrosion Treatment, US 2014/0154441 A1, USA, 2014.

[22] F. Lampert, A.H. Jensen, R.U. Din, P. Møller, Hydrogen Silsesquioxane based silica glass coatings for the corrosion protection of austenitic stainless steel, Surf. Coatings Technol.

307 (2016) 879–885.
[23] Y.K. Siew, G. Sarkar, X. Hu, J. Hui, A. See, C.T. Chua, Thermal Curing of Hydrogen Silsesquioxane, J. Electrochem. Soc. 147 (2000) 335.
[24] J.N. Bremmer, Y. Liu, K.G. Gruszynski, F.C. Dall, Cure of Hydrogen Silsesquioxane for Intermetal Dielectric Applications, Mater. Res. Soc. Symposium Proc. 476 (1997) 37–44.
[25] M.J. Loboda, C.M. Grove, R.F. Schneider, Properties of a-SiOx:H Thin Films Deposited form Hydrogen Silsesquioxane Resins, J. Electrochem. Soc. 145 (1998) 2861–2866.
[26] A. Stoch, J. Stoch, A. Rakowska, An XPS and SEMS study of silica sol-gel/metal substrate interaction, Surf. Interface Anal. 22 (1994) 242–247.
[27] M. Takemori, Crack formation, exfoliation, and ridge formation in 500 ^{o}C annealed sol-gel silica coatings on stainless steel SUS304: Part I. Microscopic observations and elemental analysis, Ceram. Int. 35 (2009) 1731–1746.
[28] M. Takemori, Crack formation, exfoliation, and ridge formation in 500 °C annealed sol–gel silica coatings on stainless steel SUS304: Part II Spectroscopic and mechanical analyses and insights into mechanisms controlling coating characteristics, Ceram. Int. 35 (2009) 1747–1755.
[29] D.E. Clark, C.G. Pantano, G.Y. Onoda, Auger Analysis of Brass-Enamel Stainless Steel-Enamel Interfaces, J. Am. Ceram. Soc. Notes. 58 (1975) 336–337.
[30] ISO 2409:2007(E) Paints and varnishes - Cross-cut test, 2007.
[31] E. Sacher, Asymmetries in Transition Metal XPS Spectra: Metal Nanoparticle Structure, and Interaction with the Graphene-Structured Substrate Surface, Langmuir. 26 (2010) 3807–3814.
[32] W. Fredriksson, K. Edström, C.-O.A. Olsson, XPS analysis of manganese in stainless steel passive films on 1.4432 and the lean duplex 1.4162, Corros. Sci. 52 (2010) 2505–2510.
[33] J.H. Scofield, Hartree-Slater Subshell Photoionization Cross-Sections at 1254 and 1487 eV, J. Electron Spectros. Relat. Phenomena. 8 (1976) 129–137.
[34] Y. Huh, K.J. Hong, K.S. Shin, Amorphization induced by focused ion beam milling in metallic and electronic materials, Microsc. Microanal. 19 (2013) 33–7.
[35] D.B. Williams, C.B. Carter, 39.4.B Background Subtraction, in: Transm. Electron Microsc. Part1 Basics, 2009: pp. 726–728.
[36] C.L. Bianchi, M.G. Cattania, P. Villa, XPS characterization of Ni and Mo oxides before and after "In situ" treatments, Appl. Surf. Sci. 70/71 (1993) 211–216.
[37] A.M. Rossi, B. Elsener, Ageing of Passive Films on Stainless Steels in Sulfate Solutions - XPS Analysis, Mater. Sci. Forum. 185–188 (1995) 337–346.
[38] A.G. Sault, Quantitative analysis of Auger lineshapes of oxidized iron, Appl. Surf. Sci. 74 (1994) 249–262.
[39] D.D. Hawn, B.M. DeKoven, Deconvalution as a Correction for Photoelectron Inelastic Energy Losses in the Core Level XPS Spectra of Iron Oxides, Surf. Interface Anal. 10 (1987) 63–74.
[40] E. Paparazzo, XPS analysis of oxides, Surf. Interface Anal. 12 (1988) 115–118.
[41] T. Yamashita, P. Hayes, Analysis of XPS spectra of Fe2+ and Fe3+ ions in oxide materials, Appl. Surf. Sci. 254 (2008) 2441–2449.
[42] L.I. Yin, S. Ghose, I. Adler, X-ray Photoelectron Spectroscopic Studies of Valence States Produced by Ion-Sputtering Reduction, Appl. Spectrosc. 26 (1972) 355–357.
[43] K.S. Kim, W.E. Baitinger, J.W. Amy, N. Winograd, Esca studies of metal-oxygen surfaces using argon and oxygen ion-bombardment bombardment, J. Electron Spectros. Relat. Phenomena. 5 (1974) 351–367.
[44] B.O. Elfström, I. Olefjord, Preparation of Alloys for ESCA Investigation, Phys. Scr. 16 (1977) 436–441.
[45] T.P. Moffat, R.M. Latanision, R.R. Ruf, An X-Ray Photoelectron Spectroscopy Study of Chromium-Metalloid Alloys - III, Electrochim. Acta. 40 (1995) 1723–1734.
[46] J. Finster, E.-D. Klinkenberg, J. Heeg, ESCA and SEXAFS investigations of insulating materials for U LSI microelectronics, Vacuum. 41 (1990) 1586–1589.
[47] M. Hassel, I. Hemmerich, H. Kuhlenbeck, H.-J. Freund, High Resolution XPS Study of a

Thin Cr2O3(111) Film Grown on Cr(110), Surf. Sci. Spectra. 4 (1998) 246–252.
[48] D.R. Wheeler, W.A. Brainard, Composition of RF-Sputtered Refractory Compounds Determined by X-ray Photoelectron Spectroscopy, J. Vac. Sci. Technol. 15 (1978) 24–30.
[49] H.-S. Lee, J.-S. Wi, S.-W. Nam, H.-M. Kim, K.-B. Kim, Two-step resist-development process of hydrogen silsesquioxane for high-density electron-beam nanopatterning, J. Vac. Sci. Technol. B Microelectron. Nanom. Struct. 27 (2009) 188.
[50] C.M. Hessel, E.J. Henderson, J.G.C. Veinot, An Investigation of the Formation and Growth of Oxide-Embedded Silicon Nanocrystals in Hydrogen Silsesquioxane-Derived Nanocomposites, J. Phys. Chem. C. 111 (2007) 6956–6961.
[51] C.M. Hessel, E.J. Henderson, J.G.C. Veinot, Hydrogen Silsesquioxane: A Molecular Precursor for Nanocrystalline Si-SiO2 Composites and Freestanding Hydride-Surface-Terminated Silicon Nanoparticles, Chem. Mater. 18 (2006) 6139–6146.
[52] R.F. Egerton, Electron energy-loss spectroscopy in the TEM, Reports Prog. Phys. 72 (2009) 16502.
[53] J.H. Paterson, O.L. Krivanek, ELNES of 3d transition-metal oxides II. Variations with oxidation state and crystal structure, Ultramicroscopy. 32 (1990) 319–325.
[54] R. Brydson, H. Sauer, W. Engel, E. Zeitler, EELS as a fingerpring of the chemical co-ordination of light elements, Microsc. Microanal. Microstruct. 2 (1991) 159–169.
[55] L.A.J. Garvie, P.R. Buseck, Bonding in silicates : Investigation of the Si L2,3 edge by parallel electron energy-loss spectroscopy, Am. Mineral. 84 (1999) 946–964.
[56] L.A. Grunes, R.D. Leapman, C.N. Wilker, R. Hoffmann, A.B. Kunz, Oxygen K near-edge fine structure: An electron-energy-loss investigation with comparisons to new theory for selected 3d transition metal oxides, Phys. Rev. B. 25 (1982) 7157–7173.
[57] F.M.F. Groot, M. Grioni, J.C. Fuggle, J. Ghijsen, G.A. Sawatzky, H. Peterson, Oxygen 1s x-ray-absorption edges of transition-metal oxides, Phys. Rev. B. 40 (1989) 5715–5723.
[58] J. Taftø, O.L. Krivanek, Site-Specific Valence Determination by Electron Energy-Loss Spectroscopy, Phys. Rev. Lett. 48 (1982) 560–563.
[59] H. Tan, J. Verbeeck, A. Abakumov, G. Van Tendeloo, Oxidation state and chemical shift investigation in transition metal oxides by EELS, Ultramicroscopy. 116 (2012) 24–33.
[60] L.A.J. Garvie, P.R. Buseck, Ratios of ferrous to ferric iron from nanometre-sized areas in minerals, Nature. 396 (1998) 667–670.
[61] A.M. Arévalo-López, M.A. Alario-Franco, Reliable Method for Determining the Oxidation State in Chromium Oxides, Inorg. Chem. 48 (2009) 11843–11846.
[62] E. Stoyanov, F. Langenhorst, The effect of valence state and site geometry on Cr L3,2 electron energy-loss spectra of Cr-bearing oxidic compounds, Chemie Der Erde - Geochemistry. 74 (2014) 497–505.
[63] H.K. Schmid, W. Mader, Oxidation states of Mn and Fe in various compound oxide systems, Micron. 37 (2006) 426–432.
[64] O.L. Krivanek, J.H. Paterson, ELNES of 3d transition-metal oxides I. Variation across the periodic table, Ultramicroscopy. 32 (1990) 313–318.
[65] V. Belot, R.J.P. Corriu, D. Leclercq, P.H. Mutin, A. Vioux, Redistribution reactions in silsesquioxane gels, J. Mater. Sci. Lett. 9 (1990) 1052–1054.
[66] D. Tobben, P. Weigand, M.J. Shapiro, S.A. Cohen, Influence of the cure process on the properties of hydrogen silsesquioxane spin-on-glass, Mater. Res. Soc. Somposium Proc. 443 (1997) 195–200.
[67] I. Olefjord, ESCA Studies on Films Formed on Stainless Steels during Oxidation and during Electropolishing, Scand. J. Metall. 3 (1974) 129–136.
[68] H.J. Yearian, E.C. Randell, T.A. Longo, The Structure of Oxide Scales on Chromium Steels, Corros. - NACE. 12 (1956) 515–252.
[69] T. Kosaka, S. Suzuki, H. Inoue, M. Saito, Y. Waseda, E. Matsubara, XPS/GIXS studies of thin oxide films formed on Fe-Cr alloys, Appl. Surf. Sci. 103 (1996) 55–61.
[70] T. von Moltke, P.C. Pistorius, R.F. Sandenbergh, The Influence of Heat-tinted Surface Layers on the Corrosion Resistance of Stainless Steels, in: Proc. 1st Int. Chromium Steel Alloy. Congr. Cape Town, Vol. 2, 1992: pp. 185–196.

[71] I. Olefjord, Application of ESCA to Oxide Films Formed on Stainless Steels at Intermediate and High Temperatures, Met. Sci. 9 (1975) 263–268.
[72] G. Hultquist, C. Leygraf, Selective Oxidation of a Ferritic Stainless Steel and its Influence on Resistance to Crevice Corrosion Initiation, Corros. Sci. 21 (1981) 401–408.
[73] M. Somervuori, L.-S. Johansson, M.H. Heinonen, D.H.D. van Hoecke, N. Akdut, H.E. Hänninen, Characterisation and corrosion of spot welds of austenitic stainless steels, Mater. Corros. 55 (2004) 421–436.
[74] J. Kofstad, High Temperature Oxidation of Metals, Wiley, New York, 1966.
[75] C.-C. Yang, W.-C. Chen, The structures and properties of hydrogen silsesquioxane (HSQ) films produced by thermal curing, J. Mater. Chem. 12 (2002) 1138–1141.

7 Manuscript III

Corrosion resistance of AISI 316L coated with an air-cured hydrogen silsesquioxane based spin-on-glass enamel in chloride environment*

Felix Lampert[a], Alexander Bruun Christiansen[b], Rameez Ud Din[a], Yiaza Gonzalez-Gacia[c], Per Møller[a]

[a] Technical University of Denmark, Department of Mechanical Engineering, 2800 Kgs. Lyngby, Denmark
[b] SiOx ApS, Bybjergvej 7, 3600 Espergærde, Denmark
[c] Delft University of Technology, Department of Materials Science and Engineering, 2628CD Delft, The Netherlands
[d] Technical University of Denmark (DTU), Department of Mechanical Engineering, Nils Koppels Allé, Building 404, 2800 Kgs. Lyngby, Denmark

Abstract

The efficiency of thin hydrogen silsesquioxane (HSQ) -based corrosion barrier coatings on 316L substrates after oxidative thermal curing at 400-550 ºC in air was investigated. Infrared spectroscopy and electrochemical impedance spectroscopy showed that an increasing curing temperature leads to progressing coating densification, accompanied by decreasing barrier properties. Cyclic polarization measurements indicated that defects due to substrate oxidation are detrimental for the substrate passivity. Insufficiently polymerized coatings showed poor chemical stability in neutral salt spray testing and the chemical coating stability increased with curing temperature. Oxidative curing was found inadequate as polymerization treatment of HSQ-based corrosion barrier coatings on 316L substrate.

* published work: F. Lampert, A. Christiansen, R.U. Din, Y. Gonzalez-Garcia, P. Møller, Corrosion Science (In press, August 24th 2017). The format of the article has been edited to match the dissertation.

7.1 Introduction

Gasketed plate heat exchangers find application in generic heating/cooling systems and may find use in *e.g.* marine applications, which necessitates sufficient resistance of the plate materials towards corrosion in hot seawater. Due to the highly corrosive properties of the environment during service, the heat exchangers are typically fitted with Ti-alloy plates, which behave virtually inert in this environment. Despite the outstanding performance, the high price of the material gives an incentive to change from Ti-based plates to other plate materials such as stainless steels, which may yield a significant reduction in material cost under high volume production. However, stainless steels may be sensitive to localized corrosion in seawater [1–3] and the application of stainless steels as plate material in Cl^- containing media is highly compromised due to localized corrosive failure of the plates [4], triggering the need for costly, highly alloyed steels or advanced corrosion prevention strategies. Traditional corrosion protection concepts, such as organic coatings or vitreous enamels, impair the heat transfer over the plates and are not applicable for heat exchanger plates. Moreover, advanced corrosion protection concepts such as cathodic protection are challenging, due to the complex geometry of the assembled component, triggering the need for novel concepts to increase the lifetime of stainless steels in marine heat exchangers.

As a viable concept to prevent the corrosive failure of stainless steel components in saline environment, the deposition of micrometer/sub-micrometer –thick anti-corrosion coating films based on inorganic ceramics such as TiO_2 [5–8], Al_2O_3 [9] and SiO_x [10–14] or organic/inorganic hybrid materials [15] has been investigated. In particular, inert thin coating systems, *i.e.* ~50-600 nm based on SiO_x from chemical vapor deposition (CVD) or sol-gel processing have shown promising results in suppressing both corrosion in chloride [14,16] and acid media [10,11]. Similar to traditional vitreous enamels [17], which typically exhibit thicknesses at millimeter-scale, the coating films act as a physical barrier between the substrate and the aggressive environment and show remarkable barrier properties towards ionic transport [14]. The application of thin film coating technology is of particular interest for heat exchangers, since it promises significant enhancements in material durability or resistance towards biofouling [18,19] at a minimum impairment of the heat transfer.

Despite their high potential, the applicability of the existing technologies is limited due to the high processing cost of CVD processes, which require a reactor and vacuum equipment [20], or the inherently porous nature of sol-gel SiO_2, which requires high temperature sintering (> 600 ºC) to reach fully densified ceramic films [21]. As a viable alternative to the traditional processes, the deposition of SiO_2-like films from hydrogen silsesquioxane (HSQ) precursor has been demonstrated [22–24]. Since the process relies on the deposition of a liquid precursor by *e.g.* spin-, dip- or spray- coating without the need for complex processing equipment, it shows significant economic advantages with respect to CVD processes together with a decrease in thermal budget with respect to sol-

gel processes, since inherent film porosities collapse at curing temperatures around 435 ºC [22]. Recent investigations [25–31] validated the applicability of HSQ as precursor for sub-micrometer thick coatings on metallic substrates with a particular industrial interest as planarization treatment [25,26,29] or carrier of nanopatterns [28] for injection molding tools. In addition, HSQ-based thin films have shown to possess excellent barrier properties in aqueous solutions [31] and are promising precursors for the next generation of sub-micrometer thick barrier coatings.

HSQ-based spin-on-glass has been primarily developed for the application as low dielectric constant interlayer dielectric material for microelectronics [22–24]. To avoid the deterioration of the dielectric constant, leading to increased parasitic capacitance in interlayer dielectric applications [32], the material needs to be thermally polymerized in oxygen-free atmosphere [23]. As discussed by Bremmer *et al.* [23], the introduction of oxygen to the curing atmosphere leads to a change in the predominant polymerization mechanism from a bond redistribution reaction to an oxidation/condensation of the precursor, yielding a higher curing efficiency of the process and, thus, a reduced thermal budget for oxidative curing. Despite the higher curing efficiency and decreased thermal budget of oxidative film curing [23], curing in oxygen-free environment has been adopted for coating applications [25,26,28,31], where an increase in dielectric constant does not impact the performance.

Our recent investigations [33], demonstrated the feasibility of oxidative curing of HSQ-based coatings on stainless steel substrates in air ambient at 450 ºC. The process yielded well adherent, sub-micrometer thick films with a stoichiometry close to SiO_2 and excellent substrate coverage. In contrast to curing in oxygen depleted environment [31], access to oxygen at the coating/metal interface led to thermal oxidation of the substrate, yielding a ~20-30 nm thick interface oxide in connection with a Cr-depleted zone in the substrate surface. The impact of the interfacial oxide and Cr depletion on the corrosion properties of oxidatively cured HSQ-based spin-on-glass coatings was not reported, however, it was suggested that it may compromise the advantages of the novel, more efficient curing process with respect to oxygen-free curing. Our previous investigation [31] on the anti-corrosion performance of HSQ-based coatings solely focused on non-oxidatively cured systems and, further, only assessed the coating barrier properties in *p*H-buffered solution for short immersion times. However, the successful implementation of the technology requires a detailed assessment of the coating barrier properties and polarization resistance in a technically relevant electrolyte such as NaCl solution as well as an assessment of the long-term coating stability by standardized techniques such as salt spray testing, necessitating a detailed study of the material behavior as barrier coating in chloride environment.

Hence, the present work focuses on the microstructure, corrosion performance and evaluation of HSQ-based coatings on AISI 316L substrates in the curing temperature range from 400-550 ºC in air. The effect of the curing-temperature variation on the

coating microstructure, chemistry and wetting is investigated using focused ion beam assisted scanning electron microscopy, infrared spectroscopy and water contact angle measurements, respectively. Moreover, the corrosion performance of coated substrates in chloride containing media is evaluated by cyclic polarization, electrochemical impedance spectroscopy, the scanning vibrating electrode technique and neutral salt spray testing.

7.2 Experimental

7.2.1 Thin film deposition

AISI 316L (Composition (wt.%): 17.5 Cr, 10.5 Ni, 2.2 Mo, 1.2 Mn, 0.5 Si, bal. Fe; determined by Energy dispersive X-ray spectroscopy (EDS) at 20 kV acceleration voltage on a JEOL JSM-5900 Scanning Electron Microscope (SEM) with Oxford Instruments EDS detector) test coupons with no. 2B surface finish and dimension of 50 x 100 x 1 mm^3 have been coated with the commercial product Dow Corning FOx 25 flowable oxide, which is a solution containing 22-23 wt.% HSQ, $(HSiO_{3/2})_n$, in a blend of $C_8H_{24}O_2Si_3$ with $C_6H_{18}OSi_2$ in a ratio of 1:3. The coating deposition was carried out in analogy to Lampert *et al.* [33], *i.e.* by dip-coating with 1 mm/s withdrawal speed, followed by a soft-baking step at 160 ºC for 30 min (leading to solvent evaporation) and a thermal polymerization cycle for 2 h in air, whereby the polymerization temperature was varied between 400 and 550 ºC. Prior to deposition, the metallic substrates were prepared by immersion degreasing in Schlötter Slotoclean AK 90, followed by anodic degreasing in Schlötter Slotoclean EL DCG at 8 A/dm^2 and acid picklilng in Schlötter Slotoclean Decasel 5. For thin film analysis by FT-IR, thin films were deposited on the front side of Si-wafers (Topsil FZ, 675 µm thickness, front side polished, backside etched) and cured in a similar fashion. In the following, the "uncured" sample condition refers to a soft-baked film deposited on Si-wafer substrate. The four different curing conditions of coatings on AISI 316L substrate will be denoted as "sample *curing temperature*", while uncoated, bare AISI 316L substrates will be denoted as "uncoated" reference.

7.2.2 Microstructure, chemical and electrochemical characterization

Scanning electron microscopy (SEM)

SEM analysis was performed on a Helios Nanolab 600 dual beam SEM fitted with a field emission gun and a Ga^+ focused ion beam source. Cross-sections of coated samples were prepared by ion beam milling at 30 kV acceleration voltage and imaging on the trench wall under 52 º sample tilt. Prior to ion beam milling, the surface was protected by Pt deposition to minimize the effect of ion beam damage. All samples prepared for electron microscopy were sputter coated with an Au film of a few nanometers thickness to reduce the effect of surface charging. The microscope was operated at 5 kV acceleration voltage for SEM imaging. The further microscope settings, *i.e.* detector type (Everhart-Thornley detector (ETD) or Through Lens detector (TLD)) and beam current, are indicated in the respective figure captions.

Fourier transformed infrared spectroscopy (FT-IR)

FT-IR data acquisition was carried out on a Thermo Scientific Nicolet iN10 MX on thin films deposited on Si-wafer. All measurements were performed in transmission mode, whereby the background was acquired on a Si-wafer. Quantification of the Si-H ratio was done by integration of the Si-H stretching edge on a linear background and the reported residual Si-H ratio is the peak area normalized by the peak area of a soft baked, uncured film.

Water contact angle

Water contact angles were determined on the coated AISI 316L substrates on a ramé-hart instrument co. water contact angle goniometer by the sessile drop method with a droplet volume of 10 µl of purified water at room temperature. The reported values are averaged over 3 individual measurements.

Anodic cyclic potentiodynamic polarization (anodic CP)

The coated test coupons were investigated by cyclic potentiodynamic anodic polarization (CP) in *p*H neutral 3.5 wt.% aqueous NaCl solution on an ACM Instruments GillAC potentiostat. Anodic CP experiments were conducted in a flat corrosion cell with the cell design from Qvarfort [34]. The measurements were performed on an area of 1 cm^2 and a solution volume of 400 ml against a KCl saturated silver chloride (Ag-AgCl) reference electrode. Anodic CP-scans were performed after a cell-settle time of 3600 s with a scan rate of 1 mV/s. The experiments were repeated 3 times for consistency.

Scanning vibrating electrode technique (SVET)

SVET analysis was carried out on an Applicable Electronics system, which was fitted with a platinized Pt/Ir-alloy vibrating probe and platinized Pt/Ir-alloy reference and ground electrodes. The probe diameter after platinization in 10 vol.% $PtCl_2$ + 1 vol.% $Pb(C_2H_3O_2)_2$ aqueous solution was ~30 µm. The probe capacitance was monitored before each experiment and kept above 2 nF. The sample surface was masked with a nonconductive varnish and the system was operated on the freely corroding surface with an average probe working distance of 100 µm in a solution volume of 2 ml. Since no sufficiently high corrosion rates could be obtained in NaCl aqueous solutions without external polarization, the experiments were carried out in an aqueous solution of 1 wt.% $FeCl_3$*H_2O with pH ~2 and solution resistivity of 82.03 Ωcm (determined on a Radiometer Copenhagen CDM 80 conductivity meter). The SVET maps were acquired with a size of 2.1 x 2.1 mm^2 at a resolution of 31 x 31 points, yielding a scan-rate of 20 minutes/map.

Electrochemical impedance spectroscopy (EIS)

EIS was performed on a Gamry Ref600 potentiostat in a flat, gasketed corrosion cell with 2.1 cm^2 area and 15 ml solution volume of neutral 3.5 wt.% NaCl aqueous solution. The potential was measured against a saturated calomel electrode and perturbed by a Pt-wire auxiliary electrode with an amplitude of $\pm$10 mV around the corrosion potential. The cell settle time prior to EIS measurements was 3600 s. Data analysis was carried out by equivalent circuit fitting with the commercial software Gamry Echem Analyst V 6.31 by the simplex method. The experimental data were validated by an automatic Kramers-Kronig test and all experiments were repeated 5 times to ensure consistency.

Neutral salt spray testing

Two redundant sets of samples were investigated by neutral salt spray testing in an Erichsen Corrocompact Model 612 corrosion testing apparatus. The tests were performed in accordance to EN ISO 9227:2012 [35] and discontinued after 1000 h due to severe failure of the coatings.

7.3 Results and discussion

7.3.1 Visual appearance and microstructure

Digital photographs of half-coated test coupons are shown in Figure 7.1. In general, the coated part of the coupons shows distinct discoloration, *i.e.* blue/golden, yellow/golden and brown/golden depending on the curing temperature, while the uncoated part of the coupons is tarnished due to thermal oxidation.

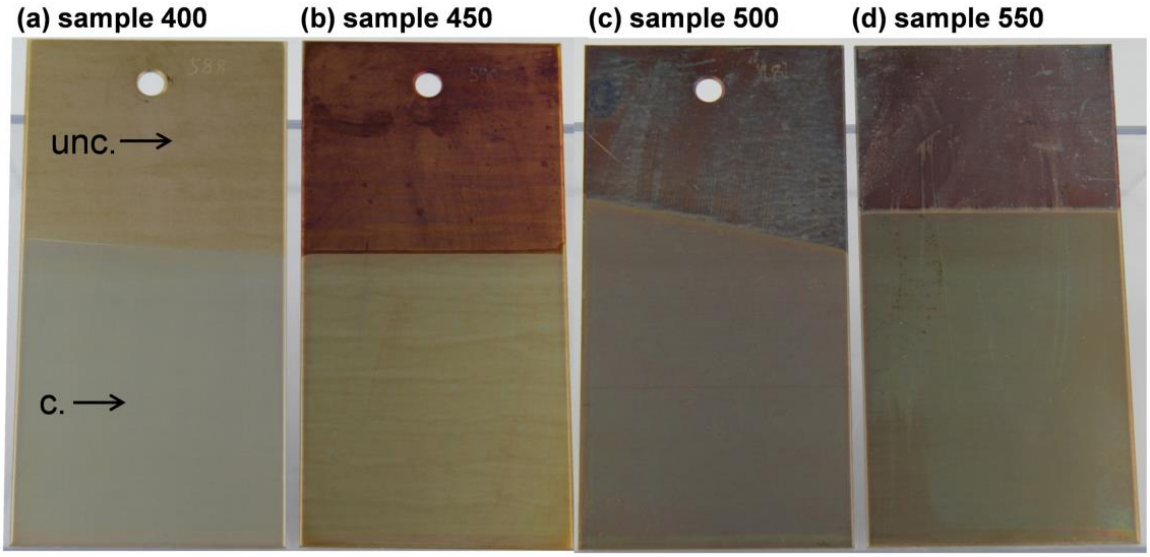

Figure 7.1: *Digital photographs of test coupons (size 100x50 mm^2) with coated (c.) and uncoated (unc.) parts after curing at: (a) 400 ˚C; (b) 450 ˚C; (c) 500 ˚C; (d) 550 ˚C.*

Similar to previous investigations [31,33], the coatings show good coverage and leveling via flowing into sub-micrometer substrate defects (Figure 7.2), leading to an inhomogeneous thickness distribution with a minimum thickness of ~200 nm, as indicated in the subfigures of Figure 7.2. Furthermore, the coatings on samples 400 and 450 are well adherent (Figure 7.2(a,b)), whereas voids at the metal-coating interface are observed for samples 500 and 550 (Figure 7.2(c,d)). All samples show a distinct interface layer at the metal-coating interface (indicated by "interface" in Figure 7.2), which increases in thickness with increasing curing temperature. As previously shown for sample 450 [33], the interface is composed of transition metal oxides from the thermal oxidation of the substrate and, in analogy, it can be assumed that the interface layers are predominantly formed by the thermal oxidation of the substrate.

7.3.2 Film chemistry

The chemistry and degree of cross-linking of HSQ-based thin films is frequently characterized by FT-IR [22,23,36]. An FT-IR absorption plot for an uncured reference film along with the cured film conditions is shown in Figure 7.3, whereby the identification of the FT-IR spectral features was carried out according to the edge

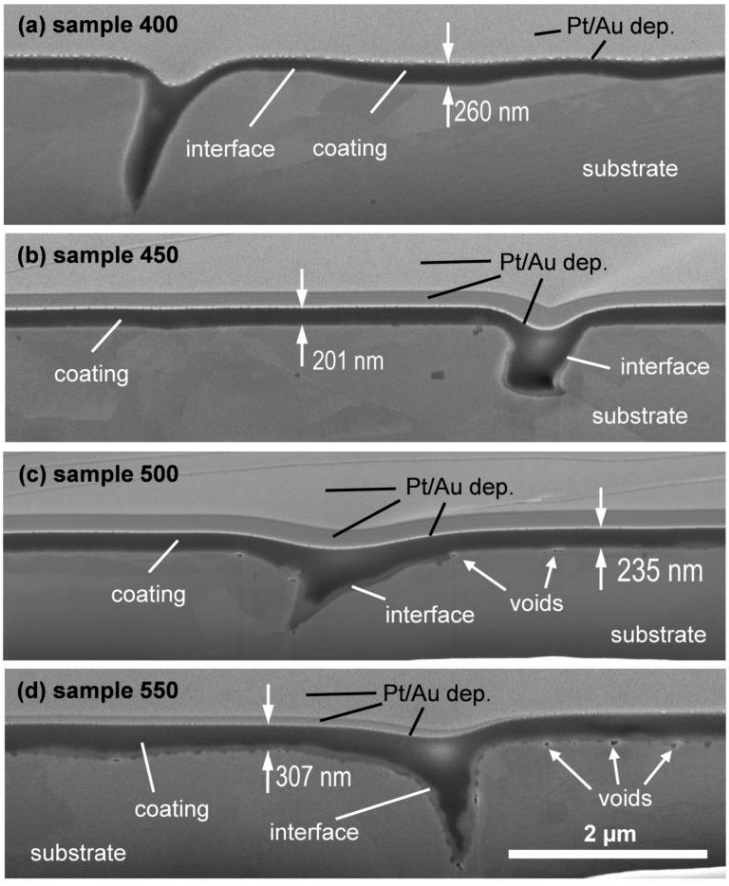

Figure 7.2: *SEM images of FIB-milled cross-sections: samples cured at (a) 400 ˚C; (b) 450 ˚C; (c) 500 ˚C; (d) 550 ˚C. The areas have been coated with Au and Pt prior to milling. Microscope settings: TLD; beam current 86 pA.*

positions summarized in Table 7.1. As shown in Figure 7.3, the FT-IR absorption spectrum of uncured HSQ is dominated by pronounced absorption from Si-H stretching and Si-O asymmetric stretching in cage structure while neither silanol nor water can be detected. Curing between 400 and 550 ºC leads to a clear shift in Si-O asymmetric stretching from 1140 cm^{-1} to 1075 cm^{-1}, together with a loss in absorption from Si-H stretching, indicating progressive polymerization of the films [36]. In addition to Si-H

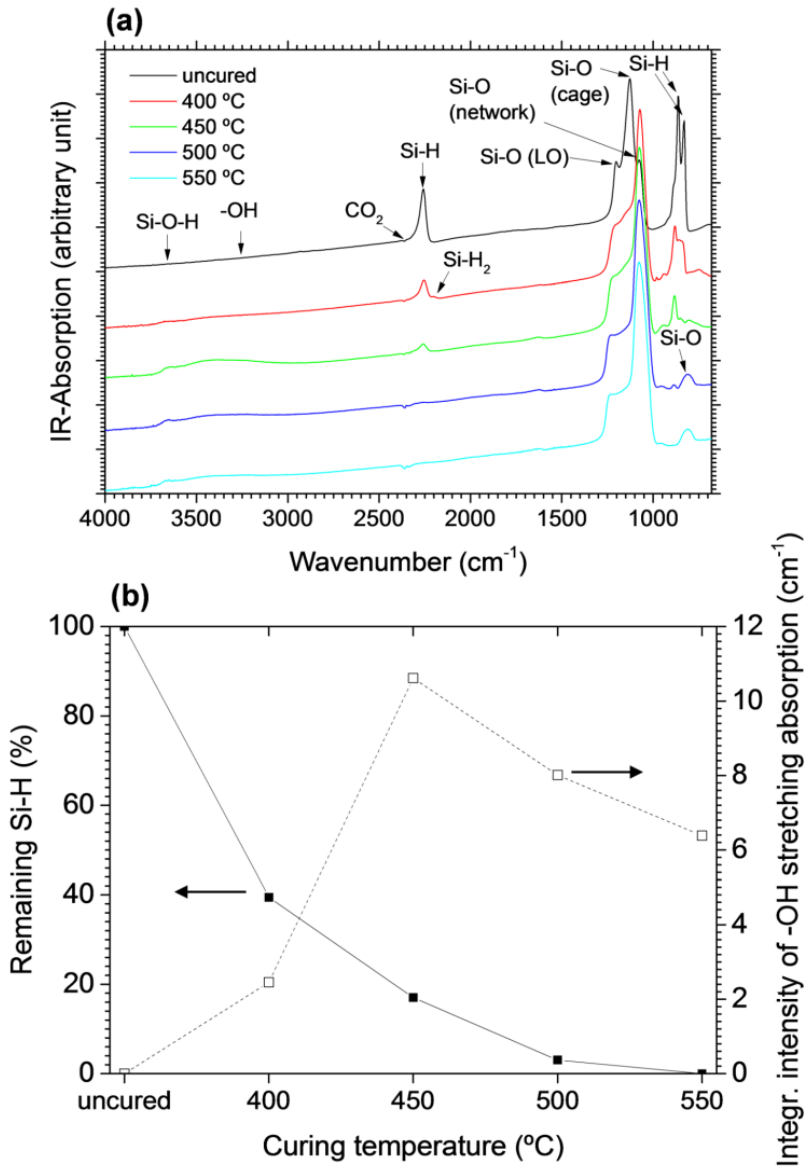

Figure 7.3: *(a) FT-IR absorption spectra of HSQ films deposited on Si wafer. The origin of the edges is summarized in Table 1. "Uncured" refers to an HSQ film which was soft-baked (dried at 160ºC for 30 min). The CO_2-edge is an atmospheric artefact. (b) Remaining percentage of Si-H based on the Si-H stretching absorption edges at 2260-2285 cm^{-1} and integrated intensity of hydroxyl stretching absorption between above 3000 cm^{-1}. 100 % remaining Si-H corresponds to the Si-H stretching absorption edge in a soft-baked HSQ film.*

Table 7.1: *FT-IR absorption edges expected in HSQ-based thin films (literature values).*

Wavenumber [cm^{-1}]	Description	Reference
795	Si-O symmetric stretching	[59]
830	Si-O bending	[37]
870	Si-H bending	[37,60]
1075	Si-O asymmetric stretching (incompletely closed cage moieties)	[36]
1140	Si-O asymmetric stretching (closed cage moieties)	[36]
1200-1300	Si-O asymmetric stretching (longitudinal optical splitting)	[59,61]
2200	Si-H stretching in $H_2SiO_{2/2}$	[37,62]
2260-2285	Si-H stretching in $HSiO_{3/2}$	[36]
2242-2208	C=O asymmetric stretching in atmospheric CO_2	[63]
3200-3500	O-H stretching of hydrogen bonded hydroxyl	[59,64]
3660	O-H stretching in Si-OH	[59,64]

stretching at 2260-2285 cm^{-1}, a Si-H pre-edge at 2200 cm^{-1} appears for curing at 400 ºC, indicating the presence of intermediate reaction products between HSQ and SiO_2 and, hence, incomplete polymerization of the film [37]. The more polymerized films do not show the presence of the Si-H pre-edge.

The degree of polymerization was quantified via the loss in integrated Si-H stretching absorption intensity, as proposed in previous works [22,23]. A plot depicting the residual Si-H absorption vs. curing temperature is shown in Figure 7.3(b). It is evident that an increase in curing temperature reduces the amount of remaining Si-H stretching absorption intensity from 39.5 % at 400 ºC curing to 0 % at 550 ºC curing. As established by Bremmer *et al.* [23], the film density increases with decreasing remaining Si-H ratio for oxidatively cured HSQ films. Based on extrapolation of their data, the films cured at 400 ºC (residual Si-H of 40 %) are expected to have a film density of ~75 % of thermal SiO_2, while the films cured at 450 ºC (residual Si-H of 17 %) are expected to have a density of ~80 % of thermal SiO_2. A further increase in film density for the higher curing temperatures is expected, however, the herein reported remaining Si-H ratios are out of the data range reported by Bremmer *et al.* [23] and, hence, cannot be extrapolated.

Apart from IR-absorption due to HSQ in its respective degrees of polymerization, significant absorption from hydroxyl stretching due to silanol and molecular water is observed above 3000 cm^{-1} for all cured films and the integrated intensity of the hydroxyl stretching features, which is indicative for the amount of silanol present [38], is plotted vs. the curing temperature in Figure 7.3(b). Clearly, the amount of hydroxyl climaxes for curing at 450 ºC and declines for curing at higher temperatures, while the amount of hydroxyl is significantly decreased for the film cured at 400 ºC.

7.3.3 Coating hydrophobicity

The effect of the coating chemistry on the coating hydrophobicity was investigated via water contact angle measurements and the relation of water contact angle vs. curing temperature, is shown in Figure 7.4. Overall, all coatings are hydrophilic, however, sample 400 shows an increased contact angle with respect to the other samples. While residual non-polar Si-H repels water, polar silanol allows hydrogen-bonding to water [39] and thus, the affinity of HSQ-based films to water is controlled by a competition between silanol and residual Si-H [23]. Hence, weakly polymerized films, as observed from the FT-IR analysis of sample 400, have a high remaining Si-H ratio in combination with a high water contact angle, as opposed to more polymerized films, which, in consequence, show a higher hydrophilicity.

7.3.4 Potentiodynamic CP testing

The anodic CP behavior of the coated samples allows an assessment of the electrochemical properties of the substrate at coating defects such as cracks, pores or pinholes. As pointed out by other authors [14], the corrosion potential of coated stainless steels is largely determined by local differences in the concentration of reactive species in microscopic coating defects. Hence, an analysis of the substrate properties based on the corrosion potential will be omitted in the following and the analysis will solely be based on the passive current and pitting potential. Representative anodic CP curves of the coated samples and an uncoated reference are shown in Figure 7.5(a). Overall, the reference and the coated samples cured at lower temperatures, *i.e.* sample 400 and 450, show distinct passive regions with significantly decreased passive current densities. Moreover, sample 500 and 550 do not exhibit passive behavior and, hence, no distinct pitting potential is observed. As shown in Figure 7.5(b), the pitting potential is not altered with respect to the reference for sample 400, while a negative shift in pitting potential is observed for sample 450.

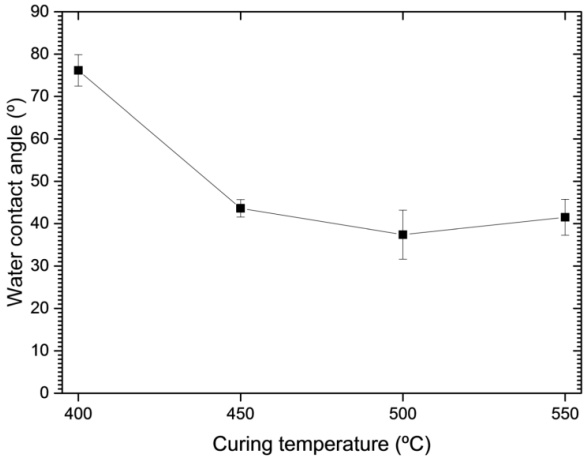

Figure 7.4: *Water contact angle vs. curing temperature on coated AISI 316L substrates. The values represent average values of 3 measurements with the indicated standard deviation.*

The observed decrease in passive current density for samples 400 and 450 is in agreement with reported data for similar coating systems [13,14,40,41]. As concluded by Pech *et al.* [14,40], this decrease in corrosion current density is predominantly attributed to a decrease in exposed substrate surface area, *i.e.* high coating coverage. However, the successful application of thin barrier coatings on stainless steels requires both high coverage and substrate passivity at coating defects and positive conclusions about the coating performance may not be drawn solely based on the passive current density. In analogy to the present investigation, a decrease in breakdown potential has been previously reported for sol-gel coated stainless steels [42] and explained by severe sensitization from $M_{23}C_6$ precipitation during the high temperature treatment. However, due to the herein presented material choice of a low carbon variant of the type 316 stainless steel (≤ 0.030 wt.% C [43]), severe material deterioration due to carbide precipitation may be ruled out within the applied temperature range and ageing time [44]. The microstructure- analysis in section 7.3.1 showed that curing at more elevated temperatures leads to the more pronounced formation of interface oxides, which is assumed to deplete the substrate subsurface in Cr [33] and, further, has a detrimental effect on the coating adhesion. Hence, in analogy to thermal oxidation of stainless steels [45,46], the observed loss in passivity for the high temperature cures can be associated with a process-induced chemical modification of the substrate surface, which compromises the resistance to localized corrosion at coating defects such as interface voids. This hypothesis is in agreement with Pech *et al.* [14], who have reported that the substrate passivity at microscopic coating effects is of utmost importance for the performance of SiO_x coated stainless steels. Thus, curing above 450 ºC in air strongly affects the coating performance in chloride-media due to the pronounced loss in substrate passivity.

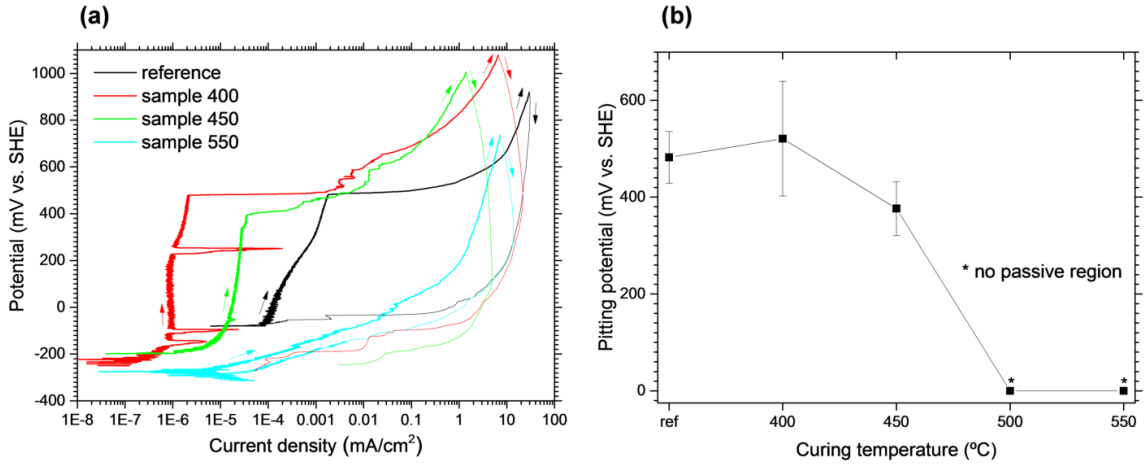

Figure 7.5: *(a) Anodic CP curves in 3.5 wt.% NaCl in water. Sample 500 is excluded from the graph (due to similarity to sample 550). (b) Pitting potential vs. curing temperature. The values represent average values of 3 measurements with the indicated standard deviation.*

7.3.5 Electrochemical impedance spectroscopy

While anodic CP measurements give detailed information about the level of substrate passivity, EIS analysis by equivalent circuit fitting allows for a distinct analysis and quantitative assessment of the coating barrier properties and gives further insight into the correlation between the previously established differences in coating properties and the barrier efficiency. Representative EIS spectra of the coated samples with their respective equivalent circuit fits are shown in Figure 7.6(a), together with data for an uncoated reference. Equivalent circuit fitting was performed based on the models derived in reported literature [31], *i.e.* with a Randle's equivalent circuit for the reference and an R-(Q(R-(Q(R-W)))) –type model (Figure 7.6(b)) for the coated samples. Capacitive elements were fit with constant phase elements and the conversion to equivalent capacitances was conducted according to the method reported by Hsu *et al.* [47]. Resulting from the equivalent circuit fit, the pore resistance, R_p, charge transfer resistance, R_{ct}, coating capacitance, C_{coat} and the double layer capacitance, C_{dl} are plotted vs. the curing temperature in Figure 7.7.

In general, a trend of decreasing R_p with increasing curing temperatures, indicating an inverse relation between curing temperature and barrier properties is observed. C_{coat} is a function of various factors as described by [48]:

$$C = \varepsilon_r \varepsilon_0 \frac{A}{d} \tag{7.1}$$

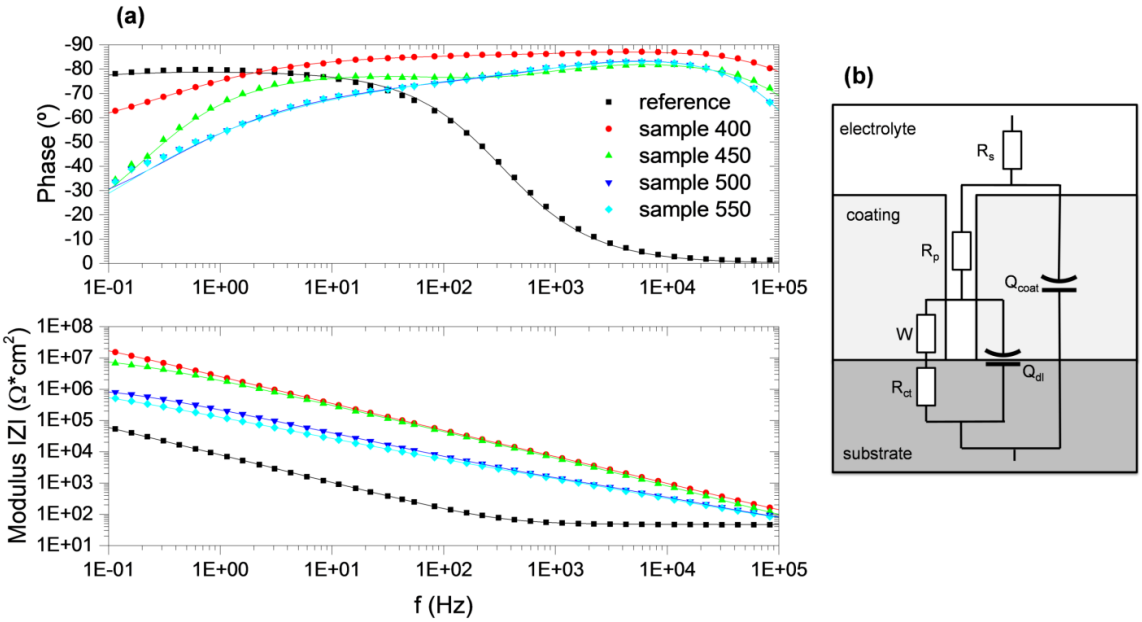

Figure 7.6: *(a) EIS Bode plots of test coupons in 3.5 wt.% NaCl. Solid lines are on the basis of the fitted model. (b) Schematic coating defect and respective equivalent circuit. With solution resistance R_s, charge transfer resistance R_{ct}, pore resistance R_p, constant phase element (CPE) of double layer Q_{dl}, CPE of coating Q_{coat} and Warburg element W.*

where A is the measured area, d the coating thickness, ε_0 the dielectric permittivity of vacuum and ε_r the dielectric coating constant. Since all coatings show full coverage at insignificant difference in coating thickness (section 7.3.1), A and d can be regarded as constant and the factor of 2.5 between the averaged coating capacitances of sample 400 and 550 likely originates from a change in dielectric constant due to higher coating density [23,49,50], formation of silanol [23] or water uptake [51–53] which was previously indicated by FT-IR and water contact angle analysis. R_{ct} is dependent on the substrate passivity and the exposed substrate surface area [40] and a clear decrease in the average R_{ct} is observed (Figure 7.7(a)), supporting the previously formulated hypothesis of a decreased substrate passivity or the increased exposed substrate area observed from Figure 7.2. Overall, the R_{ct}-values determined for the coated samples are higher than the average R_{ct} of the reference, which is in agreement with the decreased current density observed from CP experiments and supports the hypothesis that the exposed substrate surface is strongly reduced by the coating. Likewise, analysis of C_{dl} allows conclusion about the exposed substrate surface via eq. 7.1. In the dataset presented in Figure 7.7(c), the average C_{dl} steadily increases with curing temperature, indicating that curing at higher temperature allows a more efficient electrolyte penetration of the coating, thereby, in conjunction with the interface void-formation, increasing the exposed substrate surface. Overall, the results obtained by EIS indicate that the coating barrier performance does not primarily correlate with the film density, but rather is a complex relation between the film density, hydrophobicity and coating adhesion.

7.3.6 Localized corrosion assessment by the SVET

As indicated by the anodic CP measurements, the coated samples may suffer from localized breakdown in chloride containing electrolyte, however, a detailed understanding of the localized breakdown mechanism requires further insight into the microscopic mechanism of pit initiation in spin-on-glass coated stainless steels. Hence, the pit initiation and the anodic/cathodic activity of the coating system, the uncoated reference and samples 400 and 450 were studied in-situ and ex-situ by the SVET in 1 wt.% $FeCl_3$*$6H_2O$ aqueous solution in combination with SEM analysis. The uncoated reference and sample 400 remained passive within a test period of 24 h. As visible from Figure 7.8(a), sample 450 shows a clear response in form of localized anodic activity from emerging pits after ~2 h of immersion. Moreover, the anodic sites are not geometrically stable and freshly emerging sites are visible even after a prolonged immersion of ~12 h, as shown in Figure 7.8(b,c). On the contrary, the cathodic sites (indicated by arrows in Figure 7.8(a)) evolve in the early stage of the experiment and their positions remain stable over time.

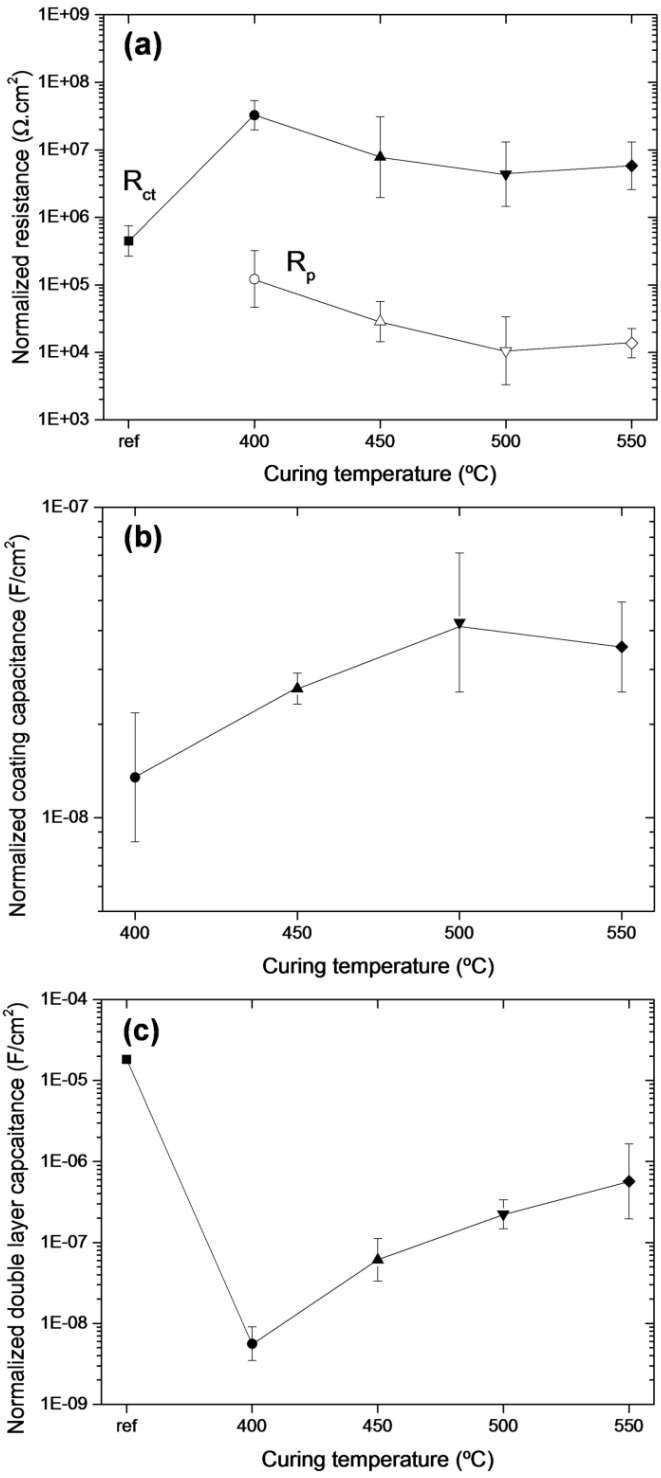

Figure 7.7: *Results of EIS fits vs. curing temperature: (a) Normalized pore/charge transfer resistance, R_p/R_{ct}; (b) Normalized coating capacitance, C_{coat}; (c) Normalized double layer capacitance, C_{dl}. The values represent average values of 5 measurements with the indicated standard deviation.*

A presumable anodic area is depicted in the SEM micrograph shown in Figure 7.9(a). As indicated by the arrows, the site shows coating fractures of several tens of micrometers in length. Cross-sectional analysis by ion beam milling (along the dashed line in Figure 7.9(a) reveals a local corrosion site which has presumably evolved around a microscopic coating defect and spread laterally to the defect underneath the coating (Figure 7.9(b)). The cathodic mechanism has been investigated based on the cathodic site labelled with "cat A" in Figure 7.8(a). It has to be emphasized that, under the given test conditions, the test electrolyte contains Fe^{3+} as oxidant and that the reduction of Fe^{3+} to Fe^{2+} is the primary cathodic reaction. Hence, the cathodic mechanism in Fe^{3+}-free electrolyte may not agree with the observations made in this paragraph. As depicted in Figure 7.9(c), the cathodic site is an approx. circular coating defect with diameter >30 µm at which the coating has blistered or mostly collapsed. The cathodic site has been investigated by ion beam milling along the dashed line in Figure 7.9(c) and an ion beam milled cross-sectional micrograph is shown in Figure 7.9(d). The micrograph reveals a large subsurface pit at which the coating has spalled off or partially collapsed. Hence, it can be concluded that large pits, which evolve early in the corrosion process, may re-passivate and consequently form the pronounced cathodic sites observed in Figure 7.8.

Based on this analysis, we propose the mechanism for unstable pit formation throughout the experiment as illustrated in Figure 7.10. In analogy to *e.g.* a resistive salt film [54], the coating serves as a stable pit cover, which helps to maintain an aggressive electrolyte [55] at the anodic site. Since stable pit growth is not observed during the course of the experiment, we suggest the rupture of the coating as terminating event. As the corrosion site increases in size, the coating ruptures, which consequently allows the dilution of the aggressive pit electrolyte by the less aggressive bulk solution and subsequently re-passivation of the active site.

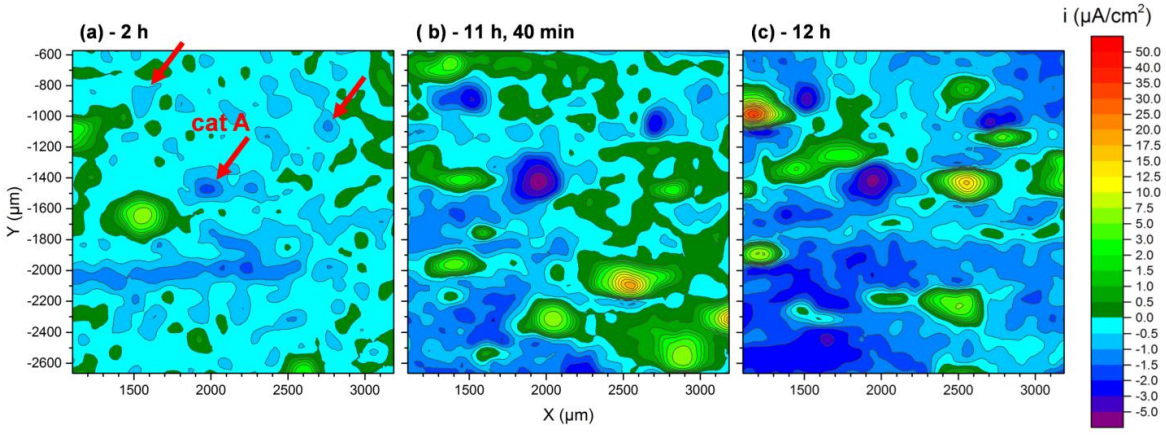

Figure 7.8: *SVET contour plot of sample 450 in 1 wt.% $FeCl_3{*}6H_2O$ after (a) 2 h; (b) 11 h, 40min; (c) 12 h immersion. The framerate of the experiment was 1 frame / 20 min. The arrows indicate the positions of the cathodic sites. "cat A" indicates the acquisition-site for the SEM micrograph in Figure 7.9(c).*

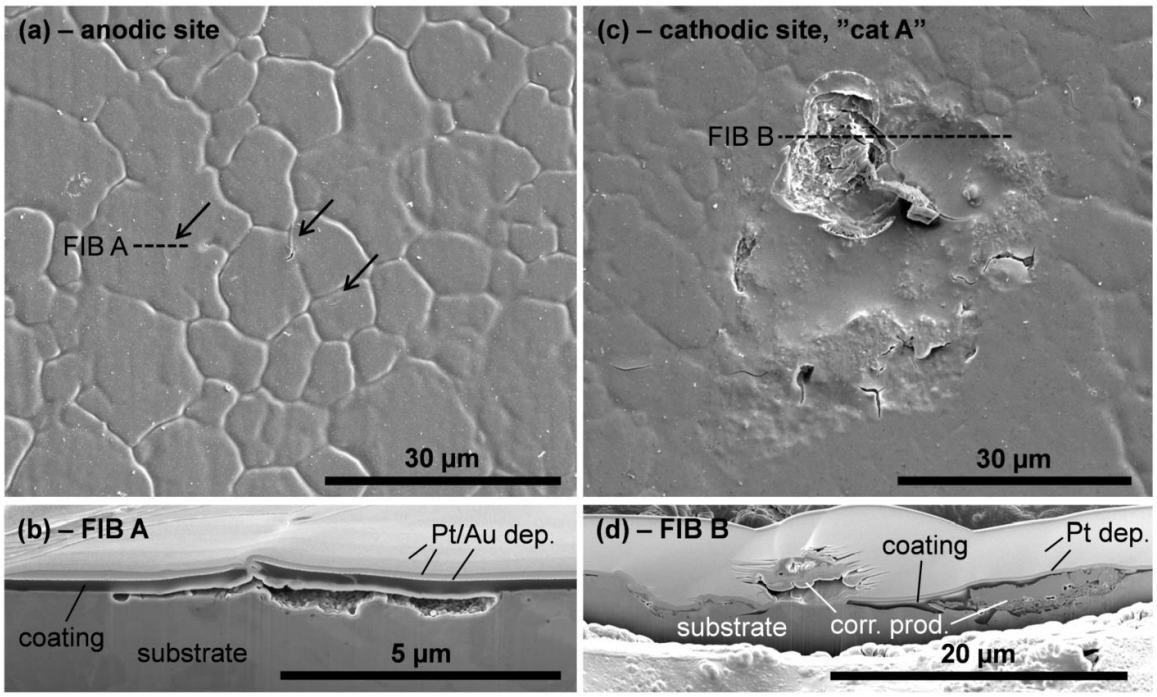

Figure 7.9: *Surface of sample 450 after SVET test: (a) SEM micrograph of anodic site in top-view. Microscope settings: ETD, beam current 0.69 nA; (b) cross-sectional view of detail FIB A. Microscope settings: TLD, beam current 86 pA; (c) SEM micrograph of cathodic site in top-view. The acquisition site is indicated with "cat A" in Figure 7.8(a). Microscope settings: ETD, beam current 0.69 nA; (d) cross-sectional view of detail FIB B. Microscope settings: TLD, beam current 86 pA.*

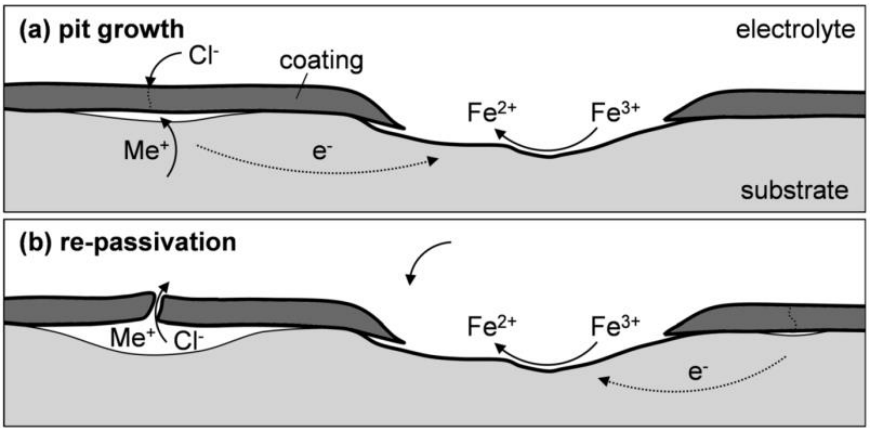

Figure 7.10: *Illustration of corrosion mechanism in SVET experiment: (a) A major coating defect supports the cathodic reaction, while the coating acts as stable pit cover to maintain the aggressive pit electrolyte in a growing pit. (b) As the pit reaches a critical size, the coating ruptures, allowing electrolyte exchange of the pit and subsequently re-passivation of the surface.*

7.3.7 Neutral salt spray testing

All of the previous techniques depict the corrosion properties of coated substrates after short immersion times (1 h of immersion prior to measurement for anodic CP and EIS or up to 24 h for SVET) and may, thus, not sufficiently illustrate the coating performance after prolonged immersion times. To test the long term coating stability, the samples have been exposed to a 1000 h neutral salt spray test according to EN ISO 9227:2012 [35]. Digital photographs of the sample surfaces after the test are shown in Figure 7.11. Areas of interest have been indicated with the letters A-D and respective micrographs are shown in Figure 7.12.

The reference sample shows corrosive failure in form of pitting in conjunction with red rust formation around the pits (Figure 7.11(a) and, in detail, Figure 7.12(a)). In contrast, the coated samples (Figure 7.11(b-e)), do not show the formation of single large pits and exhibit surface degradation, which is visible as discoloration. Moreover, the discoloration is uniform on sample 400 while samples 450-550 show incontinuous, spot-wise discoloration. SEM analysis of sample 400 (Figure 7.12(b)) shows, that the coating has mostly dissolved and only partially remains along the grain boundary valleys. Sample 550, in contrast, shows an increased coating stability with a high coating coverage after the test (Figure 7.12(c)). As exemplarily shown for sample 450 (Figure 7.12(d)), the spot-wise discoloration originates from the agglomeration of micrometer-scale corrosion pits. Cross-sectional analysis (Figure 7.12(e)) of the area shown in Figure 7.12(d) reveals

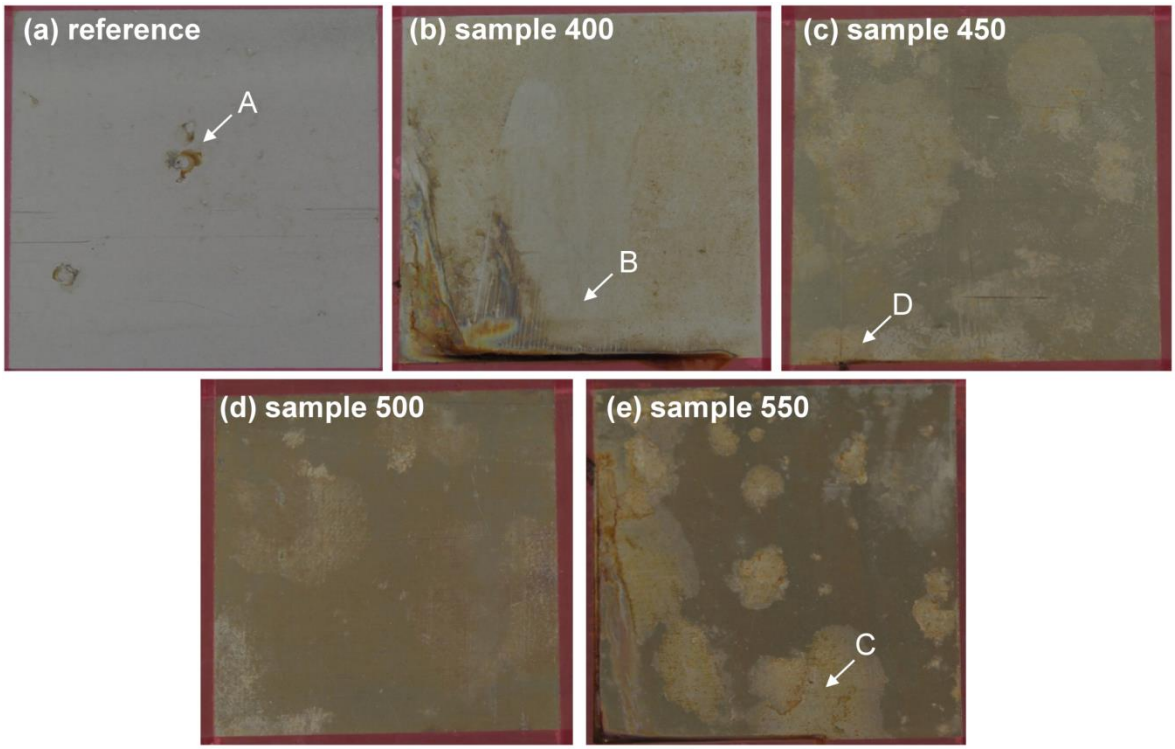

Figure 7.11: *Digital photographs of test coupons after 1000 h neutral salt spray testing: (a) reference; (b) sample 400; (c) sample 450; (d) sample 500; (e) sample 550. Detailed views of sites A-D are shown in Figure 7.12. The exposed sample area is 40x40 mm^2.*

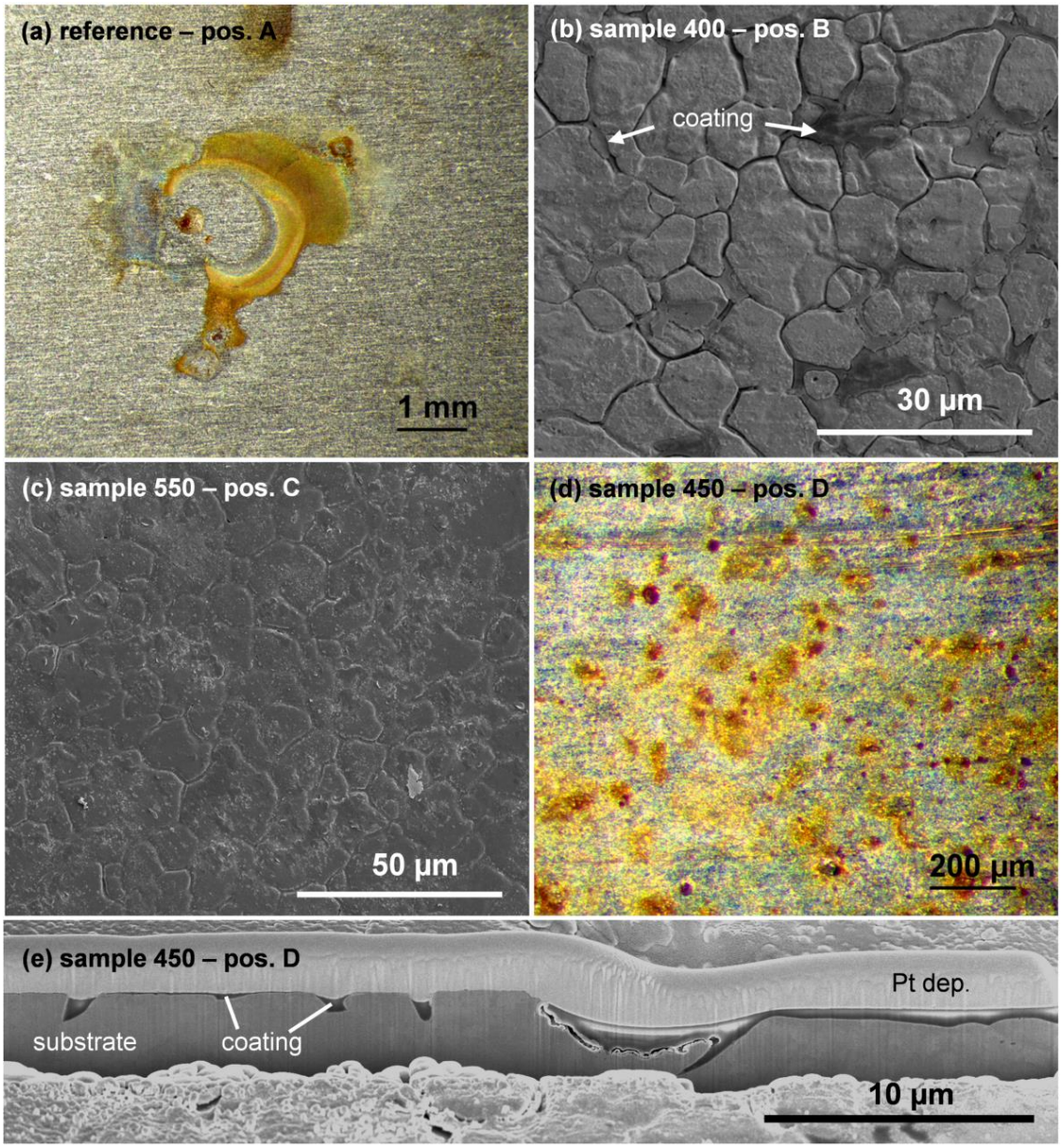

Figure 7.12: *Detailed micrographs of areas indicated in Figure 7.11: (a) LOM of reference, pos. A; (b) SEM of sample 400, pos. B. Microscope settings: ETD, beam current 0.17 nA; (c) SEM sample 550, pos. C. Microscope settings: ETD, beam current 0.34 nA; (d) LOM of sample 450, pos. D; (e) cross-sectional view of the coating cross-section of sample 450, pos. D. Microscope settings: TLD, beam current 86 pA.*

partial coating dissolution, which, however, appears less uniform with respect to sample 400. Moreover, local coating delamination in connection with the initiation of localized corrosion under the coating can be observed. Overall, the visual analysis of the coupons (Figure 7.11) indicates more severe corrosive attack for the high temperature cured samples with respect to the low temperature cures or the reference. This observation is in agreement with the previous results, where a decrease in passive and barrier properties combined with coating delamination and more efficient electrolyte penetration due to an

increased hydrophilicity was observed for the high temperature cures, which may have triggered a more rapid degradation of the substrate in the accelerated corrosion test. The inferior dissolution of the coatings cured at higher temperature can be accounted to a higher film density and degree of polymerization, which may induce a more advanced chemical stability of the coatings. These results are in agreement with reported data [56,57], where SiO_x films with poor polymerization and high defect density showed higher dissolution rates in neutral aqueous solutions. Further, the considerable amount of easily hydrolyzed residual Si-H moieties indicated by the FT-IR analysis in the low temperature cures may contribute to the coating instability [58].

7.4 Conclusions

Coatings cured at 400-450 ºC exhibit good adhesion, while void formation due to excessive thermal oxidation of the substrate can be observed for coatings cured at higher temperatures. The coating hydrophobicity correlates with the residual Si-H and silanol content and, consequently, coatings cured below 450 ºC show a significantly higher hydrophobicity with respect to coatings cured at higher temperature. Moreover, the coating barrier properties are primarily dominated by the coating hydrophobicity and do not increase for increased coating densities. Further, the coating may act as stable pit cover and, hence, actively support stable pit growth. Overall, it is evident that air curing of HSQ-based coatings on AISI 316L substrate yields unfavorable properties of either the coating or the substrate. While curing at 400 ºC does not impair the passive character of the substrate, curing above 400 ºC adversely affects the substrate passivity, leading to a complete loss of passivity for curing above 450 ºC. Furthermore, a high defect density, poor cross-linking and high residual Si-H content impair the chemical stability of the coatings cured at low temperatures in neutral solution. Hence, curing in air ambient is an inefficient curing method for HSQ-based barrier coatings on AISI 316L substrate. Exclusion of oxygen in the curing atmosphere may eliminate the issues associated with substrate oxidation and, thus, enable higher curing temperatures and more advanced cross-linking without an impairment of the substrate passivity.

Acknowledgements

The authors acknowledge SiOx Aps for the deposition of coatings and all other project partners. Further, Innovation Fund Denmark is acknowledged for providing financial support for the project Q-HEX under grant number 50-2014-1.

References

[1] N.J. Laycock, J. Stewart, R.C. Newman, The Initiation of Crevice Corrosion in Stainless Steel, Corros. Sci. 39 (1997) 1791–1809.

[2] Z. Szklarska-Smialowska, J. Mankowski, Crevice Corrosion of Stainless Steels in Sodium Chloride Solution, Corros. Sci. 18 (1978) 953–960.

[3] M. Torkar, F. Tehovnik, M. Godec, Crevice corrosion of stainless-steel fastening components in an indoor marine-water basin, Mater. Technol. 46 (2012) 423–427.

[4] K.M. Deen, M. a. Virk, C.I. Haque, R. Ahmad, I.H. Khan, Failure investigation of heat exchanger plates due to pitting corrosion, Eng. Fail. Anal. 17 (2010) 886–893.

[5] L. Ćurković, H.O. Ćurković, S. Salopek, M.M. Renjo, S. Šegota, Enhancement of corrosion protection of AISI 304 stainless steel by nanostructured sol–gel TiO2 films, Corros. Sci. 77 (2013) 176–184.

[6] S. Li, J. Fu, Improvement in corrosion protection properties of TiO2 coatings by chromium doping, Corros. Sci. 68 (2013) 101–110.

[7] S.T. Döşlü, B.D. Mert, B. Yazıcı, Polyindole top coat on TiO2 sol–gel films for corrosion protection of steel, Corros. Sci. 66 (2013) 51–58.

[8] S. Meth, N. Savchenko, M. Koltypin, D. Starosvetsky, F.A. Viva, A. Groysman, C.N. Sukenik, Corrosion studies of stainless steel protected by a TiO2 thin film deposited on a sulfonate-functionalized self-assembled monolayer, Corros. Sci. 52 (2010) 125–129.

[9] G. Ruhi, O.P. Modi, I.B. Singh, Pitting of AISI 304L stainless steel coated with nano structured sol–gel alumina coatings in chloride containing acidic environments, Corros. Sci. 51 (2009) 3057–3063.

[10] D.C.L. Vasconcelos, J.A.N. Carvalho, M. Mantel, W.L. Vasconcelos, Corrosion resistance of stainless steel coated with sol–gel silica, J. Non. Cryst. Solids. 273 (2000) 135–139.

[11] M. Atik, P. de Lima Neto, L.A. Avaca, M.A. Aegerter, J. Zarzycki, Protection of 316L stainless steel against corrosion by SiO2 coatings, J. Mater. Sci. Lett. 13 (1994) 1081–1085.

[12] O. de Sanctis, L. Gomez, N. Pellegri, C. Parodi, A. Marajofsky, A. Duran, Protective Glass Coatings on Metallic Substrates, J. Non. Cryst. Solids. 121 (1990) 338–343.

[13] T. Hwang, H. Lee, H. Kim, G. Kim, Two layered silica protective film made by a spray-and-dip coating method on 304 stainless steel, J. Sol-Gel Sci. Technol. 55 (2010) 207–212.

[14] D. Pech, P. Steyer, J.-P. Millet, Electrochemical behaviour enhancement of stainless steels by a SiO2 PACVD coating, Corros. Sci. 50 (2008) 1492–1497.

[15] T. Wang, J. He, D. Sun, J. Zhou, Y. Guo, X. Ding, S. Wu, J. Zhao, J. Tang, Fabrication of continuous mesoporous organic–inorganic nanocomposite films for corrosion protection of stainless steel in PEM fuel cells, Corros. Sci. 53 (2011) 1498–1504.

[16] R.F.S. Lenza, W.L. Vasconcelos, Synthesis and properties of microporous sol–gel silica membranes, J. Non. Cryst. Solids. 273 (2000) 164–169.

[17] P. Møller, L.P. Nielsen, Vitreous Enamel, in: Adv. Surf. Technol. Vol 2, 2013: pp. 645–654.

[18] O. Santos, T. Nylander, R. Rosmaninho, G. Rizzo, S. Yiantsios, N. Andritsos, A. Karabelas, H. Müller-Steinhagen, L. Melo, L. Boulangé-Petermann, C. Gabet, A. Braem, C. Trägårdh, M. Paulsson, Modified stainless steel surfaces targeted to reduce fouling—surface characterization, J. Food Eng. 64 (2004) 63–79.

[19] R. Rosmaninho, O. Santos, T. Nylander, M. Paulsson, M. Beuf, T. Benezech, S. Yiantsios, N. Andritsos, A. Karabelas, G. Rizzo, H. Müller-Steinhagen, L.F. Melo, Modified stainless steel surfaces targeted to reduce fouling – Evaluation of fouling by milk components, J. Food Eng. 80 (2007) 1176–1187.

[20] J. Foggiato, Chemical Vapor Deposition of Silicon Dioxide Films, in: Handb. Thin Film Depos. Process. Tech. (Second Ed., 2nd ed., Elsevier B.V., 2001: pp. 111–149.

[21] C.J. Brinker, G.W. Scherer, Sintering, in: Sol-Gel Sci., Academic Press, Inc., San Diego, 1990: pp. 675–742.

[22] Y.K. Siew, G. Sarkar, X. Hu, J. Hui, A. See, C.T. Chua, Thermal Curing of Hydrogen Silsesquioxane, J. Electrochem. Soc. 147 (2000) 335.
[23] J.N. Bremmer, Y. Liu, K.G. Gruszynski, F.C. Dall, Cure of Hydrogen Silsesquioxane for Intermetal Dielectric Applications, Mater. Res. Soc. Symp. Proc. 476 (1997) 37–44.
[24] M.J. Loboda, C.M. Grove, R.F. Schneider, Properties of a-SiOx:H Thin Films Deposited form Hydrogen Silsesquioxane Resins, J. Electrochem. Soc. 145 (1998) 2861–2866.
[25] K. Mohaghegh, H.N. Hansen, H. Pranov, G. Kofod, A study on the surface roughness of a thin HSQ coating on a fine milled surface, in: 14th Euspen Int. Conf. - Dubrovink, 2014.
[26] K. Mohaghegh, H.N. Hansen, H. Pranov, G. Kofod, Verification of thickness and surface roughness of a thin film transparent coating, in: Proc. 13th Euspen Int. Conf., Berlin, 2013.
[27] H. Pranov, Spin-on-glass assisted polishing of rough substrates, WO 2013/083129 A1, 2013.
[28] J. Cech, H. Pranov, G. Kofod, M. Matschuk, S. Murthy, R. Taboryski, Surface roughness reduction using spray-coated hydrogen silsesquioxane reflow, Appl. Surf. Sci. 280 (2013) 424–430.
[29] T.C. Hobæk, M. Matschuk, J. Kafka, H.J. Pranov, N.B. Larsen, Hydrogen silsesquioxane mold coatings for improved replication of nanopatterns by injection molding, J. Micromechanics Microengineering. 25 (2015) 035018 (9pp).
[30] H. Pranov, Reactive Silicon Oxide Precursor Facilitated Anti-Corrosion Treatment, US 2014/0154441 A1, USA, 2014.
[31] F. Lampert, A.H. Jensen, R.U. Din, P. Møller, Hydrogen Silsesquioxane based silica glass coatings for the corrosion protection of austenitic stainless steel, Surf. Coatings Technol. 307 (2016) 879–885.
[32] P. Kohl, Low-dielectric constant insulators for future integrated circuits and packages, Annu. Rev. Chem. Biomol. Eng. 2 (2011) 379–401.
[33] F. Lampert, S. Kadkhodazadeh, A.H. Jensen, R.U. Din, P. Møller, Interfacial Interaction of Oxidatively Cured Hydrogen Silsesquioxane Spin-On-Glass Enamel with Stainless Steel Substrate, J. Electrochem. Soc. 164 (2017) C231–C239.
[34] R. Qvarfort, New Electrochemical Cell for Pitting Corrosion Testing, Corros. Sci. 28 (1988).
[35] EN ISO 9227:2012 Corrosion tests in artificial atmospheres - Salt spray tests, (2012).
[36] C.L. Frye, W.T. Collins, The Oligomeric Silsesquioxanes, (HSiO3/2)n, J. Am. Chem. Soc. 92 (1970) 5586–5588.
[37] M.G. Albrecht, C. Blanchette, Materials Issues with Thin Film Hydrogen Silsesquioxane Low K Dielectrics, J. Electrochem. Soc. 145 (1998) 4019–4025.
[38] W.A. Pliskin, Comparison of properties of dielectric films deposited by various methods, J. Vac. Sci. Technol. 14 (1977) 1064.
[39] W. Hertl, M.L. Hair, Adsorption of Water on Silica, Nature. 223 (1969) 1150–1151.
[40] D. Pech, P. Steyer, A.-S. Loir, J.C. Sánchez-López, J.-P. Millet, Analysis of the corrosion protective ability of PACVD silica-based coatings deposited on steel, Surf. Coatings Technol. 201 (2006) 347–352.
[41] B. Nikrooz, M. Zandrahimi, H. Ebrahimifar, High temperature oxidation resistance and corrosion properties of dip coated silica coating by sol gel method on stainless steel, J. Sol-Gel Sci. Technol. 63 (2012) 286–293.
[42] P.P. Trazaskoma-Paulette, A. Nazeri, Effects of Sol-Gel Coatings on the Localized Corrosion Behavior of 304 Stainless Steel, J. Electrochem. Soc. 144 (1997) 1307–1310.
[43] Designation: A959-16 Standard Guide for Specifying Harmonized Standard Grade Compositions for Wrought Stainless Steels, 2016.
[44] A. Kriaa, N. Hamdi, H. Sidhom, Assessment of Intergranular Corrosion of Heat Treated Austenitic Stainless Steel (AISI 316L Grade) by Electron Microscopy and Electrochemical Tests, Prot. Met. 44 (2008) 506–513.
[45] G. Hultquist, C. Leygraf, Selective Oxidation of a Ferritic Stainless Steel and its Influence on Resistance to Crevice Corrosion Initiation, Corros. Sci. 21 (1981) 401–408.
[46] F. Elshawesh, A. Elhoud, Role of heat tint on pitting corrosion of 304 austenitic stainless

steel in chloride environment, in: Eur. Corros. Conf. Long Term Predict. Model. Corros. EUROCORR 2004, 2004.
[47] C.H. Hsu, F. Mansfeld, Technical Note: Concerning the Conversion of the Constant Phase Element Parameter Y0 into a Capacitance, Corrosion. 57 (2001) 747–748.
[48] F. Mansfeld, H. Shih, H. Greene, C.H. Tsai, Analysis of EIS Data for Common Corrosion Processes, in: Electrochem. Impedance Anal. Interpret., 1993: pp. 37–53.
[49] Y. Toivola, J. Thurn, R.F. Cook, Structural, Electrical, and Mechanical Properties Development during Curing of Low-k Hydrogen Silsesquioxane Films, J. Electrochem. Soc. 149 (2002) F9–F17.
[50] W.-C. Liu, C.-C. Yang, W.-C. Chen, B.-T. Dai, M.-S. Tsai, The structural transformation and properties of spin-on poly(silsesquioxane) films by thermal curing, J. Non. Cryst. Solids. 311 (2002) 233–240.
[51] D.M. Brasher, A.H. Kingsbury, Electrical Measurements in the Study of Immersed Paint Coatings on Metal. 1. Comparison between Capacitance and Gravimetric Methods of Estimating Water-Uptake, J. Appl. Chem. 4 (1954) 62–72.
[52] A.S. Castela, A.M. Simões, An impedance model for the estimation of water absorption in organic coatings. Part I: A linear dielectric mixture equation, Corros. Sci. 45 (2003) 1631–1646.
[53] Lindqvist S.A., Theory of Dielectric Properties of Heterogeneous Substances Applied to Water in a Paint Film, Corros. - NACE. 41 (1985) 69–75.
[54] G.S. Frankel, L. Stockert, F. Hunkeler, H. Boehni, Metastable Pitting of Stainless Steel, Corros. - NACE. 43 (1987) 429–436.
[55] P.C. Pistorius, G.T. Burstein, Metastable pitting corrosion of stainless steel and the transition to stability, Philos. Trans. R. Soc. Ser. A. 341 (1992) 531–559.
[56] M. Klause, U. Rothhaar, M. Bicker, W. Ohling, Dissolution of thin SiO2-coatings – Characterization and evaluation, J. Non. Cryst. Solids. 356 (2010) 141–146.
[57] S.-K. Kang, S.-W. Hwang, H. Cheng, S. Yu, B.H. Kim, J.-H. Kim, Y. Huang, J.A. Rogers, Dissolution Behaviors and Applications of Silicon Oxides and Nitrides in Transient Electronics, Adv. Funct. Mater. 24 (2014) 4427–4434.
[58] C.J. Brinker, G.W. Scherer, Hyrdolysis and Condensation of Silicon Alkoxides, in: Sol-Gel Sci., Academic Press, Inc., San Diego, 1990: pp. 108–216.
[59] P. Innocenzi, Infrared spectroscopy of sol-gel derived silica-based films: A spectra-microstructure overview, J. Non. Cryst. Solids. 316 (2003) 309–319.
[60] P. Bornhauser, G. Calzaferri, Ring-Opening Vibrations of Spherosiloxanes, J. Phys. Chem. 100 (1996) 2035–2044.
[61] I.P. Lisovskii, V.G. Litovchenko, V.G. Lozinskii, G.I. Steblovskii, IR spectroscopic investigation of SiO2 film structure, Thin Solid Films. 213 (1992) 164–169.
[62] D.L. Olynick, B. Cord, A. Schipotinin, D.F. Ogletree, P.J. Schuck, Electron-beam exposure mechanisms in hydrogen silsesquioxane investigated by vibrational spectroscopy and in situ electron-beam-induced desorption, J. Vac. Sci. Technol. B Microelectron. Nanom. Struct. 28 (2010) 581–587.
[63] S.W. Bruun, A. Kohler, I. Adt, G.D. Sockalingum, M. Manfait, H. Martens, Correcting Attenuated Total Reflection – Fourier Transform Infrared Spectra for Water Vapor and Carbon Dioxide, Appl. Spectrosc. 60 (2006) 1029–1039.
[64] C.J. Brinker, G.W. Scherer, 2.4.3. IR-Raman investigations of gel dehydroxylation, in: Sol Gel Sci. Phys. Chem. Sol-Gel Process., 1990: pp. 582–588.

8 Manuscript IV

Probing the chemistry of adhesion between a 316L substrate and spin-on-glass coating*

Felix Lampert[a], Shima Kadkhodazadeh[b], Takeshi Kasama[b], Kristian Vinter Dahl[a], Alexander Bruun Christiansen[c], Per Møller[d]

[a] Technical University of Denmark, Department of Mechanical Engineering, Produktionstorvet 425, 2800 Kgs. Lyngby, Denmark
[b] Technical University of Denmark, Center for Electron Nanoscopy (CEN), Fysikvej 307, 2800 Kgs. Lyngby, Denmark
[c] SiOx ApS, Bybjergvej 7, 3600 Espergærde, Denmark
[d] Technical University of Denmark (DTU), Department of Mechanical Engineering, Nils Koppels Allé, Building 404, 2800 Kgs. Lyngby, Denmark

Abstract

Hydrogen silsesquioxane ($[HSiO_{3/2}]_n$)-based "spin-on-glass" has been deposited on 316L substrate and cured in Ar/H_2 gas atmosphere at 600 ºC to form a continuous surface coating with sub-micrometer thickness. The coating functionality depends primarily on the adhesion to the substrate, which is largely affected by the chemical interaction at the interface between the coating and the substrate. We have investigated this interface by transmission electron microscopy and electron energy loss spectroscopy. The analysis identified a 5-10 nm thick interaction zone containing signals from O, Si, Cr and Fe. Analysis of the energy loss near edge structure of the present elements identified predominantly signal from $[SiO_4]^{4-}$ units together with Fe^{2+}, Cr^{2+} and traces of Cr^{3+}. High-resolution transmission electron microscopy images of the interface region confirm a crystalline Fe_2SiO_4 interfacial region. In agreement with computational thermodynamics, it is proposed that the spin-on-glass forms a chemically bonded silicate-rich interaction zone with the substrate. It was further suggested that this zone is composed of a corundum-type oxide at the substrate surface, followed by an olivine-structure intermediate phase and a spinel-type oxide in the outer regions of the interfacial zone.

* unpublished work at date of submission. The final article may deviate from the herein presented manuscript.

8.1 Introduction

Due to their inherent resistance towards galvanic corrosion combined with good formability, austenitic stainless steels belong to the most widely used engineering materials. Apart from the chemical composition and the mechanical/thermal history, the functionality of the materials is greatly determined by the surface finish, and hence their surface modification plays a major role in the development of improved stainless steel engineering components. Over the recent years, intense research effort has been directed into the surface modification by SiO_x-based micrometer/sub-micrometer thick coatings to improve the wear resistance [1,2], biocompatibility [3,4], bio fouling characteristics and cleanability [5,6], surface morphology [7–10] and corrosion resistance [11–20] of stainless steel components at a minimal impact on the component geometry. Apart from the traditional deposition processes, such as chemical vapor deposition [21], physical vapor deposition [22], sol-gel processing [23] or liquid phase deposition [24], the deposition from hydrogen silsesquioxane (HSQ), $[HSiO_{3/2}]_n$, spin-on-glass (SOG) has shown excellent results for the processing of high quality SiO_x-like thin films [25,26]. In addition to the deposition of near stoichiometric silica films, SOG-technology offers the possibility to deposit fully inorganic films with various degrees hydrogenation as intermediate reaction products, resulting in a broad range of film properties [25–27]. While the material was mainly developed for microelectronics applications [27,28] or as electron beam resist [29], it has recently emerged into the surface finishing industry and shown an outstanding performance as coating material for metallic substrates such as aluminum or tool steel [7–10].

Recently, we have shown the applicability of SOG as material for sub-micrometer thick coatings on stainless steel substrates [30–32]. Our studies have proven the concept of precursor deposition by an industrially applicable dip-coating process and the subsequent coating curing in both oxidizing [31,32] and non-oxidizing [30] atmosphere, showing that both processes may yield well adherent coatings, which efficiently cover substrate defects and improve the surface smoothness. Further, we have shown that oxidative curing induces thermal oxidation of the substrate [31], leading to adhesive failure of the coating and ultimately to functional component failure [32]. In our previous study, we reported that issues associated with a thick interface oxide can be overcome by curing in a non-oxidizing atmosphere such as Formiergas [30]. However, the methods applied in the previous work were inadequate to clearly resolve the interface between the coating and the substrate and, hence, the interfacial chemistry, morphology and the bonding mechanism between coating and substrate are unclear.

In agreement with other studies [16,20,33–38], our previous findings [31,32] emphasize the significance of the coating/substrate interface for both the adhesion and the performance of glass coatings on stainless steel. However, to the author’s knowledge, previous studies have generally focused on the formation of thick interface oxides [34–36], traditional enameling technology of complex industrial porcelains [33] or on vapor

deposition techniques [37,38], which may lead to significantly different bonding mechanisms. Consequently, the interface formation of well adherent, non-oxidatively cured HSQ-based coatings cannot be adequately deduced based on previous literature. Hence, the present study aims at a detailed characterization of the interfacial chemistry of non-oxidatively cured SOG on type 316L substrate by Transmission Electron Microscopy (TEM). The interface was characterized by electron energy loss spectroscopy in scanning-TEM together with and high resolution TEM and the analytical results are discussed based on the thermodynamical oxide/metal phase equilibrium at the interface. This analysis provides novel insights into the metal-glass bonding mechanism of silica-like coatings on stainless steel substrate and, in conclusion, the adhesive performance of the coatings.

8.2 Experimental section

To analyze the bonding mechanism between a stainless steel substrate and a SOG coating, AISI 316L substrates (composition in Table 8.1) with no. 2B surface finish were coated with HSQ-based SOG by the method previously described in Lampert *et al.* [30]: The test coupons were dip-coated in commercial HSQ-solution (Dow Corning FOx 25) and subjected to a two stage heat treatment, the first step being a soft bake at 160 ºC in air and the second a polymerization at 600 ºC under flow of 0.5 l/min Ar/H_2 gas mixture (10 vol.% H_2) for 2 h. The temperature of the polymerization stage was elevated with respect to our previous work [30] in order to decrease the susceptibility of the coating material to ionizing irradiation [39] during ion beam milling and the TEM investigation.

Lamellae for TEM investigations were prepared by focused ion beam (FIB) milling in a FEI Helios NanoLab 600 dual beam scanning electron microscope (SEM). The specimens were first sputter coated with 20-30 nm of Au to avoid surface charging during the FIB preparation, followed by in-situ deposition of a Pt layer prior to milling to protect the sample from irradiation damage. FIB-milling was carried out at 30 kV ion beam accelerating voltage, followed by final polishing at 2 kV ion beam accelerating voltage and 0.44 nA ion beam current. The lamellae were additionally polished in a Fischione NanoMill precision Ar-ion mill (500 V accelerating voltage and 100 pA beam current) to remove the residual FIB damage. The TEM examination of the samples was performed in a FEI Titan 80-300kV instrument fitted with a FEG electron source, a monochromator and a GIF Tridiem electron energy loss spectroscopy (EELS) spectrometer. Scanning-TEM (STEM) -EELS measurements were carried out at 120 kV accelerating voltage. In STEM, spatial resolutions of 5 Å and 1.5 Å, respectively with and without the

Table 8.1: *Chemical composition of the substrates (by Optical Emission Spectroscopy). In addition, traces (< 0.1 wt.%; > 0.01 wt.%) of P, Nb, V, W were also detected.*

Element	**Cr**	**Ni**	**Mo**	**Mn**	**Si**	**Cu**	**Co**	**N**	**C**	**Fe**
Composition (wt.%)	16.8	10.4	2.07	0.92	0.47	0.41	0.21	0.048	0.019	bal.

monochromator excited, were obtained. The EELS measurements were acquired with the monochromator excited and had an energy resolution of 0.15 eV. High-resolution TEM (HRTEM) imaging was carried out at 300 kV and with the point to point resolution of 1.4 Å. Thermodynamic phase equilibrium calculations were performed in Thermo-Calc version 2017a [40] using version 7.0 of the Thermo-Calc Software steel database TCFE. The elements Fe, Cr, Mn, Ni, Si and O were considered in the calculations.

8.3 Results and discussion

A high-angle annular dark-field (HAADF) STEM image of the coating – substrate cross-section is shown in Figure 8.1(a). Image intensity in HAADF STEM is primarily related to the atomic number (Z-contrast) of the material, indicating an interfacial region distinct from the coating and the substrate (labelled "interface"). This is similar to our previous investigation of an oxidatively cured coating [31], where an interfacial reaction zone was detected. Here, a much thinner interfacial zone of 5 – 10 nm is detected, compared to in the oxidatively cured coating. EELS line scans spanning energy ranges 400 – 1000 eV (covering the O K-edge and Cr, Mn, Fe and Ni $L_{2,3}$-edges) and 90 – 150 eV (containing the Si $L_{2,3}$-edge) were acquired from the coating/substrate interface, in order to probe the chemistry of this interfacial zone. The Si $L_{2,3}$-edge had to be recorded separately, as our experimental setup limits the spectral energy range to 600 eV at most, and thus we were unable to record all edges of interest together in the same spectrum. The relative composition profile of O, Cr and Fe calculated from the EEL spectra along with the HAADF intensity profile and the intensity of the Si signal along a line across the interface are plotted in Figure 8.1(b). Approximate boundaries for the substrate and the coating, determined from the changes in the HAADF image intensity profile along the recorded line scans, are marked in the graphs. We were unable to analyze the composition profile of Ni, due to the pronounced overlap between the Ni $L_{2,3}$-edge and the Fe L_1-edge. The detection of the Mn $L_{2,3}$-edge was also hindered due to its low concentration and low signal level in the measurements. The measurements were repeated across different regions of the sample and were found to be reproducible. As evident from the graphs in Figure 8.1(b) the constituent elements have relatively unchanged concentrations in the substrate and the coating. An interfacial zone of approximately 6 nm, containing all four elements Fe, Cr, O and Si is detected. The concentrations of Fe and Cr in the interface decrease from the substrate towards the coating and those of O and Si increase.

The energy-loss near-edge fine-structure (ELNES) in EELS is a powerful tool in probing the local chemistry of a sample, containing information such as chemical bonding, oxidation state, crystal structure and coordination [41]. EEL spectra recorded at different points along the interface are plotted in Figure 8.2(a) (O, Cr, Fe) Figure 8.2(b) (Si). Here we analyze the ELNES of the spectra in different regions:

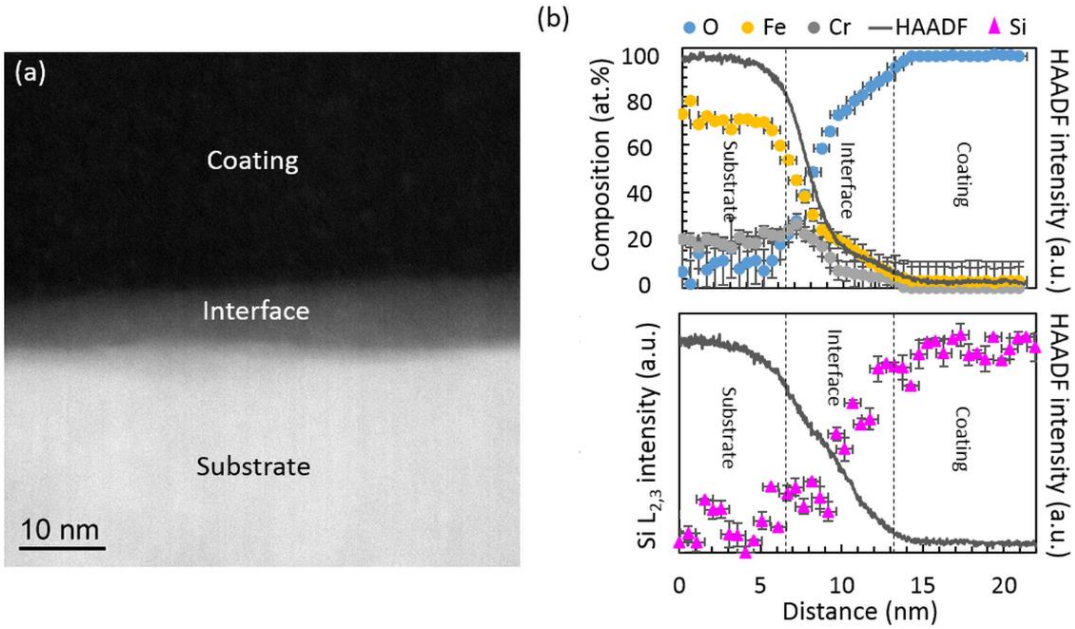

Figure 8.1: *(a) HAADF STEM images of the coating on AISI 316L substrates in the cross-sectional geometry. (b) Relative composition profiles of O, Cr and Fe and the Si signal intensity across the interface extracted from EELS plotted together with the intensity profile of the HAADF STEM image along the line the EEL spectra were acquired from.*

Coating. The signal acquired in the coating contains the Si L- and the O K-edges. The ELNES in both the Si $L_{2,3}$- and O K-edges in this region (spectra at position (i)) resemble closely those for amorphous SiO_2 with SiO_4 tetrahedral networks [42–44]: the Si $L_{2,3}$-edge contains three main peaks at ~106 eV, ~108 eV and ~115 eV. The first peak corresponds to 2p to unoccupied s-type states in Si and its onset has been shown to vary from ~100 eV for Si^0 to ~103 eV for Si^{2+} to ~105 eV for Si^{4+} [45]. The peaks at 108 eV and 115 eV arise from 2p to dominantly d-type states, and are influenced by the Si – O tetrahedral coordination in silica [42,43]. The O K-edge in the coating features a main peak at ~537 eV and a broad peak at ~560 eV.

Interface. The spectra acquired in the interface contains signals from Si, O, Cr and Fe. Little change is observed in the fine structure of Si $L_{2,3}$-edge at position (ii) in the interface relative to the coating. This indicates the continued dominant presence of $[SiO_4]^{4-}$ units in the interface. The splitting in the initial peak at 106 eV, due to spin-orbit coupling of 2p electrons in Si, can be clearly resolved here [44,46]. A pre-peak at ~103 eV appears in the spectra at positions (iii) and (iv). The reduced onset energy of the Si $L_{2,3}$ edge signifies a decreased covalency of the Si–O bonds at these positions [42], which may be related to the presence of Fe and Cr in the interface, *e.g.* of olivine (Me_2SiO_4)-structure phases such as Fe_2SiO_4 [42] or Cr-bearing Si sub-oxides [43]. The O K-edges from positions (ii) and (iii) have overall similar profiles to that acquired in the coating. The first peak at ~537 eV arises mainly from scattering of excited electrons (from 1s state

in O) by second nearest O neighbors and beyond [47] and has been shown to have little dependence on *e.g.* the Si – O – Si bond angle [48,49]. The peak at ~560 eV has been shown to shift to lower energies with increasing Si – O bond length (*i.e.* reduced ionic character) [47]. Such a shift is observed in the O K-edge at position (ii) and (iii). Additionally, the peak at ~537 eV in the spectra acquired at positions (ii), (iii) and (iv) contains a shoulder on the right hand side, indicating a larger crystal field effect [50] compared to position (i). This could be the result of distortion or change in the structure of the interface relative to the coating. A decrease in the onset energy of the O K-edge and a hint of a pre-peak can be seen in the spectra at positions (iii) and (iv). A pre-peak is typically present in the ELNES of the O K-edge of transition metal oxides [51,52] and a similar decrease in onset energy of the O K-edge can be observed for silicates such as Fe_2SiO_4 (fayalite) [53]. The $L_{2,3}$ edges of transition metals reveal valuable information regarding their oxidation state, crystal structure and chemical environment. For example, the position of the L_2 and L_3 peaks are shown to be sensitive to their oxidation and shift typically to higher energies with increasing oxidation state [52,54–57]. The intensity ratio of L_3/L_2 edges in transition metals is another important parameter related to the d-orbital occupancy (and subsequently the oxidation state). Each of the L_2 and L_3 peaks can also contain fine details, stemming from crystal field effects, which provide further clues to the chemical state of the transition metal [52,54,57]. The peak maxima of the Fe L_3 and L_2 here are positioned respectively at ~707 eV and ~720 eV, without showing any noticeable change across the interface (see spectra (ii) – (iv)). The average integrated intensity of L_3/L_2 edges of Fe in the interface region determined according to the method described by van Aken *et al.* [50] is 3.5 (L_3/L_2 ratio in the substrate is ~2.8). Both the peak maxima energies and the L_3/L_2 ratio in the interface region correspond well to those for Fe^{2+} [50,52,54,58]. The fine structure present on the Fe $L_{2,3}$ edge across the interface is also consistent with this observation: A splitting in the L_3 edge (marked with arrows in spectra (ii) and (iii) of Fe $L_{2,3}$ edges in Figure 8.2(a)) can be resolved, characterized by a small bump at ~710 eV after the main peak [50,52,54]. We thus conclude that the Fe present in the interface region is predominantly in Fe^{2+} state. In the case of Cr, small shifts in the L_3 peak maxima at different points across the interface are detected. The measured L_3 and L_2 peak maxima at position (iii) of ~576 eV and ~585 eV correspond closely to Cr^{2+} [55,57]. Although the fine structure on the Cr L_3 edge cannot be clearly resolved in our measurements, its overall profile at position (iii) also suggests the presence of Cr^{2+} [55,57]. In comparison, the Cr L_3 peaks at positions (ii) and (iv) have their maxima at slightly higher energies (approximately 1.0 eV and 0.6 eV shifts at positions (ii) and (iv), respectively). Their overall shapes also varies compared to the Cr $L_{2,3}$ edge at position (iii): this is in particular clear at position (ii), where Cr L_3 has a longer tail to the left of its main peak, suggesting that Cr^{3+} may also be present [55,57].

Substrate. The spectra collected from the substrate contain signals from Fe and Cr in metallic form.

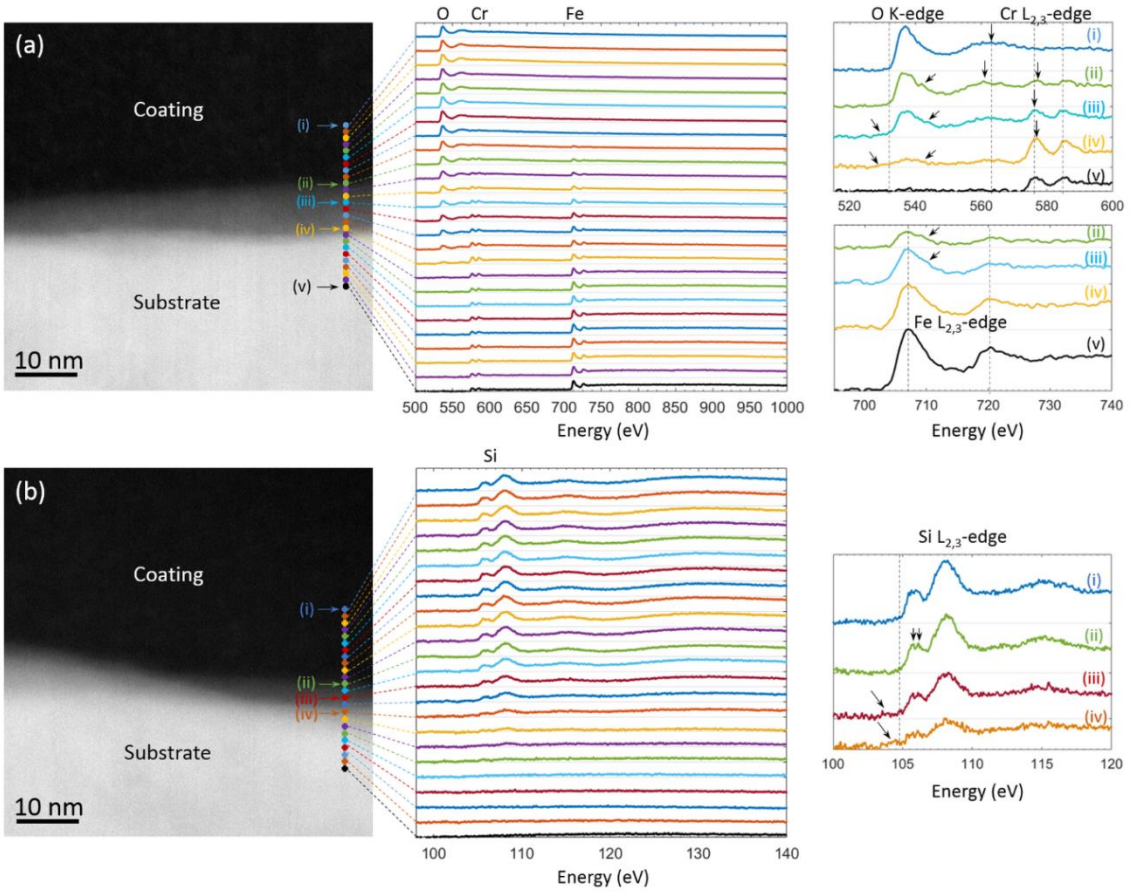

Figure 8.2: *EELS spectra along a line across the coating – AISI 316L interface containing the (a) O K-, Cr $L_{2,3}$- and Fe $L_{2,3}$-edges and (b) Si $L_{2,3}$-edge.*

A reasonable hypothesis based on the results of our ELNES analysis of the interface is that it is composed of Fe_2SiO_4, Cr_2SiO_4 and small amounts of Cr^{3+}-rich oxides such as Cr_2O_3 or Cr^{3+}-bearing spinel, which have previously been reported as high temperature oxides of CrNi steels [59]. High-resolution TEM (HRTEM) images of the structure reveals that the interface is crystalline (see also Figure S8.1 in the supporting information (SI)). A HRTEM image of the substrate – coating structure with fast Fourier transform (FFT) patterns corresponding to regions within each of the substrate, interface and the coating are depicted in Figure 8.3. The crystalline nature of the substrate and the interface can be clearly seen in the image. Comparing the FFT pattern obtained from the interface to that of the substrate, no relation between the crystal structures of the two regions is observed, indicating that the interface is distinctly different from the substrate. Although not in a low-index zone-axis orientation, the FFT pattern of the interface is compatible with a Fe_2SiO_4 structure (see Figure S8.2 in the SI). The interface formation is expected to resemble the thermal oxidation of the substrate at low oxygen partial pressure (O_2 pp.) and elevated Si-access, whereby the O_2 pp. is expected to show a decrease from the outer region of the interface (*e.g.* position (ii) in Figure 8.2) to its inner region (*e.g.* position (iv) in Figure 8.2). Thus, the interface formation has been simulated by computation of the phase equilibrium of the substrate composition vs. O_2 pp. at 600 ºC at elevated Si-level

(for the computation a Si content of 2 wt.% has been assumed). The respective property diagram showing the phase equilibrium is shown in Figure 8.4. Clearly, the oxide-phase equilibrium is dominated by a Fe/Cr/Ni/Mn-rich spinel-structure oxide (M_3O_4), together with an Fe/Cr-rich corundum-structure oxide (M_2O_3) at high O_2 pp. and a stoichiometric Cr_2O_3 (corundum-structure) at low O_2 pp., which generally agrees with the medium temperature oxides that have been experimentally identified after the oxidation of CrNi steel [59]. Neither of the previously discussed phases is enriched in Si. Si is entirely bound in form of quartz (SiO_2) over a broad range of O_2 pp. or a Fe-rich olivine-structure phase at medium O_2 pp. (*i.e.* fayalite). Overall, the equilibrium calculation supports the hypothesis of fayalite formation in the interfacial zone together with the formation of Cr_2O_3 directly at the substrate surface, where the lowest O_2 pp. is expected. Further, the calculated phase equilibrium is in agreement with the observation of Cr^{3+} in the outer region of the interfacial zone, which may be bound in a spinel-type oxide where the highest O_2 pp. is expected. Since no trace of Fe^{3+} was evident from the experiment, we propose that the formation of an outer corundum-structure layer was suppressed by the low oxygen availability during the thermal treatment. The formation of a thin, chemically bonded interfacial zone has been previously linked to good adhesion between glasses and metals [38,43]. Hence, the herein presented formation of a silicate-rich interaction zone may be directly linked to the SOG adhesion and ensure an excellent performance of SOG-based coatings in industrial applications.

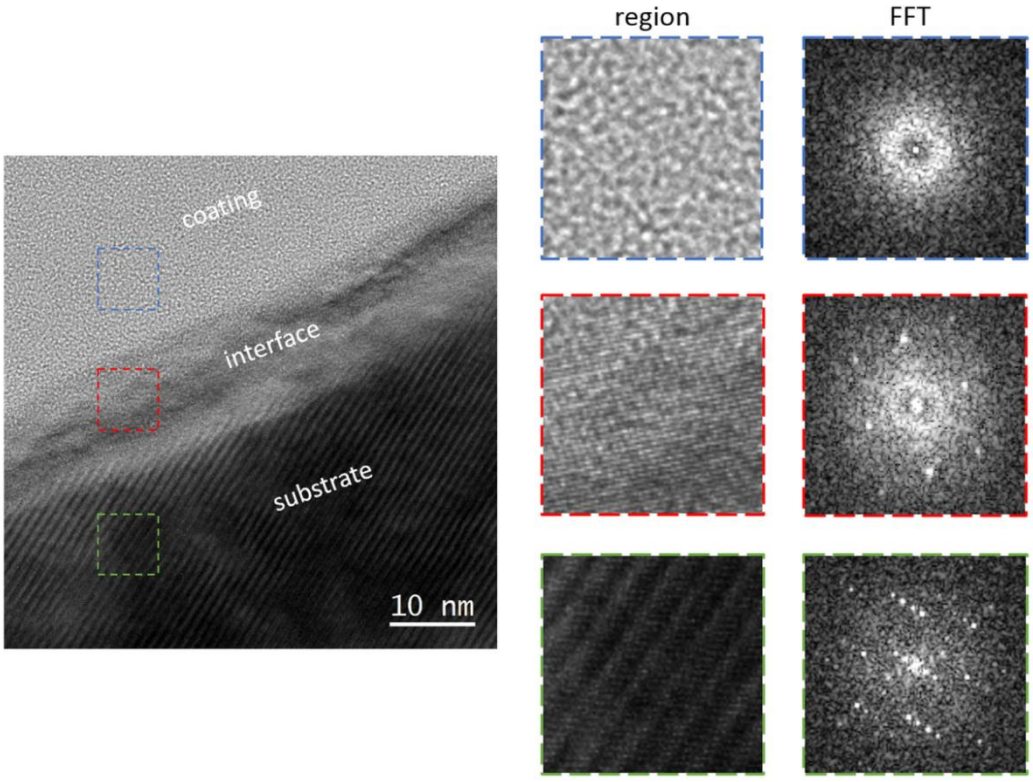

Figure 8.3: *HRTEM image of the coating – AISI 316L interface, with FFT patterns of selected regions from the coating, interface and the substrate.*

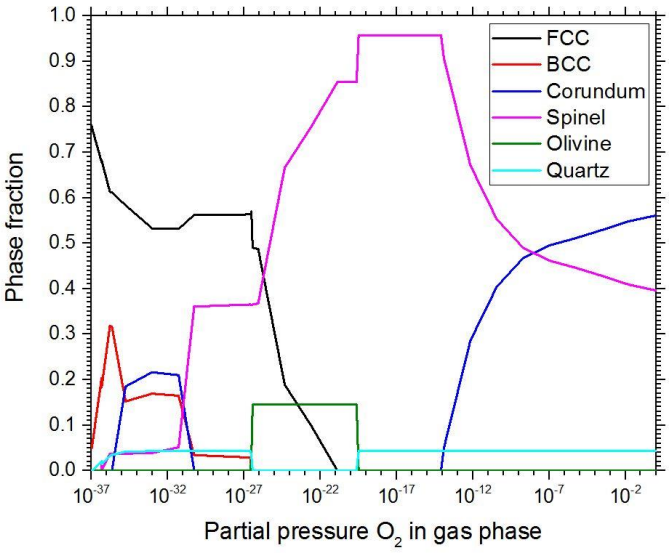

Figure 8.4: *Phase equilibrium vs. O_2 partial pressure diagram of the substrate composition at increased (2 wt.%) Si-level. The property diagram was computed with Thermo-Calc Software version 2017a[40], TCFE7.0.*

8.4 Summary and conclusions

In summary, we investigated the chemistry of the interface between AISI 316L and SOG coating using STEM-EELS and HRTEM imaging. An interfacial region of ~10 nm thickness, containing Si, O, Cr and Fe was detected. Analysis of the ELNES indicated these elements to be in Fe^{2+}, Cr^{2+} (as well as, small amounts of Cr^{3+}) and $[SiO_4]^{4-}$ forms. HRTEM images of the structure reveals that the interface is crystalline, with the FFT patterns matching a Fe_2SiO_4 (fayalite) -structure. The experimental results have been validated by thermodynamics simulations and we suggest that thermal processing of the SOG leads to the formation of a chemical interaction zone with the substrate which may generate excellent adhesion of the coating.

Acknowledgements

This work is funded by Innovation Fund Denmark under grant number 50-2014-1. The authors acknowledge SiOx Aps, Denmark, for the deposition of the coatings and all other project partners. The A. P. Møller and Chastine Mc-Kinney Møller Foundation is gratefully acknowledged for their contribution toward the establishment of the Centre for Electron Nanoscopy at the Technical University of Denmark.

References

[1] G.A. Garzino-Demo, F.L. Lama, Friction and wear of uncoated or SiO2-coated 329 stainless steel and of uncoated or A1N-coated aluminium surfaces, Surf. Coatings Technol. 68/69 (1994) 507–511.

[2] J. Gallardo, A. Duran, I. Garcia, J.P. Celis, M.A. Arenas, A. Conde, Effect of Sintering Temperature on the Corrosion and Wear Behavior of Protective SiO2-Based Sol-Gel Coatings, J. Sol-Gel Sci. Technol. 27 (2003) 175–183.

[3] W. Walke, Z. Paszenda, M. Basiaga, P. Karasinski, M. Kaczmarek, EIS Study of SiO2 Oxide Film on 316L Stainless Steel for Cardiac Implants, in: E. Piętka, J. Kawa, W. Wieclawek (Eds.), Inf. Technol. Biomed. Vol 4., Springer International Publishing, Cham, 2014: pp. 403–410.

[4] W. Walke, Z. Paszenda, T. Pustelny, Z. Opilski, S. Drewniak, M. Ko, M. Basiaga, Evaluation of physicochemical properties of SiO2-coated stainless steel after sterilization, Mater. Sci. Eng. C. 63 (2016) 155–163.

[5] O. Santos, T. Nylander, R. Rosmaninho, G. Rizzo, S. Yiantsios, N. Andritsos, A. Karabelas, H. Müller-Steinhagen, L. Melo, L. Boulangé-Petermann, C. Gabet, A. Braem, C. Trägårdh, M. Paulsson, Modified stainless steel surfaces targeted to reduce fouling—surface characterization, J. Food Eng. 64 (2004) 63–79.

[6] R. Rosmaninho, O. Santos, T. Nylander, M. Paulsson, M. Beuf, T. Benezech, S. Yiantsios, N. Andritsos, A. Karabelas, G. Rizzo, H. Müller-Steinhagen, L.F. Melo, Modified stainless steel surfaces targeted to reduce fouling – Evaluation of fouling by milk components, J. Food Eng. 80 (2007) 1176–1187.

[7] K. Mohaghegh, H.N. Hansen, H. Pranov, G. Kofod, A study on the surface roughness of a thin HSQ coating on a fine milled surface, in: 14th Euspen Int. Conf. - Dubrovink, 2014.

[8] K. Mohaghegh, H.N. Hansen, H. Pranov, G. Kofod, Verification of thickness and surface roughness of a thin film transparent coating, in: Proc. 13th Euspen Int. Conf., Berlin, 2013.

[9] J. Cech, H. Pranov, G. Kofod, M. Matschuk, S. Murthy, R. Taboryski, Surface roughness reduction using spray-coated hydrogen silsesquioxane reflow, Appl. Surf. Sci. 280 (2013) 424–430.

[10] T.C. Hobæk, M. Matschuk, J. Kafka, H.J. Pranov, N.B. Larsen, Hydrogen silsesquioxane mold coatings for improved replication of nanopatterns by injection molding, J. Micromechanics Microengineering. 25 (2015) 035018 (9pp).

[11] L. Ćurković, H.O. Ćurković, S. Salopek, M.M. Renjo, S. Šegota, Enhancement of corrosion protection of AISI 304 stainless steel by nanostructured sol–gel TiO2 films, Corros. Sci. 77 (2013) 176–184.

[12] S. Li, J. Fu, Improvement in corrosion protection properties of TiO2 coatings by chromium doping, Corros. Sci. 68 (2013) 101–110.

[13] S.T. Döşlü, B.D. Mert, B. Yazıcı, Polyindole top coat on TiO2 sol–gel films for corrosion protection of steel, Corros. Sci. 66 (2013) 51–58.

[14] S. Meth, N. Savchenko, M. Koltypin, D. Starosvetsky, F.A. Viva, A. Groysman, C.N. Sukenik, Corrosion studies of stainless steel protected by a TiO2 thin film deposited on a sulfonate-functionalized self-assembled monolayer, Corros. Sci. 52 (2010) 125–129.

[15] G. Ruhi, O.P. Modi, I.B. Singh, Pitting of AISI 304L stainless steel coated with nano structured sol–gel alumina coatings in chloride containing acidic environments, Corros. Sci. 51 (2009) 3057–3063.

[16] D.C.L. Vasconcelos, J.A.N. Carvalho, M. Mantel, W.L. Vasconcelos, Corrosion resistance of stainless steel coated with sol–gel silica, J. Non. Cryst. Solids. 273 (2000) 135–139.

[17] M. Atik, P. de Lima Neto, L.A. Avaca, M.A. Aegerter, J. Zarzycki, Protection of 316L stainless steel against corrosion by SiO2 coatings, J. Mater. Sci. Lett. 13 (1994) 1081–1085.

[18] O. de Sanctis, L. Gomez, N. Pellegri, C. Parodi, A. Marajofsky, A. Duran, Protective Glass Coatings on Metallic Substrates, J. Non. Cryst. Solids. 121 (1990) 338–343.

[19] T. Hwang, H. Lee, H. Kim, G. Kim, Two layered silica protective film made by a spray-and-dip coating method on 304 stainless steel, J. Sol-Gel Sci. Technol. 55 (2010) 207–212.
[20] D. Pech, P. Steyer, J.-P. Millet, Electrochemical behaviour enhancement of stainless steels by a SiO2 PACVD coating, Corros. Sci. 50 (2008) 1492–1497.
[21] J. Foggiato, Chemical Vapor Deposition of Silicon Dioxide Films, in: Handb. Thin Film Depos. Process. Tech. (Second Ed., 2nd ed., Elsevier B.V., 2001: pp. 111–149.
[22] P. Møller, L.P. Nielsen, Physical Vapor Deposition, in: Adv. Surf. Technol. Vol 1, 2013: pp. 457–482.
[23] C.J. Brinker, G.W. Scherer, Hyrdolysis and Condensation of Silicon Alkoxides, in: Sol-Gel Sci., Academic Press, Inc., San Diego, 1990: pp. 108–216.
[24] H. Nagayama, H. Honda, H. Kawahara, A New Process for Silica Coating, J. Electrochem. Soc. 135 (1988) 2013–2016.
[25] D. Többen, P. Weigand, M.J. Shapiro, S.A. Cohen, Influence of the cure process on the properties of hydrogen silsesquioxane spin-on-glass, Mater. Res. Soc. Somposium Proc. 443 (1997) 195–200.
[26] M.J. Loboda, C.M. Grove, R.F. Schneider, Properties of a-SiOx:H Thin Films Deposited form Hydrogen Silsesquioxane Resins, J. Electrochem. Soc. 145 (1998) 2861–2866.
[27] Y.K. Siew, G. Sarkar, X. Hu, J. Hui, A. See, C.T. Chua, Thermal Curing of Hydrogen Silsesquioxane, J. Electrochem. Soc. 147 (2000) 335.
[28] J.N. Bremmer, Y. Liu, K.G. Gruszynski, F.C. Dall, Cure of Hydrogen Silsesquioxane for Intermetal Dielectric Applications, Mater. Res. Soc. Symp. Proc. 476 (1997) 37–44.
[29] S.K. Choi, Nanolitography and Nanofabrication using Hydrogen Silsesquioxane Resists (Dissertation), University of Illinois, 2009.
[30] F. Lampert, A.H. Jensen, R.U. Din, P. Møller, Hydrogen Silsesquioxane based silica glass coatings for the corrosion protection of austenitic stainless steel, Surf. Coatings Technol. 307 (2016) 879–885.
[31] F. Lampert, S. Kadkhodazadeh, A.H. Jensen, R.U. Din, P. Møller, Interfacial Interaction of Oxidatively Cured Hydrogen Silsesquioxane Spin-On-Glass Enamel with Stainless Steel Substrate, J. Electrochem. Soc. 164 (2017) C231–C239.
[32] F. Lampert, A.B. Christiansen, R.U. Din, Y. Gonzalez-Garcia, P. Møller, Corrosion Resistance of AISI 316L Coated with an Air-Cured Hydrogen Silsesquioxane Based Spin-On-Glass Enamel in Chloride Environment, Corros. Sci. (In Press. August 24th 2017). (2017).
[33] F.S. Shieu, M.J. Deng, K.C. Lin, J.C. Wong, J.Y. Wu, Effect of surface pretreatments on the adherence of porcelain enamel to a type 316L stainless steel, J. Mater. Sci. 34 (1999) 5265–5272.
[34] A. Stoch, J. Stoch, A. Rakowska, An XPS and SEMS study of silica sol-gel/metal substrate interaction, Surf. Interface Anal. 22 (1994) 242–247.
[35] M. Takemori, Crack formation, exfoliation, and ridge formation in 500 ^{o}C annealed sol-gel silica coatings on stainless steel SUS304: Part I. Microscopic observations and elemental analysis, Ceram. Int. 35 (2009) 1731–1746.
[36] M. Takemori, Crack formation, exfoliation, and ridge formation in 500 °C annealed sol–gel silica coatings on stainless steel SUS304: Part II Spectroscopic and mechanical analyses and insights into mechanisms controlling coating characteristics, Ceram. Int. 35 (2009) 1747–1755.
[37] E.C. Onyiriuka, L.D. Kinney, N.J. Binkowski, Adhesion and delamination of tantalum and chromium films on glass, J. Adhes. Sci. Technol. 11 (1997) 929–940.
[38] P. Benjamin, C. Weaver, The Adhesion of Evaporated Metal Films on Glass, Proc. R. Soc. London. Ser. A, Math. Phys. 261 (1961) 516–531.
[39] M. Peuker, M.H. Lim, H.I. Smith, R. Morton, A.K. van Langen-Suurling, J. Romijn, E.W.J.M. van der Drift, F.C.M.J.M. van Delft, Hydrogen SilsesQuioxane, a high-resolution negative tone e-beam resist, investigated for its applicability in photon-based lithographies, Microelectron. Eng. 61–62 (2002) 803–809.
[40] J.O. Andersson, T. Helander, L. Höglund, P.F. Shi, B. Sundman, Thermo-Calc and

DICTRA, Computational tools for materials science, Calphad. 26 (2002) 273–312.
[41] V.J. Keast, J. Bruley, Electron energy-loss near-edge structure - a tool for the investigation of electronic structure on the nanometre scale, J. Microsc. 203 (2001) 135–175.
[42] L.A.G. Garvie, P.R. Useck, Bonding in silicates : Investigation of the Si L 2,3 edge by parallel electron energy-loss spectroscopy, Am. Mineral. 84 (1999) 946–964.
[43] N. Jiang, J. Silcox, N. Jiang, J. Silcox, Observations of reaction zones at chromium / oxide glass interfaces, J. Appl. Phys. 87 (2000)
[44] P.E. Batson, Atomic Resolution Electronic Structure in Silicon-Based Semiconductors, J. Electron Microsc. (Tokyo). 45 (1996) 51–58.
[45] P.E. Batson, Simultaneous STEM imaging and electron energy-loss spectroscopy with atomic-column sensitivity, Nature. 366 (1993) 727–728.
[46] O.L. Krivanek, T.C. Lovejoy, N. Dellby, R.W. Carpenter, Monochromated STEM with a 30 meV-wide , atom-sized electron probe, Microscopy. 62 (2013) 3–21.
[47] D.J. Wallis, P.H. Gaskell, R. Brydson, Oxygen K near-edge spectra of amorphous silicon suboxides, J. Microsc. 180 (1986) 307–312.
[48] I. Davoli, E. Paris, E. Stizza, S. Benfatto, M. Fanfoni, M. Gargano, A. Bianconi, F. Seifert, Structure of Densified Vitreous Silica : Silicon and Oxygen XANES Spectra and Multiple Scattering Calculations, Phys. Chem. Miner. 19 (1992) 171–175.
[49] G.E. Brown, G.A. Waychunas, J. Stohr, F. Sette, Near-edge structure of oxygen in inorganic oxides: Effect of local geometry and cation type, Le J. Phys. Colloq. 47 (1986) C8-685-C8-689.
[50] P.A. van Aken, B. Liebscher, Quantification of ferrous / ferric ratios in minerals : new evaluation schemes of Fe L 23 electron energy-loss near-edge spectra, Phys. Chem. Miner. 29 (2002) 188–200.
[51] O.L. Krivanek, J.H. Paterson, ELNES of transition metal oxides I. Variations across the periodic table, Ultramicroscopy. 32 (1990) 313–318.
[52] J.H. Paterson, O.L. Krivanek, ELNES OF 3d TRANSITION-METAL OXIDES 2. Variations with oxidation state and crystal structure, Ultramicroscopy. 32 (1990) 319–325.
[53] L.A.G. Garvie, Can electron energy-loss spectroscopy (EELS) be used to quantify hydrogen in minerals from the O K edge?, Am. Mineral. 95 (2010) 92–97.
[54] H. Tan, J. Verbeeck, A. Abakumov, G. Van Tendeloo, Oxidation state and chemical shift investigation in transition metal oxides by EELS, Ultramicroscopy. 116 (2012) 24–33.
[55] A.M. Arévalo-López, M.A. Alario-Franco, Reliable Method for Determining the Oxidation State in Chromium Oxides, Inorg. Chem. 48 (2009) 11843–11846.
[56] M.D. Malinsky, K.L. Kelly, G.C. Schatz, R.P. Van Duyne, Nanosphere lithography: effect of substrate on the localized surface plasmon resonance spectrum of silver nanoparticles, J. Phys. Chem. B. 105 (2001) 2343–2350.
[57] E. Stoyanov, F. Langenhorst, The effect of valence state and site geometry on Cr L3,2 electron energy-loss spectra of Cr-bearing oxidic compounds, Chemie Der Erde - Geochemistry. 74 (2014) 497–505.
[58] F.M.F. de Groot, J.C. Fuggle, B.T. Thole, G.A. Sawatzky, 2p x-ray absorption of 3d transition-metal compounds: An atomic multiplet description including the crystal field, Phys. Rev. B. 42 (1990) 5459–5468.
[59] D. Lussana, D. Baldissin, M. Massazza, M. Baricco, Thermodynamic and kinetics aspects of high temperature oxidation on a 304L stainless steel, Oxid. Met. 81 (2014) 515–528.

Supporting information

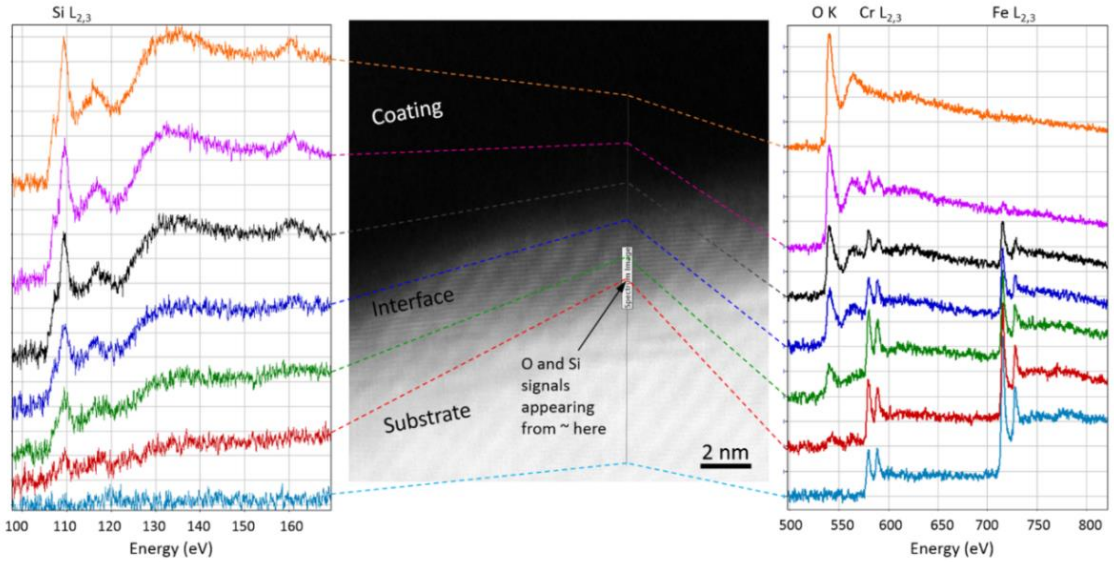

Figure S8.1: *HAADF STEM image of the coating on AISI 316L substrates in the cross-sectional geometry and EEL spectra collected at different points along a line across the interface. The measurements were recorded without the monochromator excited, giving better spatial resolution in STEM images compared to those presented in the manuscript. The interface is identified as the region containing Si, O, Cr and Fe and lattice planes in this region are clearly visible in the STEM image.*

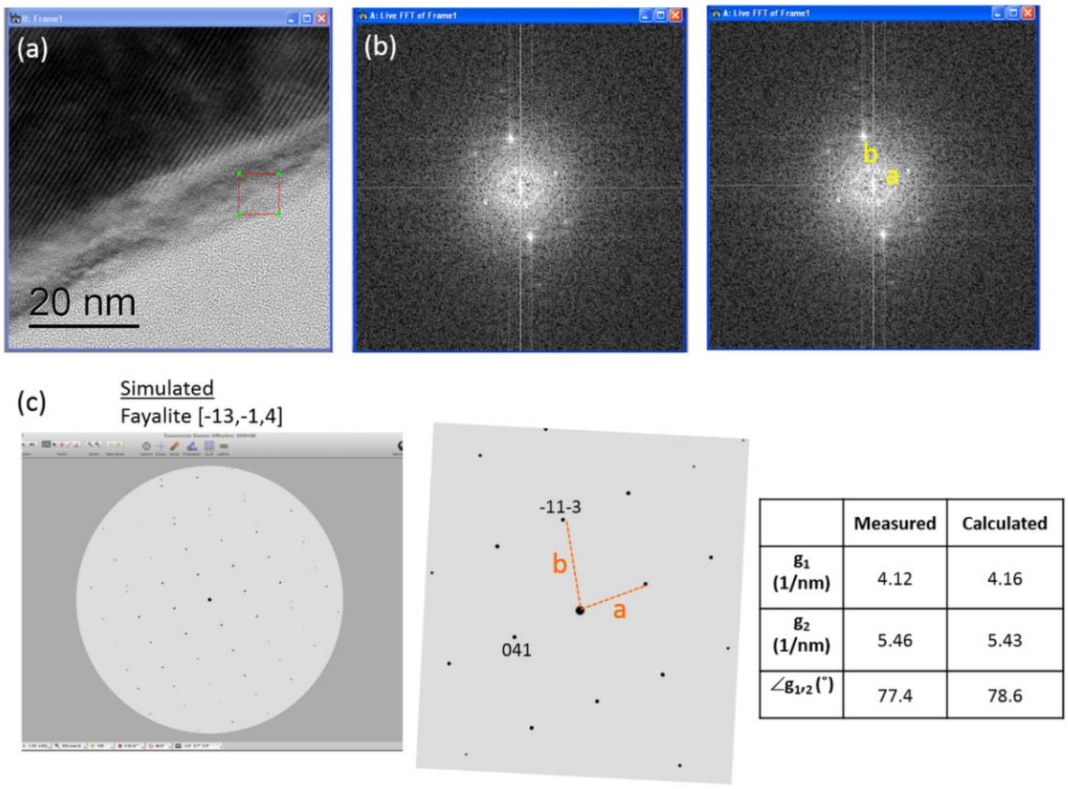

	Measured	Calculated
g_1 (1/nm)	4.12	4.16
g_2 (1/nm)	5.46	5.43
$\angle g_{1,2}$ (°)	77.4	78.6

Figure S8.2: *(a) HRTEM image of the coating on an AISI 316L substrate in the cross-sectional geometry. (b) FFT pattern acquired from a region within the interface marked with a box and (c) the simulation. The FFT pattern matches the pattern simulated for fayalite [-13,-1,4] using CrystalMaker and SingleCrystal software. The crystallographic parameters of fayalite were used from J.R. Smyth, Am. Mineral. 60, 1092 (1975).*

9 Manuscript V

Properties and performance of spin-on-glass coatings for the corrosion protection of stainless steels in chloride media*

Felix Lampert[a], Annemette Hindhede Jensen[b], Rameez Ud Din[a], Yaiza Gonzalez-Garcia[c], Per Møller[d]

[a] Technical University of Denmark, Department of Mechanical Engineering, 2800 Kgs. Lyngby, Denmark
[b] SiOx ApS, Bybjergvej 7, 3600 Espergærde, Denmark
[c] Delft University of Technology, Department of Materials Science and Engineering, 2628CD Delft, The Netherlands
[d] Technical University of Denmark (DTU), Department of Mechanical Engineering, Produktionstorvet, Building 425, 2800 Kgs. Lyngby, Denmark

Abstract

Spin-on-glass deposition was investigated as viable alternative to increase the durability and performance of 316L steel in chloride environment. The buildup of a detrimental interface oxide was prevented by non-oxidative thermal curing of the coatings, which leads to a transformation to an inorganic, SiO_2-like material. The degree of polymerization was found dependent on the curing temperature; however, curing at the maximum investigated curing temperature of 800 ºC led to an incomplete transformation, showing less SiO_2-like character with respect to thermally grown oxide or fused silica. Electrochemical analysis by electrochemical impedance spectroscopy and anodic cyclic polarization indicated that the coatings behave as imperfect barrier coatings, which may enhance the passive properties of the substrates. The coatings showed, in association with substrate defects, unevenly distributed coating flaws, which may act as initiation points for pitting corrosion and decrease the corrosion resistance of coated substrates in Cl^- containing media. The films showed instability in aqueous environment due to imperfect polymerization.

* unpublished work at date of submission. The final article may deviate from the herein presented manuscript.

9.1 Introduction

Gasketed plate heat exchangers are widely applied in *e.g.* generic heating or cooling systems in marine applications. Since the corrosion resistance of many alloys is strongly compromised in hot sea water, the application necessitates the use of highly corrosion resistant plate materials such as Ti-alloys, which exhibit outstanding performance in aggressive Cl^- containing media. Due to the high material cost, novel corrosion protection concepts are under investigation to enable the use of new and more cost efficient materials. In the present work, surface modified AISI 316L steel is investigated as potential candidate for the next generation heat exchanger plates. In our previous work [1], we have demonstrated the deposition of thin SiO_2-like coatings from a spin-on-glass (SOG) precursor as viable process to modify the surface of stainless steel components. The process of SOG deposition originates from the deposition of highly insulating interlayer dielectric films in microelectronics applications [2,3] and has recently emerged into the surface finishing industry due to its good applicability to metallic substrates and its high potential to modify the surface characteristics of the substrate [4–6]. Similar surface modifications by the incumbent processes (sol-gel, vapor or liquid phase deposition) have shown to improve the corrosion resistance [7–10], wear properties [11,12], surface roughness [13,14] and resistance towards biofouling [13,15] or biocompatibility [16,17] in the past. In analogy, SOG deposition is under investigation as viable surface modification to improve the corrosion resistance of the substrate [18], whilst significantly decreasing the surface roughness [4–6] and decreasing the susceptibility towards biofouling and scaling in heat exchanger applications.

The process generally relies on the deposition of a liquid hydrogen silsesquioxane (HSQ) containing precursor solution, followed by a thermal polymerization, forming a fully inorganic, SiO_2-like surface film [2,3,19,20], which offers potential advantages in processing cost, ease of application, reduction of hazardous reaction products or film quality with respect to the incumbent deposition processes [1]. Further, due to the gradual transformation from the resinous precursor to an inorganic ceramic, the process offers a wide range of possible coating properties, ranging from loosely bonded, hydrogenated films to highly polymerized and virtually hydrogen-free coatings [19,20].

Our recent studies of SOG curing in air [21,22] showed an extensive degradation of the substrate surface due to thermal oxidation at the coating/substrate interface. The buildup of a thick thermal oxide at the interface impaired the corrosion performance and coating adhesion of samples cured above 400 ºC and restricted the curing temperature and achievable degree of coating polymerization. Further, the coatings, suffered from inadequate chemical stability due to their loose cross-linking, and hence curing in air was found to be inappropriate for the polymerization of HSQ-based corrosion barrier coatings on stainless steel substrates. Our previous results [1] have shown that the formation of a thick interfacial reaction zone between the coating and substrate can be efficiently suppressed by lowering of the oxygen partial pressure in the curing atmosphere, enabling

the deposition of HSQ-based coatings without the unfavorable oxidation of the coating/substrate interface. Thus, curing in non-oxidative atmosphere revokes the restrictions in curing temperature and enables higher degrees of coating polymerization, *i.e.* potentially higher chemical coating stability.

Our recent investigations on air-cured SOG systems [21,22] emphasized that severe corrosive failure of inadequately coated stainless steels may be expected in Cl^- containing media. Since our previous investigation of non-oxidatively cured coatings was solely focused on curing at 500 ºC and electrochemical testing in Cl^- -free, buffered neutral solution [1], the successful application of the technology as coating for marine heat exchanger plates necessitates a comprehensive investigation of the corrosion performance as well as the coating properties over a broad curing temperature range and in Cl^- containing media. Further, the previously indicated poor chemical stability of loosely polymerized coatings was only studied on inhomogeneous and rough substrate, demanding for further systematic research to conclude on the chemical coating stability and the chemical coating breakdown of HSQ-based films in aqueous environment.

In this work, HSQ-based coatings were deposited on AISI 316L substrates and thermally polymerized in protective atmosphere at temperatures between 400 and 800 ºC to form highly cross-linked, sub-micrometer thick surface coatings. The coating morphology and microstructure was studied by atomic force microscopy and scanning/transmission electron microscopy. Further, the coating chemistry was characterized by infrared spectroscopy and X-ray photoelectron spectroscopy and the coating properties were investigated by water contact angle and nanoindentation measurements. Moreover, the barrier efficiency of the coatings was studied electrochemical impedance spectroscopy and the effect of coating on the substrate passivity was characterized by potentiodynamic cyclic polarization and spot-testing in aqueous NaCl solution. Lastly, the long term coating stability was investigated by ageing in a salt spray chamber.

9.2 Experimental

9.2.1 Thin film deposition

SOG films were deposited on AISI 316L substrates with no. 2B surface finish (dimensions: 100 x 50 mm^2 area and 1 mm thickness; chemical composition shown in Table 9.1 and Si-wafer (thickness 675 µm, front side polished, backside etched) substrates. The deposition was carried out by the process previously described by Lampert *et al.* [1], *i.e.* the deposition of a flowable oxide film (Dow Corning FOx 25) by dip-coating, followed by solvent evaporation (soft-bake) at 160 ºC for 0.5 h in an open furnace and thermal polymerization in a retort furnace under constant flow of 0.45 l/min Ar with addition of 0.05 l/min H_2 gas at atmospheric pressure. The annealing temperature of the polymerization treatment was varied between 400 and 800 ºC and the coated metallic substrates are designated with "sample *curing temperature*" in the following. The metallic substrates were prepared by immersion degreasing, followed by anodic

Table 9.1: *Chemical composition of the substrates (by Optical Emission Spectroscopy). In addition, traces (< 0.1 wt.%; > 0.01 wt.%) of P, Nb, V, W were detected.*

Element	Cr	Ni	Mo	Mn	Si	Cu	Co	N	C	Fe
Composition (wt.%)	16.8	10.4	2.07	0.92	0.47	0.41	0.21	0.048	0.019	bal.

degreasing and activation [22] and the Si substrates were cleaned by flushing in organic solvent. All substrates were allowed to dry in air before further processing. Generally, the substrates were dip-coated with 1 mm/s withdrawal rate; however, due to the particular needs for valid nanoindentation measurements, the withdrawal rate was increased to 5-10 mm/s for the samples used for nanoindentation. A SiO_2 reference was grown by wet oxidation of a Si wafer (thickness 500 µm, front side polished, backside etched) substrate under flow of 3 l/min H_2 together with 2 l/min O_2 at 1050 ºC, yielding an oxide thickness of 464 nm (measured by spectral reflectance).

9.2.2 Characterization

Coating microstructure and properties

Atomic force microscopy (AFM). Measurements were performed using a Bruker-Dimension Edge instrument (BRUKER AXS SAS, France) operating in tapping mode. The microscope was fitted with a Bruker model RTESP probe with a Sb doped Si cantilever with ~300 kHz resonance frequency.

Nanoindentation. Nanoindentation was performed on a CSM-Instruments system on thin films deposited on Si wafer. To avoid substrate-induced artefacts [23,24], an indentation depth/film thickness ratio of max. 1:10 was maintained for all films by varying the film thickness (thickness values of the measured films are shown in Table 9.2). An increase in film thickness beyond the values reported in Table 9.2 was impractical due to film fracture during curing. The system was operated with a Berkovich indenter at 0.5 mN maximum load and 1 mN/min linear loading/unloading rate. The indentation modulus was calculated as described by ISO 14577-1 [25] based on the indenter area function derived by the method described by Oliver *et al.* [26]. The indenter area function was calibrated on fused silica reference slide with a plane strain modulus of 75.2 ± 0.4 GPa (indentation modulus of 73.3 ± 0.4 GPa).

Electron microscopy. Scanning electron microscopy (SEM) was performed on a Helios Nanolab 600 dual beam microscope fitted with a field emission gun, Pt gas insertion system and a Ga^+-ion source. SEM images were acquired under 5 kV accelerating voltage with a through-lens detector and the beam currents indicated in the respective figure captions. Coating cross sections were prepared by Focused Ion Beam (FIB)-milling at 30 keV accelerating voltage. Prior to SEM analysis, the samples were sputter-coated with a conductive Au-film and the investigated areas were protected by a Pt deposition before

Table 9.2: *Final film thickness (determined from cross-sectional imaging on fractured wafers) of films used for nanoindentation.*

Curing temp. (ºC)	400	500	600	700	800
Thickness (µm)	1.41	1.16	0.89	0.89	0.82

ion beam milling. Transmission electron microscopy (TEM) was carried out on a FEI Tecnai T20 TEM fitted with a LaB_6 filament electron source operated at 200 kV. TEM lamellae were prepared by the method described by Lampert *et al.* [22].

Fourier transformed infrared spectroscopy (FT-IR). FT-IR was performed on a Thermo Scientific Nicolet iN10 MX in transmission mode on films deposited on Si-wafer (deposited by dip-coating at 1 mm/s withdrawal speed). The IR-background was acquired on an uncoated reference wafer.

X-ray photoelectron spectroscopy (XPS). XP-spectra were acquired on a Thermo Scientific K-Alpha$^+$ instrument fitted with a monochromated Al K-Alpha X-ray source at a photon energy of 1486.7 eV. The spectra were recorded under ultrahigh vacuum on a circular area with a diameter of 400 µm and with the use of a flood gun to compensate for surface charging. The peak fitting was performed using the commercial software Thermo Avantage 5.949.

Water contact angle. The water contact angle was measured on coated AISI 316L substrates on an Attension Theta contact angle meter by the sessile drop method, using a droplet volume of 10 µl at room temperature. The values reported herein are the standard deviated averages of five individual measurements.

Electrochemical/chemical properties

Spot testing. For spot testing, 5 g $K_3Fe(CN)_6$ was dissolved in 1 l of in 3.5 wt.% NaCl aqueous solution. The solution was deposited on the surface with a pipette and allowed to soak for 5 min. Afterwards the liquid was carefully removed with a pipette and the surface was allowed to fully dry in air prior to further investigation.

Anodic cyclic potentiodynamic polarization (anodic CP). Anodic CP was performed with an ACM Instruments GillAC potentiostat in a flat corrosion cell which suppresses localized corrosion at the crevice between the rubber gasket and substrate [27]. The measurements were conducted in 400 ml of 3.5 wt.% NaCl aqueous solution on an area of 1 cm^2. The system was excited with a Pt counter electrode and the potential was measured with a KCl saturated Ag-AgCl electrode. The measurements were performed after a settling time of 3600 s with a scan rate of 1 mV/s. The experiments were repeated at least three times for consistency.

Electrochemical impedance spectroscopy (EIS). EIS data acquisition was performed on a Gamry Ref600 potentiostat in a flat cell with 2.1 cm^2 sample area and in 15 ml of 3.5 wt.% NaCl aqueous solution. The potential was measured with a saturated calomel electrode (SCE) and perturbed by a Pt counter electrode with an amplitude of 10 mV around the open circuit potential after a cell settling time of 3600 s. The data analysis was carried out by the electrical equivalent circuit approach with the commercial software Gamry Echem Analyst V 6.31. Data validation was carried out by an automatic Kramers-Kronig test and conversion between constant phase elements and equivalent capacitance was carried out by the approach presented by Hsu *et al.* [28]. The individual measurements were repeated five times for consistency.

Accelerated corrosion testing. Coatings on stainless steel substrates and films on Si-wafer (HSQ-based films were deposited by dip-coating at 1 mm/s withdrawal speed) were artificially aged by neutral salt spray testing according to ISO 9227 [29]. The coatings on stainless steel were investigated after ageing for 1000 h and the films deposited on Si wafers were periodically investigated in two-week intervals with a maximal ageing time of six weeks.

9.3 Results and discussion

9.3.1 Coating topography

The surface morphology of a coated substrate (sample 600) has been studied by AFM and compared to an uncoated reference substrate, as presented in Figure 9.1(a). The reference exhibits roughness average of R_a = 38.9 nm with flat plateaus on the hills, which are separated by the characteristic valleys along the grain boundaries from the descaling step during sheet metal production [30] (Figure 9.1(a)). However, this absolute roughness is, to a large extend, constituted by the grain narrow and deep boundary valleys which partially undercut the grains [1] and limits the roughness profile determination by the applied method. As previously shown on coating cross sections [1], the coating deposition from a liquid allows for flow of the precursor into substrate defects, yielding an overall decrease in R_a surface roughness by 60.4 % to R_a = 15.4 nm (calculated from Figure 9.1(b)). Despite the excellent leveling capability, the grain boundary structure from the substrate protrudes through the coating and constitutes the major contribution to the overall surface roughness (Figure 9.1(b)). To determine the physical roughness of the spin-on-glass coating, the coating topography was acquired on a near-planar coating region and the residual waviness imposed from the substrate was levelled and filtered by 2D Fast Fourier Transform Filtering. Without influence from the substrate, the coating shows nanometer-scale topography with a R_a roughness of 0.19 nm (Figure 9.1(c)).

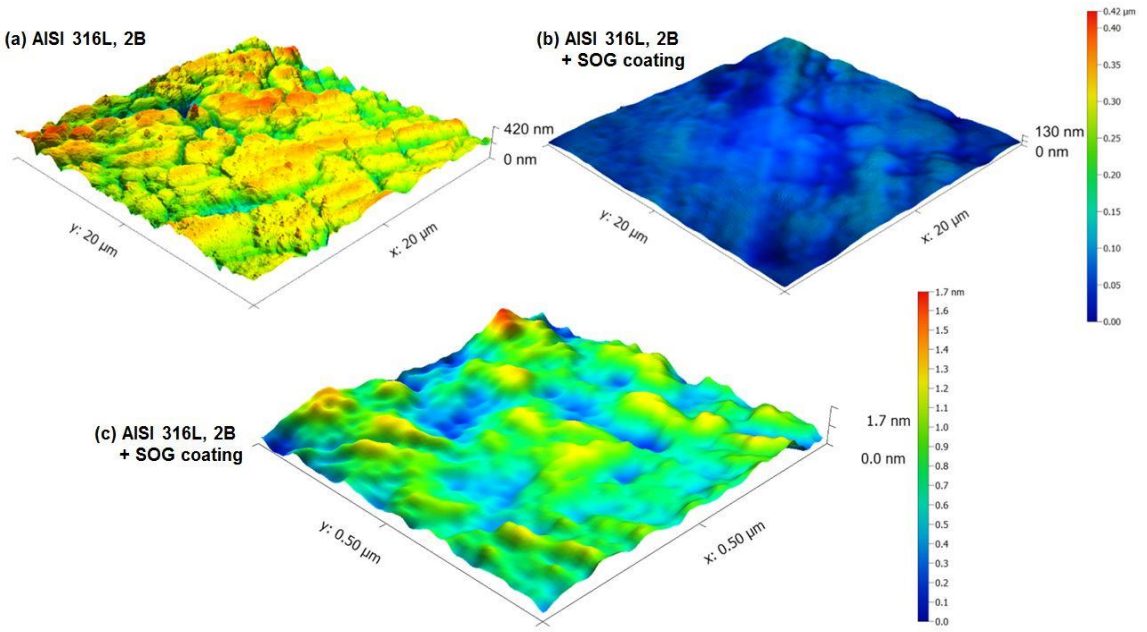

Figure 9.1: *AFM plots of (a) uncoated reference coupon, map size 20x20 µm^2; (b) SOG coated substrate, map size 20x20 µm^2; (c) SOG coated substrate (high magnification), map size 0.5x0.5 µm^2.*

Overall, the coating morphology deviates from the morphologies that can be achieved by competitive processes such as chemical vapor deposition [13], which does not significantly level substrate roughness, or liquid phase deposition [31], which yields inherently rough films. Due to the similarities in process characteristics, SOG-deposition shows similarities in surface morphology to sol-gel silica [13], which has previously shown excellent substrate levelling and a decrease in R_a roughness of 45 % with respect to untreated 2B finished stainless steel. These results have a strong impact on the prospective application of the technology on heat exchanger plates, since the surface roughness is expected to strongly affect the adherence of contaminants such as inorganic deposits or biological films and the cleanability of the components. Further detailed investigations are necessary to verify this hypothesis.

9.3.2 Film and interface chemistry

The coating microstructure with focus on the interface between coating and substrate has been investigated by TEM and a bright field micrograph of a coating cross-section is shown in Figure 9.2. The coating/substrate transition is rendered sharp in the micrograph, indicating that the curing process has successfully suppressed the buildup of a unfavorable, thick interfacial oxide, like it was previously reported for air-cured HSQ-based enamels [21,22].

Further, the coating chemistry was characterized by FT-IR and the FT-IR absorbance spectra of all curing conditions, together with an absorbance plot of a thermally grown SiO_2 are shown in Figure 9.3(a). The spectral features were identified based on the data

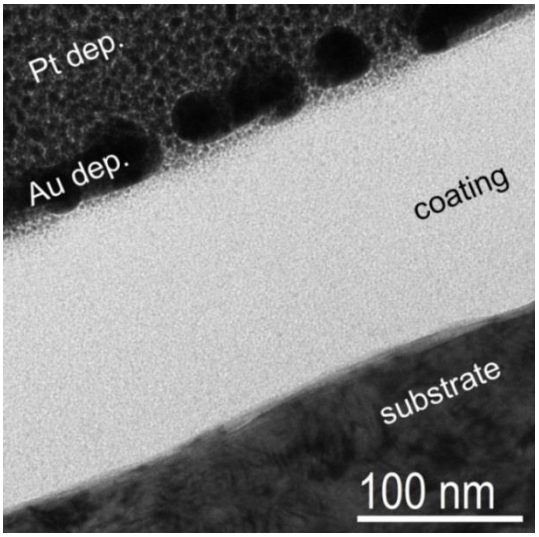

Figure 9.2: *Bright-field TEM image of the coating (cured at 600 ºC) on AISI 316L substrate in cross-sectional geometry.*

reviewed by Lampert *et al.* [21]. In agreement with other groups [2,32], the thermal treatment leads to a distinct shift from HSQ-cage- to ladder-structure (*i.e.* polymerization of the oligomeric precursor), together with a distinct decrease in intensity of the Si-H stretching vibration and the various bending vibrations below 950 cm^{-1} wavenumber. Similar to previous reports [2,3,21], the degree of polymerization is assessed based on the normalized integrated Si-H stretching absorption, as shown in Figure 9.3(b). The residual Si-H absorption decreases to 72% for curing at 400 ºC and to 0 % for curing at 700 ºC, indicating a significantly increased thermal budged of the process with respect to curing in air ambient [21] and the formation of virtually hydrogenation-free oxides for curing above 700 ºC. Furthermore, hydroxylation, based on a broad absorption band between 3200 and 3660 cm^{-1} wavenumber [33,34], is evident for films cured at 600-700 ºC. As visualized in Figure 9.3(b), the film cured at 600 ºC shows a significantly increased integrated area of the hydroxyl absorption feature with respect to the film cured at 700 ºC, indicating an increased silanol content [35]. The presence of hydroxyl in non-oxidatively cured HSQ-based films has been previously observed by other groups [20], who have hypothesized that the hydroxylation originates from rapid water uptake of the incompletely polymerized films after curing. In comparison to the thermal oxide, the film cured at 800 ºC retained a vibrational feature at 878 cm^{-1} wavenumber (circled feature in Figure 9.3), which has previously been assigned to the Si-H bending vibrations [32,36] in a Si-rich oxide. Further, the feature indicates that, despite the complete loss of the Si-H stretching feature, even films cured at 800 ºC contain a minor degree of hydrogenation and are, thus, incompletely transformed to SiO_x.

The film stoichiometry after the maximum expected conversion (800 ºC) has been investigated by XPS and compared to the thermally grown oxide. The emissions were fit on a Shirley-type background and routinely deconvoluted into the Si $2p_{1/2, 3/2}$ spin-orbit components (Figure 9.4) with a peak-to-peak offset of 0.63 eV. Surface charging was

referenced to the adventitious C1s, C-C, peak at 284.8 eV. The thermally grown oxide is fit to a single set of partner lines with a Si $2p_{3/2}$ peak position of 103.3 eV, indicating the presence of stoichiometric SiO_2 (Figure 9.4 (a)) [37,38]. Similarly, the Si $2p_{3/2}$ peak position for the HSQ-based oxide (Figure 9.4(b)), indicates the presence of SiO_2; however, the peak shoulder on the low binding energy side of the dominating emission reveals a divergence from the thermal oxide. In analogy to previous investigations [39,40], the shoulder is interpreted as Si emission due to the formation of Si nano-domains in the film and fit to a set of partner lines with a Si $2p_{3/2}$ peak position of 99.5 eV [41–43]. Apart from S^{4+} and Si^0 -emissions, the deconvolution of the Si 2p emission reveals a further spin-orbit couple with a Si $2p_{3/2}$ peak position of 101.5 eV. In agreement with previous investigations [42,44], we correlate the 101.5 eV peak to Si^{2+}, indicating the presence of Si-sub-oxides, such as SiO.

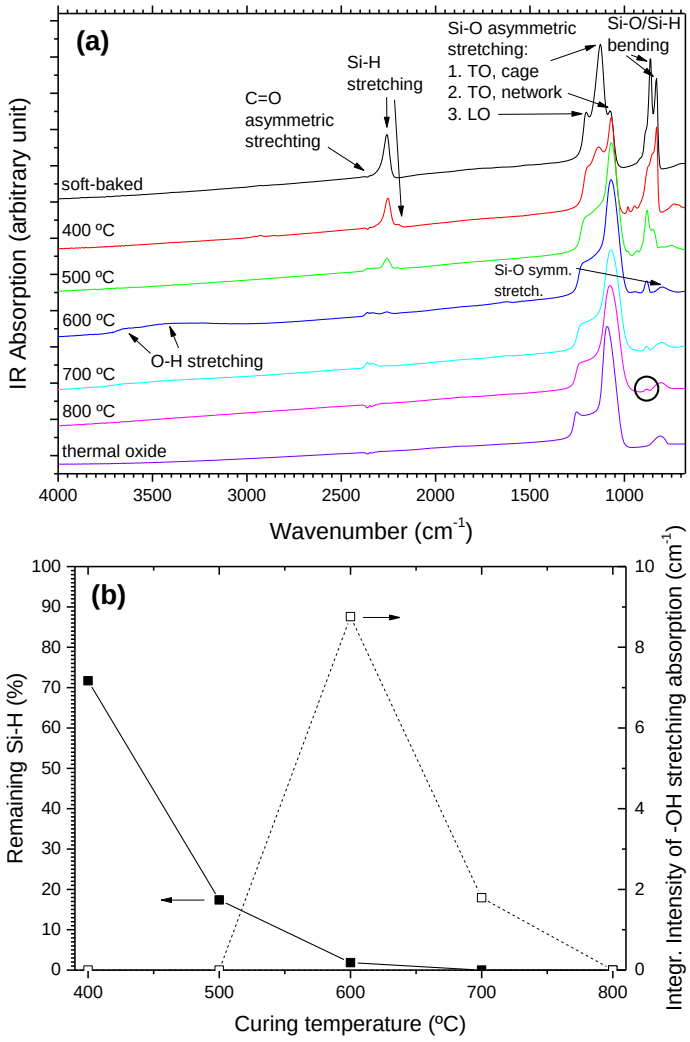

Figure 9.3: *(a) FT-IR absorption spectra of HSQ films deposited on Si wafer after curing at various temperatures. The identification of the spectral features was carried out according to the data reviewed by Lampert et al. [21]; (b) Remaining percentage of Si-H based on the Si-H stretching absorption edges at 2260-2285 cm^{-1} observed in FT-IR.*

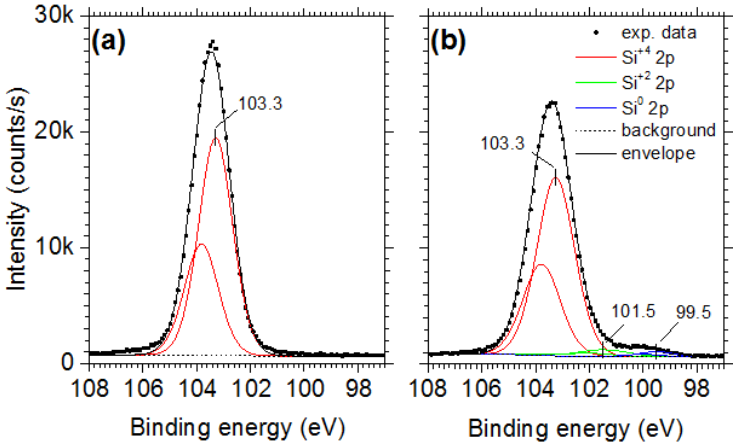

Figure 9.4: *Deconvolution of Si 2p emissions: (a) Thermal oxide; (b) HSQ-resin after curing at 800 ºC.*

9.3.3 Film hydrophobicity

A plot of water contact angle vs. curing temperature is shown in Figure 9.5. Samples 400-500 show a decreasing water contact angle with increasing curing temperature; however, hydrophobic behavior (contact angle >90 º). For sample 600, the average contact angle steeply decreases to 57 º, followed by a local minimum for sample for sample 700 (average 44.5 º). Further, an increase in the curing temperature leads to a recovery in average contact angle to 57 º for sample 800. In agreement with earlier observations [3,21], the hydrophobicity of HSQ-based coatings primarily depends on the competition between water repellency from non-polar Si-H bonds and water attraction from polar silanol. While samples 400 and 500 appear hydrophobic due to their high Si-H ratios, the samples cured at higher temperatures retain less hydrophobic character, due to their high degree of Si-H dissociation in combination with the formation of silanol. Hereby, the local minimum in contact angle of sample 700 likely arises from hydrophilicity due to the presence of polar silanol under absence of retained Si-H.

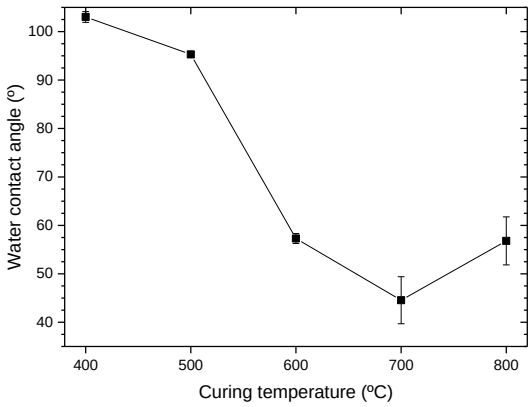

Figure 9.5: *Water contact angle vs. curing temperature on coated AISI 316L substrates.*

9.3.4 Mechanical properties

The mechanical properties, *i.e.* the film hardness and the elastic modulus, have been determined on films deposited on Si wafer by depth-sensing nanoindentation. Representative load vs. displacement curves for all curing conditions and a fused silica reference slide are shown in Figure 9.6(a). Clearly, all curves show hysteretic behavior without sudden compliance changes and non-linear unloading, indicating the typical elastic/plastic behavior expected for amorphous SiO_2 [26]. In agreement with the spectroscopic analysis, increasing the curing temperature increases the SiO_2-like character of the films; however, the curve-shape does not fully converge towards the shape determined for the thermally grown oxide. The load vs. displacement curves shown in Figure 9.6(a) were analyzed with the routine outlaid by Oliver *et al.* [26], requiring the assumption of a Poisson's ratio for the calculation of the indentation modulus. Liou *et al.* [19] assumed a Poisson's ratio of 0.33 for HSQ-based films irrespective of the degree of polymerization, which conflicts with the observation that high temperature-cured HSQ-based films behave strongly SiO_2-like (the Poisson's ratio of amorphous silica is 0.17 [26,45]). Consequently, we propose that the Poisson's ratio assumed by Liou *et al.* [19] is an overestimate for the SiO_x-like films investigated in this study and we suggest, in analogy to the value determined by other groups for generic SOG films [45,46], a Poisson's ratio of 0.25 for further analysis.

The indentation moduli for the investigated films are, together with the indentation hardness, plotted in Figure 9.6(b). Both, the indentation modulus and the indentation hardness obtained for the fused silica slide are within the previously reported range for SiO_2 [23,24,26,47], validating the accuracy of the applied method. Further, in agreement with previous results [19], both the indentation modulus and hardness increase with curing temperature. However, the quantification conflicts with the data presented by Liou *et al.* [19] and we report significantly more compliant and softer properties for the films

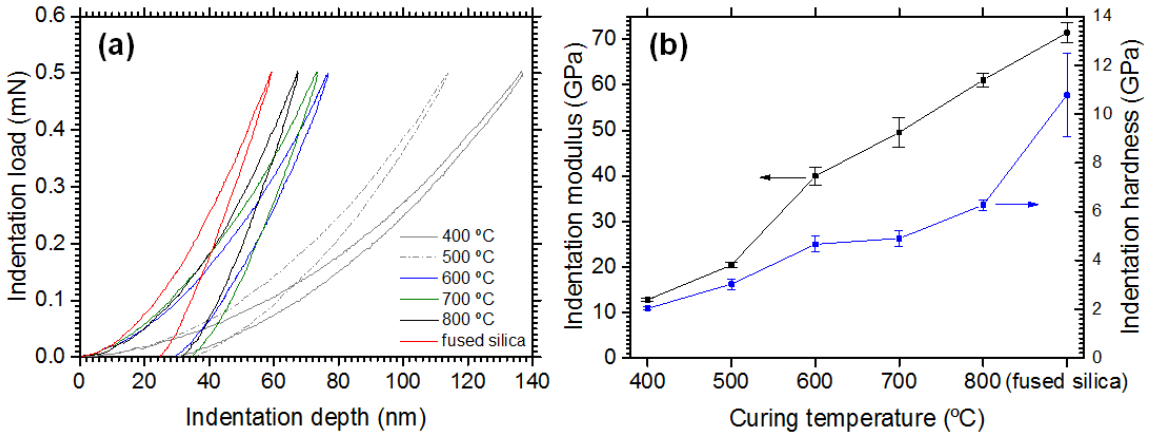

Figure 9.6: *(a) Indentation load vs. displacement curves determined on HSQ-based films and fused silica as reference. (b) Indentation modulus for different curing treatments. The error bars indicate the standard deviation over 5 individual measurements.*

cured at high temperature. The observed deviation may originate from differences in curing conditions and applied indentation loads or, since the group used a simplified model for the indenter-area function, differences in analysis procedure.

Overall, the distinctly more compliant behavior together with the decreased indentation hardness of the film cured at 800 ºC with respect to the fused silica reference indicates, in agreement with the spectroscopic analysis, weaker polymerization or incomplete densification [24], even at the highest investigated curing temperature.

9.3.5 Electrochemical barrier properties

The coating barrier properties were evaluated by EIS and a representative EIS Bode plots for determined on sample 400, 600, 800 and an uncoated reference is shown in Figure 9.7. Samples 500 and 700 showed equivalent results and were excluded from the plot. In accordance with previous investigations [1,21], the experimental data of the coated samples were fit as a porous coating with the electrical equivalent circuit R_s-(Q_{coat}(R_p-(Q_{dl}(R_{ct}-W)))) and the reference with a Randles equivalent circuit [48]. The results of the equivalent circuit fit are indicated by the solid lines in Figure 9.7. Further, the standard deviated average fitting results (based on five measurements) are plotted vs. the curing temperature in Figure 9.8. As visible from Figure 9.8(a), the charge transfer resistance stays constant over curing temperature within the given certainty limit. Similarly, the average pore resistance stays constant, with exception of sample 700, where the pore resistance is decreased with respect to the other curing temperatures. In analogy to our previous investigation [21], the coating capacitance increases with curing temperature (Figure 9.8(b)), which is presumably due to an increase in coating density [3,49,50], hydroxylation [3] and water uptake [51–53]. The double layer capacitance (Figure 9.8(c))

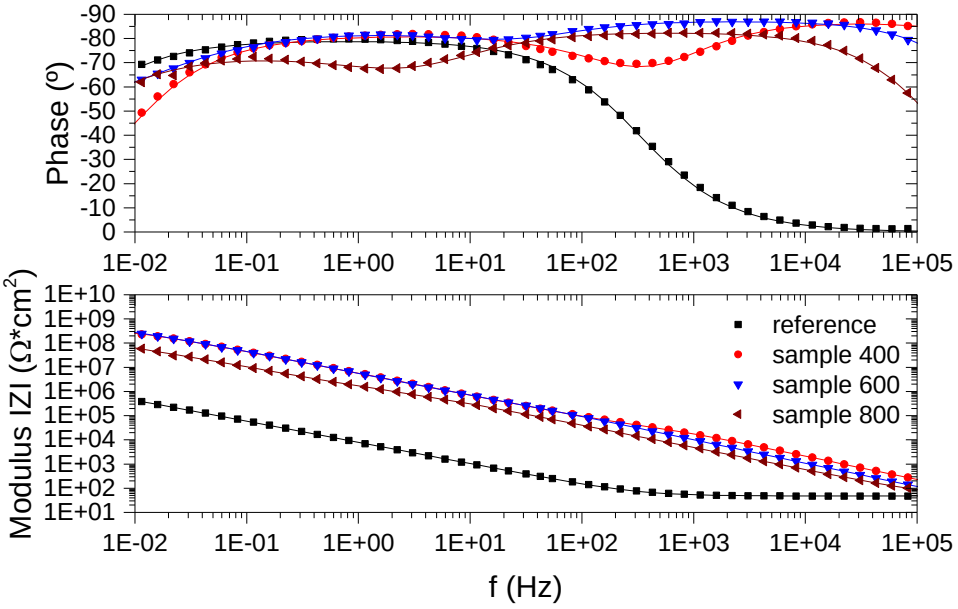

Figure 9.7: *EIS Bode plots of test coupons in 3.5 wt.% NaCl aqueous solution. The solid lines are on the basis of the fitted model.*

remains, with exception of sample 700, constant throughout the curing temperature range, indicating good and virtually constant substrate coverage, while the strayed value obtained for sample 700 is in agreement with the decreased pore resistance. Considering both the coating density and hydrophobicity as governing factors for the barrier efficiency, the strayed value may originate from an unfavorable combination of hydrophilic behavior (Figure 9.5) together with incomplete polymerization.

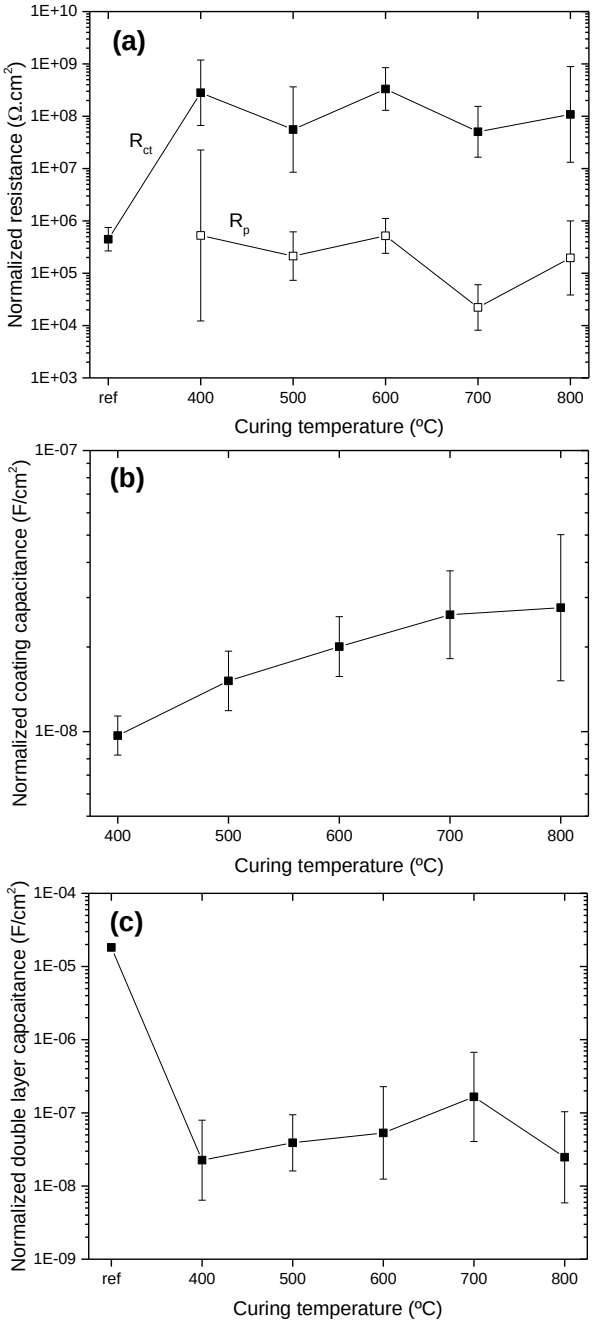

Figure 9.8: *Results of EIS fits vs. curing temperature: (a) Normalized pore/charge transfer layer resistance (R_p/R_{ct}); (b) Normalized coating capacitance, C_{coat}; (c) Normalized double layer capacitance, C_{dl}. The values represent average values of 5 measurements with the indicated standard deviation.*

Overall, the resistive coating behavior appears increased with respect to the previously reported air-cured films [21] (with exception of sample 700). This increase in coating performance may originate from an increased hydrophobicity for the temperature regime from 400-600 ºC and an increased coating density at high curing temperatures. Since the data allow a clear distinction between coating and charge transfer resistance, the coating acts as an imperfect barrier and clearly possesses defects which allow electrolyte transfer to the substrate. Thus, the coating quality clearly deviates from *e.g.* CVD-based SiO_x coatings on mirror polished substrates, which have previously shown perfect barrier performance with a single capacitive plateau over the entire frequency domain [7]. The nature of the given defects cannot be determined solely based on EIS analysis; however, the significant experimental error observed from Figure 9.8 indicates that the coating defects are unevenly spread over the surface, *i.e.* originate from inhomogeneous coating imperfections such as cracks, pinholes or delamination.

9.3.6 Passivity breakdown

It was shown by EIS that the coated substrates have access to the electrolyte. Hence, an electrochemical response of the substrate at externally imposed polarization is expected and the coated substrates were, together with an uncoated reference substrate, investigated by anodic CP. As reference, a representative polarization curve of an uncoated substrate is indicated in in all potential vs. current diagrams in Figure 9.9. Similar to our previous investigation, the reference material shows a clear hysteresis loop with a distinct breakdown and re-passivation at the corrosion potential together with current transients from metastable pit formation [54] below the breakdown potential (Figure 9.9(a-c)). The reference measurements showed excellent repeatability with an average breakdown potential of 529 mV vs. Ag-AgCl at a standard deviation of 24 mV (at a population of six measurements). Generally, the coated samples show a significant decrease in corrosion potential. In analogy to a previous study [7], we suggest that the decrease in corrosion potential originates from a locally changed electrolyte composition in microscopic coating defects; however, due to the significant changes in both passive layer composition and morphology [55], we cannot exclude that the potential shift originates from an alteration of the electrochemical characteristics of the substrate. In contrast to the uncoated reference, the coated samples show a significant spread in breakdown potential. Representative CP plots of samples 400, 600 and 800 are shown in Figure 9.9(a-c). Since samples 500 and 700 showed qualitatively similar behavior, representative curves for these samples are omitted from the plots.

In agreement with other groups [7,56–58], the application of the coating reduces the passive current density, indicating a reduction of the exposed substrate surface. Analysis of sample 400 (Figure 9.9(a)) shows a general increase in breakdown potential with respect to the reference together with depression of metastable pitting during the positive sweep, indicating excellent barrier efficiency of the coated system. Similarly, an increase in breakdown potential is observed for sample 600, as shown by curve A in Figure 9.9(b).

The increase in breakdown potential is inconsistent and, as shown by curve B, the surface treatment may decrease the breakdown potential and initiate pronounced current transients below the breakdown potential. A further increase in curing temperature, as in the case of sample 800 (Figure 9.9(c)), yields similar behavior, *i.e.* a possible anodic shift in breakdown potential (curve A), together with a possible cathodic shift in breakdown potential (curve B). The increased performance obtained over the entire curing temperature range demonstrates that well-functioning coatings may efficiently suppress the initiation of pitting corrosion. Similar observations have been previously reported for a variety of silica coatings on stainless steels [7,9,12], together with the herein observed

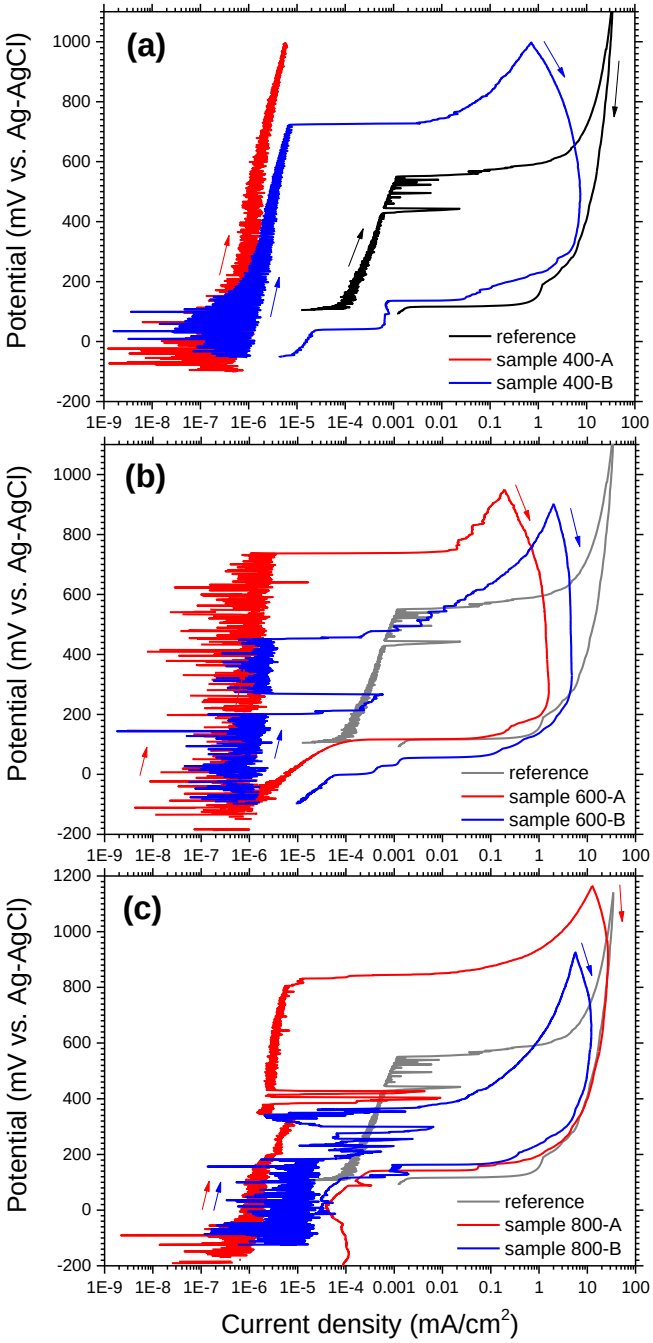

Figure 9.9: *Anodic CP curves in neutral 3.5 wt.% NaCl aqueous solution: (a) sample 400; (b) sample 600; (c) sample 800. The reference is indicated in all figures.*

fluctuations in breakdown potential [7]. The fluctuations were previously presumed to be due to a large disparity of the dielectric coating rigidity, which may induce local coating breakdown at varying potentials. However, negative-shifts in breakdown potential or pronounced current transients on the forward sweep were not reported [7]. Hence, the herein observed deterioration in passive properties cannot be explained solely by the previously outlaid dielectric film breakdown theory [7]. Other authors [59] reported substrate sensitization due to carbide precipitation as failure mechanism of sol-gel coated stainless steels after high temperature sintering. The effect can, however, be neglected due to the low carbon content of the herein used substrates (Table 9.1), which is expected to prevent carbide sensitization within the applied temperature range and the short applied curing times [60]. Consequently, we suggest, in analogy to the breakdown theory previously outlaid for air-cured HSQ-based coatings [21], that the coating may act as micro-crevice or stable pit cover at microscopic coating defects.

To conclude on the nature of the preliminary breakdown and potential coating defects, sample 600 has been investigated by spot testing in 3.5 wt.% NaCl aqueous solution with addition of $K_3Fe(CN)_6$. The sample shows a clear response to the indicator solution after 5 min of immersion in form of irregularly distributed precipitation of blue pigment (Figure 9.10(a)), indicating the local release of Fe^{2+} through the coating due to the initiation of localized corrosion. The localized pigmentation was analyzed by ion beam cross-sectioning (Figure 9.10(b)). Although not shown here, the analysis was repeated on several spots and the following observations were found to be reproducible. Void formation between the coating and the substrate in interrelation with coating delamination is visible in the immediate vicinity of the pigment, supporting the hypothesis of micro-crevice corrosion at microscopic coating defects. Further, the defect is observed directly at a grain boundary, *i.e.* at a particularly large coating cross-section induced by substrate roughness. The exact origin for the coating delamination was not investigated in this study; however, we suggest that the observed coating failure roots from inappropriate pretreatment, leading to residual surface contamination in narrow surface voids, mismatch in thermal expansion coefficient between the resinous HSQ and the substrate, or stress due to volumetric shrinkage of the coating.

Based on the observation of pronounced metastable pitting during anodic polarization and the localized release of Fe^{2+} at microscopic coating delamination, we propose the failure mechanism schematically illustrated in Figure 9.11: The coating delaminates at a substrate defect such as a grain boundary valley. The so created micro-crevice fills up with electrolyte through a coating defect such as a micro-fissure or general coating porosity and is subsequently acidified in analogy to conventional crevice corrosion theory (i) [61]. As the occluded anodic site evolves in size, the coating may rupture, leading to dissolution of the aggressive crevice electrolyte, and consequently re-passivation (ii). Alternatively, the coating is sustained during the growth of the anodic site, yielding a large subsurface pit, which may eventually grow to a sufficient size to sustain stable growth after rupture of the covering coating (iii).

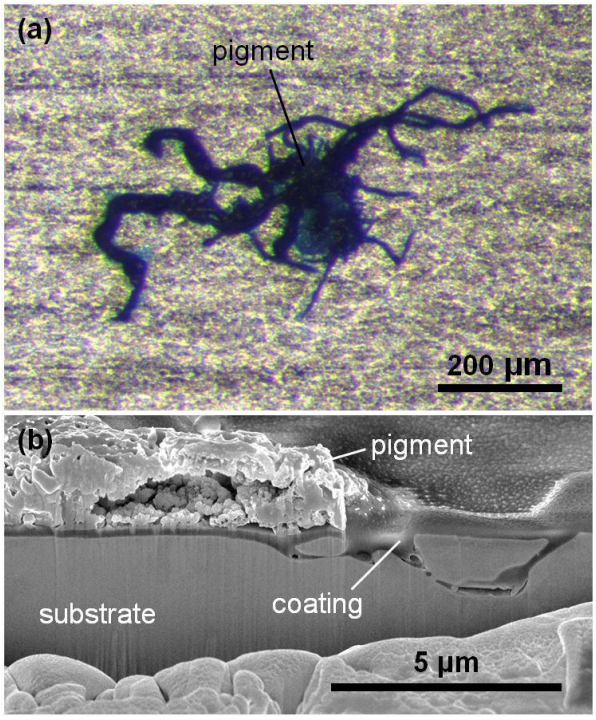

Figure 9.10: *Spot test on sample 600: (a) Top view optical micrograph of a pigment precipitated within the spot test on sample 600; (b) SEM image of ion beam milled cross section along pigment precipitation. Microscope settings: beam current 43 pA.*

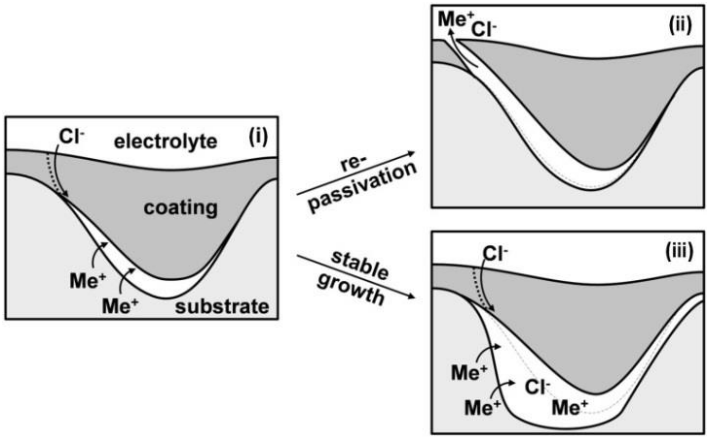

Figure 9.11: *Schematic illustration of micro-crevice corrosion at delaminated coating cross-sections.*

Overall, the results emphasize the importance of the substrate finish and pretreatment on the performance of (sub-) micron barrier coatings, showing that *e.g.* excessive substrate roughness may lead to preliminary coating failure. Further, the results indicate that HSQ-based coatings pose a viable solution to increase the corrosion performance of stainless steels in the absence of coating defects. Since the defects were associated with the substrate roughness, we propose that the preliminary failure may be eliminated by the use of a higher-grade substrate finish, yielding more reliable coating systems.

9.3.7 Chemical coating stability

In our previous study [21] it was suggested that HSQ-based coatings are, dependent on the degree of polymerization, chemically unstable during ageing under salt spray testing conditions. To analyze the coating dissolution rate, a thermal oxide grown on Si-wafer and HSQ-based films cured between 400 and 800 ºC were aged by neutral salt spray testing and periodically analyzed by (FIB-)SEM. The ion beam milled cross sections of the oxides at the initial state (reference) and terminal state (full dissolution or end of the experiment) are shown in Figure 9.12. The respective reduction in film thickness vs. ageing time is plotted in Figure 9.13(a). All HSQ-based films show a significant decrease in thickness, leading to full dissolution of the films cured at 400 ºC (after 2 weeks of ageing) and 500 ºC (after 4 weeks of ageing) together with a partial dissolution of the films cured above 500 ºC. Moreover, the remaining films show a homogeneous coverage, indicating that the material dissolution occurs from the film surface, leading to successive material removal and thinning on the films. In agreement with our previous observations [21], the dissolution rate (indicated in Figure 9.13(b)) correlates with the curing temperatures, whereby higher curing temperatures yield higher coating stabilities. The dissolution of the thermal oxide is insignificant.

Amorphous SiO_2 is thermodynamically unstable in aqueous solution at 35 ºC and may dissolve into silicic acid under the given test conditions (Figure 9.14). This is in agreement with results from Deltomee *et al.* [62], who stated that silica dissolves into

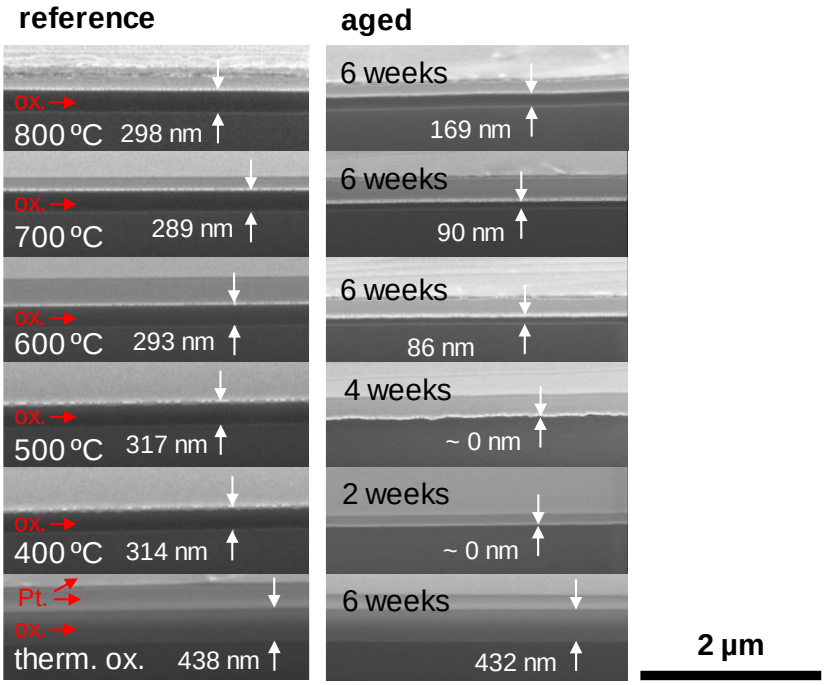

Figure 9.12: *SEM analysis on ion beam etched cross sections of HSQ-based films cured at different temperatures and thermal oxide grown on Si-wafer substrate before (reference) and after ageing by neutral salt spray testing. "ox." indicates the thermal/SOG oxide layer. All films were protected by a double layered Pt. deposition ("Pt") during analysis. SEM settings: beam current 26 pA.*

various forms of silicic acid in neutral aqueous solution, whereby the solubility is significantly increased for the amorphous silica polymorphs with respect to the crystalline ones. Moreover, previous groups [63,64] have shown that the dissolution kinetics of SiO_2 films in near neutral solution may be significantly increased for SiO_x films of poor quality. As revealed by IR-spectroscopy, film curing up to 700 ºC leads to films defects, such as significant hydrogenation or film hydroxylation. Even for the films cured at 800 ºC, the spectroscopy analysis indicated a minor degree of hydrogenation together with the presence of Si-sub-oxides while the nanoindentation analysis revealed inferior mechanical properties with respect to fused silica, and thus indicated weaker cross-linking or a decreased film density [24]. Overall, the coating analysis indicated an imperfect transformation of the resin to SiO_2 or an incomplete densification for HSQ-based films for curing temperatures ≤ 800 ºC, which may greatly account for the advanced dissolution speed of the HSQ-based films with respect to the thermally grown oxide.

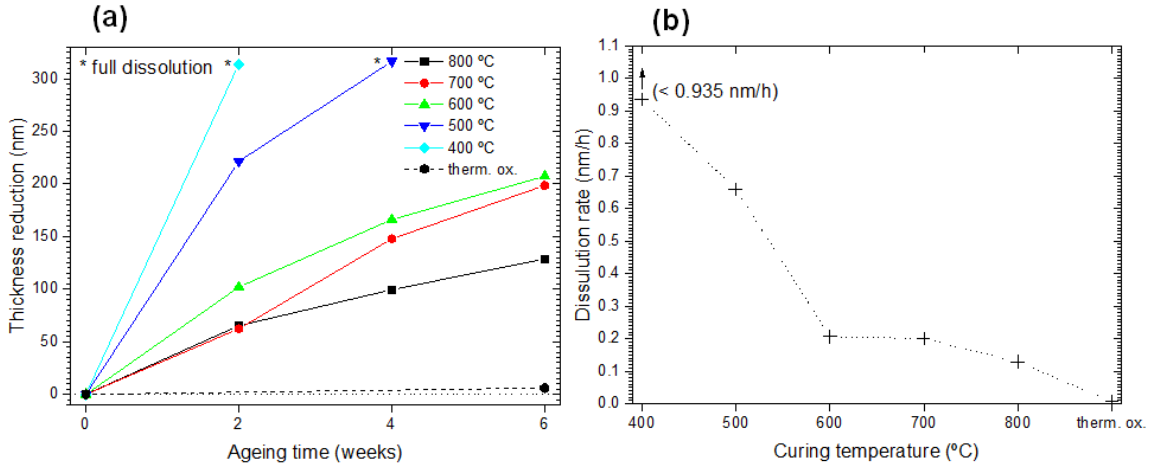

Figure 9.13: *(a) Thickness reduction vs. ageing time based on SEM analysis; (b) Dissolution rate vs. curing temperature. The rates for curing from 400-500 ºC were calculated based on 2 weeks of ageing and the rates for curing from 600-800 ºC and the thermal oxide were calculated based on 6 weeks of ageing.*

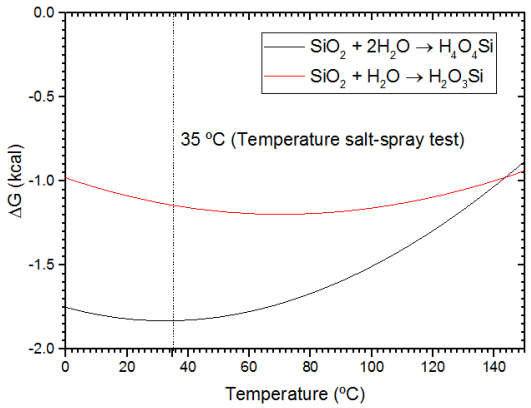

Figure 9.14: *Free energy vs. temperature for the dissolution of amorphous silica to silicic acid. Calculated with HSC Chemistry 5.11.*

In analogy to our previous work [21], the coated stainless steel substrates have been subjected to 1000 h of salt spray testing and investigated by FIB-SEM to conclude about the film chemistry in the application. Cross-sectional micrographs of sample 400, 600 and 800 after salt spray testing, together with a cross section of sample 600 before salt spray testing, are shown in Figure 9.15. In agreement with the dissolution rates described in Figure 9.13(b), difference in residual coating thickness and coverage is evident for the coatings cured at different temperatures. While the reference exhibited a thickness of ~0.17-1.27 µm (indicated in Figure 9.15(a)), the coating of sample 400 is fully removed (Figure 9.15(b)) and only coating remnants remain at the previously large coating cross-sections of sample 600 (Figure 9.15(c)). Analysis of sample 800 (Figure 9.15(d)) shows that the coating thickness is significantly reduced; however, a thin coating film with high coverage remains on the surface. These results indicate that further work on the optimum curing parameters is necessary to enable long-term performance of the coatings in applications such as heat exchanges. Results from Liou *et al.* [19] indicated that SOG films may be fully transformed to SiO_2 by highly oxidative curing, which is, however, not feasible on stainless steel substrates due to the previously described deterioration of substrate properties [21,22]. As shown by Bremmer *et al.* [3], SOG films are susceptible to very low concentrations of O_2 and we propose that *e.g.* a precise dosing of O_2 into an inert atmosphere may increase the curing performance without deterioration of the substrate properties, and thus increase the SiO_2-like character of the material significantly.

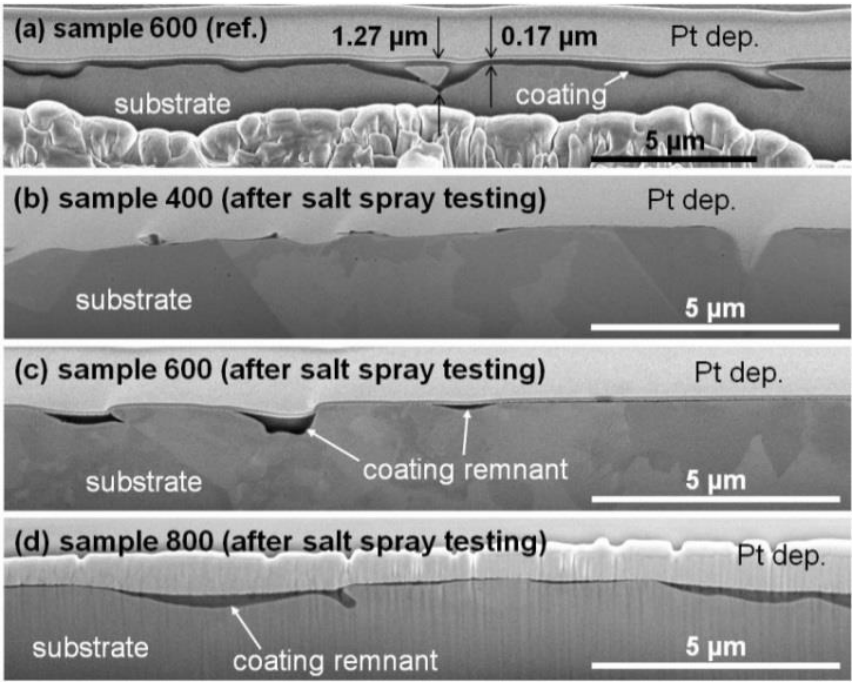

Figure 9.15: *SEM micrographs of ion beam milled cross sections of: (a) sample 600 before salt spray testing (reference); (b) sample 400 after salt spray testing; (b) sample 600 after salt spray testing; (c) sample 800 after salt spray testing. SEM settings: beam current 86 pA.*

9.4 Conclusions

The deposition of thin films from HSQ precursor was demonstrated as a viable process to deposit (sub)-µm thick coatings on stainless steel substrates. The coating precursor could flow freely on the surface during deposition and the coating was capable of leveling the pickled surface of a no. 2B finished stainless steel substrate to a R_a roughness of 15 nm. The degree of film polymerization was dependent on the curing temperature, yielding virtually hydrogenation free oxides for curing above 700 ºC. However, curing at 800 ºC in Ar/H_2 atmosphere did not lead to complete transformation to SiO_2 and a significant amount of lower valent Si was detected in the films. Further, the elastic modulus and film hardness showed an increasing trend with increasing curing temperature, however, remained below the values observed for fused silica. The coating hydrophobicity correlated with the residual hydrogenation and hydroxylation, showing hydrophobic behavior for films cured below 600 ºC and hydrophilic behavior for films cured above 500 ºC. All films showed high barrier properties in NaCl electrolyte, however, generally acted as imperfect barrier coatings which allowed electrolyte to penetrate to the substrate. Polarization measurements indicated a potential increase in breakdown potential for coated films. This increase was inconsistent due to the presence of inhomogeneously spread coating defects. Defects originating from substrate roughness were found to trigger microscopic coating delamination, which further triggers the initiation of micro-crevice corrosion between the coating and the substrate. All coatings cured with the herein applied curing conditions were unstable in aqueous environment and showed significant dissolution rates during neutral salt spray testing. Further, a trend between dissolution rate and degree of polymerization was evident, with increasing polymerization leading to higher coating stability.

Acknowledgements

We thank SiOx Aps, Espergærde, DK, for the deposition of coatings and acknowledge the work done by all other project partners. Further, Innovation Fund Denmark is acknowledged for funding this work under grant number 50-2014-1.

References

[1] F. Lampert, A.H. Jensen, R.U. Din, P. Møller, Hydrogen Silsesquioxane based silica glass coatings for the corrosion protection of austenitic stainless steel, Surf. Coatings Technol. 307 (2016) 879–885.

[2] Y.K. Siew, G. Sarkar, X. Hu, J. Hui, A. See, C.T. Chua, Thermal Curing of Hydrogen Silsesquioxane, J. Electrochem. Soc. 147 (2000) 335.

[3] J.N. Bremmer, Y. Liu, K.G. Gruszynski, F.C. Dall, Cure of Hydrogen Silsesquioxane for Intermetal Dielectric Applications, Mater. Res. Soc. Symp. Proc. 476 (1997) 37–44.

[4] K. Mohaghegh, H.N. Hansen, H. Pranov, G. Kofod, A study on the surface roughness of a thin HSQ coating on a fine milled surface, in: 14th Euspen Int. Conf. - Dubrovink, 2014.

[5] K. Mohaghegh, H.N. Hansen, H. Pranov, G. Kofod, Verification of thickness and surface roughness of a thin film transparent coating, in: Proc. 13th Euspen Int. Conf., Berlin, 2013.

[6] T.C. Hobæk, M. Matschuk, J. Kafka, H.J. Pranov, N.B. Larsen, Hydrogen silsesquioxane mold coatings for improved replication of nanopatterns by injection molding, J. Micromechanics Microengineering. 25 (2015) 035018 (9pp).

[7] D. Pech, P. Steyer, J.-P. Millet, Electrochemical behaviour enhancement of stainless steels by a SiO2 PACVD coating, Corros. Sci. 50 (2008) 1492–1497.

[8] S. Meth, N. Savchenko, F.A. Viva, D. Starosvetsky, A. Groysman, C.N. Sukenik, Siloxane-based thin films for corrosion protection of stainless steel in chloride media, J. Appl. Electrochem. 41 (2011) 885–890.

[9] D.C.L. Vasconcelos, J.A.N. Carvalho, M. Mantel, W.L. Vasconcelos, Corrosion resistance of stainless steel coated with sol–gel silica, J. Non. Cryst. Solids. 273 (2000) 135–139.

[10] M. Atik, P. de Lima Neto, L.A. Avaca, M.A. Aegerter, J. Zarzycki, Protection of 316L stainless steel against corrosion by SiO2 coatings, J. Mater. Sci. Lett. 13 (1994) 1081–1085.

[11] G.A. Garzino-Demo, F.L. Lama, Friction and wear of uncoated or SiO2-coated 329 stainless steel and of uncoated or A1N-coated aluminium surfaces, Surf. Coatings Technol. 68/69 (1994) 507–511.

[12] J. Gallardo, A. Duran, I. Garcia, J.P. Celis, M.A. Arenas, A. Conde, Effect of Sintering Temperature on the Corrosion and Wear Behavior of Protective SiO2-Based Sol-Gel Coatings, J. Sol-Gel Sci. Technol. 27 (2003) 175–183.

[13] O. Santos, T. Nylander, R. Rosmaninho, G. Rizzo, S. Yiantsios, N. Andritsos, A. Karabelas, H. Müller-Steinhagen, L. Melo, L. Boulangé-Petermann, C. Gabet, A. Braem, C. Trägårdh, M. Paulsson, Modified stainless steel surfaces targeted to reduce fouling—surface characterization, J. Food Eng. 64 (2004) 63–79.

[14] K. Baba, R. Hatada, S. Nagata, H. Fujiyama, G.K. Wolf, W. Einsinger, SiO2 coatings produced by ion beam assisted ECR-plasma CVD, Surf. Coatings Technol. 75 (1995) 292–296.

[15] R. Rosmaninho, O. Santos, T. Nylander, M. Paulsson, M. Beuf, T. Benezech, S. Yiantsios, N. Andritsos, A. Karabelas, G. Rizzo, H. Müller-Steinhagen, L.F. Melo, Modified stainless steel surfaces targeted to reduce fouling – Evaluation of fouling by milk components, J. Food Eng. 80 (2007) 1176–1187.

[16] W. Walke, Z. Paszenda, T. Pustelny, Z. Opilski, S. Drewniak, M. Ko, M. Basiaga, Evaluation of physicochemical properties of SiO2-coated stainless steel after sterilization, Mater. Sci. Eng. C. 63 (2016) 155–163.

[17] W. Walke, Z. Paszenda, M. Basiaga, P. Karasinski, M. Kaczmarek, EIS Study of SiO2 Oxide Film on 316L Stainless Steel for Cardiac Implants, in: E. Piętka, J. Kawa, W. Wieclawek (Eds.), Inf. Technol. Biomed. Vol 4., Springer International Publishing, Cham, 2014: pp. 403–410.

[18] H. Pranov, Reactive Silicon Oxide Precursor Facilitated Anti-Corrosion Treatment, US 2014/0154441 A1, USA, 2014.

[19] H. Liou, J. Pretzer, Effect of curing temperature on the mechanical properties of hydrogen

silsesquioxane thin films, Thin Solid Films. 335 (1998) 186–191.
[20] D. Többen, P. Weigand, M.J. Shapiro, S.A. Cohen, Influence of the cure process on the properties of hydrogen silsesquioxane spin-on-glass, Mater. Res. Soc. Somposium Proc. 443 (1997) 195–200.
[21] F. Lampert, A.B. Christiansen, R.U. Din, Y. Gonzalez-Garcia, P. Møller, Corrosion Resistance of AISI 316L Coated with an Air-Cured Hydrogen Silsesquioxane Based Spin-On-Glass Enamel in Chloride Environment, Corros. Sci. (In Press. August 24th 2017). (2017).
[22] F. Lampert, S. Kadkhodazadeh, A.H. Jensen, R.U. Din, P. Møller, Interfacial Interaction of Oxidatively Cured Hydrogen Silsesquioxane Spin-On-Glass Enamel with Stainless Steel Substrate, J. Electrochem. Soc. 164 (2017) C231–C239.
[23] H. Li, J.J. Vlassak, Determining the elastic modulus and hardness of an ultra-thin film on a substrate using nanoindentation, J. Mater. Res. 24 (2009) 1114–1126.
[24] C.G. Kallingal, M. Tomozawa, S.P. Murarka, Substrate Effects on Hardness and Polishing of SiO2 Thin Films, J. Electrochem. Soc. 145 (1998) 1790–1794.
[25] E.C. for Standardization, ISO 14577-1:2002 E Metallic materials - Instrumented indentation test for hardness and materials parameters - Part 1: Test method, (2003) 1–25.
[26] W.C. Oliver, G.M. Pharr, An improved technique for determining hardness and elastic modulus using load and displacement sensing indentation experiments, J. Mater. Res. 7 (1992) 1564–1583.
[27] R. Qvarfort, New Electrochemical Cell for Pitting Corrosion Testing, Corros. Sci. 28 (1988).
[28] C.H. Hsu, F. Mansfeld, Technical Note: Concerning the Conversion of the Constant Phase Element Parameter Y0 into a Capacitance, Corrosion. 57 (2001) 747–748.
[29] EN ISO 9227:2012 Corrosion tests in artificial atmospheres - Salt spray tests, (2012).
[30] Designation: A959-16 Standard Guide for Specifying Harmonized Standard Grade Compositions for Wrought Stainless Steels, 2016.
[31] L. Wang, S. Yu, J. Cho, Properties of Liquid-Phase Deposited Silica Films for Low- k Dielectric Applications, J. Am. Ceram. Soc. 92 (2009) 2388–2391.
[32] M.G. Albrecht, C. Blanchette, Materials Issues with Thin Film Hydrogen Silsesquioxane Low K Dielectrics, J. Electrochem. Soc. 145 (1998) 4019–4025.
[33] C.J. Brinker, G.W. Scherer, 2.4.3. IR-Raman investigations of gel dehydroxylation, in: Sol Gel Sci. Phys. Chem. Sol-Gel Process., 1990: pp. 582–588.
[34] P. Innocenzi, Infrared spectroscopy of sol-gel derived silica-based films: A spectra-microstructure overview, J. Non. Cryst. Solids. 316 (2003) 309–319.
[35] W.A. Pliskin, Comparison of properties of dielectric films deposited by various methods, J. Vac. Sci. Technol. 14 (1977) 1064.
[36] G. Lucovsky, J. Yang, S.S. Chao, J.E. Tyler, W. Czubatyj, Oxygen-bonding environments in glow-discharge-deposited amorphous silicon-hydrogen alloy films, Phys. Rev. B. 28 (1983) 3225–3233.
[37] M.S. Donley, D.R. Baer, T.G. Stoebe, Nitrogen 1s charge referencing for Si3N4 and related compounds, Surf. Interface Anal. 11 (1988) 335–340.
[38] V.I. Nefedov, Y. V. Salyn, G. Leonhardt, R. Scheibe, A comparison of different spectrometers and charge corrections used in X-ray photoelectron spectroscopy, J. Electron Spectros. Relat. Phenomena. 10 (1977) 121–124.
[39] C.M. Hessel, E.J. Henderson, J.G.C. Veinot, Hydrogen Silsesquioxane: A Molecular Precursor for Nanocrystalline Si-SiO2 Composites and Freestanding Hydride-Surface-Terminated Silicon Nanoparticles, Chem. Mater. 18 (2006) 6139–6146.
[40] C.M. Hessel, E.J. Henderson, J.G.C. Veinot, An Investigation of the Formation and Growth of Oxide-Embedded Silicon Nanocrystals in Hydrogen Silsesquioxane-Derived Nanocomposites, J. Phys. Chem. C. 111 (2007) 6956–6961.
[41] P.J.W. Weijs, J.F. van Acker, J.C. Fuggle, P.A.M. van der Heide, H. Haak, K. Horn, The Ba/Si(100)-2x1 interface II. XPS, BIS and synchrotron PS studies of Schottky-barrier formation, Surf. Sci. 260 (1992) 102–112.

[42] T.P. Nguyen, S. Lefrant, XPS study of SiO thin films and SiO-metal interfaces, J. Phys. Condens. Matter. 1 (1999) 5197–5204.
[43] M. Wittmer, P. Oelhafen, K.N. Tu, Electronic structure of iridium silicides, Phys. Rev. B. 33 (1986) 5391–5400.
[44] R. Alfonsetti, L. Lozzi, M. Passacantando, P. Picozzi, S. Santucci, XPS studies on SiOx thin films, Appl. Surf. Sci. 70–71 (1993) 222–225.
[45] L. Doucet, G. Carlotti, Elastic Properties of Silicate Glass and Spin-On Glass Thin Films, Mater. Res. Soc. Somposium Proc. 356 (1994) 215–220.
[46] G. Carlotti, G. Socino, L. Doucet, Elastic properties of thin films, Appl. Phys. Lett. 66 (1995) 2682–2684.
[47] Z. Cao, X. Zhang, Nanoindentation creep of plasma-enhanced chemical vapor deposited silicon oxide thin films, Scr. Mater. 56 (2007) 249–252.
[48] F. Mansfeld, H. Shih, H. Greene, C.H. Tsai, Analysis of EIS Data for Common Corrosion Processes, in: Electrochem. Impedance Anal. Interpret., 1993: pp. 37–53.
[49] Y. Toivola, J. Thurn, R.F. Cook, Structural, Electrical, and Mechanical Properties Development during Curing of Low-k Hydrogen Silsesquioxane Films, J. Electrochem. Soc. 149 (2002) F9–F17.
[50] W.-C. Liu, C.-C. Yang, W.-C. Chen, B.-T. Dai, M.-S. Tsai, The structural transformation and properties of spin-on poly(silsesquioxane) films by thermal curing, J. Non. Cryst. Solids. 311 (2002) 233–240.
[51] D.M. Brasher, A.H. Kingsbury, Electrical Measurements in the Study of Immersed Paint Coatings on Metal. 1. Comparison between Capacitance and Gravimetric Methods of Estimating Water-Uptake, J. Appl. Chem. 4 (1954) 62–72.
[52] A.S. Castela, A.M. Simões, An impedance model for the estimation of water absorption in organic coatings. Part I: A linear dielectric mixture equation, Corros. Sci. 45 (2003) 1631–1646.
[53] Lindqvist S.A., Theory of Dielectric Properties of Heterogeneous Substances Applied to Water in a Paint Film, Corros. - NACE. 41 (1985) 69–75.
[54] P.C. Pistorius, G.T. Burstein, Metastable pitting corrosion of stainless steel and the transition to stability, Philos. Trans. R. Soc. Ser. A. 341 (1992) 531–559.
[55] F. Lampert, S. Kadkhodazadeh, T. Kasama, K.V. Dahl, A.B. Christiansen, P. Møller, Probing the chemistry of adhesion between a 316L substrate and spin-on-glass coating, To Be Submitt. 2017. (2017).
[56] T. Hwang, H. Lee, H. Kim, G. Kim, Two layered silica protective film made by a spray-and-dip coating method on 304 stainless steel, J. Sol-Gel Sci. Technol. 55 (2010) 207–212.
[57] D. Pech, P. Steyer, A.-S. Loir, J.C. Sánchez-López, J.-P. Millet, Analysis of the corrosion protective ability of PACVD silica-based coatings deposited on steel, Surf. Coatings Technol. 201 (2006) 347–352.
[58] B. Nikrooz, M. Zandrahimi, H. Ebrahimifar, High temperature oxidation resistance and corrosion properties of dip coated silica coating by sol gel method on stainless steel, J. Sol-Gel Sci. Technol. 63 (2012) 286–293.
[59] P.P. Trazaskoma-Paulette, A. Nazeri, Effects of Sol-Gel Coatings on the Localized Corrosion Behavior of 304 Stainless Steel, J. Electrochem. Soc. 144 (1997) 1307–1310.
[60] A. Kriaa, N. Hamdi, H. Sidhom, Assessment of Intergranular Corrosion of Heat Treated Austenitic Stainless Steel (AISI 316L Grade) by Electron Microscopy and Electrochemical Tests, Prot. Met. 44 (2008) 506–513.
[61] N.J. Laycock, J. Stewart, R.C. Newman, The Initiation of Crevice Corrosion in Stainless Steel, Corros. Sci. 39 (1997) 1791–1809.
[62] E. Deltomee, N. de Zoubov, M. Pourbaix, Silicon, in: Atlas Electrochem. Equilibria Aqueous Solut., Houston, 1996: pp. 458–463.
[63] M. Klause, U. Rothhaar, M. Bicker, W. Ohling, Dissolution of thin SiO2-coatings – Characterization and evaluation, J. Non. Cryst. Solids. 356 (2010) 141–146.
[64] S.-K. Kang, S.-W. Hwang, H. Cheng, S. Yu, B.H. Kim, J.-H. Kim, Y. Huang, J.A. Rogers, Dissolution Behaviors and Applications of Silicon Oxides and Nitrides in Transient

Electronics, Adv. Funct. Mater. 24 (2014) 4427–4434.

References

10 Manuscript VI

Corrosion properties of SiO_x-like thin film coatings from spin-on-glass precursor and reactive bipolar PVD on bright annealed stainless steel substrate*

Felix Lampert[a], René Bang Madsen[b], Alexander Bruun Christiansen[c], Rameez Ud Din[d], Per Møller[e]

[a] Technical University of Denmark, Department of Mechanical Engineering, Produktionstorvet 425, 2800 Kgs. Lyngby, Denmark
[b] Polyteknik A/S, Moellegade 21, 9750 Oestervraa, Denmark
[c] SiOx ApS, Bybjergvej 7, 3600 Espergærde, Denmark

Abstract

Thin ceramic films are well-known for their excellent performance in improving both the surface characteristics and the corrosion resistance of stainless steels in a variety of applications. In this work, sub-micrometer thick coatings have been deposited on bright annealed 316L substrates by spin-on-glass (SOG) processing and physical vapor deposition (PVD) and assessed as corrosion barrier coatings in saline, aqueous milieu. The coating chemistry was assessed by infrared spectroscopy, showing that both processes yielded SiO_x-like, partially hydroxylated coatings and the spin-on-glass coating retained hydrogenation due to imperfect conversion of the precursor. Adhesion testing by increasing load scratch testing indicated superior adhesion of the spin-on-glass coating with respect to the PVD coating. Although all investigated coatings showed imperfect barrier behavior during electrochemical impedance measurements, the spin-on-glass coatings generally generated an anodic shift in breakdown potential during an anodic potentiodynamic polarization test in saline solution, indicating good coating performance. The measured breakdown potentials measured on PVD coated substrates were generally shifted to more cathodic values. This was explained by the presence of microscopic voids due to coating delamination and consequently the initiation of crevice corrosion in the voids. The spin-on-glass coatings maintained, despite observable coating dissolution, their performance after 1000 h neutral salt spray testing, while the PVD coatings showed significant coating delamination which further triggered the initiation of localized corrosion along coating defects.

---

* unpublished work at date of submission. The final article may deviate from the herein presented manuscript.

10.1 Introduction

Thin film coatings, in particular thin ceramic films such as TiO_2 [1], ZrO_2 [2], CeO_2[3,4], or SiO_x [5–10] are widely handled as promising surface modification to improve the surface characteristics and the corrosion resistance of stainless steel engineering components. The coatings are particularly promising as corrosion barrier coating for applications such as marine heat exchanger plates. In this application, service in highly corrosive hot sea water limits the material choice to costly materials such as Ti alloys and traditional corrosion protection strategies are unfeasible, due to the complex component geometry or since they impair the heat transfer. Since coatings based on SiO_x have shown promising results to improve the corrosion performance of stainless steel substrates [5–8], they may enable the application of stainless steels as marine heat exchanger plate materials, and thus lead to a significant decrease in component cost. Additionally, the coatings may decrease the component roughness [11,12], which may increase the resistance towards biofouling [11,13], and thus lead to further increase in component performance.

Generally, the deposition of thin SiO_x films relies on sol-gel or chemical vapor deposition processes, which exhibit shortcomings in processing cost or film quality [14]. As potential alternative for the deposition of highly insulating SiO_x-like thin films in microelectronic applications, the deposition of spin-on-glass (SOG) films based on hydrogen silsesquioxane (HSQ) precursor has been developed [15]. This process relies predominantly on cross-linking the HSQ, $(HSiO_{3/2})_n$, precursor via a thermally activated redistribution reaction, which may result in the formation of a fully inorganic continuous surface film with properties and stoichiometry close to SiO_2 [16]. Recently, the technology has been transferred from microelectronics to the surface finishing of metallic components, which enabled the efficient levelling of polymer molding tools, thereby increasing the quality of microinjection-molded components [17]. In our previous work [14,18], we have successfully demonstrated the transfer of the coating technology from aluminum and tool steels to stainless steel substrates. For the coating deposition, a commercial SOG solution was deposited on AISI 316L substrates by dip-coating, followed by thermal curing of the continuous film in Formiergas atmosphere. Further, it was demonstrated that that the process may increase the passive properties of the substrates in chloride media significantly; however, in our previous approach the coatings were deposited on pickled substrates and we identified adhesive coating failure in connection with the rough, pickled finish and showed that this microscopic delamination may lead to preliminary passivity breakdown of the substrate [18]. Based on this analysis, we proposed that a decrease in substrate roughness, *e.g.* by using of a polished or bright annealed substrate finish, may eliminate the observed preliminary failure and increase the coating reliability significantly. The effect of SOG-deposition on bright surface finishes has not been investigated yet and a detailed investigation of the effect of surface modification by SOG deposition of bright annealed stainless steel substrates is the core objective of the present work.

In addition to an assessment of the coating performance at an improved substrate quality, the effect of SOG coating on the corrosion resistance of stainless steel substrates has not been directly compared with similar coating types deposited by the incumbent processes. Apart from sol-gel processing [19] and chemical vapor deposition [20], physical vapor deposition (PVD) processes are well established for the deposition of thin SiO_x films on a variety of substrates. In particular, reactive bipolar magnetron sputtering has been demonstrates as suitable process to deposit high quality SiO_2 films from Si targets at high deposition rates [21,22], without processing issues due to target poisoning [23,24]. To the author's knowledge, the deposition of SiO_2 from reactive bipolar magnetron sputtering has not been attempted for the deposition of corrosion barrier coatings on stainless steel substrates at present; however, the films are expected to form a dense deposit on the surface without a significant chemical interaction zone with the substrate, and thus pose an excellent reference system for the performance of the SOG-films.

The present work focuses on a detailed investigation sub-micrometer thick SOG and PVD SiO_x-like coatings on bright annealed AISI 316L substrates and their performance as corrosion barrier coatings in chloride containing electrolyte. To conclude about the microstructure, chemistry and the adhesion, the coatings have been investigated by electron microscopy, infrared spectroscopy and increasing load scratch testing. Further, the electrochemical properties and the barrier efficiency of the coatings were evaluated by electrochemical impedance spectroscopy and linear potentiodynamic polarization measurements and the long-term coating behavior was studied by neutral salt spray testing.

10.2 Experimental

10.2.1 Thin film deposition

SOG and PVD coatings were deposited on bright annealed AISI 316L, substrates with the chemical composition shown in Table 10.1 and dimensions of 100x50 mm^2 (0.5 mm thickness). The substrate surfaces were pretreated by a commercial cleaning sequence including immersion degreasing, followed by anodic degreasing and followed by activation in the commercial solution Schlötter Slotoclean Decasel 5.

The SOG deposition was carried out by dip-coating in the commercial SOG solution Dow Corning FOx 25 flowable oxide, followed by soft-baking at 160 ºC and subsequent coating curing in a retort furnace under flow of 0.45 l/min Ar with addition of 0.05 l/min H_2 gas at atmospheric pressure at 800 ºC for 2 h. The PVD coatings were deposited by reactive bipolar sputtering in a Polyteknik Cryofox Discovery 500 magnetron sputter deposition unit. The unit was equipped with two Testbourne Ltd. Si P-type targets of 99.999% purity, 76.2 mm diameter and 6.35 mm thickness. Prior to sputter deposition, the substrates were plasma etched in the magnetron chamber under flow of 20 cm^3/min Ar and 20 cm^3/min O2 gas at a pressure of 8 x 10^{-2} mbar for 9 min at 400 mA plasma current. After plasma etching, the chamber was pumped to 2 x 10^{-5} mbar base pressure.

Deposition of SiO_2 was carried out under flow of 30 vol.% O_2 dosed into Ar working gas at a rate of ~3 Å/s. The withdrawal speeds/deposition times and the obtained coating thicknesses (determined from coating cross sections) are specified in Table 10.2.

10.2.2 Characterization techniques and materials testing

Focused ion beam (FIB) scanning electron microscopy (SEM). SEM imaging and FIB milling was carried out on a Helios NanoLAB 600 dual beam (field emission gun electron source; Ga^+ liquid metal ion source) microscope. Specimens were sputter coated with Au prior to analysis and irradiation damage during FIB milling was prevented by Pt deposition on the site of interest. The used detector (Everhart-Thronley (ETD)/Through-lens (TLD)) and the used beam currents are indicated in the respective figure captions.

Fourier transformed infrared spectroscopy (FT-IR). The film chemistry was characterized by Attenuated Total Reflectance (ATR) FT-IR on a Thermo Scientific Nicolet iN 10 MX instrument.

Scratch testing. Scratch testing was performed on a ST Instruments Micro Scratch Tester on a STeP 4 Platform fitted with a 100 µm radius Rockwell-C diamond tip. Scratching was performed with linearly progressing load from 10 mN to 500 mN at 8 mm/min scratch speed on a 2 mm scratch track. The experiments were repeated three times on independent sample areas and the standard deviated (SD) average values are reported.

Table 10.1: *Chemical composition of the substrates (by Optical Emission Spectroscopy). In addition, traces (< 0.1 wt.%; > 0.01 wt.%) of P, Nb, V, W were detected.*

Element	Cr	Ni	Mo	Mn	Si	Cu	Co	N	C	Fe
Composition *wt.%)	16.2	10.2	1.99	1.32	0.43	0.31	0.23	0.052	0.021	bal.

Table 10.2: *Summary of specimen designations and processing conditions. The coating thickness refers to the thickness in the center of the coupon (determined from ion beam milled cross sections).*

Specimen designation	Processing conditions	Coating thickness
"uncoated reference"	Reference substrate, pretreatment as specified	
SOG-252	Dip-coating with 1 mm/s withdrawal rate	252 nm
SOG-463	Dip-coating with 2 mm/s withdrawal rate	463 nm
PVD-460	Bipolar pulse sputtering for 23 min	460 nm
PVD-900	Bipolar pulse sputtering for 50 min	900 nm

Hardness testing. The substrate hardness was tested on a Future Tech FM-700 micro hardness tester fitted with a Vickers micro indenter and operated with an indentation load of 10 g and a dwell time of 5 s. The reported hardness values are based on a standard deviated average of ten measurements.

Electrochemical impedance spectroscopy (EIS). EIS was performed in a gasketed corrosion cell with 2.1 cm^2 sampling area and 15 ml solution volume of neutral 3.5 wt.% NaCl aqueous solution. The cell was fitted with a saturated calomel electrode and a Pt auxiliary electrode. The system was perturbed with an amplitude of ± 10 mV around the corrosion potential by a Gamry Ref600 potentiostat after a cell settling time of 3600 s. The experimental data were validated by a Kramers-Kronig test.

Potentiodynamic polarization. Potentiodynamic polarization experiments were conducted in acidified 3.5 wt.% NaCl aqueous solution (*p*H 2.5, adjusted with H_2SO_4). All experiments were conducted with an ACM Instruments GillAC potentiostat fitted with a Ag/AgCl reference electrode in de-aerated electrolyte (continuous feeding with N_2 gas, starting 1 h before the potentiodynamic scan) and the scan parameters suggested in ASTM G61 [25], *i.e.* 3600 s cell settling time and 10 mV/min scan rate. The scanning was conducted in anodic direction, initiated 50 mV below the measured open circuit potential. To prevent artefacts due to crevice corrosion at the rubber gasket the experiments were conducted in a corrosion cell with the cell design specified by Qvarfort [26]. The cell was operated with a solution volume of 400 ml and sample area of 1 cm^2 and a constant injection of deionized water with a rate of 7.4 ml/h.

Neutral salt spray testing. Salt spray testing was carried out for 1000 h according to EN ISO 9227:2012.

10.3 Results and discussion

10.3.1 Coating appearance, morphology and chemistry

In accordance with the standard specification [27], the uncoated reference exhibits a smooth, bright finish (Figure 10.1(a)), while coating with both the PVD and SOG process leads to significant discoloration of the sample due to thin film interference. As visible from Figure 10.1(b), the PVD film exhibits a color change from the center of the coupon towards the edges, indicating a process-related inhomogeneity in film thickness. The SOG film, on the contrary, exhibits a largely homogeneous coloration, indicating the excellent material distribution of the process. Coating cross-sections have been prepared by FIB milling and cross-sections of SOG-463 and PVD-460 (taken in the center of the substrate) are shown in Figure 10.2. As evident from the micrographs, both coating processes yield adherent coatings without apparent delamination at the interface between the coating and the substrate. Further, the surface roughness protrudes through the PVD coating (Figure 10.2(a)) while the SOG process levels the substrate, yielding a smooth surface finish (Figure 10.2(b)).

The chemical bonding of the films has been investigated by FT-IR and the respective absorbance plots, including a spectral feature identification based on the data reviewed by Lampert *et al.* [28], are shown in Figure 10.3. PVD-460 exhibits the typical features expected for SiO_2, *i.e.* a major absorbance edge from Si-O asymmetric stretching at 1049 cm^{-1}, together with a minor edge from Si-O symmetric stretching at the low frequency side and a peak shoulder due to longitudinal optical (LO) splitting at the high frequency side. In addition to features from the Si-O bonding, absorption due to hydroxylation/moisture adsorption is apparent. As previously described [18], SOG-463 exhibits distinct features from Si-O bonding, hydroxylation and Si-H bending. In contrast to our previous investigation, which was carried out in transmission mode, the current ATR method distinctly shows residual hydrogenation of the coating based on the Si-H stretching absorption at 2268 cm^{-1}, indicating, despite the high curing temperature, incomplete transformation from the resinous precursor to hydrogenation-free SiO_x.

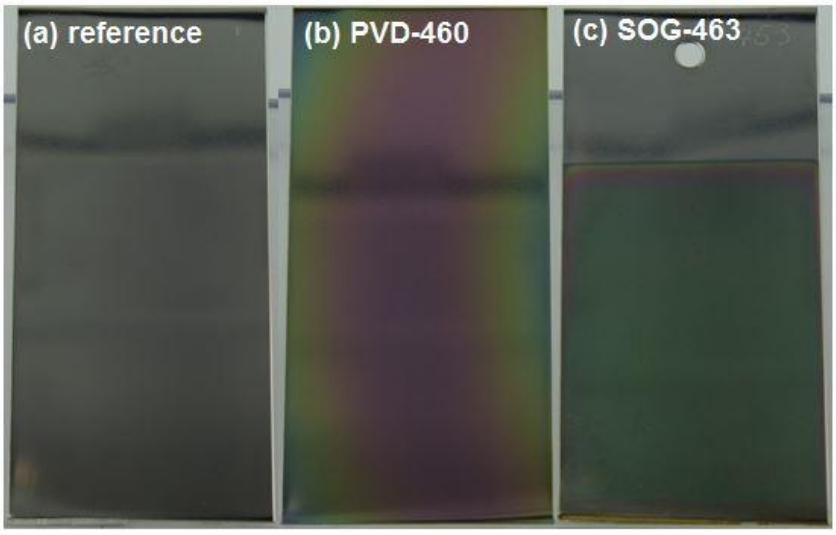

Figure 10.1: *Digital photographs of (a) uncoated reference; (b) PVD-460; (c) SOG-463. The sample size is 100 mm x 50 mm.*

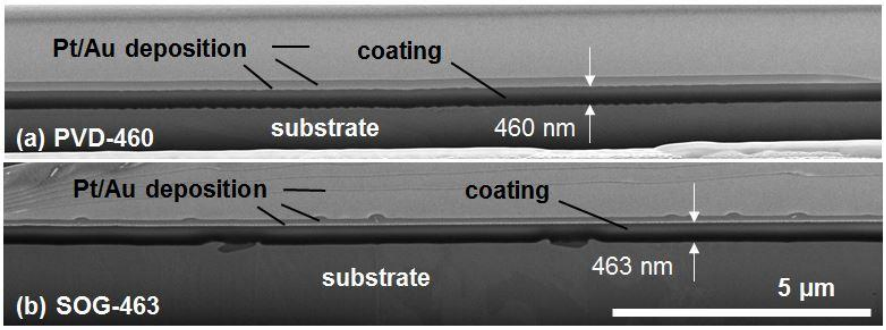

Figure 10.2: *(FIB)-SEM micrograph of coating cross sections (TLD detector, 86 pA beam current): (a) PVD-460; (b) SOG-463.*

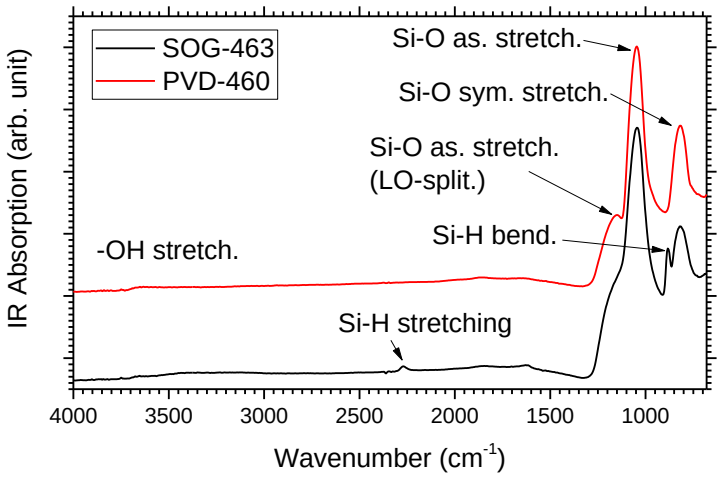

Figure 10.3: *(ATR) FT-IR absorption spectra of SOG-463 and PVD 460.*

10.3.2 Coating adhesion

The film adhesion was assessed by scratch testing and representative scratch tracks measured on a PVD-460 and a SOG-463 sample are shown in Figure 10.4. Since the critical loads are largely dependent on the coating thickness [29,30], only the samples with a thickness around ~ 460 nm were investigated. As visible from Figure 10.4, the initial critical load (Lc_1), determined on the optical micrographs as the first visible coating spallation, is reached at significantly shorter scratch length for PVD-460 with respect to SOG-463. Overall, adhesion testing of PVD-460 yielded an average critical load of Lc_1=194.4 (*SD*=12.9) mN, while the test yielded an average critical load of Lc_1=290.6 (*SD*=9.7) mN for SOG-463, which may be correlated with significantly increased adhesion of SOG-463 with respect to PVD 460. As shown previously [31], the SOG and the stainless steel substrate are capable of forming composite material with a thin (~5-10 nm) interfacial layer and we suggest that the increased chemical bonding accounts for the increased coating adhesion. However, the accuracy of the method is sensitive to a variety of coating and substrate properties such as film/substrate hardness, film toughness or substrate hardness [29]. Thermal processing of the substrate led to recovery of the substrate hardness from 237.2 (*SD*=11.9) to 209.5 (*SD*=10.4) HV0.010, while the film hardness is expected to be significantly lower for the SOG film with respect to dense SiO_2

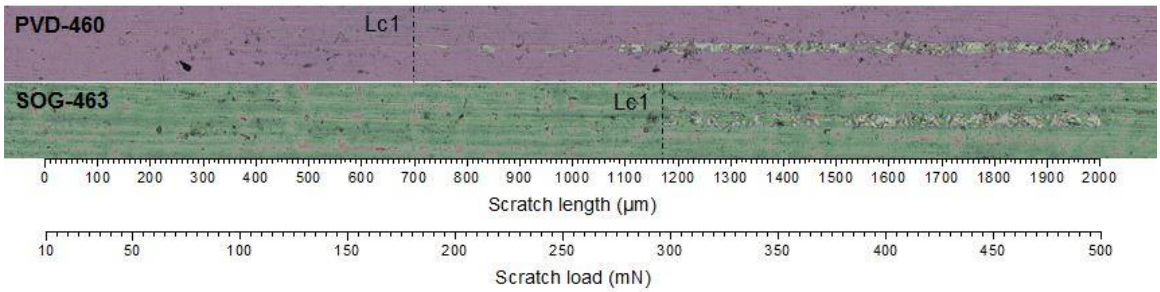

Figure 10.4: *Light-optical micrograph of scratch tracks on PVD-460 and SOG463 with indication of the critical load, Lc_1.*

[18]. Consequently, the outcome of the test may have been compromised by the differences in mechanical properties of the systems.

10.3.3 Coating performance in saline solution

As demonstrated previously [18,28], EIS analysis gives valuable information about the barrier performance of thin-film coated stainless steels and allows direct conclusions about the quality of the films. The typical EIS response observed for both the SOG and PVD coatings acquired in neutral 3.5 wt.% NaCl aqueous solution is depicted in Figure 10.5. The qualitative response was found reproducible over a large surface area; however, presumably due to inhomogeneous distribution of coating flaws, the quantitative results widely fluctuated and quantification by equivalent circuit fitting is omitted in the following. Clearly, both coating systems show multiple capacitive features and may be, in analogy to our previous work [14,18], characterized as imperfect barrier coatings which allow electrolyte transport via pores or coating defects. As previously demonstrated, coating flaws such as delamination may assist the initiation of localized passivity breakdown of the substrate and the passive behavior of all coatings has been investigated by anodic linear potentiodynamic polarization.

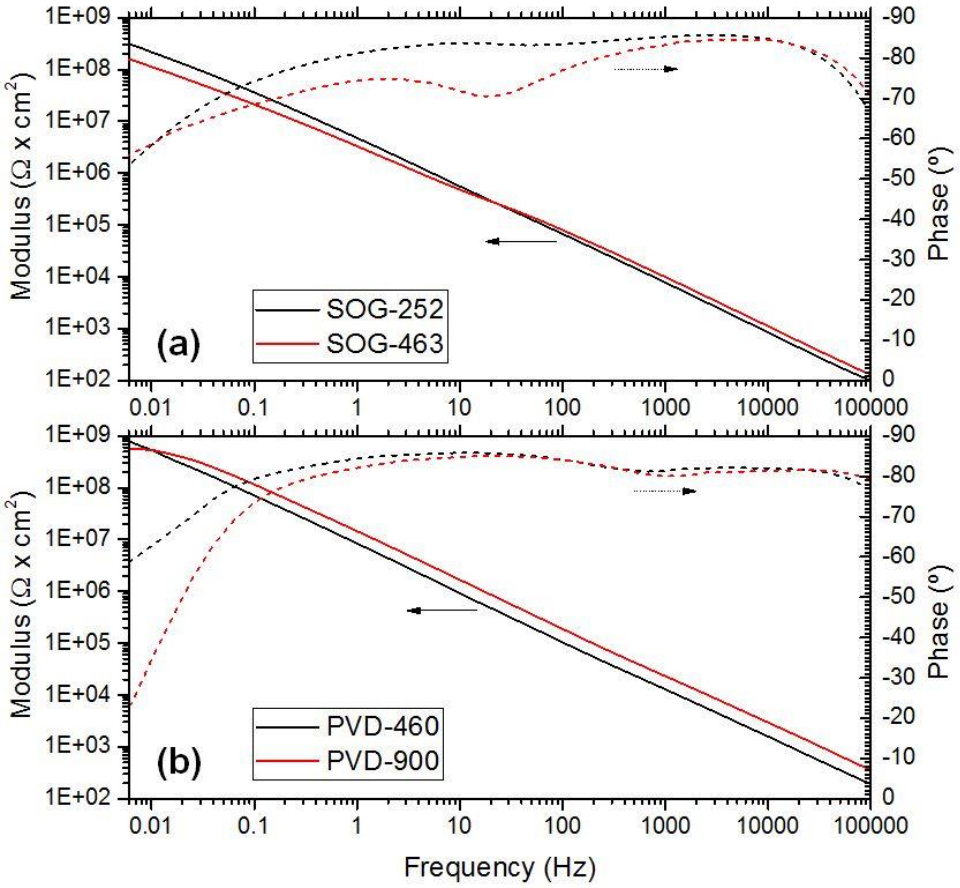

Figure 10.5: *Bode diagrams obtained in 3.5 wt.% NaCl aqueous solution on (a) SOG coatings; (b) PVD coatings.*

The experiments have been conducted in acidified (*p*H 2.5) 3.5 wt.% NaCl aqueous solution and a typical polarization curve obtained from an uncoated reference sample together with representative curves of both the SOG and the PVD coatings (curves obtained for the highest and lowest measured breakdown potential) are plotted in Figure 10.6. The reference (Figure 10.6(a)) shows the characteristic breakdown behavior expected for stainless steel, indicating a distinct passive region with sudden breakdown. Since the breakdown potential strayed between 505 and 681 mV vs. Ag-AgCl over six individual measurements, the standard deviated average breakdown potential of the reference is indicated in all subfigures of Figure 10.6. To rule out process-induced degradation of the substrate due to carbide sensitization [4,32] or the reductive annealing of the native passivation [33] as primary reason for changes in the breakdown potential, annealed uncoated reference substrates have been tested by the same routine. Since the substrates showed an average breakdown potential of 561 mV vs. Ag-AgCl (*SD*=44 mV, based on four individual measurements), the changes were found insignificant with respect to the as-received reference condition.

In agreement with our previous investigations [14,28], the corrosion potential of all SOG-coated samples is shifted to more cathodic values and the passive current density is decreased by approx. two orders of magnitude (Figure 10.4(a)). In contrast to observations made on rough substrates [18], a cathodic shift in breakdown potential, *i.e.* below the breakdown potential observed for the reference, is not observed. The breakdown potential is unaltered with respect to the averaged reference breakdown potential (SOG-463-B) or shifted to more anodic values (SOG-252-A/B; SOG-463-A), which may reach into the transpassive region. In agreement with our previous investigation [18], erratic transient currents, which do not affect the final breakdown potential, may be observed during the passive anodic sweep (*e.g.* SOG-252-A; SOG-463-B).

The polarization behavior of the PVD-based coating systems is visualized in Figure 10.6(b) and Figure 10.6(c). Similar to the SOG-based systems, coating with PVD silica leads to a general cathodic shift in corrosion potential, together with a decrease in passive current density, while pronounced erratic transient currents may be observed during the anodic sweep. In contrast to the SOG-based coating systems, the breakdown potential may be unaltered (PVD-460-A) with respect to the reference or shifted to more cathodic values (PVD-460-B; PVD-900-A/B).

Similar to the present investigation, Pech *et al.* [5] observed a fluctuating shift in breakdown potential for SiO_2 coated stainless steel substrates in aqueous NaCl solution and argued that the breakdown potential was determined by the dielectric rigidity of the coating. Since the dielectric rigidity may show a high disparity, significant variations in breakdown potential may be observed during different potentiodynamic anodic polarization measurements; however, the group generally observed anodic shifts in breakdown potential and the theory fails to explain the cathodic shift observed for the

PVD coated samples. Hence, in analogy to our previous investigation [18], we propose that the PVD coatings fail by microscopic delamination and subsequent initiation of crevice corrosion in the narrow gap between the coating and the substrate.

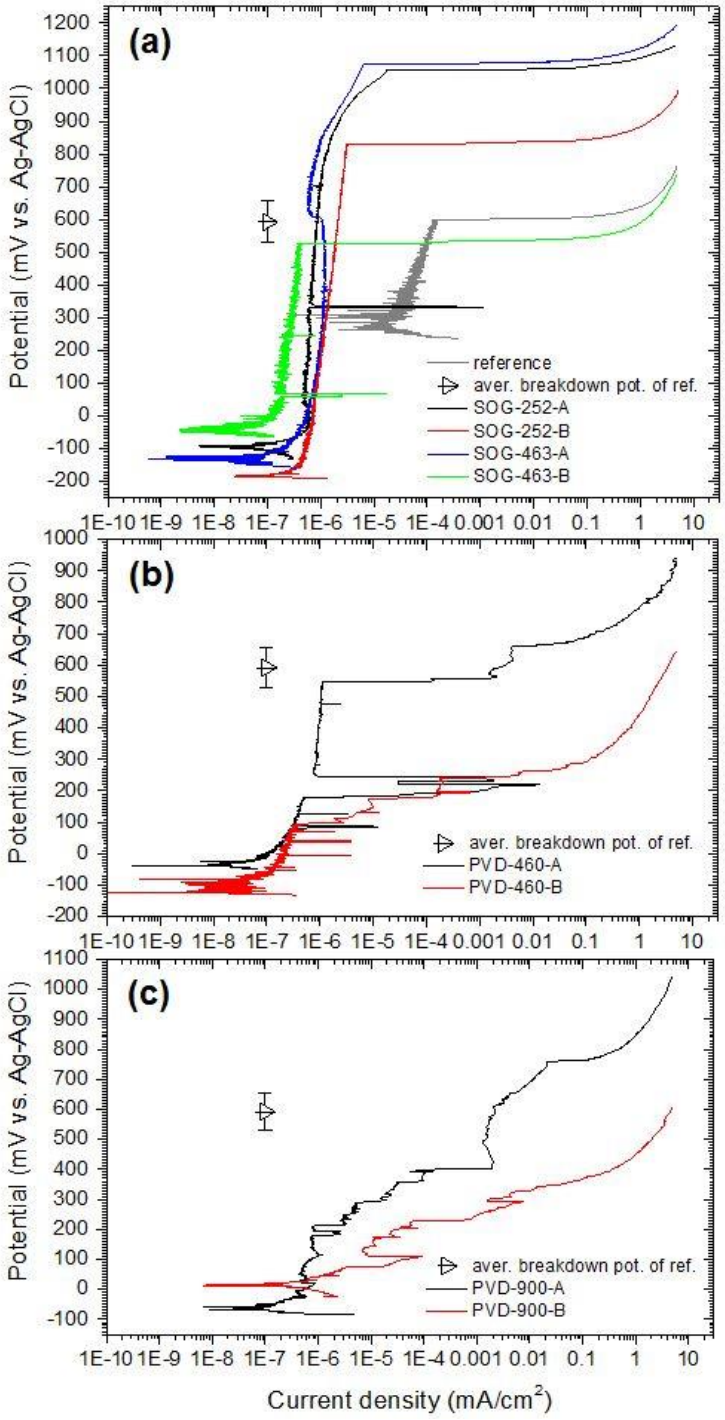

Figure 10.6: *Anodic polarization curves in acidified (pH 2.5) 3.5 wt.% NaCl aqueous solution: (a) SOG coatings together with uncoated reference sample; (b) PVD-460 samples; (c) PVD-900 samples. The standard deviated average breakdown potential of the uncoated reference in indicated in each subfigure (based on 6 individual measurements).*

To verify the presence voids between the coating and the substrate, a test coupon was investigated after the potentiodynamic polarization experiment by SEM-analysis and, apart from deep pits due to polarization beyond the breakdown potential, localized flaking/bulging of the coating was observed. Figure 10.7(a) shows a 50-100 µm sized defect, which has led to fracture and spallation of the coating. In addition to a spalled segment, a bulged segment in the lower section of the defect is visible from the micrograph. To conclude on the nature of the bulged portion of the defect, it was dissected by ion beam milling, along the marker in Figure 10.7(a). The cross sectional view Figure 10.7(b) clearly shows that the defect originates from coating delamination followed by outwards bulging of the coating, which further leads to void formation between the coating and the substrate.

No similar defects were observed during SEM analysis of the SOG coatings, supporting the observation of increased adhesion of SOG coatings with respect to PVD coatings. Moreover, the absence of coating delamination may allow the validity of the previously outline hypothesis of a distinct correlation between the breakdown potential and the inhomogeneous dielectric rigidity. However, Pech *et al.* [5] reported coatings with a perfectly capacitive response, while the herein investigated coatings deviated significantly from a perfect capacitor, allowing penetration of the electrolyte. Hence, the initiation of pitting corrosion may occur at coating defects prior to breakdown of the dielectric and we propose the further hypothesis for the passive breakdown of SOG coated substrates at elevated breakdown potentials: assuming that only a fracture of the surface is susceptible to general pitting initiation at substrate defects such as *e.g.* sulphide inclusions [34,35], the coating may sufficiently cover the majority of defects, and thus only allow breakdown at sufficiently high potential to activate the less critical defects or initiate breakdown by

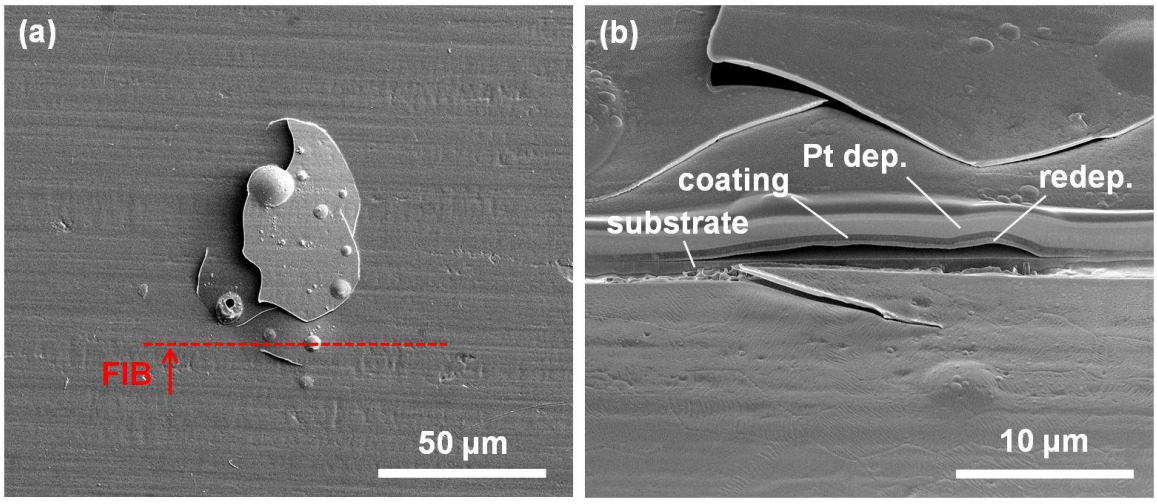

Figure 10.7: *SEM micrographs of coating defects in PVD-460: (a) top-view of flaking/bulging (ETD detector, 0.69 nA beam current); (b) (FIB)-SEM cross section through the bulging coating (TLD detector, 86 pA beam current). The locating and direction of view of the cut are indicated in Figure 10.7(a). Redeposition (redep.) of evaporated material (ion beam milling artefact) can be observed below the delaminated coating section.*

transpassive corrosion. Alternatively, we have shown that the SOG process alters the chemical composition of the underlying substrate surface [31]. Since the passive layer chemistry largely determines the corrosion resistance, an increase in *e.g.* Si- [33,36] or Cr- content [33,37,38] due to the complex interaction between the coating and the substrate may have yielded the observed increase in passive properties. Since the observed breakdown can be explained by multiple mechanisms, a conclusion about the breakdown mechanism of SOG coated stainless steels cannot be drawn based on the data presented here and we propose a further detailed investigation to elaborate on the precise breakdown mechanism.

10.3.4 Coating performance after 1000 h of salt spray testing

Previously, we reported coating breakdown by homogeneous dissolution of SOG coatings during ageing by salt spray testing and found the resilience to neutral salt spray testing to be a valuable indicator for the long-term behavior of the coatings. Hence, all coating systems were subjected to 1000 h of neutral salt spray testing, followed by a detailed investigation of their breakdown. Digital photographs of the aged PVD-460 and SOG-463 coatings are shown in Figure 10.8. Clearly, both coatings have suffered from extensive degradation throughout ageing; however, the appearance of the coating failure differs significantly. PVD-460 (Figure 10.8(a)) maintains its initial interference colors, however, appears mildly blurred and exhibits streak-like discoloration dispersed over the surface. SOG-463 (Figure 10.8(b)), in contrast, exhibits a distinct, largely homogeneous color change with inhomogeneously washed-out areas.

Surface analysis of PVD-460 (Figure 10.9(a)) identifies that the streak-like features originate from streak-like adhesive coating failure in combination with spallation. Further, ion beam cross sectioning on the center of the sample (Figure 10.9(b)) shows a distinct reduction in coating thickness to 413 nm, indicating dissolution of the coating film at a rate of ~ 0.05 nm/h, which is presumably due to a high defect density in the

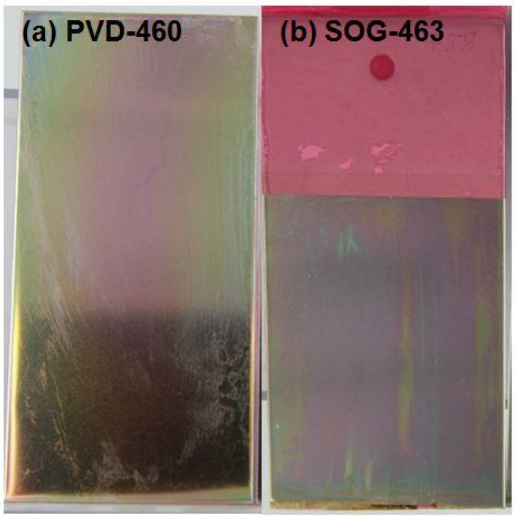

Figure 10.8: *Samples after 1000 h of salt spray testing: (a) PVD-460; (b) SOG-463.*

oxide, as previously outlaid by Klause *et al.* [39] based on chemical vapor deposited SiO_2 films. No major coating defects such as spallation or fracture were observed on the SOG coatings. The micrographs shown in Figure 10.10(a) and in Figure 10.10(b), however, clearly reveal a distinct decrease in coating thickness with dissolution rates of >0.1 nm/h, which is in good agreement with the data previously presented for SOG films [18].

To conclude on the implications of the observed coating defects, the coatings have been investigated by potentiodynamic anodic polarization and representative polarization plots are shown in Figure 10.11. Similar to the initial investigation, the PVD coated substrates show preliminary failure together with pronounced transient currents during the anodic sweep (PVD-460). Furthermore, the passive current density may be significantly increased with respect to the initial condition, presumably due to the large exposed substrate area (PVD-460). The SOG coatings, on the contrary, maintain their protective behavior, indicating that the observed thickness reduction does not pose a critical coating defect for the passive behavior of the coating system.

To countercheck the hypothesis of pit initiation at distinct coating defects, the surface of PVD-460 was further investigated by microscopy. The light-optical micrograph shown in Figure 10.12(a) reveals that pitting occurred site specific in connection with the previously described adhesive coating failure, implicating that the coating delamination poses a critical defect to the substrate passivity. SEM analysis of the region reveals, apart from the large pits visible in Figure 10.12(a), smaller emerging pits, as exemplarily

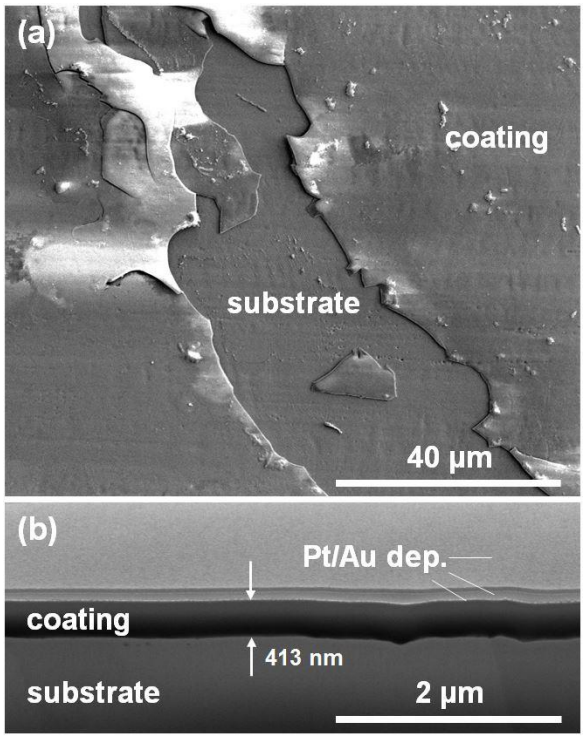

Figure 10.9: *SEM micrographs of PVD-460 after 1000 h salt spray ageing: (a) Top view of streak-like delamination (ETD detector, 0.34 nA beam current); (b) (FIB)-SEM cross section of an adherent site in the center of the sample (TLD detector, 86 pA beam current).*

shown in Figure 10.12(b). As visible from the micrograph, the corrosion evolves around the brink of the delaminating coating, further supporting the hypothesis that a narrow crevice between the delaminating coating and the substrates may act as critical defect. Further, the micrograph indicates that emerging pits may be partly occluded by the coating, and thus stabilized.

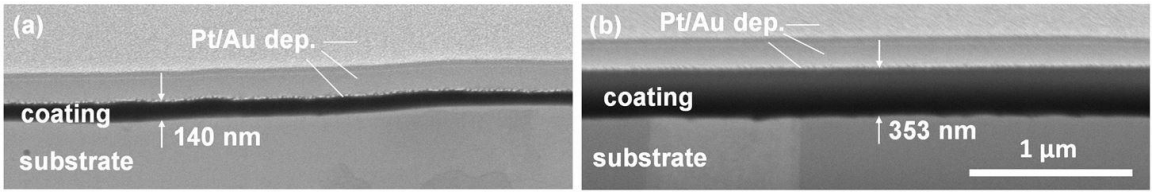

Figure 10.10: *(FIB)-SEM coating cross sections of SOG samples after 1000 h salt spray ageing, acquired in the center of the samples (TLD detector, 86 pA beam current): (a) SOG-252; (b) SOG-463.*

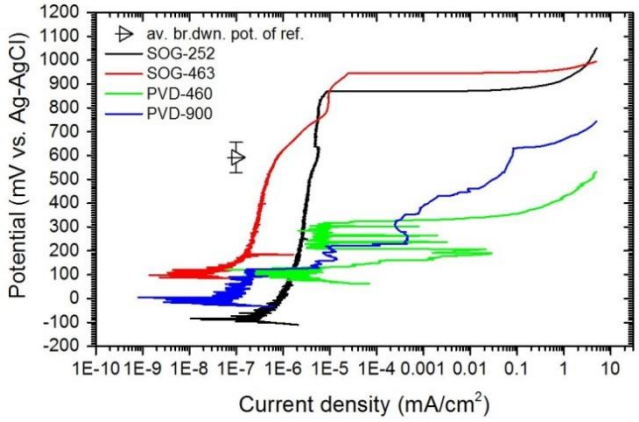

Figure 10.11: *Anodic polarization curves of 1000 h salt spray aged samples in acidified (pH 2.5) 3.5 wt.% NaCl aqueous solution. The standard deviated averaged breakdown potential obtained for uncoated reference samples is indicated in the figure.*

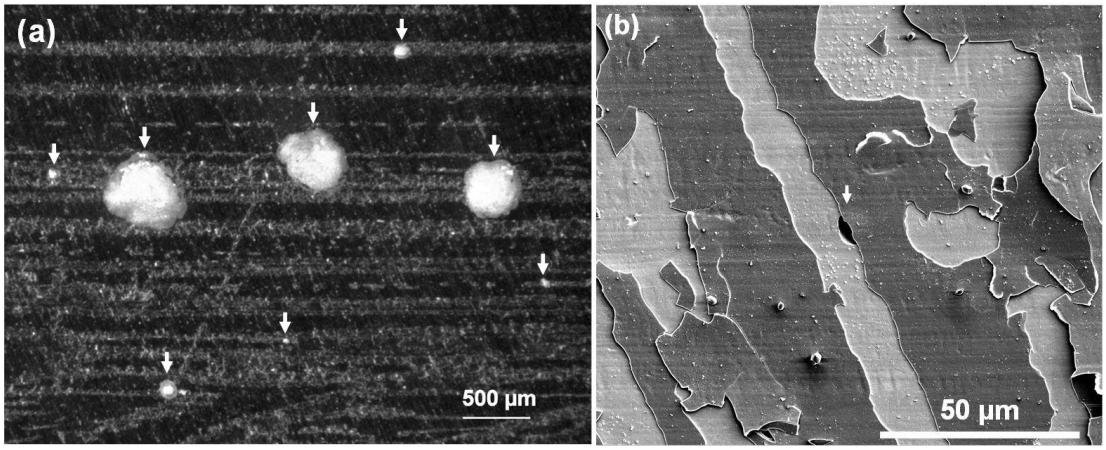

Figure 10.12: *Pitting failure of 460 after 1000 h salt spray ageing followed by potentiodynamic anodic polarization: (a) Light-optical micrograph indicating site-specific pitting (individual pits are indicated by arrows) at streak-like delamination. (b) SEM micrograph showing an evolving pit (indicated by arrow) at the border of a delaminated site (ETD detector, 0.69 nA beam current).*

10.4 Conclusion

The corrosion resistance of SOG- and PVD-based sub-micrometer thick SiO_x-like coatings has been investigated. The PVD coatings showed the typical infrared analysis features expected for SiO_x, while the SOG coatings remained partially hydrogenated due to imperfect conversion of the highly hydrogenated precursor. Increasing load scratch testing indicated a superior adhesion of the SOG coatings with respect to the PVD coatings and both coatings showed imperfect barrier response, indicating the presence of coating flaws which allowed electrolyte penetration to the substrate. Anodic polarization measurements showed that the SOG process may increase the breakdown potential, while the PVD process generally decreased the breakdown potential with respect to an uncoated substrate. Microstructure analysis revealed microscopic coating delamination and spallation of the PVD coatings and it was suggested that micro-crevice corrosion under delaminated deposits were the predominant origin of the decreased passive properties. The failure mode was absent in the SOG coatings and it was concluded that the coatings show a good performance due to their excellent barrier properties or a stabilization of the native passivation. The coatings maintained their breakdown characteristics after ageing for 1000 h in a neutral salt spray test. Ageing induced significant spallation of the PVD coating and breakdown of the oxide film during anodic polarization occurred site specific at the delaminated regions, supporting the hypothesis of passivity breakdown via micro-crevice corrosion. Overall, the work stresses the importance of adhesion and interfacial properties of electrochemically inert coatings on stainless steels and exemplifies how insufficient adhesion may deteriorate the corrosion performance of the substrates.

Acknowledgements

The authors acknowledge Innovation Fund Denmark for providing financial funding under grant no. 50-2014-1 and all project partners. SiOx Aps and Polyteknik A/S are gratefully acknowledged for the deposition of coatings.

References

[1] L. Ćurković, H.O. Ćurković, S. Salopek, M.M. Renjo, S. Šegota, Enhancement of corrosion protection of AISI 304 stainless steel by nanostructured sol–gel TiO2 films, Corros. Sci. 77 (2013) 176–184.

[2] P. de Lima-Neto, L.A. Avaca, Electrochemical Studies of the Corrosion of 316L Stainless Steel coated with Sol-Gel ZrO2, J. Braz. Chem. Soc. 6 (1995) 33–37.

[3] H. Hasannejad, T. Shahrabi, A.S. Rouhaghdam, M. Aliofkhazraei, Effect of Temperature on Pitting Corrosion Resistance of 316 Stainless Steel Coated by Cerium Oxide Film in 3.5 % NaCl Solution, J. Mater. Sci. Technol. 24 (2008) 715–717.

[4] P.P. Trazaskoma-Paulette, A. Nazeri, Effects of Sol-Gel Coatings on the Localized Corrosion Behavior of 304 Stainless Steel, J. Electrochem. Soc. 144 (1997) 1307–1310.

[5] D. Pech, P. Steyer, J.-P. Millet, Electrochemical behaviour enhancement of stainless steels by a SiO2 PACVD coating, Corros. Sci. 50 (2008) 1492–1497.

[6] S. Meth, N. Savchenko, F.A. Viva, D. Starosvetsky, A. Groysman, C.N. Sukenik, Siloxane-based thin films for corrosion protection of stainless steel in chloride media, J. Appl. Electrochem. 41 (2011) 885–890.

[7] D.C.L. Vasconcelos, J.A.N. Carvalho, M. Mantel, W.L. Vasconcelos, Corrosion resistance of stainless steel coated with sol–gel silica, J. Non. Cryst. Solids. 273 (2000) 135–139.

[8] M. Atik, P. de Lima Neto, L.A. Avaca, M.A. Aegerter, J. Zarzycki, Protection of 316L stainless steel against corrosion by SiO2 coatings, J. Mater. Sci. Lett. 13 (1994) 1081–1085.

[9] G.A. Garzino-Demo, F.L. Lama, Friction and wear of uncoated or SiO2-coated 329 stainless steel and of uncoated or A1N-coated aluminium surfaces, Surf. Coatings Technol. 68/69 (1994) 507–511.

[10] J. Gallardo, A. Duran, I. Garcia, J.P. Celis, M.A. Arenas, A. Conde, Effect of Sintering Temperature on the Corrosion and Wear Behavior of Protective SiO2-Based Sol-Gel Coatings, J. Sol-Gel Sci. Technol. 27 (2003) 175–183.

[11] O. Santos, T. Nylander, R. Rosmaninho, G. Rizzo, S. Yiantsios, N. Andritsos, A. Karabelas, H. Müller-Steinhagen, L. Melo, L. Boulangé-Petermann, C. Gabet, A. Braem, C. Trägårdh, M. Paulsson, Modified stainless steel surfaces targeted to reduce fouling—surface characterization, J. Food Eng. 64 (2004) 63–79.

[12] K. Baba, R. Hatada, S. Nagata, H. Fujiyama, G.K. Wolf, W. Einsinger, SiO2 coatings produced by ion beam assisted ECR-plasma CVD, Surf. Coatings Technol. 75 (1995) 292–296.

[13] R. Rosmaninho, O. Santos, T. Nylander, M. Paulsson, M. Beuf, T. Benezech, S. Yiantsios, N. Andritsos, A. Karabelas, G. Rizzo, H. Müller-Steinhagen, L.F. Melo, Modified stainless steel surfaces targeted to reduce fouling – Evaluation of fouling by milk components, J. Food Eng. 80 (2007) 1176–1187.

[14] F. Lampert, A.H. Jensen, R.U. Din, P. Møller, Hydrogen Silsesquioxane based silica glass coatings for the corrosion protection of austenitic stainless steel, Surf. Coatings Technol. 307 (2016) 879–885.

[15] Y.K. Siew, G. Sarkar, X. Hu, J. Hui, A. See, C.T. Chua, Thermal Curing of Hydrogen Silsesquioxane, J. Electrochem. Soc. 147 (2000) 335.

[16] H. Liou, J. Pretzer, Effect of curing temperature on the mechanical properties of hydrogen silsesquioxane thin films, Thin Solid Films. 335 (1998) 186–191.

[17] J. Cech, H. Pranov, G. Kofod, M. Matschuk, S. Murthy, R. Taboryski, Surface roughness

reduction using spray-coated hydrogen silsesquioxane reflow, Appl. Surf. Sci. 280 (2013) 424–430.

[18] F. Lampert, A.H. Jensen, R.U. Din, Y. Gonzalez-Garcia, P. Møller, Properties and performance of spin-on-glass coatings for the corrosion protection of stainless steels in chloride media, Unpubl. Work. (2017).

[19] C.J. Brinker, G.W. Scherer, Sol-gel science: the physics and chemistry of sol-gel processing, in: Acad. Press London, 1990: pp. 108–152.

[20] J. Foggiato, Chemical Vapor Deposition of Silicon Dioxide Films, in: Handb. Thin Film Depos. Process. Tech. (Second Ed., 2nd ed., Elsevier B.V., 2001: pp. 111–149.

[21] H. Bartzsch, D. Glöß, B. Böcher, P. Frach, K. Goedicke, Properties of SiO2 and Al2O3 films for electrical insulation applications deposited by reactive pulse magnetron sputtering, Surf. Coatings Technol. 174–175 (2003) 720–724.

[22] P. Frach, H. Bartzsch, D. Glöß, M. Fahland, F. Händel, Electrically insulating Al2O3 and SiO2 films for sensor and photovoltaic applications deposited by reactive pulse magnetron sputtering, hollow cathode arc activated deposition and magnetron-PECVD, Surf. Coatings Technol. 202 (2008) 5680–5683.

[23] P.J. Kelly, R.D. Arnell, Magnetron sputtering: a review of recent developments and applications, Vacuum. 56 (2000) 159–172.

[24] P.J. Kelly, J.W. Bradley, Pulsed magnetron sputtering – process overview and applications, J. Optoelectron. Adv. Mater. 11 (2009) 1101–1107.

[25] ASTM Standard G61-86, "Standard Test Method for Conducting Cyclic Potentiodynamic Polarization Measurements for Localized Corrosion Susceptibility of Iron, Nickel or Cobalt Based Aalloys," Annu. B. ASTM Stand. (2010) 1–5.

[26] R. Qvarfort, New Electrochemical Cell for Pitting Corrosion Testing, Corros. Sci. 28 (1988).

[27] ASTM Standard A480/A480M 14b: Standard Specification for General Requirements for Flat-Rolled Stainless and Heat- Resisting Steel Plate, Sheet, and Strip, (2016) 1–26.

[28] F. Lampert, A.B. Christiansen, R.U. Din, Y. Gonzalez-Garcia, P. Møller, Corrosion Resistance of AISI 316L Coated with an Air-Cured Hydrogen Silsesquioxane Based Spin-On-Glass Enamel in Chloride Environment, Corros. Sci. (In Press. August 24th 2017). (2017).

[29] J.E. Pawel, C.J. McHargue, Testing of adhesion of thin films to substrates, J. Adhes. Sci. Technol. 2 (1988) 369–383.

[30] T.R. Hull, J.S. Colligon, A.E. Hill, Measurement of thin film adhesion, Vacuum. 37 (1987) 327–330.

[31] F. Lampert, S. Kadkhodazadeh, T. Kasama, K.V. Dahl, A.B. Christiansen, P. Møller, Probing the chemistry of adhesion between a 316L substrate and spin-on-glass coating, Unpubl. Work. (2017).

[32] A. Kriaa, N. Hamdi, H. Sidhom, Assessment of Intergranular Corrosion of Heat Treated Austenitic Stainless Steel (AISI 316L Grade) by Electron Microscopy and Electrochemical Tests, Prot. Met. 44 (2008) 506–513.

[33] D. Wallinder, I.O. Wallinder, C. Leygraf, Influence of surface treatment of type 304L stainless steel on atmospheric corrosion resistance in urban and marine environments, Corrosion. 59 (2003) 220–227.

[34] P.C. Pistorius, G.T. Burstein, Detailed Investigation of Current Transients from Metastable Pitting Events on Stainless Steel - The Transition to Stability, Mater. Sci. Forum. 111–112 (1992) 429–452.

[35] G. Wranglén, Pitting and Sulphide Inclusions in Steel, Corros. Sci. 14 (1974) 331–349.
[36] S. Ito, H. Omata, T. Murata, Y. Yabumoto, Atmospheric Corrosion and Development of a Stainless Steel Alloy Against Marine Environments, in: S.W. Dean, T.S. Lee (Eds.), Degrad. Met. Atmos. ASTM STP 965, American Society for Testing and Materials, Philadelphia, USA, 1988: pp. 68–77.
[37] T. Hong, T. Ogushis, M. Nagumo, The Effect of Chromium Enrichment in the Film Formed by Surface Treatments on the Corrosion Resistance of Type 430 Stainless Steel, Corros. Sci. 38 (1996) 881–888.
[38] D. Wallinder, J. Pan, C. Leygraf, A. Delblanc-Bauer, EIS and XPS study of surface modification of 316LVM stainless steel after passivation, Corros. Sci. 41 (1998) 275–289.
[39] M. Klause, U. Rothhaar, M. Bicker, W. Ohling, Dissolution of thin SiO2-coatings – Characterization and evaluation, J. Non. Cryst. Solids. 356 (2010) 141–146.

11 Technical Note 1

Low temperature curing of hydrogen silsesquioxane films by electron beam curing*

Felix Lampert[a], Annemette H. Jensen[b], Per Møller[a]

[a] Technical University of Denmark, Department of Mechanical Engineering, Produktionstorvet 425, 2800 Kgs. Lyngby, Denmark
[b] SiOx ApS, Bybjergvej 7, 3600 Espergærde, Denmark

Abstract

The effect of electron beam curing at irradiation doses between 2 and 12 MGy on the degree of cross-linking of HSQ-based thin films has been studied by FT-IR and compared to a film which was thermally cured in air at 450 ºC. Curing at increasing irradiation doses leads to processing polymerization of the films and cured the films exhibit a strong tendency for water adsorption. The achievable degree of polymerization is significantly lower than the thermally cured reference. Due to the low achievable degree of transformation, curing by electron beam irradiation under the applied parameters and irradiation doses was found inadequate as polymerization treatment for HSQ-based wet-corrosion barrier coatings.

* The technical note is based on data published in a white paper: F. Lampert, A.H. Jensen, P. Møller, Low Temperature Curing of Hydrogen Silsesquioxane Surface Coatings for Corrosion Protection of Aluminum, NASF Surface Technology White Papers 80(4), 1-8, 2016

11.1 Introduction

Within the project, electron beam curing was investigated as alternative approach to thermal curing, since thermal curing on Al-substrates led to severe mechanical deterioration of the substrates. The study [1] is not presented in detail, since it was primarily conducted on Al 1050 substrates, and thus out of scope for the present thesis. The key findings of the study, leading to a negative assessment of electron beam curing as alterative curing method for SOG-coatings are summarized in the following.

11.2 Experimental methods

Within the study, HSQ-based films were deposited on Si wafer substrates and the effect of thermal curing in air at 450 ºC (process in analogy to chapters 5,6) was compared to electron beam curing on a Comet EBLab low energy accelerator with an acceleration voltage of 100 kV and a beam current of 5.281 mA. The irradiation was dosed by iterative exposure to multiple cycles of electron beam exposure at 38.6 kGy/cycle (1 Gy: Absorption of 1 J of ionizing radiation per kg of matter), yielding irradiation doses between 2 and 12 MGy. The film thickness was investigated by ellipsometry on a VASE ellipsometer and the degree of polymerization was assessed by FT-IR on a Thermo Scientific Nicolet iN10 MX instrument in transmittance mode. The obtained IR data were normalized by the wafer thickness and referenced against an air background. Further, the data were digitally modified by baseline subtraction and removal of the C=O asymmetric stretching edge at 2242-2208 cm^{-1}.

11.3 Results and discussion

The FT-IR absorption spectra of the electron beam cured films in reference to an uncured (soft-baked) film and the thermally cured film are visualized in Figure 11.1. In agreement with the observations made in chapter 6, curing at 450 ºC led to a change from cage to network structure together with a significant decrease in Si-H content. Further, hydroxylation of the film was present. As shown by the curves labelled with 2 MGy to 12 MGy, irradiation curing led to progressing polymerization of the films (indicated by the characteristic shift from Si-O cage to Si-O network peak absorption) together with a decreasing Si-H peak. However, even after the highest applied irradiation dose, the irradiated film shows a lesser degree of polymerization with respect to the thermally cured reference: Based on qualitative analysis of spectrum labelled “12 MGy”, the Si-O cage absorption peak is distinctly visible together with a more pronounced Si-H peak. Moreover, electron beam curing has led to significant hydroxylation, as visible from the distinct hydroxyl feature.

Since the precursor is widely used as electron beam resist, the effect of electron beam curing on HSQ films has been extensively studied [2–5] and the electron beam induced polymerization has been described as an irradiation induced redistribution reaction [3] or a mechanism based on the formation of radical Si· sites with a subsequent formation of silanol groups with atmospheric water and a following condensation, forming siloxane bonds between neighboring oligomers [2]. Since the herein investigated films show significant hydroxylation which may originate from electron beam induced film oxidation, this study supports the curing mechanism presented by Namatsu *et al.* [2]; however, further dedicated studies are necessary to conclude on the curing mechanism. Since only low degrees polymerization are necessary to provide sufficient integrity to give negative tone, the studied irradiation doses were generally lower than the herein applied maximum dose of 12 MGy. Considering the high degree of polymerization which is necessary to maintain long term stability in aqueous environment (chapter 8), electron beam curing at room temperature in the herein applied irradiation needs to be assessed as inadequate for the purpose of barrier coatings in aqueous environment. A further increase in irradiation dose was not attempted in the present study, since the necessary irradiation dose was found excessive with respect to the typically applied doses (typical doses for the industrial curing of composites or adhesives are in the range of 50-200 kGy [6]). A study by Lee *et al.* [7], however, has shown that significantly higher conversions can be achieved by an electron beam superimposed thermal treatment. The possibility of lowering the curing temperature or increasing the overall obtainable conversion rate has to be investigated in further studies.

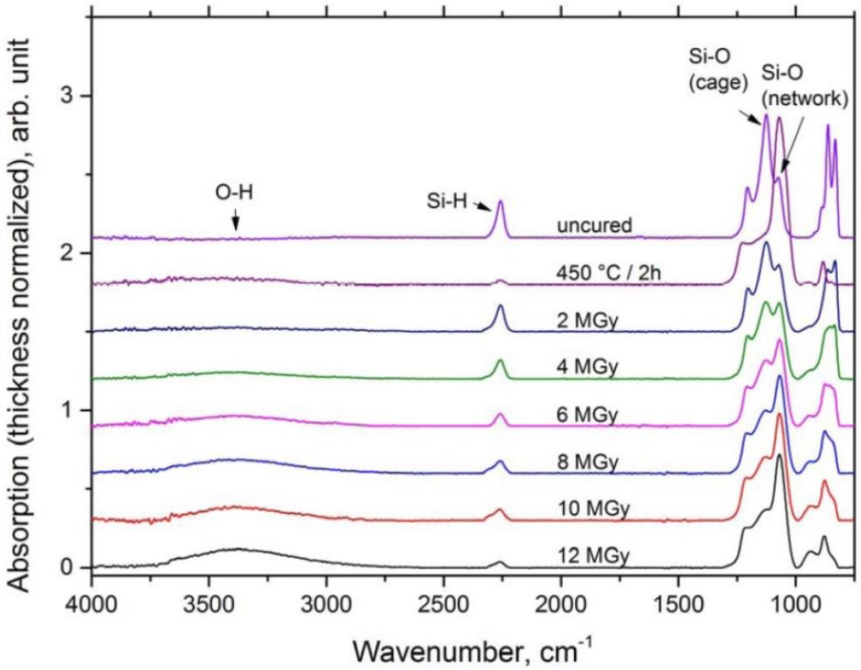

Figure 11.1: *Thickness normalized absorption in FT-IR for uncured (soft-baked at 160 ºC for 30 min), thermally cured and electron beam cured HSQ-based films deposited on Si wafer substrates. [1].*

References

[1] F. Lampert, A.H. Jensen, P. Møller, Low Temperature Curing of Hydrogen Silsesquioxane Surface Coatings for Corrosion Protection of Aluminum, NASF Surf. Technol. White Pap. 80 (2016) 1–8.

[2] H. Namatsu, Y. Takahashi, K. Yamazaki, T. Yamaguchi, M. Nagase, K. Kurihara, Three-dimensional siloxane resist for the formation of nanopatterns with minimum linewidth fluctuations, J. Vac. Sci. Technol. B. 16 (1998) 69.

[3] D.L. Olynick, B. Cord, A. Schipotinin, D.F. Ogletree, P.J. Schuck, Electron-beam exposure mechanisms in hydrogen silsesquioxane investigated by vibrational spectroscopy and in situ electron-beam-induced desorption, J. Vac. Sci. Technol. B Microelectron. Nanom. Struct. 28 (2010) 581–587.

[4] T. Nakamura, M. Sasaki, A. Kobayashi, K. Sawa, K. Mine, Oxidative Curing of Hydrogen Silsesquioxane Resin Films by Electron Beam Irradiation without Additional Heatings and Characterization of the Cured Films, Jpn. J. Appl. Phys. 40 (2001) 6187–6191.

[5] S. Choi, M.J. Word, V. Kumar, I. Adesida, Comparative study of thermally cured and electron-beam-exposed hydrogen silsesquioxane resists, J. Vac. Sci. Technol. B. 26 (2008) 1654–1659.

[6] D.L. Goodman, G.R. Palmese, Curing and Bonding of Composites using Electron Beam Processing Curing and Bonding of Composites using Electron Beam Processing, in: A.K. Kulshreshtha, C. Vasile (Eds.), Handb. Polym. Blends Compos. Vol. 1, 202AD: pp. 459–500.

[7] H.-J. Lee, J. Goo, S.-H. Kin, J.-G. Hong, H.-D. Lee, H.-K. Kang, S.-I. Lee, M.Y. Lee, A New, Low-Thermal-Budget Planarization Scheme for Pre-Metal Dielectric Using Electron- Beam Cured Hydrogen Silsesquioxane in Device, Jpn. J. Appl. Phys. 39 (2000) 3924–3929.

12 General discussion

Since the experimental chapters (5-11) depict a progressive evolution of the coating system, including detailed, however, narrowly focused discussions of the particular research topics and coating functionality, this chapter provides a general discussion of the functionality and applicability of HSQ-based films as barrier coatings for stainless steels.

12.1 Process feasibility and coating characteristics

As demonstrated in chapters 5-11, the deposition of HSQ-based films by the dip-coating method on stainless steel substrates is generally feasible and yields well-adherent, transparent thin film coatings with excellent coverage and an average thickness in the sub-micrometer range. In analogy to pre-existing literature [1–3], the coating precursor can freely flow into substrate defects before polymerization, and thus smoothen and level the surface (chapter 5).

12.2 Curing of SOG-coatings

12.2.1 Impact of the curing conditions on the coating chemistry

As expected from previous reports [4], oxidative film curing in air yielded higher efficiencies with respect to non-oxidative curing in Formiergas. This was shown by transmission FT-IR, which indicated advanced loss in hydrogenation for oxidatively cured films above ~550 ºC (chapter 7) with respect to non-oxidatively cured films, which remained (to a minor extend) hydrogenated even at the maximum applied curing temperature of 800 ºC. Oxidative curing induced significant hydroxylation for all investigated films, whereby non-oxidatively cured films did not hydroxylate at similar curing temperatures. This was explained by artefacts from the oxidative curing, which polymerizes the material via an oxidation/condensation reaction [4] and may leave uncondensed hydroxyl groups in the films. Despite the oxygen-free curing, hydroxylation was detected in the non-oxidatively cured films between 600-700 ºC, which was explained by rapid water absorption from the ambient air between curing and analysis [4–6], indicating that the material was imperfectly cured at the given temperature. From transmission FT-IR analysis, a SOG-film cured at 800 ºC in non-oxidative environment appeared hydroxyl-free, indicating that SOG-films with a higher degree of polymerization exhibit an increased resilience to moisture absorption from the air. ATR FT-IR investigation of a coating cured under similar conditions, however, showed clear signs of hydroxylation (chapter 10). While the films for transmission analysis were stored for ~48 h under ambient conditions between curing and analysis, the films coated on metallic substrates were stored ~6 months under ambient conditions. As shown by Lifshitz *et al.* [7], low density SOG materials may show significant water uptake during ambient storage over several months and in analogy, the deviations in film hydroxylation between the initial analysis (chapter 9) and the final analysis (chapter 10) likely originated from ambient moisture absorption during the prolonged sample storage.

In addition to the material characterization by IR spectroscopy, XPS analysis (chapter 9) showed that curing with Formiergas at 800 ºC leads to incomplete film polymerization, with the predominant Si species being Si^{4+} (from the SiO_2 backbone) together with a minor quantity of Si^0 (due the formation of Si nano-domains) and lower valent Si, such as Si^{2+}, indicating the presence of Si-suboxides. Curing temperatures exceeding 800 ºC were not investigated, since competitive processes (*e.g.* sol-gel) may yield similar oxide qualities at similar or lower temperatures [8]. Hence, none of the herein investigated non-oxidatively cured coating films were fully polymerized, giving direct incentives to the mechanical properties (see section 12.2.3) and to the coating stability (see section 12.3.1).

Clearly, the herein applied curing conditions only partially convert the precursor, while higher degrees of cross-linking are desirable to enable the industrial application of the technology. As discussed by Bremmer *et al.* [4], HSQ-resin is highly sensitive to extremely low oxygen concentration in the curing ambient (concentrations as low as 10 ppm O_2 in inert N_2 curing atmosphere have shown to increase the curing efficiency) and a controlled dosage of O_2 into an inert curing atmosphere may increase the film density to an acceptable level without inducing unacceptable substrate deterioration. Curing in a controlled and mildly oxidizing atmosphere was not attempted in this study and further research is suggested to conclude on the feasibility and efficiency of mildly oxidizing curing.

As an alternative approach to high temperature curing, low temperature curing by electron beam irradiation was attempted; however, the maximum applied dose of 12 MGy was found insufficient for the application as a corrosion barrier coating in aqueous environment (chapter 11). Hence, it was evident that sufficiently high coating polymerization requires an excessive irradiation dose with respect to electron beam curing of existing technologies (*i.e.* polymers and adhesives), which lies between 50-200 kGy [9]. Lee *et al.* [10] demonstrated the synergistic effect of electron beam curing with superimposed heating at 400 ºC, and demonstrated significantly increased conversion rates for irradiation curing of heated samples with respect to solely irradiation cured samples. Hence, superimposed irradiation curing and sample heating may be a viable alternative to either decrease the overall thermal budget of the curing process, or achieve sufficiently high conversion to SiO_2 to guarantee an appropriate chemical coating stability for the process.

Since the precursor is sensitive to various types of irradiation [11], other types of irradiation have shown promising degrees of conversion and may be viable alternatives to increase the processing efficiency. In particular high power plasma treatments have shown high degrees of film densification [12]. However, the previously applied plasma energies were not sufficient to induce a chemical stability similar to thermal oxide and may be insufficient for the application as barrier coatings. Even though not previously investigated, plasma treatments may, similar to electron beam treatments, show synergistic effects with superimposed sample heating and it is proposed that a low

temperature thermal treatment together with a superimposed high energy plasma treatment may yield sufficient densification to enable the application of the coating in aqueous environments. Lastly, rapid thermal processing by heating with *e.g.* high power lamps may portray a viable alternative to furnace curing, since the process has shown to induce high degrees of precursor conversion at short processing times [13]. The effect of RTP on coating curing on metallic substrates needs to be investigated in further research.

12.2.2 Impact of the curing conditions on the coating interface and adhesion

Chapters 6 and 8 demonstrated the fundamentally different impact of the curing conditions on the coating/substrate transition. While curing in air led to thermal oxidation of the substrate, curing in Formiergas atmosphere led to the formation of a thin interface in form of crystalline silicates. In analogy to thermal oxidation of stainless steels [14–16], the interfacial oxidation in the air-cured system led to Cr-depletion of the substrate, which further impacted the corrosion performance of the systems. In contrast to the air-cured system, curing in Formiergas atmosphere suppressed the formation of a thick thermal oxide at the interface and induced the formation of a Si/Cr-rich silicate interfacial layer. The role of interface formation in both air- and Formiergas-cured systems is discussed in section 12.3.2.

Both curing methods yielded well adherent coatings which showed only microscopic delamination by cross-cut testing. However, while Formiergas-cured coatings showed primarily adhesive coating failure, air-cured systems exhibited crack propagation between the outer and inner region of the thermal oxide, indicating that the interface may guide cracks and pose a potential weakness to the adhesion of the coating [17,18]. In addition to crack propagation within the interface, interfacial oxidation led to void formation for coatings cured above 450 ºC, illustrating a further detrimental effect of the interfacial oxidation and posing a further potential weakness for the corrosion resistance (section 12.3.2).

Formiergas-cured coatings showed an increased adhesion with respect to PVD-silica coated substrates, which was interpreted as an increased adhesion due to the silicate rich bonding layer expected for the Formiergas-cured system. However, it was suggested that a distinct difference in film compliance and the recovery of deformation hardening during the thermal annealing may have impacted the adhesion testing results.

12.2.3 Impact of the curing conditions on the mechanical properties

The previously discussed deviation in coating chemistry and coating density directly affected the mechanical integrity of the SOG-films. Formiergas-curing at temperatures between 400-800 ºC led to progressive stiffening of the films together with an increase in film (nanoindentation) hardness. Comparison to fused silica, however, showed that even films cured at 800 ºC had significantly lower mechanical integrity: The films showed an indentation modulus of maximal 61 GPa (*c.f.* 71 GPa for fused silica) and a maximum

indentation hardness of 6.3 GPa (*c.f.* 10.8 GPa for fused silica), which again indicates imperfect polymerization or a lower density of the SOG-film with respect to fused silica. Overall, the present quantification deviates significantly from a previous study by Liou *et al.* [19], which assumed similar mechanical properties of SOG-films to SiO_2. Since the herein presented analysis was verified on a fused silica slide, uncertainties in analysis routine or inadequate determination of the indenter area function in this report were excluded as potential origin for this deviation. However, the results presented by Liou *et al.* [19] showed an increased modulus of HSQ-films (>80 GPa) with respect to the literature values for SiO_2 (~70 GPa [20]), indicating that the accuracy of their analysis may have been compromised by an inadequate analysis routine (*e.g.* inaccurate calculation of indenter area function). Alternatively, the observed effect may originate from the differences in curing ambient (Formiergas-curing with respect to N_2 inert gas curing) or differences in applied indentation depth, which has been shown to affect the quantification of nanoindentation data, in particular at shallow indentations [20]. Since Liou *et al.* [19] do neither present their load vs. indenter displacement data, nor verify their analysis routine on a standardized sample, the exact origin for the deviation could not be substantiated.

12.3 Application of SOG as corrosion barrier on stainless steel substrates

12.3.1 Chemical stability of the coatings

Chemical dissolution of the coating was generally observed during ageing in an artificial salt spray atmosphere (chapters 7, 9 & 10) and was correlated with the thermodynamical instability of the SiO_x-like material together with high dissolution kinetics due to film imperfections. Plausible present film imperfections, such as residual Si-H, silanol, low valent Si, film porosity or molecular porosity due to poor cross-linking, were identified by FT-IR, XPS or nanoindentation testing. Generally, higher dissolution rates were obtained for films which were cured at lower curing temperatures with respect to films which were cured at high temperatures or thermally grown SiO_2, which was virtually stable under the applied ageing conditions (chapter 9). It was suggested that the higher defect densities in the films cured at lower temperatures are accountable for the higher dissolution kinetics. Similar to SOG, PVD-based SiO_2 showed instability during neutral salt spray testing; however, the dissolution rate was decreased with respect to SOG (chapter 10), which supports the hypothesis of accelerated coating dissolution at high defect densities. Further, the hypothesis is in line with previous reports, which have shown that SiO_x films with large defect densities may lead to accelerated dissolution kinetics [21,22]. Overall, this study has shown that SOG curing under the herein applied curing conditions does not yield chemically stable films, which gives a motivation for further research into curing processes that may yield higher cross-linking. Possible curing mechanisms have been discussed in section 12.2.1.

While several groups have identified stress corrosion cracking (SCC) as possible failure mechanism of SOG in moist environment [23–25], no case of SCC was found for SOG-coatings on stainless steel substrates in this study. Cook *et al.* [23] identified the driving factors for SCC in SOG-films and showed that highly cross-linked films exhibit a decreased tendency to fail via SCC. Since the focus of the present study was set on films with high cross-linking, the driving force for SCC may have been too low to initiate coating failure. Further, the films tested in this study were generally deposited with low thickness (<500 nm), which additionally decreases the tendency for SCC. Lastly, SCC failure of SOG-films requires tensile stress in the material; however, the stress-state of the films on stainless steel remains unknown and compressive stress (as it was observed on Si wafer for curing above 600 ºC in inert atmosphere) may prevent failure via SCC.

12.3.2 Corrosion resistance of glass coated type 316L stainless steel

Barrier performance

All investigated coatings showed two distinct capacitive features in EIS, indicating contact between the electrolyte and the substrate. Thus all coatings deviated from the ideal response for excellent thin film SiO_x barrier coatings reported by Pech *et al.* [26], who measured a single capacitive plateau over the entire frequency domain on CVD SiO_x –coated, mirror polished stainless steel substrates. Further, the distinct EIS response of SOG coated stainless steel indicated coating flaws which expose the substrate to the electrolyte and cannot be prevented under application of the herein applied SOG deposition process. The distinct origin of the coating flaws could not be determined from EIS analysis by the equivalent circuit approach; however, the highly scattered values of the pore resistance suggest an inhomogeneous distribution of the coating defects rather than a uniformly distributed defect source such as homogeneous coating porosity. Since all SOG-coatings in this work have been deposited under ambient conditions without control of the particle density in the air, the present defects may, apart from coating delamination (observed in form of “void formation” in chapter 7 and “micro-crevice formation” in chapter 9) originate from incorporated external particles.

Comparison of the EIS response between air and Formiergas-cured systems generally showed an increased average pore resistance of the Formiergas-cured systems with respect to the air-cured systems. This deviation may originate from the increased defect density due to voids at the coating interface which was observed for the air-cured systems, or from the highly hydrophilic properties of the air cured systems at low curing temperatures, *i.e.* at low densification. Similar to the SOG-coatings, the PVD coatings exhibited an imperfect barrier response. Analysis of the coating microstructure revealed that the coatings were susceptible to bulging and flaking, and thus coating delamination together with spallation was identified as the primary defect in the PVD-based systems.

Substrate passivity

As shown in chapter 6, air curing under the applied parameters leads to a distinct Cr-depletion of the surface of the substrate which further decreases the passive layer stability (chapter 7). A negative impingement of the curing mechanism on the substrate stability was found throughout the entire investigated curing temperature domain (curing between 400-550 ºC) and the effect was most pronounced at elevated curing temperatures where a full loss in passivity was evident. Further, as proposed in chapter 7, the coating itself may act as a stable pit cover, thereby stabilizing growing pits. Hence, curing in air was generally assessed as an inadequate process to polymerize SOG-coatings on stainless steel substrates in the application as barrier coatings for chloride media.

As demonstrated in chapter 8, interfacial oxidation together with process-induced sensitization due to Cr-depletion of the substrate subsurface region may be prevented by curing in Formiergas. Further, SOG-coatings may effectively increase the breakdown potential (chapters 9, 10), *i.e.* stabilize the native oxide or form an efficient barrier that shields the substrate; however, a wide spread in obtainable breakdown potential was observed and it was shown that the breakdown potential measured on coated substrates may be decreased with respect to uncoated reference samples. While similar effects have been observed for sol-gel coated AISI 316 steel [27], which showed severe effects of carbide-induced sensitization after high temperature curing, significant effects from carbide sensitization were suppressed due to the use of carbon depleted steel, which is not expected to show sensitization at the applied curing temperatures and within the short curing times which were applied in this work [28]. As a potential weakness, microscopic delamination at substrate defects in connection with substrate roughness was identified and it was shown that pitting corrosion may be initiated at these defects. Based on this observation it was proposed that decreasing the substrate roughness may increase the stability towards preliminary passivity breakdown.

This hypothesis was investigated by substitution of the etched no. 2B substrate finish used in chapters 5-9 by a smooth bright annealed substrate finish (chapter 10). Evidently, changing to a higher grade substrate finish eliminated the problems identified in chapter 9. Moreover, the effect was persistent even after aging of the coating, showing that the positive effect of SOG-coating on the corrosion resistance of stainless steel substrates may be maintained even when the coating is chemically attacked. However, the nature of this increase could not be clearly identified: Pech *et al.* [26] observed similar behavior for perfectly capacitive SiO_x barrier coatings and argued that the positive shift in breakdown potential originates from shielding of the substrate, followed by dielectric breakdown of the coating at the breakdown/pitting potential observed during potentiodynamic anodic polarization. Since the herein investigated coatings showed imperfect barrier behavior (chapter 7, 9 & 10) and potentially negative shifts in breakdown potential on flawed coatings, the observed behavior cannot be fully explained by dielectric breakdown of the coating. It was suggested that the anodic shift in breakdown potential may originate from the chemical alteration of the native oxide due to *e.g.* a distinct increase in Si [29,30] or

Cr [29,31,32] content (chapter 8). Alternatively, it was suggested that the anodic shift in breakdown potential arise from a high probability to cover weak spots in the substrate, such as sulphide inclusions [33,34], which may efficiently prevent pitting initiation within the experiment.

Finally, the general effect of a thin glass coating on the corrosion resistance of stainless steel was studied based on a PVD SiO_2 film on stainless steel substrate. It was demonstrated that the film strongly impaired the corrosion resistance of the substrate, leading to significant metastable pitting and preliminary passivity breakdown during potentiodynamic anodic polarization. In analogy to the previous investigation (chapter 9), it was proposed that the preliminary breakdown may originate from coating delamination followed by the initiation of micro-crevice corrosion, which occurred on occluded sections of the substrate.

References

[1] K. Mohaghegh, H.N. Hansen, H. Pranov, G. Kofod, A study on the surface roughness of a thin HSQ coating on a fine milled surface, in: 14th Euspen Int. Conf. - Dubrovink, 2014.

[2] K. Mohaghegh, H.N. Hansen, H. Pranov, G. Kofod, Verification of thickness and surface roughness of a thin film transparent coating, in: Proc. 13th Euspen Int. Conf., Berlin, 2013.

[3] J. Cech, H. Pranov, G. Kofod, M. Matschuk, S. Murthy, R. Taboryski, Surface roughness reduction using spray-coated hydrogen silsesquioxane reflow, Appl. Surf. Sci. 280 (2013) 424–430.

[4] J.N. Bremmer, Y. Liu, K.G. Gruszynski, F.C. Dall, Cure of Hydrogen Silsesquioxane for Intermetal Dielectric Applications, Mater. Res. Soc. Symp. Proc. 476 (1997) 37–44.

[5] D. Többen, P. Weigand, M.J. Shapiro, S.A. Cohen, Influence of the cure process on the properties of hydrogen silsesquioxane spin-on-glass, Mater. Res. Soc. Somposium Proc. 443 (1997) 195–200.

[6] B.K. Hwang, J.H. Choi, H.J. Lee, J.S. Goo, U.-I. Chung, Y. Lee, Moon, Simple and Low Thermal Budget Planarization Process for Premetal Dielectric Based Spin-on Hydrogen Silsesquioxane (HSQ), in: VLSI Multilevel Interconnect. Conf., Santa Clara, CA, USA, 1996: pp. 623–625.

[7] N. Lifshitz, G. Smolinsky, Hot-Carrier Aging of the MOS Transistor in the Presence of Spin-on Glass as the Interlevel Dielectric, IEEE Electron Device Lett. 12 (1991) 140–142.

[8] C.J. Brinker, G.W. Scherer, Sintering, in: Sol-Gel Sci., Academic Press, Inc., San Diego, 1990: pp. 675–742.

[9] D.L. Goodman, G.R. Palmese, Curing and Bonding of Composites using Electron Beam Processing Curing and Bonding of Composites using Electron Beam Processing, in: A.K. Kulshreshtha, C. Vasile (Eds.), Handb. Polym. Blends Compos. Vol. 1, 202AD: pp. 459–500.

[10] H.-J. Lee, J. Goo, S.-H. Kin, J.-G. Hong, H.-D. Lee, H.-K. Kang, S.-I. Lee, M.Y. Lee, A New, Low-Thermal-Budget Planarization Scheme for Pre-Metal Dielectric Using Electron- Beam Cured Hydrogen Silsesquioxane in Device, Jpn. J. Appl. Phys. 39 (2000) 3924–3929.

[11] M. Peuker, M.H. Lim, H.I. Smith, R. Morton, A.K. van Langen-Suurling, J. Romijn, E.W.J.M. van der Drift, F.C.M.J.M. van Delft, Hydrogen SilsesQuioxane, a high-resolution negative tone e-beam resist, investigated for its applicability in photon-based lithographies, Microelectron. Eng. 61–62 (2002) 803–809.

[12] J. Penaud, F. Fruleux, E. Dubois, Transformation of hydrogen silsesquioxane properties with RIE plasma treatment for advanced multiple-gate MOSFETs, Appl. Surf. Sci. 253 (2006) 395–399.

[13] T.E. Gentle, Oxidation of Hydrogen Silsesquioxane, (HSiO3/2)n, by Rapid Thermal Processing, in: SPIE Vol. 1595 Rapid Therm. Integr. Process., 1991: pp. 146–164.

[14] I. Olefjord, Application of ESCA to Oxide Films Formed on Stainless Steels at Intermediate and High Temperatures, Met. Sci. 9 (1975) 263–268.

[15] G. Hultquist, C. Leygraf, Selective Oxidation of a Ferritic Stainless Steel and its Influence on Resistance to Crevice Corrosion Initiation, Corros. Sci. 21 (1981) 401–408.

[16] M. Somervuori, L.-S. Johansson, M.H. Heinonen, D.H.D. van Hoecke, N. Akdut, H.E. Hänninen, Characterisation and corrosion of spot welds of austenitic stainless steels, Mater. Corros. 55 (2004) 421–436.

[17] M. Takemori, Crack formation, exfoliation, and ridge formation in 500 °C annealed sol–gel silica coatings on stainless steel SUS304: Part II Spectroscopic and mechanical analyses and insights into mechanisms controlling coating characteristics, Ceram. Int. 35 (2009) 1747–1755.

[18] M. Takemori, Crack formation, exfoliation, and ridge formation in 500 ^{o}C annealed sol-gel silica coatings on stainless steel SUS304: Part I. Microscopic observations and elemental analysis, Ceram. Int. 35 (2009) 1731–1746.

[19] H. Liou, J. Pretzer, Effect of curing temperature on the mechanical properties of hydrogen silsesquioxane thin films, Thin Solid Films. 335 (1998) 186–191.
[20] H. Li, J.J. Vlassak, Determining the elastic modulus and hardness of an ultra-thin film on a substrate using nanoindentation, J. Mater. Res. 24 (2009) 1114–1126.
[21] M. Klause, U. Rothhaar, M. Bicker, W. Ohling, Dissolution of thin SiO2-coatings – Characterization and evaluation, J. Non. Cryst. Solids. 356 (2010) 141–146.
[22] S.-K. Kang, S.-W. Hwang, H. Cheng, S. Yu, B.H. Kim, J.-H. Kim, Y. Huang, J.A. Rogers, Dissolution Behaviors and Applications of Silicon Oxides and Nitrides in Transient Electronics, Adv. Funct. Mater. 24 (2014) 4427–4434.
[23] R.F. Cook, E.G. Liniger, Stress-Corrosion Cracking of Low-Dielectric-Constant Spin-On-Glass Thin Films, J. Electrochem. Soc. 146 (1999) 4439–4448.
[24] Y. Toivola, J. Thurn, R.F. Cook, Structural, Electrical, and Mechanical Properties Development during Curing of Low-k Hydrogen Silsesquioxane Films, J. Electrochem. Soc. 149 (2002) F9–F17.
[25] E.P. Guyer, R.H. Dauskardt, Fracture of nanoporous thin-film glasses., Nat. Mater. 3 (2004) 53–7.
[26] D. Pech, P. Steyer, J.-P. Millet, Electrochemical behaviour enhancement of stainless steels by a SiO2 PACVD coating, Corros. Sci. 50 (2008) 1492–1497.
[27] P.P. Trazaskoma-Paulette, A. Nazeri, Effects of Sol-Gel Coatings on the Localized Corrosion Behavior of 304 Stainless Steel, J. Electrochem. Soc. 144 (1997) 1307–1310.
[28] A. Kriaa, N. Hamdi, H. Sidhom, Assessment of Intergranular Corrosion of Heat Treated Austenitic Stainless Steel (AISI 316L Grade) by Electron Microscopy and Electrochemical Tests, Prot. Met. 44 (2008) 506–513.
[29] D. Wallinder, I.O. Wallinder, C. Leygraf, Influence of surface treatment of type 304L stainless steel on atmospheric corrosion resistance in urban and marine environments, Corrosion. 59 (2003) 220–227.
[30] S. Ito, H. Omata, T. Murata, Y. Yabumoto, Atmospheric Corrosion and Development of a Stainless Steel Alloy Against Marine Environments, in: S.W. Dean, T.S. Lee (Eds.), Degrad. Met. Atmos. ASTM STP 965, American Society for Testing and Materials, Philadelphia, USA, 1988: pp. 68–77.
[31] T. Hong, T. Ogushis, M. Nagumo, The Effect of Chromium Enrichment in the Film Formed by Surface Treatments on the Corrosion Resistance of Type 430 Stainless Steel, Corros. Sci. 38 (1996) 881–888.
[32] D. Wallinder, J. Pan, C. Leygraf, A. Delblanc-Bauer, EIS and XPS study of surface modification of 316LVM stainless steel after passivation, Corros. Sci. 41 (1998) 275–289.
[33] P.C. Pistorius, G.T. Burstein, Detailed Investigation of Current Transients from Metastable Pitting Events on Stainless Steel - The Transition to Stability, Mater. Sci. Forum. 111–112 (1992) 429–452.
[34] Wranglén, Pitting and Sulphide Inclusions in Steel, Corros. Sci. 14 (1974) 331–349.

References

13 Conclusions

The detailed conclusions derived from the experimental work are available in the experimental chapters (5-11). In the following, a collection of the overall key-conclusions, based on the experimental work and discussions, is given.

1. SOG can be applied on stainless steel to form virtually crack free thin film enamels with a stoichiometry close to SiO_2 and overall good adhesion.
2. SOG-coatings are inherently smooth and decrease the roughness of pickled stainless steel substrates significantly. Major topographical features from the substrate, such as grain boundary voids from a pickled surface, may protrude through the coating.
3. Oxidative curing increases the curing efficiency of SOG-films with respect to reductively cured films and leads to more efficient Si-H dissociation.
4. SOG-coatings with high degrees of polymerization are prone to moisture absorption and hydroxylation. Hydroxylation may be induced due to oxidation during polymerization or absorption of atmospheric moisture after curing.
5. Curing at 450 ºC in air leads to the formation of a thick interfacial zone with characteristics similar to conventional medium temperature oxides on stainless steels.
6. The formation of a thick interfacial zone after oxidative curing may lead to void formation and/or dealloying of the substrate surface, thus impairing the passive performance of the substrate alloy. This may lead to full loss of substrate passivity.
7. Suppression of substrate oxidation by reductive annealing (at 600 ºC) may lead to the formation of a 5-10 nm thick interaction zone and presumably to the formation of transition metal silicates. It was suggested that the interface zone acts as an adhesion layer.
8. Non-oxidatively cured SOG-films cured by the herein applied methods do not fully polymerize when cured up to 800 ºC and consequently form partially hydrogenated SiO_x:H with the presence of low valent Si/Si suboxides and inferior mechanical integrity with respect to amorphous SiO_2.
9. As a result of incomplete densification/polymerization, the herein observed SOG-coatings exhibited decreased chemical stability with respect to amorphous SiO_2 and showed significant dissolution in aqueous media.
10. Local loss of coating adhesion, *i.e.* in deep substrate voids, may act as potent sites for the initiation of crevice corrosion/pitting, and thus poses a critical coating defect. This critical failure mode may be prevented for of SOG-coated stainless steels by selection of a smooth, void free substrate finish such as a bright annealed finish.
11. Inert thin film coatings may act as a stable pit cover and induce crevice corrosion at delaminated cross-sections or stabilize growing pits.

12. SOG-coatings can efficiently increase the breakdown potential of stainless steel substrates. This may be due to their good barrier performance or due to changes in the surface chemistry of the substrates. The effect was inhomogeneous, presumably due to locally varying coating properties/quality.
13. Under the herein applied conditions, SOG-coatings show an imperfect capacitive response and, in conclusion, act as imperfect barrier coatings in NaCl aqueous solutions.
14. Electron beam curing with dosages up to 12 MGy leads to polymerization of the SOG material. The achievable degree of polymerization is, however, low with respect to thermal curing and the method was found inappropriate as polymerization treatment for SOG barrier coatings.

14 Further work

The present dissertation explores the possibility of SOG deposition on austenitic stainless steels, leading to the key-conclusions presented in chapter 13. In addition to the presented experimental work, the following suggestions for further work are given:

1. The present work focused on SOG-coatings as barrier material for chloride-induced corrosion. It was indicated that the coatings significantly alter the surface properties, which may lead to improvements in material performance in applications such as anti-fouling or anti-scaling surfaces. Laboratory and field testing of these properties is ongoing (September 2017). Further, previous research has shown that thin barrier coatings may increase the performance of stainless steels in acidic media or show beneficial effects in high temperature oxidation. A detailed investigation of the performance of SOG coated stainless steel substrates in different applications (in particular as anti-fouling/-scaling treatment) and under different conditions is therefore suggested.
2. All presented investigations showed a significant deviation from ideal barrier behavior, which was interpreted as an indication for coating defects. The coatings appeared virtually free of pinholes or cracks; however, defects due to external particle contamination cannot be categorically excluded since both the coating deposition and curing were performed under ambient conditions. The possibility of improving the coating quality by deposition under cleanroom-conditions should therefore be explored.
3. The presented work solely focused on stainless steel substrates. In further work (not presented here) we have demonstrated successful application of well adherent coatings on ferritic steels, iron and aluminum, while coatings on copper, brass and silver substrate generally showed poor adhesion. Further work on the fundamentals of metal/coating adhesion is necessary to understand the fundamentals of HSQ adhesion on metals and to predict viable coating systems.
4. In this work it was demonstrated that the material may polymerize under different curing conditions or different curing treatments. In addition to thermal curing, electron beam curing and sol-gel transformation (not presented here) was attempted; however, the methods were abandoned due to insufficient cross-linking (electron beam curing) or film fracture (sol-gel transformation). As an alternative approach for curing, in particular combined curing treatments, such as electron beam curing with superimposed heating have shown promising results and should be assessed as a novel approach for highly efficient curing at comparably low temperatures.
5. As an alternative to conventional furnace curing, rapid thermal processing has shown excellent conversion of the precursor at a minimum heat input to the substrate and minimum processing time. The process may induce excellent precursor conversion at a significant decrease of processing time and thermomechanical alteration of the substrate, and thus should be evaluated.

6. Previous research has shown that HSQ resin is sensitive to low levels of O_2 in the atmosphere during thermal processing. Controlled dosing of oxygen into the curing atmosphere may significantly increase the curing efficiency at tolerable degrees of substrate oxidation. Thus, the effect of mildly oxidizing conditions on the performance of SOG coated components should be assessed.
7. The present work showed chemical instability of the coatings in aqueous media due to imperfect densification of the coating films. The work indicated that higher chemical stability may be achieved by higher degrees of film densification; however, increasing the chemical stability beyond the presented levels was not attempted. Since a technological implementation of the material requires higher chemical stability, further work on an increase in film density is proposed.
8. It was previously reported that HSQ films are inherently under macro-stress. The stress state (previously determined by Si wafer curvature measurements) is tensile at low curing temperatures and reversed to compressive stress for curing above ~600 ºC. The herein presented change from Si to austenitic stainless steel substrates largely changes the coefficient of thermal expansion of the substrate and may lead to significant changes in both magnitude and sign of the stress in the film. A detailed investigation on the stress state and the implications on the coating performance is therefore suggested.